Surface Science Reports 74 (2019) 1–95

Contents lists available at ScienceDirect

Surface Science Reports

journal homepage: www.elsevier.com/locate/surfrep

Hexagonal boron nitride monolayers on metal supports: Versatile templates for atoms, molecules and nanostructures

Willi Auwärter

Physics Department, Technical University of Munich, James-Franck-Str. 1, 85748, Garching, Germany

ARTICLE INFO

Article history:
Received 10 March 2018
Revised 11 September 2018
Accepted 6 October 2018
Available online 2 November 2018

Keywords:
Hexagonal boron nitride
Template
Self-assembly
Two-dimensional materials
Heterostructure
Interface

ABSTRACT

Hexagonal boron nitride (*h*BN) monolayers have attracted considerable interest as atomically thin sp^2-hybridized sheets that are readily synthesized on various metal supports. They complement the library of two-dimensional materials including graphene and open perspectives for van der Waals heterostructures. In this review, we discuss the surface science of *h*BN including its growth, the *h*BN/metal interface and its application as template for adsorbates. We mainly focus on experimental studies on *h*BN/metal single crystals under ultra-high vacuum conditions. The interfaces are classified regarding their geometric structure - ranging from planar to strongly corrugated overlayers - and their electronic properties - covering weakly and strongly interacting systems. The main part of this review deals with *h*BN/metal substrates acting as supports for adsorbates such as individual atoms, metal clusters, organic molecules, metal-organic complexes and networks. We summarize recent surface science studies that reveal the unique role of the *h*BN/metal interfaces in tailoring characteristic properties of such adsorbates. Central aspects include templating and self-assembly, catalytic activity and on-surface reactions, electronic and magnetic structure. As many of the resulting systems feature superstructures with periodicities in the nanometer range, a length scale also reflecting the size of adsorbates, scanning probe microscopy is one of the most common techniques employed. In short, the goal of this review is to give an overview on the experimental and complementary theoretical studies on *h*BN templates available to date and to highlight future perspectives.

Contents

E-mail address: wau@tum.de.

https://doi.org/10.1016/j.surfrep.2018.10.001

List of acronyms

ALE	Atomic layer epitaxy
APCVD	Atmospheric pressure chemical vapor deposition
ARPES	Angular resolved photoemission spectroscopy
BE	Binding energy (in XPS)
BLAG	Buffer-layer assisted growth
BNNS	Boron nitride nanosheet
CVD	Chemical vapor deposition
DFT	Density functional theory
DRS	Differential reflectance spectroscopy
E_F	Fermi level
EFM	Electrostatic force microscopy
ER	Eley-Rideal
FER	Field emission resonance
FLAPW	Full potential augmented plane wave method
GB	Grain boundary
GGA	Generalized gradient approximation
GIXD	Grazing incidence X-ray diffraction
*h*BN	hexagonal boron nitride
HER	Hydrogen evolution reaction
HOMO	Highest occupied molecular orbital
HOPG	Highly oriented pyrolytic graphite
HREELS	High resolution electron energy loss spectroscopy
KPFM	Kelvin probe force microscopy
L	Langmuir (1 L = 10^{-6} Torr s)
LEED	Low energy electron diffraction
LEEM	Low energy electron microscope/microscopy
LEIS	Low energy ion scattering
LH	Langmuir-Hinshelwood
LPCVD	Low pressure chemical vapor deposition
LUMO	Lowest unoccupied molecular orbital
MBE	Molecular beam epitaxy
MD	Molecular dynamics
ML	Monolayer
nc-AFM	non-contact atomic force microscope/microscopy
NEB	Nudged elastic band method
NEXAFS	Near edge X-ray absorption fine structure
NIXSW	Normal incidence X-ray standing wave
OFET	Organic field effect transistor
ORR	Oxygen reduction reaction
PAX	Photoemission of adsorbed xenon
PED	Photoelectron diffraction (see PhD, XPD)
PEEM	Photoemission electron microscope/microscopy
PES	Photoelectron spectroscopy
PBE	Perdew Burke Ernzerhof
PDOS	Projected density of states
PhD	(Energy scanned) X-ray photoelectron diffraction (see XPD)
PSID	Photon-stimulated ion desorption
RES	Rotational excitation spectroscopy
RHEED	Reflection high-energy electron diffraction
rt	Room temperature
SEM	Scanning electron microscope/microscopy
SMM	Single molecule magnet
SPMDS	Spin-polarized metastable de-excitation spectroscopy
STEM	Scanning transmission electron microscope/microscopy
STS	Scanning tunneling spectroscopy
STM	Scanning tunneling microscope/microscopy
SW	Stone-Wales
SXRD	Surface X-ray diffraction
Θ	Coverage (ML)
TEM	Transmission electron microscope/microscopy
TER	Termolecular Eley-Rideal
TDS	Thermal desorption spectroscopy
TH	Tersoff-Hamann
TMD	Transition metal dichalcogenide
TPD	Temperature-programmed desorption
TPG	Temperature-programmed growth
UHV	Ultra-high vacuum
UPS	Ultraviolet photoelectron spectroscopy
vdW	Van der Waals
WC	Wu and Cohen
XMCD	X-ray magnetic circular dichroism
XPD	(Angle scanned) X-ray photoelectron diffraction (see PED, PhD)
XPS	X-ray photoelectron spectroscopy
XRD	X-ray powder diffraction
XSW	X-ray standing wave

1. Introduction

Structure. Hexagonal boron nitride (*h*BN) monolayers are fascinating, atomically thin materials consisting of boron (B) and nitrogen (N) atoms with a 1:1 stoichiometry arranged in an sp^2-bonded honeycomb lattice. These sheets are isostructural and isoelectronic to graphene [1], with B and N framing carbon (C) in the periodic table, featuring eight valence electrons per BN that engage in the strong in-plane σ and weaker π bonds. In analogy to the carbon-based relatives, two-dimensional (2D) *h*BN sheets constitute bulk-like *h*BN, with a layered structure reminiscent of graphite, and BN nanotubes and fullerene-like structures exist [2,3]. Furthermore, one-dimensional (1D) *h*BN nanoribbons and porous 2D networks, i.e., BNyne, BNdiyne, and BNtriyne (analogues of graphyne, graphdiyne, and graphtriyne) are predicted based on first-principles calculations [4–7].

Properties. The binary elemental composition of BN introduces striking differences to the C allotropes. A considerable charge transfer from B to N - triggered by the difference in electronegativity between the two elements - induces an ionic character and renders *h*BN an insulator with a large band gap of about 6 eV [8–10]. In addition, *h*BN features a low dielectric constant, large breakdown voltage, low defect density, an absence of dangling bonds, high chemical and thermal stability, and excellent thermal conductivity. A selection of *h*BN properties is compiled in Table 1, covering *h*BN monolayers, thin *h*BN films consisting of few layers (named nanosheets or BNNS), and bulk-like *h*BN for comparison (including *h*BN single crystals [8]). Many of the beneficial *h*BN attributes prevail for monolayers or nanosheets. For example, high-quality *h*BN monolayers and nanosheets on copper provide a strong corrosion resistance in NaCl or NaOH solution [11–13] and a single *h*BN sheet heated in air can sustain temperatures up to 1123 K [14] -

Table 1
Properties of *h*BN. "exp." signals experimental values, "calc." calculated values. More detailed, tabulated information, e.g., about the calculated band gaps in *h*BN monolayers (and other BN polymorphs) [15,37], mechanical [55] or physicochemical *h*BN characteristics [15], is available in recent reports.

*h*BN monolayer			
Lattice constant a_{hBN}	2.488 ± 0.016 Å	exp.	[56]
Young's modulus	0.865 ± 0.073 TPa	exp.	[57]
	0.75 TPa [58], 0.8811 TPa [55]	calc.	←
Poisson's ratio	0.297 [58], 0.2176 [59]	calc.	←
Fracture strength	70.5 ± 5.5 GPa	exp.	[57]
	133.3 GPa	calc.	[55]
Bending rigidity	0.54 eV @ 0 K	calc.	[60]
Penetration barrier	Proton: 0.11 eV, H atom: 6.38 eV	calc.	[61]
Band gap	5.9 eV [62], 6.06 eV [63],	exp.	←
Band gap	6.0 eV (GW) [10], 4.5 eV (LDA), 4.6–4.77 eV (GGA) [64,65]	calc.	←
Raman signature	1369 ± 1 cm^{-1}	exp.	[66]
Zero-bias conductivity	1 $k\Omega^{-1}\mu m^{-2}$	exp.	[67]
Charge carrier mobility	≤0.01 $cm^2\ V^{-1}\ s^{-1}$ at fields up to 100 kV/cm	exp.	[56]
Thermal conductivity	≥600 $Wm^{-1}K^{-1}$ @ rt	calc.	[68]
Thermal conductivity (nanoribbons)	1700 - 2000 $Wm^{-1}K^{-1}$ @ rt	calc.	[69]
*h*BN nanosheets/flakes			
B—N bond length	1.44 Å	exp.	[15]
Dielectric constant	2 - 4 [70], 2.7–8 [46], 3–4 [71]	exp.	←
Electrical breakdown field	0.8 V/nm [71], 1 V/nm [67], 1.2–2 V/nm [72]	exp.	←
	0.15–0.25 V/nm (polycrystalline *h*BN)	exp.	[70]
Zero-bias conductivity (4 layers)	0.1 $G\Omega^{-1}\mu m^{-2}$	exp.	[67]
Thermal conductivity (5 layers)	≈250 $Wm^{-1}K^{-1}$ @ rt	exp.	[73]
Thermal conductivity (9 layers)	243 $Wm^{-1}K^{-1}$	exp.	[74]
Thermal conductivity (10, 20 nm)	100 ± 10 $Wm^{-1}K^{-1}$	exp.	[75]
Elastic moduli	C_{11} = 65 GPa, C_{13} = 7 GPa, C_{33} = 92 GPa, C_{44} = 53 GPa	exp.	[76]
Bending modulus	18–28 GPa	exp.	[77]
Poisson's ratio	0.35	exp.	[76]
bulk-like *h*BN			
Lattice constant a_{hBN}	2.50424 ± 0.0001 Å @ 273 K	exp.	[78]
a_{hBN}(T) 10–128 K	2.50589 + 1.641 × $10^{-8}T^2$-1.773 × $10^{-10}T^3$ Å, T in K	exp.	[79]
a_{hBN}(T) 128–297.5 K	2.50666–6.810 × 10^{-6}T Å, T in K	exp.	[79]
a_{hBN}(T) 273–1073 K	2.50424–7.42 × 10^{-6}T+4.79 × $10^{-9}T^2$ Å, T = 0–800 °C	exp.	[78]
Thermal expansion coefficient	−2.9 × 10^{-6} K^{-1} @ rt [78], −2.72 × 10^{-6} K^{-1} @ rt [79]	exp.	←
Interlayer spacing	3.3258 ± 0.001 Å @ 273 K	exp.	[78]
Elastic moduli	C_{11} = 811 GPa, C_{12} = 169 GPa, C_{13} = 0 GPa, C_{33} = 27 GPa, C_{44} = 7.7 GPa	exp.	[80]
Thermal conductivity	≈400 $Wm^{-1}K^{-1}$ @ rt	exp.	[81]
Dielectric constant	5.06–5.09 (E‖c), 6.85–7.04(E ⊥c)	exp.	[82]
Band gap (direct)	5.971 eV	exp.	[8]
Band gap (indirect)	5.955 eV	exp.	[9]
Band gap (GW)	5.4 eV	calc.	[10]
Band gap (single particle)	6.08 ± 0.015 eV	exp.	[9]
Effective charges (Mulliken, electrons)	B: 2.70, N: 5.30	calc.	[83]
Raman signature	1366 cm^{-1}	exp.	[66]

thus outperforming graphene regarding thermal stability [15]. Based on such unique characteristics, *h*BN is recognized as relevant 2D material, complementing the library of 2D crystals and constituting a highly important building block for van der Waals (vdW) heterostructures [16–23].

Applications. A wealth of *h*BN applications in diverse fields were reported, as highlighted by the following examples. Ultra-thin *h*BN is successfully applied as insulating barrier and gate dielectric layer in field effect transistors [24–27], sensor material [28,29], protective cover in devices [30,31], pore material for DNA detection [32], and buffer layer in film growth [33]. Additionally, *h*BN crystals, films, powders, and nanomaterials are used in deep-UV photonic devices including lasers [8,34,35] and neutron detectors [36], furthermore offering prospects for high-power electronic devices [37], heterogeneous catalysis [38–40], low friction materials [41,42], ceramics [43], electrodes in Li-ion batteries [44], and anti-cancer drug delivery [45]. The good environmental compatibility of non-toxic *h*BN renders it specifically interesting for green technologies [43]. Several detailed reviews elaborate on (2D) *h*BN applications (including fabrication and properties) [3,15,46–54].

Monolayer growth. Already in the 1990s, it was recognized that *h*BN monolayers can be readily prepared on transition metal supports via chemical vapor deposition (CVD) in ultra-high vacuum (UHV) environments [84–86]. As the catalytic activity of such metal surfaces considerably exceeds the one of *h*BN, the CVD growth of *h*BN is "self-terminated" as soon as the metal is covered by a single *h*BN sheet. To date - even with exfoliation protocols emerging - CVD is the method of choice for the scalable synthesis of *h*BN monolayers. This ease of fabrication combined with the unique *h*BN properties outlined above not only put the atomically sharp *h*BN/metal interfaces into the research focus, but also triggered their use as templates and supports for adsorbates. Here, the fascination of surface-supported *h*BN monolayers is not just given by the characteristics of the isolated *h*BN sheet, but rather by the tunability of their properties based on *h*BN - substrate interactions. The resulting *h*BN/metal interfaces might be topographically planar or corrugated, providing 1D or

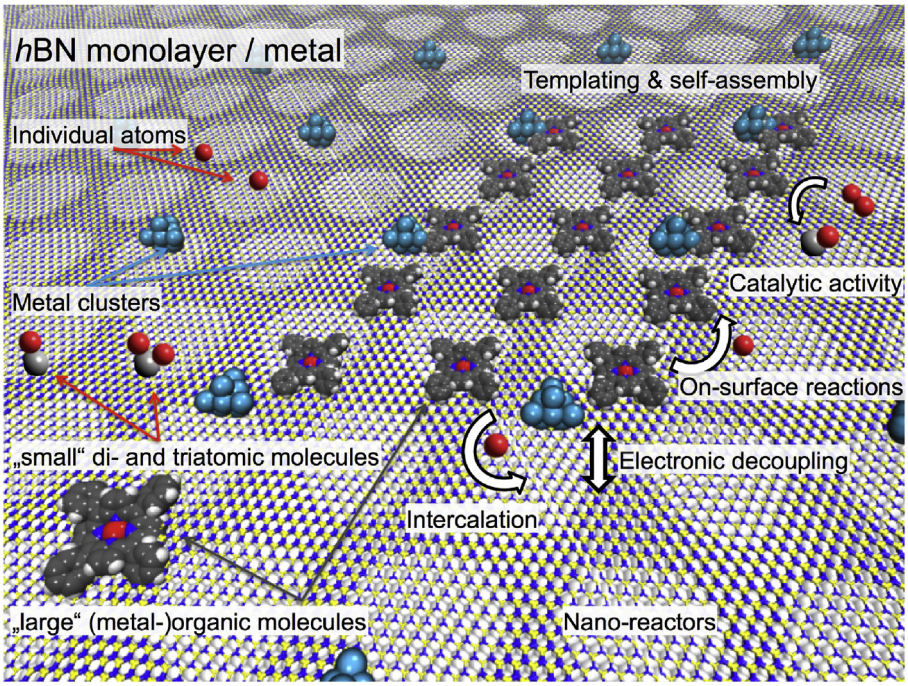

Fig. 1. Illustration of adsorbates (atoms, clusters, molecules) interacting with a superstructured, surface-supported *h*BN monolayer (colored in blue and yellow). Characteristic functionalities of the *h*BN/metal interfaces (such as templating, electronic decoupling, catalytic activity, intercalation) are highlighted on the right. (For interpretation of the references to color in this figure legend, the reader is referred to the Web version of this article.)

2D superstructures, such as the prominent nanomesh morphologies [87–89].

Template. Depending on the electronic structure of the interface, some of the *h*BN/metal systems indeed provide a smooth, inert platform for the growth of metal films, the self-assembly of molecular arrays, or the synthesis of graphene, while others enable site-selective adsorption and surface-chemistry. Accordingly, surface supported *h*BN monolayers represent multifaceted templates, covering manifold aspects as spacer layers in hybrid architectures, superstructures with trapping functionality, or catalytically active supports. Strikingly, a single sheet of *h*BN thus can play various roles and combine functionalities rarely provided by another single material - accordingly complementing other nanoscale templates, as briefly discussed in the following. Graphene [90–92] shares many properties with *h*BN and thus might be considered the most similar template material. Subtle yet important differences between these sp^2/metal supports will be emphasized throughout this review. SiC nanomeshes [93,94] and the Si(111) 7 × 7 reconstruction can support arrays of nano-objects, including magic metal clusters, i.e., clusters of a specific size [95–97]. Reconstructions and alloys [98–104], vicinal surfaces [105–107], strain-relief and moiré patterns [108–111] on metal surfaces can induce site-selective adsorption of atoms and molecules [112], but lack any considerable electronic decoupling ability. Supramolecular assemblies on metal supports might reduce the interaction of adsorbates with the substrate while providing site-specificity [113–118] or feature cavities for the trapping of atoms and molecules [119–131]. The thermal stability of such architectures is however limited, e.g., hampering their applicability in temperature-controlled on-surface chemistry experiments. Ultra-thin oxide [132–145], metal nitride [146–149], and halide films [150–161] on the other hand can serve as templates and spacer layers for adsorbates - approaching the ultra-thin limit of insulators [162–164] - with doping applicable to tune the films' properties [165]. However, they represent challenging platforms regarding self-assembly and homogeneity, e.g., due to the intricate synthesis of large-area films of uniform thickness, the polarity [166], and layer-dependent adsorption/diffusion [167,168]. Thicker, truly insulating films and bulk insulators (such as ionic crystals of NaCl, KCl, calcite, or bulk *h*BN) obviously can provide a complete electronic insulation of individual adsorbates and molecular nanostructures [169–181], but lack easy tunability and accessibility by some of the most prominent surface science techniques, such as scanning tunneling microscopy and spectroscopy.

Naturally, the atomically thin character of *h*BN monolayers induces some limitations, e.g., regarding electronic "insulation", but contributes to the fascination of this material as evidenced throughout this review.

An exemplary *h*BN/metal structure and its use as template is schematically illustrated in Fig. 1.

Outline of this review. Fig. 1 can also be considered as an outline of this review. In the next chapter (chapter 2) we will review selected *h*BN/metal interfaces, focusing on properties relevant in view of their templating functionality (i.e., geometric and electronic structure). In chapter 3, we then describe adsorbate/*h*BN/systems (see left part of Fig. 1), starting with single atoms and clusters (section 3.1), proceeding via "small" molecules (3.2) to larger (metal-)organic complexes (3.3) and heterostructures (3.4). The right part of Fig. 1 lists functionalities and processes that will be addressed, including templated self-assembly, electronic decoupling, catalytic activity, on-surface reactions, and intercalation.

Focus of this review. This review is primarily concerned with experimental surface science studies addressing adsorbates on *h*BN monolayers grown on metal single crystals in UHV conditions. Even though a battery of experimental techniques is employed in *h*BN research, studies employing local probes as scanning tunneling microscopy preponderate in this review, providing the high spa-

tial resolution needed for the characterization of superstructured *h*BN templates and (individual) adsorbates. Studies on commercially applicable supports as metal foils and complementary theoretical modeling have only sporadically been taken into account to establish context. Accordingly, the following topics are *not covered* by this review: details on *h*BN growth mechanisms, low-pressure and (near-)ambient pressure synthesis of *h*BN monolayers or BNNS (which have been competently summarized in recent reviews (see below)), preparation and characterization of thick *h*BN films, experimental studies at solid/liquid interfaces, systems that were exclusively addressed by theoretical studies, e.g., free-standing *h*BN sheets and their modifications, *h*BN transfer, and device fabrication.

Notation in this review. In the sequel of this review the term "*h*BN" in notations as "*h*BN/metal" refers to a single *h*BN monolayer, unless otherwise specified. Expressions as "*h*BN", "*h*BN monolayer", or "*h*BN sheet" are used interchangeably. We refrain from using the denomination "boronitrene" that was introduced, e.g., to highlight the structural similarities to graphene [182], as it is not fully established in the field and avoid the misleading, yet popular "white graphene" nomenclature. In the context of this review, the expression "boron nitride nanosheet (BNNS)", which is indiscriminatingly used in literature for ultra-thin *h*BN films of mono- and few layer thickness, is no synonym for a *h*BN monolayer, but only denotes multilayers.

2. Hexagonal boron nitride/metal interfaces

The versatility of *h*BN/metal interfaces arises from the interaction of the *h*BN monolayer with its support (see Fig. 2). Mainly four parameters can be identified as "control knobs" for the resulting interface structure: (i) the substrate symmetry, (ii) the substrate lattice constant a_{metal}, (iii) the substrate electronic structure, and (iv) the surface composition. They dictate the lattice mismatch and the (local) registry in the *h*BN/metal pair, as well as the interfacial bonding. The broad range of lattice mismatches ranging from about −0.4% (on Ni(111), where "-" signals $a_{metal} < a_{hBN}$, i.e., compressive strain in a commensurate 1 × 1 structure) to 14% (on Au(111)) and the varying d-band occupancy in transition metals throughout the periodic table already point to a considerable tunability of *h*BN/metal interfaces. The combination of a *h*BN sheet with the atomic lattice of a single crystalline support can result in a moiré-like superstructure that depends on the lattice mismatch (i.e., (i) and (ii)) and the rotational alignment of the two constituting structures [183–186]. Indeed, many of the studies summarized below show that a simplistic approach assuming rigid *h*BN and metal lattices can approximately describe experimentally observed superstructures at *h*BN/metal interfaces, even if the negative thermal expansion coefficient of *h*BN (see Table 1) and strain add complexity. Furthermore, this somewhat naive picture (see below) also illustrates the emergence of homogeneous, 1D- and 2D-nanostructured *h*BN systems (Fig. 2).

For a deeper understanding, the local registry of BN units in *h*BN to the underlying metal atoms needs to be considered in more detail. As the vast majority of studies reviewed below relies on (111)-terminated surfaces of face centered cubic (fcc) crystals for *h*BN synthesis, we focus in the following on such symmetry-matched situations. Assuming a commensurate 1 × 1 overlayer structure, i.e. zero lattice mismatch and no rotation, six distinct adsorption configurations with B and N in high-symmetry substrate sites (on-top, hcp hollow, fcc hollow) can be devised. The corresponding registries are typically denoted as $B_{hcp}N_{fcc}$, $B_{fcc}N_{hcp}$, $B_{top}N_{hcp}$, $B_{top}N_{fcc}$, $B_{hcp}N_{top}$, and $B_{fcc}N_{top}$ (see Fig. 7 (d)). Only the latter two usually represent bonding interactions. The electron deficient B atoms - attracted by the surface

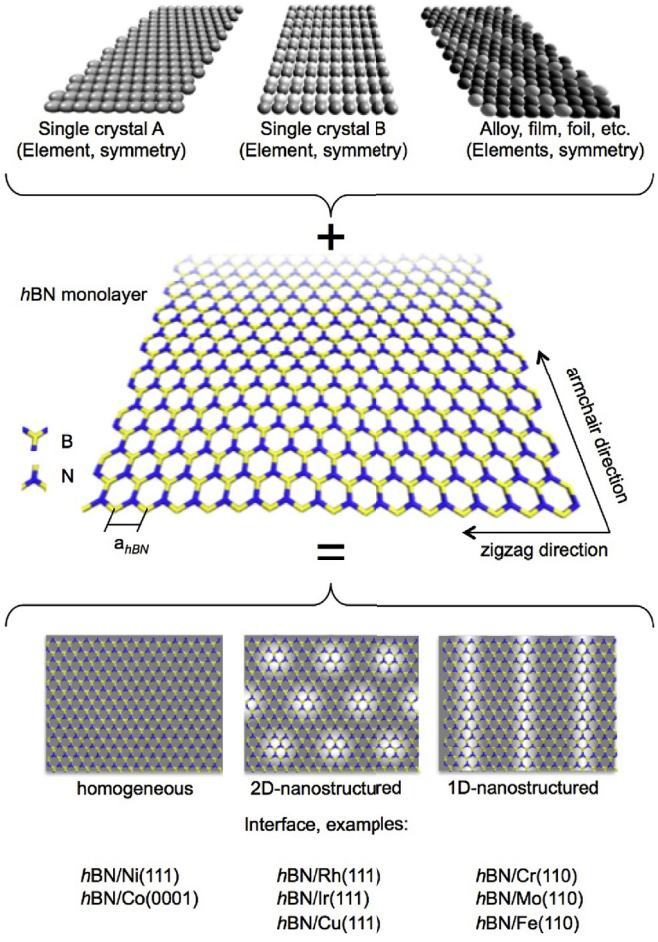

Fig. 2. Scheme illustrating the formation of homogeneous or electronically, topographically and chemically nanostructured *h*BN/metal interfaces with distinct symmetries and periodicities by choice of a suitable *h*BN/substrate pair. The selected examples for homogeneous, 2D-nanostructured, and 1D-nanostructured systems will be discussed in section 2.2.

- can bind to three metal atom when occupying a hollow site, resulting in attractive forces prevailing over the repulsion of N atoms from the surface [187–189]. Only recently, a DFT study reported bond formation instead of repulsion for N atoms atop of Ir substrate atoms [190]. Additional configurations can be constructed by laterally shifting the B and N atoms away from the above sites [189]. Allowing for mixed adsorption sites (e.g., $B_{top\&bridge}N_{bridge\&top}$), overlayer configurations featuring a 30° rotation can be achieved (see Fig. 7 (e)), representing larger overlayer periodicities (e.g., 2 × 2) [188]. Such rotational domains might be introduced to reduce the lattice mismatch, e.g., in systems like Ag, Au or Al(111) [188,191]. It should be noted that even in non-commensurate *h*BN/metal pairs featuring for example the aforementioned moiré-like superstructures, the *local* adsorption configuration can be approximated by the above registries.

The binding of *h*BN to transition metals involves interaction between the B and N p-states (which constitute the antibonding π^* band and the bonding π band, respectively) and the metal d-band. It thus sensitively depends on the d-band occupation (see (iii, iv) above) and the local registry at the interface [187,192], i.e., the position of the B and N atoms relative to the outermost metal atoms (i, ii). An absence of considerable hybridization results in weakly interacting systems (i.e., physisorbed *h*BN),

whereas stronger interactions result in chemisorbed *h*BN. Even if assignments of the interaction strength are often not clear-cut, paragraph 2.4 will attempt such a classification of *h*BN/metal interfaces. In summary, the resulting topographic and electronic interface structure is dictated by a subtle balance between local registry, lattice mismatch and electronic interaction - all influenced by parameters (i-iv). *h*BN/metal pairs with strong interactions and small lattice mismatch, where the adsorption energy can compensate energy costs induced by strain in the *h*BN will typically form smooth commensurate overlayers with a single *h*BN domain. Weak interactions will rather result in multiple (rotational) domains. Intermediate systems frequently adopt a considerable topographic corrugation, featuring coexisting strongly and weakly bound *h*BN areas. Additionally, depending on preparation conditions, both single and multiple domains might be stabilized and both physisorbed and chemisorbed *h*BN islands might coexist on the very same surface. Accordingly, as will be evident from paragraph 2.2 below, *h*BN/metal single crystal interfaces provide a wealth of different structures and properties.

2.1. Growth of hBN on metals

Before addressing properties of selected *h*BN/metal interfaces in paragraph 2.2, we briefly address *h*BN growth. The synthesis of *h*BN sheets and the fabrication of *h*BN/metal interfaces are comprehensively summarized in recent reviews (e.g., Refs. [2,3,22,43,47–50,53,54,193–195]). Accordingly, the respective preparation protocols - including mechanical or chemical exfoliation [196–198], chemical vapor deposition (at ambient pressure - APCVD, or low-pressure - LPCVD), segregation, (plasma-assisted) molecular beam epitaxy [199–208], sputtering, and pulsed laser deposition [209] - are not detailed here. We focus on the two main UHV-based approaches employed to achieve the well-defined *h*BN/metal interfaces: Direct growth of the *h*BN sheet on the chosen metal support via chemical or physical vapor deposition, addressed in the next subsection, and intercalation of a selected metal following the synthesis of a *h*BN (sub-)monolayer on an interim support, described in the subsequent subsection.

2.1.1. Chemical and physical vapor deposition

Table 2 summarizes typical chemical vapor deposition (CVD) parameters employed for successful *h*BN growth on selected metal single crystals under UHV conditions. In a standard CVD process, the hot metal substrate is exposed to one or two precursors containing B and N that adsorb and react to form *h*BN. In the widespread case of single precursor usage, the precursor is usually chosen in a way to provide a stoichiometric 1:1 ratio for B and N.

Borazine $(HBNH)_3$ was established as the most often used precursor, despite its moisture sensitivity and slow decomposition at rt. Alternatively, B-trichloroborazine $(ClBNH)_3$, a solid at rt, was applied on selected supports [210,211] and ammonia borane (NH_3BH_3) - also called borazane - is a popular precursor [212,213]. Upon modest heating (typically 400 K), it transforms to borazine, molecular hydrogen and polyminoborane. Thus, also in the case of ammonia borane, borazine is often the actual precursor interacting with the metal surface. A combination of diborane (B_2H_6) with ammonia gas (NH_3)

Table 2
CVD growth parameters of *h*BN/metal interfaces in UHV (if available). It should be noted that in many experimental setups, the precursor is dosed via a nozzle. Accordingly, the precursor partial pressure at the sample position can strongly exceed the value recorded by the pressure gauge, which is usually listed in the Table. For systems where different experimental growth parameters were reported, typical values representing optimized growth conditions are listed. (* 3-step boration-oxidation-nitration process, ** sputter-gun assisted).

Metal	Precursor	Growth T	Pressure	Time/Dose	Refs.
Cr(110)	Borazine	1000 K	4×10^{-7} mbar	5 min	[191]
Mo(110)	Borazine	950 K	3×10^{-7} mbar	3 min	[217]
Re(0001)	Ammonia borane	exposure at 920, annealing at 1000 K	5×10^{-8} mbar	10–20 min	[84,218,219]
Fe(110)	Borazine	1020–1070 K	1×10^{-7} mbar	5–10 min	[220]
Ru(0001)	Borazine	1050 K	1.8×10^{-8} mbar	25 min	[88,89,221–228]
Co(0001)	Ammonia borane	900–970 K	7×10^{-8} mbar	–	[228]
	Ammonia borane	1273 K	LPCVD	–	[62,193]
	BCl_3 & NH_3	exposure at 550 K, annealing > 700 K	ALD (multilayers)	–	[229,230]
Rh(111)	Borazine	1050 K	1×10^{-7} mbar	50 L	[87,88,182,192,231–243]
	Trimethylborate	800–900 K*	4.4×10^{-7} mbar	150 L	[215]
(110)	Borazine	1073 K	3.4×10^{-8} mbar	35 min	[244]
Ir(111)	Borazine	1220 K	1×10^{-6} mbar	100 s	[88,245–253]
Ni(111)	Borazine	1050 K	–	100 L	[189,231,254–275]
	Ammonia borane	973, 1100 K	2×10^{-7} mbar	up to 480 L	[189,276]
	Ammonia borane	773–923 K,	2.7×10^{-8} mbar	Epitaxial & non-epitaxial	[277]
	Trichloroborazine	1000 K	–	200 L	[210]
(110)	Borazine	1000 K	–	70 L	[278]
(100)	NH_3 & B_2H_6	950 K	$1.33 \times 10^{-7}/1.33 \times 10^{-8}$ mbar	30 min	[214]
Pd(111)	Borazine	1000 K	–	50–70 L	[257,279]
(110)	Borazine	1000 K	3×10^{-6} mbar	40s	[280]
Pt(111)	Borazine	1073 K	2×10^{-8} mbar	100 L	[85,86,88,192,231,256,257,281–283]
	Trichloroborazine	1000 K	5×10^{-7} mbar	2 min	[211]
Cu(111)	Borazine	1073 K	1×10^{-6} mbar	2000 L	[265,284–289]
	Ammonia borane	exposure at 600 K, annealing at 1000 K	5×10^{-6} mbar	5 min	[290]
(110)	Borazine	1010 K	1×10^{-6} mbar	3900 L for 0.6 ML, after H_2 treatment	[291]
Ag(111)	(Trichloro)borazine	950 K	–	13500 L	[292]
	Borazine**	900 K	–	2700 L	[293]
(100)	Borazine	850 K	4×10^{-7} mbar	3000 L	[294]
Au(111)	Solid B target & N_2	820–1000 K	–	–	[295]

Table 3
Intercalation of metal films to form *h*BN/metal$_1$/metal$_2$).

Intercalated metal (metal$_1$)	Supporting metal (metal$_2$)	Intercalation temperature	Thickness	Refs.
Ag	Cu(111)	573 K	1–3 ML	[293]
Au	Ru(0001)	1050 K	14 ML	[321]
	Ir(111)	573 K	5–10 ML	[322]
	Ni(111)	773 K	–	[318]
		673 K	6 ML	[276]

was successfully applied by Desrosier et al. as early as 1996 [214]. Müller et al. introduced a three-step boration-oxidation-nitration protocol for *h*BN synthesis on Rh(111), employing trimethylborate [215]. Furthermore, Sachdev et al. demonstrated that oxidation converts *h*BN/Rh(111) into an unordered boron oxide layer that can be reconverted to a pure *h*BN film by an ammonia treatment [182]. A follow-up study by the same authors reports on *h*BN formation from a boron ester precursor, proceeding via oxidation and nitrification of a boride-type layer [216]. Remnant contaminants from the precursors after *h*BN film production were not reported, e.g., the upper limit for Cl coverage (after B-trichloroborazine usage) was estimated by XPS to be below 3% of a ML [210] and no O signal was detected after trimethylborate usage [215].

To enhance *h*BN synthesis on catalytically weakly active supports and to promote growth at lower substrate temperature, electron-beam or ion-gun assisted CVD of borazine was employed on Ag(111) [293] and Cu(111) [285]. While in a standard UHV-CVD protocol, the precursor is dosed on the hot metal substrate kept at the reaction temperature, also rt precursor adsorption followed by heating to the decomposition and *h*BN synthesis temperature is reported. Several cycles of such temperature-programmed growth (TPG) can be applied, e.g., to increase coverage [248,250]. It should be noted that UHV-CVD processing can give access to high quality *h*BN monolayers on wafer-scale single crystalline metal films as demonstrated for *h*BN/Rh(111) [236,239].

In general, the *h*BN growth rate usually drops considerably after completion of the first monolayer, as a successful *h*BN synthesis on metal surfaces relies on a non-vanishing sticking coefficient of the precursor combined with its cracking promoted by the metal. This renders the growth of a single *h*BN sheet on metals with a certain reactivity straightforward, but hampers the synthesis of *h*BN on non-reactive supports as well as the growth of *h*BN multilayers. Thus, beyond these standard protocols, additional recipes were introduced in literature, partially permitting the fabrication of *h*BN multilayers. Ammonia was used in sequential atomic layer deposition cycles with boron trichloride (BCl_3) for the controlled growth of *h*BN multilayers on Co(0001) [230]. Combining magnetron sputtering of B with an N_2/Ar environment, the Sutter group grew *h*BN multilayer structures on Ru(0001) [223] and Au(111) [295]. Recently, Siegel et al. applied triethylborane and ammonia in a heterogeneous pyrolysis procedure for the controlled growth of several *h*BN layers on Cu(111) [296]. In a different approach, segregation is exploited for *h*BN mono- and multilayer synthesis, retrieving B and/or N from the bulk of support materials, for example after including BN in layered substrates [297,298]. Indeed, both B and N dissolve in Fe while only B features a relevant solubility in Cu [299–301], which can also have detrimental effects on *h*BN monolayer formation. Accordingly, the solubility of B and N in metals is of interest [302]. Caneva et al. introduced a "pre-filling" process of the Fe support with N from NH_3 to steer and limit the B and N uptake in the subsequent borazine CVD step, controlling the *h*BN growth kinetics [300]. MBE growth of *h*BN on different metal foils was reported, with selected examples discussed in the respective paragraphs in section 2.2. Recently, Tian et al. discussed the role of carbon interstitials in Ni and Co films for the control of *h*BN growth. For example, carburized Ni supported the growth of single-crystalline *h*BN flakes with an edge length of ≈600 μm [303].

Complementing these experimental studies, theoretical endeavors contributed to the understanding of *h*BN growth on metals via CVD, e.g., focusing on the role of edge terminations and edge-support interactions or the formation of the BN six-atom rings [296,304].

2.1.2. Intercalation

In this review, we use the term "intercalation" to describe the placement of an adsorbate (atom, ion, or molecule) between the *h*BN sheet and its metal support. The intercalation follows the formation of the initial *h*BN/metal interface. This definition, frequently employed in the context of 2D materials on supports (e.g., Refs. [305–314]), thus differs from the one established for (bulk-like) intercalation compounds, where the ions or molecules are placed between alike layers (e.g., Refs. [315–317]).

The intercalation of (sub-)ML amounts of metals in pre-assembled *h*BN/metal supports is frequently applied to engineer interface properties. Such procedures and systems will be discussed in detail in section 3.1. In rare cases, intercalation is used to prepare buried multilayer metal films. In the resulting *h*BN/metal$_1$/metal$_2$ interfaces, the film of the intercalated metal$_1$ can be prepared thick enough to mimic bulk properties, and the only role of metal $_2$ is to support the layered structure. Naturally, this approach is mainly chosen to achieve *h*BN/metal$_1$ interfaces that are not easily achieved by direct CVD synthesis due to the low reactivity of metal$_1$. As shown in Table 3, Ag and Au are the elements of choice in this procedure.

It should be noted that - aside from intercalation - layered structures including a terminal metal film (metal$_1$) on a support are commonly used for *h*BN growth. Besides cases where this support represents a metal single crystal (metal$_2$) [318], sapphire (Al_2O_3(0001)) [62,240,319] or Si(111) with a yttria-stabilized zirconia (YSZ) buffer layer [236] are used. The resulting single-crystalline metal$_1$ films (e.g., Ir, Rh, Pt, Ru) offer advantages regarding the cleaning procedure and are cheaper than bulk single crystals [320]. As *h*BN monolayers of equal quality are reported for such single-crystalline film and bulk supports, we do not discriminate the two in the following sections and in Table 2.

2.2. Structure of hexagonal boron nitride/metal interfaces

In this section, we review selected *h*BN/metal interfaces that were introduced in Table 2. Hereby, we focus on aspects which are relevant for the use of *h*BN monolayers as templates for adsorbates (see chapter 3) and do not provide a detailed and complete characterization of these systems, which can be found in the cited publications. We aim for a concise summary of the current understanding of the *h*BN/metal interfaces and do not elaborate on its evolution with time. In the last paragraph of this section, we will provide a com-

parative assessment of selected *h*BN/metal interfaces, focusing on morphology, geometric corrugation, electronic integrity and work function.

2.2.1. Chromium(110)

The *h*BN/Cr(110) system was comprehensively characterized by Müller et al. [191]. This interface is peculiar as it involves the (110) surface of a bcc crystal, in contrast to the frequently employed fcc(111) terminations (see below). Furthermore, upon annealing to the growth temperature of *h*BN (1000 K), the Cr(110) surface develops a 1 × 5 reconstruction, as evidenced by LEED measurements. This superstructure is assigned to missing rows, separating the pseudohexagonal areas. Accordingly, borazine exposure results in a BN structure that is chemically not uniform. XPS provides evidence for *h*BN-like B and N species (B 1s: 190.6 eV, N 1s: 398.2 eV) as well as B—Cr and N—Cr bonding featuring lower binding energies (B 1s*: 187.5 eV, N 1s*: 396.5 eV). The former are assigned to the unpinned regions of an undulated *h*BN layer, while the latter are attributed to a pinning of BN to the 1 × 5 missing row superstructure (see Fig. 3(a)). The undulated structure is reflected in stripe-like features along the [1–10] direction in the B 1s* XPD pattern. Annealing to 1075 K results in desorption of the *h*BN with only the B* and N* species interacting with the missing row reconstruction and the Cr remaining. Accordingly, the stripe-like features in the B 1s* XPD disappear [191].

2.2.2. Molybdenum(110)

Allan et al. explored the growth of *h*BN on Mo(110) [217]. Depending on the substrate temperature during borazine exposure, they report the growth of two different structures, which can coexist at intermediate temperature. Based on XPD, ARPES and LEED experiments, the low-temperature (950 K) assembly was assigned to a single *h*BN layer exhibiting a 4 × 1 superstructure. STM images visualized the corresponding stripe-like *h*BN pattern following the [1–10] directions of the Mo(110) surface lattice (Fig. 3(c)) and revealed a high defect density which was tentatively attributed to a competition with the high-temperature phase. This phase, prevalent at 1170 K, contains only B, no N was detected by XPS. Based on STM images and B 1s XPD patterns, the surface structure was attributed to boron "nanowires" aligned perpendicular to the Mo[1–10] directions (Fig. 3(b)) [217,266]. The transition from the stripe-like *h*BN to the B phase can also be induced by thermal annealing, where B 1s spectra reveal a characteristic chemical shift from a high-binding energy (BE) species (≈190.4 eV) to a low-BE species (188.3 eV) (Fig. 3(d)) [217].

2.2.3. Rhenium(0001)

To this author's knowledge, Re(0001) is the first surface ever used to deliberately study the interaction with borazine in view of boron nitride synthesis. In a pioneering study employing LEED, TDS. AES and EELS, He and Goodman discussed the physisorption, chemisorption and dissociation of borazine on Re(0001). While providing LEED images of B and N superstructures, no indication for *h*BN formation upon annealing borazine covered Re(0001) was reported [84]. Two recent studies by Qi et al. characterized *h*BN/Re(0001) by STM, XPS and complementary DFT modeling, reporting a 12 × 12 *h*BN/11 × 11 Re coincidence lattice, with an alignment of the *h*BN and Re(0001) lattices [218,219]. The nanomesh-like structure featuring pore and wire regions has a periodicity of about 3 nm and showed an apparent corrugation of 0.152 nm. In the context of supported 2D materials, the term "pore" describes the confined areas (featuring a round, triangular, or hexagonal shape) of a corrugated

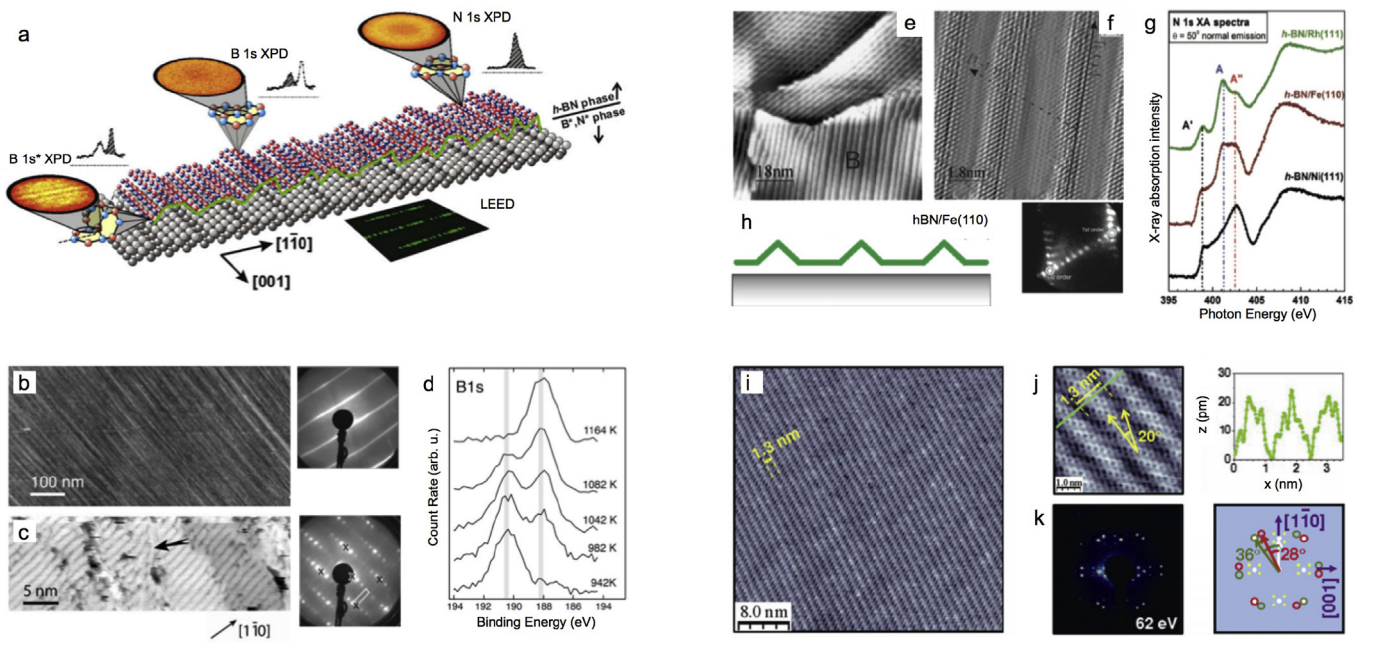

Fig. 3. One-dimensional *h*BN superstructures on M(110) supports: (a) *h*BN/Cr(110), (b–d) *h*BN/Mo(110), (e–h) *h*BN/Fe(110), and (i–k) *h*BN/Rh(110). (a) Schematic drawing of *h*BN on reconstructed Mo(110). The insets show the XPS/XPD signatures and the LEED pattern, respectively. (b) STM image of the boron "nanowire" phase on Mo(110) and corresponding LEED image (right panel). (c) STM image of *h*BN/Mo(110) and LEED image. (d) Series of B 1s XPS spectra from the *h*BN phase at lower preparation temperature (bottom spectrum) to the B phase at higher temperature (top spectrum). (e,f) STM images of *h*BN/Fe(110) with LEED image (bottom right panel). (g) NEXAFS spectrum in comparison to corrugated *h*BN/Rh(111) and planar *h*BN/Ni(111). (h) Schematic *h*BN corrugation profile. (i) Overview STM image of *h*BN/Rh(110). (j) Atomically-resolved STM image (left panel) and height profile (right panel). (k) LEED image (left panel) and corresponding schematics (right panel) highlighting contributions from the two *h*BN domains (red, green). (a) Adapted with permission from Ref. [191] © (2008) Elsevier, (b–d) Adapted with permission from Ref. [217], (e–h) Adapted with permission from Ref. [220] © (2012) American Chemical Society, (i–k) Adapted with permission from Ref. [244]. (For interpretation of the references to color in this figure legend, the reader is referred to the Web version of this article.)

superstructure, which typically lie closer to the metal support than the height average of the 2D sheet. The term "wire" is used for the continuous, connected areas between the pores (see Fig. 11). XPS revealed binding energies of 190.1 eV (B 1s) and 397.57 eV (N1s), respectively and showed two components in the Re 4f signal, where the high BE component was attributed to substrate areas strongly interacting with the *h*BN. Furthermore, based on STS data a reduction of the *h*BN band gap to 3.5 and 3.3 eV for the wire and pore regions, respectively, was proposed [218]. A DFT comparison of *h*BN/Re(0001), *h*BN/Rh(111), and *h*BN/Ir(111) identified *h*BN to interact most strongly with Re(0001), followed by Rh(111) and Ir(111) [218].

2.2.4. Iron(110)

Vinogradov et al. provided a multi-technique (XPS, XAS, LEEM, μ-LEED, STM) characterization of *h*BN on Fe(110) films grown on W(110), revealing a 1D, wave-like corrugation of the *h*BN featuring a periodicity of about 2.6 nm (see Fig. 3(e,f,h)). Hereby, two primary domains were identified and attributed to two equivalent crystallographic directions of the Fe(110) support. STM images show the coexistence of both domains and reveal the high structural quality on an atomic level as well as long-range order in the "washboard-like" superstructures, and point to a geometric origin of the apparent corrugation (0.8 Å). N 1s XA spectra reveal resonances characteristic for both *h*BN strongly interacting and nearly non-interacting with its support, and are thus in line with a corrugated nanostructure (Fig. 3(g)). The N 1s XPS data however do not reveal an apparent splitting of the peak in two components (BE ≈ 398.2 eV). This observation was tentatively assigned to the lack of extended flat regions of "free-standing" *h*BN in the 1D superstructures [220].

It should be mentioned that also Fe foils and films were applied for CVD growth of *h*BN, resulting for example in large *h*BN domains with overlapping grain boundaries [323]. Hereby, the *h*BN growth morphology can be controlled by dissolution of nitrogen into the Fe bulk prior to the actual *h*BN synthesis step or by Si supply [299,300] and high-quality, large-area *h*BN multilayers can be achieved [324]. Furthermore, the growth of thick *h*BN films on carbon steel was explored as early as 1979 [325].

2.2.5. Ruthenium(0001)

The first CVD growth of *h*BN on Ru(0001) was reported by Paffett et al. in 1990, with a LEED and AES analysis yielding a 12 × 12 coincidence superstructure and a *h*BN monolayer coverage [85]. On a local scale, the *h*BN/Ru(0001) interface was described by Goriachko et al. in 2007 [226] showing similarities to the previously discovered *h*BN/Rh(111) nanomesh structure (vide infra) [89]. STM data reveal a 3.25 nm periodicity - consistent with a 12 × 12 superstructure - and an apparent corrugation between hole/pore and wire regions of 0.07 ± 0.02 nm (see Fig. 30(m)). However, this early study evidenced rather frequent structural distortions with the nanomesh not overgrowing Ru step edges, in contrast to the findings on *h*BN/Rh(111) [226]. Surface X-ray diffraction (SXRD) - the method of choice to determine superstructure lattice constants with high precision - shows a 14-on-13 superstructure (i.e., a 14 × 14 unit cell of B and N atoms, respectively, on a 13 × 13 unit cell of Ru atoms) with 3.5 nm periodicity [227], thus disagreeing with the previous reports. Photoemission experiments yielded a σ and π band splitting (0.92 and 0.83 eV, respectively) indicative of weakly and strongly bonded areas in the nanomesh structure, and an average work function of 4.0 ± 0.1 eV [226]. The XPS binding energies correspond to 190.83 ± 0.15 (B 1s) and 398.63 ± 0.15 eV (N 1s) [326]. Preobrajenski et al. resolved a modest splitting of the N1s signal into two resonances, where the higher BE component corresponds to the stronger bond pore regions. From the intensity ratio, a pore radius of 1.17 ± 0.05 nm was inferred [88]. Brugger et al. confirmed the σ and π splitting in ARPES experiments and showed that He II_α Fermi surface maps of *h*BN/Ru(0001) only feature contributions already contained in the respective maps of the bare Ru(0001) substrate - in contrast to the Fermi surface modifications induced in graphene/Ru(0001) representing a metallic system. These finding were corroborated by DFT calculations (PBE-GGA), which however overestimate the corrugation [89]. AES and TPD experiments revealed a thermal stability of the *h*BN/Ru(0001) nanomesh up to 1275 K under UHV conditions [226].

In 2011, Sutter et al. provided new insights into the CVD growth of *h*BN/Ru(0001) and the role of hydrogen in the growth and etching processes of *h*BN [221]. The real-time LEEM observations revealed how *h*BN growth at 1073 K and low borazine pressure gets initiated with a low-density of *h*BN nuclei that expand and coalesce into a *h*BN film of very high crystalline quality, whereby both Ru(0001) single crystals and epitaxial Ru(0001) films on sapphire can be applied [221]. In a follow-up study, Sutter et al. introduced a scalable synthesis approach for few-layer *h*BN on Ru(0001) based on magnetron sputtering of B in an N_2/Ar environment (vide supra) [223]. Applying an atomic layer deposition process involving BCl_3 and NH_3, Bjelkevig et al. synthesized *h*BN/Ru(0001) featuring a R30($\sqrt{3} \times \sqrt{3}$) structure in LEED, thus deviating substantially from the usual nanomesh pattern [327].

A detailed STM characterization of *h*BN morphologies at sub-ML coverage on Ru(0001) was provided by Lu et al., specifically addressing void defects and fault lines created by the merging of *h*BN grains during growth with high nucleation density. At low nucleation density, step flow growth of *h*BN, i.e., a single crystal *h*BN domain growing over Ru step edges (both in the uphill and downhill directions) was observed [222], corroborating the LEEM results [221]. A further in-situ LEEM study by Yang et al. confirmed both the *h*BN growth across step edges and the emergence of pinhole and vacancy defects upon merging of *h*BN domains to a full layer [228]. Furthermore, it was highlighted that the growth proceeds fastest along step edges, with downhill growth being faster than uphill growth [228]. Recently, Zhang et al. corroborated the high structural quality achievable for *h*BN/Ru(0001) by in-situ RHEED and STM measurements [225].

In a combined experimental and theoretical endeavor, Kutana et al. explored *h*BN/graphene alloys on Ru(0001) [224]. Hereby, they modeled *h*BN/Ru(0001) by a 14-on-13 coincidence lattice, yielding a 3.52 nm periodicity, which agrees with the SXRD results [227], but exceeds the value of ≈3.33 nm observed in STM [224]. This discrepancy was tentatively assigned to various irregularities and defects in the *h*BN superstructure observed in the experimental STM data [224]. The *h*BN corrugation was calculated to be ≈ 1.5 Å with an average *h*BN-Ru separation of 2.60 Å. This value for the corrugation is smaller than the one resulting from a previous DFT study using a smaller coincidence lattice (Brugger et al. [89], discussed above), but exceeds the experimentally observed height differences (≈1 Å [224], 0.5–0.7 Å [89,226]).

Summarizing, *h*BN/Ru(0001) represents a geometrically distinctly corrugated interface, where the low-lying regions of the nanomesh-like structure interact considerably with Ru.

2.2.6. Cobalt(0001)

CVD growth of *h*BN on Co(0001) films was reported by Orofeo et al., who characterized the interface structure by LEEM, LEED, TEM, and Raman [62,193]. At sub-ML coverage, individual triangular *h*BN islands with side lengths exceeding 10 μm were observed. Two orientations, differing by 180°, were observed and assigned to $B_{hcp}N_{top}$ and $B_{fcc}N_{top}$ registries, respectively, similar to the case of *h*BN/Ni(111). Indeed, also for *h*BN/Co(0001) a commensurate 1 × 1 structure was proposed [193]. The *h*BN growth saturated at one

monolayer, which revealed an optical gap of 5.9 eV. Interestingly, a rougher substrate allowed for the synthesis of *h*BN multilayers, where the number of layers could be determined by LEEM [62]. Driver et al. grew up to seven *h*BN layers on Co(0001) films using atomic layer epitaxy (ALE) [230] and characterized these thin *h*BN films by XPS, LEED, and TEM. In the ALE process, highly oriented and continuous *h*BN sheets were formed. The authors found no evidence for strong interfacial charge transfer and thus highlight the potential of *h*BN/Co(0001) for spintronic applications [229,230]. The XPS binding energies (B 1s: 191.9 eV, N 1s: 398.7 eV) for a coverage of 1.7 ML evidence an energy difference between the B 1s and N 1s peak that is reduced by about 1 eV compared to typical ML *h*BN/metal systems (compare Fig. 13). On the other hand, a DFT study by Joshi et al. reported on considerable hybridization of *h*BN states and Co d states, resulting in a gain of 0.21 electrons on B and a loss of 0.15 and 0.01 electrons on Co and N, respectively [328]. The calculated work function for *h*BN/Co(0001) amounts to 3.5 eV and the magnetic moment of the interfacial Co is 1.56 μ_B, slightly reduced compared to the 1.69 μ_B calculated for the bare surface [328]. An earlier first principle study in the GGA framework without vdW corrections by Zhou et al. focusing on *h*BN/Co(111) reported a high spin polarization induced in the *h*BN, with a magnetic moment of 0.2 μ_B for each BN pair [329]. In a DFT comparison of *h*BN/Co(0001) with *h*BN/Ni(111) and *h*BN/Cu(111), Koitz et al. reveal that the adsorption energy of *h*BN is largest on Co(0001). Besides the most stable $B_{fcc}N_{top}$ registry of the chemisorbed layer, a physisorbed configuration was determined similar to the *h*BN/Ni(111) case [330]. Returning to experimental studies, Xu et al. reported the growth of three-point star-shaped *h*BN flakes on 400 nm thick, SiO_2/Si(100)-supported Co films by plasma-assisted MBE [331]. Besides SEM imaging, XPS revealed B 1s and N 1s binding energies of 190.6 and 398.0 eV, respectively for the ML-thick islands. Upon C exposure, lateral and vertical graphene-*h*BN interfaces were achieved [331]. 5–6 nm thick *h*BN films - sandwiched between the Co support and Co contacts - featured a breakdown electric field of about 3.0–3.3 MV/cm [208].

2.2.7. Rhodium(111), (110)

Rh(111). The discovery of the intriguing structure of *h*BN/Rh(111) reported by Corso et al. in 2004 triggered considerable interest in this system and coined the term "nanomesh" [87]. In this early study, the - unprecedented - splitting of the σ band in ARPES data (≈1 eV, Fig. 4 (f)) was taken as an indication of a *h*BN double-layer nanostructure, where STM and LEED revealed a superstructure periodicity of 3.2 nm corresponding to a 13 × 13 *h*BN/12 × 12 Rh coincidence lattice (Fig. 4 (a)). In 2007, DFT calculations by Laskowski et al. provided an alternative model for the nanomesh structure, namely a corrugated single-layer *h*BN sheet with the *h*BN-metal separation varying between 2.17 Å and 2.72 Å [332,333]. With further experimental evidence emerging [88,192,231,240], this single-layer structure including strongly and weakly interacting areas (the pore and wire regions, respectively) representing favorable and unfavorable adsorption sites within the supercell was soon established [233]. Accordingly, XPS measurements show two main components, with a N 1s BE of typically 398.6 and 397.9 eV, assigned to the pore and wires, respectively [192,313] (see Fig. 30 (a)). An SXRD study of the nanomesh in air proved the 13-on-12 unit cell and demonstrated the nanomesh stability under ambient condition and X-ray radiation [232]. This 13-on-12 superstructure persists up to 1100 K as demonstrated by SXRD [334]. STM experiments confirmed that the nanomesh sustains temperatures up to 1160 K [234] and revealed its stability in liquids (ultra-pure water [240] and perchloric acid ($HClO_4$) [240,241,335]).

Interestingly, the use of a 150 nm thick Rh(111) film on YSZ-Si(111) as support results in a larger 14 × 14 *h*BN/13 × 13 Rh superstructure, which was attributed to different thermal expansion behavior between this multilayer substrate and single crystals [182,336]. An in-situ STM study under growth conditions by Dong et al. provided fascinating details on the nucleation and growth of *h*BN on Rh(111) [234]. Borazine already adsorbs at rt. Around 930 K, B—N bonds can break, resulting in the formation of the compact *h*BN structure. Indeed, the observed island morphologies imply a cracking of the borazine precursor - similar to the situation reported for Ni(111) [261]. However, the high nucleation density at these moderate temperatures induces many line defects between grains that could not be reduced by slow annealing up to 1180 K - in contrast to the situation reported for *h*BN/Cu(111) [290]. Thus, a high substrate temperature of typically 1050 K is best suited for high-quality *h*BN growth on Rh(111), as it enables an efficient diffusion [234]. A combined AES, HREELS and TPD study by Farkas et al. confirmed the growth of well defined *h*BN at ≈ 1000 K and showed that the *h*BN layer formation began above 600 K, while borazine adsorbs molecularly at 140 K on clean Rh(111) with dehydrogenation reactions already starting below 200 K [242]. Recently, the growth of a high quality *h*BN nanomesh on a four-inch wafer scale, single crystalline Rh(111) thin film in a custom-designed apparatus was reported, thus demonstrating a scalable, inexpensive large-area coating process [236,239].

The stiffness of the corrugated *h*BN sheets on Rh(111) was addressed in two nc-AFM studies at rt [235] and 1.5 K [238], respectively. A contrast inversion of the nanomesh superstructure upon reducing the tip-sample distance was attributed to local elastic deformation of the wire regions of the nanomesh induced by tip-sample interactions [235]. Indeed, the atomically-resolved, low-temperature measurements revealed lateral and vertical deformations due to tip-sample forces. Specifically, a very low stiffness of ≈1 N/m was derived, showing the "softness" of the corrugated *h*BN sheet, with indentation experiments revealing an elasticity on the wire regions comparable to free membranes [238].

The spatially averaged work function of *h*BN/Rh(111) amounts to 4.15 eV [226,339]. Lateral variations of the local work function (see Ref. [340]) resulting in so-called dipole rings - an important aspect of the nanomesh structure - were experimentally recognized for the first time by Dil et al. in 2008 [339]. Xe core-level binding energies in XPS (i.e., the application of the photoemission of adsorbed Xe (PAX) technique introduced by Wandelt [340–342]) and the Xe desorption temperatures yielded information on the electrostatic landscape of the nanomesh and the local Xe bonding strength, respectively. The pores of the nanomesh represent regions of lower local work function or potential, as corroborated by DFT calculations (Fig. 4 (h)). The resulting trapping potential - given by in-plane dipoles - is localized at the rim of the pores [233,339,343,344] (see Fig. 4 (g)). The lower local work function on the pores as compared to the wire sites was confirmed in real space measurements by Kelvin probe force microscopy (KPFM), even though the measured variation (15–20 meV) is considerably lower than the PAX value (0.31 eV) [235].

In a recent combined STM and DFT study, Dubout et al. rationalized how apparent lateral displacements of atoms in high-resolution STM data of corrugated sp^2 sheets (including *h*BN/Rh(111)) emerge from the directionality of the layer's π-orbitals that dominate the STM contrast [237]. Such lattice distortions - that might be (mis-)interpreted as representing large strain - can thus reflect imaging artifacts. Photon maps recorded on *h*BN/Rh(111) showed strong STM-induced electroluminescence from the nanomesh pores, exceeding the one from the wire regions by more than one order of magnitude [345].

A DFT optimization (revPBE-D3) of a 13 × 13 *h*BN/12 × 12 Rh cell by Ding et al. reproduced the expected corrugated structure [338]: The pore regions feature a BN adsorption height of 2.2 Å and constitute about 30% of the *h*BN layer. The wire regions with an adsorption height of 3.1 Å represent more than 30% of the

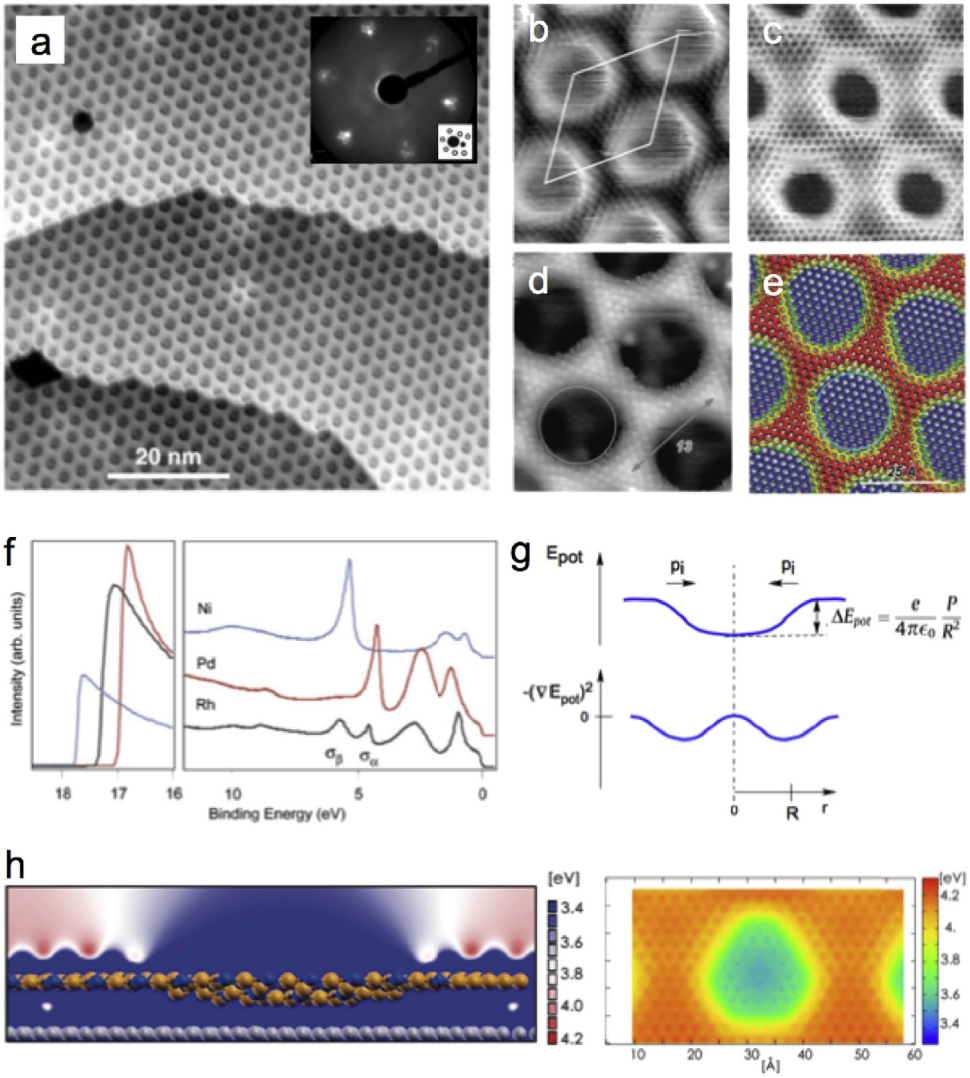

Fig. 4. *h*BN/Rh(111). (a) Large-scale STM image and LEED pattern (inset). (b-d) Atomically resolved STM images of the nanomesh. Note the different contrast ("pore-wire" (in c,d) versus "separated coin" (in b) [243]). (e) Calculated, color-coded height map. (f) UPS spectrum of *h*BN/Rh(111) in comparison to *h*BN/Ni(111) and *h*BN/Pd(111). Note the σ band splitting for the nanomesh system and the cut-off energies representing work function differences. (g) Scheme of the potential energy (top) and polarization energy (bottom) across a nanomesh pore. In-plane dipoles (p_i) emerge at a radius R. (h) Calculated electrostatic potential above the nanomesh structure in a vertical cut (left panel) and a top view (right panel). (a) Adapted from Ref. [87] with permission from AAAS. (b) Adapted with permission from Ref. [192] © (2007) American Physical Society, (c) Adapted with permission from Ref. [237], (d,e) Adapted with permission from Ref. [337] © (2014) Royal Society of Chemistry, (f,g) Adapted with permission from Ref. [233] © (2009) Elsevier, (h) Adapted with permission from Ref. [338] © (2011) American Chemical Society. (For interpretation of the references to color in this figure legend, the reader is referred to the Web version of this article.)

monolayer. The considerable height change between the pore and wires occurs within two atomic rows [338]. A comparison of the electronic structure and the electrostatic potential of this *h*BN/Rh(111) system with a corrugated, but free-standing *h*BN sheet showed the importance of the *h*BN-Rh interaction in the pore regions, resulting in a charge redistribution [338]. A recent DFT study by Ianuzzi et al. systematically addressed the subtle role played by the combination of exchange and correlations functionals in the description of the corrugation, but also the size and the shape of the nanomesh pores, which could not be described precisely in the previous DFT studies [337]. The PBE-rVV10 functional gave the best agreement with STM experiments, with atoms adsorbed below a height of 2.5 Å assigned to the pores that reflect 45% of the *h*BN layer and atoms adsorbed above a height of 3.7 Å assigned to the wire regions, respectively, that represent 29% of the *h*BN layer (see Fig. 4 (e)). A study by Patterson et al. - published in the same month - on the other hand reports a larger maximum geometric corrugation of 2.647 Å (LDA), 2.204 Å (GGA-PBE), and 2.385 Å (optB86b vdW-DF) for *h*BN/Rh(111) [346]. Furthermore, Laskowski et al. calculated NEXAFS spectra for the B and N K-edges by DFT, highlighting strong spectral features originating from the interaction between *h*BN and Rh [347]. Recently, Musso et al. simulated the *h*BN/Rh(111) interface at different temperatures employing a second-generation Car-Parrinello molecular dynamics scheme [348]. The nanomesh corrugation is preserved up to temperatures of about 800 K, even though the bimodal height distribution representing pore and wire regions, respectively, "blurs" with increasing temperature and the pore shapes distort. The dynamic effects include migration of nanomesh

pores. At 1380 K, the calculations yield a single broad height distribution - pore and wire regions can thus not be distinguished anymore [348].

Rh(110). Recently, Martínez-Galera and Gómez-Rodríguez explored structural properties of *h*BN/Rh(110) by STM and LEED [244]. Two isostructural *h*BN/Rh(110) domains were observed, resulting in a unique quasi-1D stripe-like moiré pattern with a periodicity of 1.3 ± 0.1 nm (see Fig. 3(i–k)). Despite a considerable interaction of *h*BN with the Rh(110) surface, the STM images reveal only a very moderate apparent corrugation (below 30 pm), in contrast to the strongly corrugated *h*BN/Rh(111) nanomesh structure. This behavior was rationalized by the lack of subregions within moiré supercells that contain favorable sites for orbital mixing between *h*BN and the symmetry-mismatched (110) support [244].

2.2.8. Iridium(111)

The first study on *h*BN/Ir(111) by Preobrajenski et al. in 2007 provided evidence for a non-negligible geometric corrugation, as N 1s XPS and NEXAFS data included components representing weakly and strongly bond *h*BN areas [88]. The interaction of borazine with Ir(111) was studied within a large temperature range (170–1270 K) by Orlando et al., presenting LEED data of a *h*BN monolayer on Ir(111) that were interpreted as a 13-on-12 superstructure [245]. In a follow-up study employing XPD, the authors showed that a single domain *h*BN layer can be grown on Ir(111) by a temperature-programmed growth (TPG) protocol involving cycles of rt borazine adsorption followed by flashing to 1270 K, while the usual CVD method (*i.e.*, borazine dosage at 1070 K) resulted in *h*BN monolayers including two domain orientations rotated by 180° [248]. This finding was confirmed by STM data that however revealed an inferior structural quality resulting from the TPG approach [250].

Recently, Petrović et al. applied LEEM, combined with PEEM and μLEED to characterize the epitaxy of *h*BN submonolayers [252]. Two types of islands - reaching sizes up to 10 µm - were identified, featuring distinct shapes and growth modes, representing the two domain orientations just mentioned. Interestingly, these two island types exhibit different work function (4.78 and 4.68 eV, respectively) and binding to the Ir(111) support (Fig. 5 (e)). Furthermore, this study highlighted the influence of Ir steps on the *h*BN growth and recommends synthesis temperatures below ≈1220 K to avoid B dissolution in Ir and the formation of B reconstructed areas [252].

Based on LEED and XPS measurements, Usachov et al. showed that *h*BN/Ir(111) decomposes at temperatures exceeding 1273 K. Importantly, they provide ARPES data evidencing a rather weak chemical interaction between the *h*BN sheet and the Ir support, where replicated σ and π bands originate from the geometric corrugation [246] (Fig. 5 (j)). Contrasting the situation on graphene/Ir(111), a large gap was observed in STS measurements by Liu et al. (Fig. 5 (i)). Combined STM and DFT studies by Schulz et al. and Liu et al. visualized the moiré pattern of *h*BN/Ir(111) in real space and determined a superstructure periodicity of ≈2.9 nm [247] and ≈3.2 nm [249], respectively (Fig. 5(a–c)). Both reports also yield distinctly different values of the geometric corrugation, specifically ≈0.4 Å [247] and ≈1.4 Å [249]. These ambiguities were recently resolved by a multi-method study from Hagen et al., employing XPS, XSW, LEED, STM, and DFT comprehensively characterizing *h*BN/Ir(111). From XSW - giving access to adsorption distances - a height difference of ≈1.55 Å between the strongly bound species (average adsorption height ≈ 2.2 Å) and the weakly bound species (average adsorption height ≈ 3.7 Å) was determined and corroborated by DFT, classifying *h*BN/Ir(111) as a geometrically strongly corrugated system [250] (Fig. 5 (d)). Furthermore, atomically resolved STM images yielded a moiré periodicity of 11.7 ± 0.3 times the one of *h*BN or 2.91 nm, only consistent with an approximate 12-on-11 superstructure [250] (Fig. 5 (b)). Recently, Seitsonen, Schulz, and Liljeroth extracted an average corrugation of 1.65 ± 0.23 Å from Δf(z) curves recorded by nc-AFM at different positions of the moiré superstructure and used this value - combined with the XSW results discussed above - to benchmark vdW-treated DFT [349]. For the *h*BN/Ir(111) system, distinct approximations (including vdW-DF-rB86, vdW-DF2-C09, vdW-DF2-rB86) yielded a good agreement with the experimental values, while others fail (e.g., vdW-DF-optB88) despite properly describing related interfaces as graphene/Ir(111) [349].

In the work of Schulz et al. (already mentioned above), a very important aspect of *h*BN/Ir(111) was explored, namely the local work function variation within the moiré superstructure. As evident from the bias-dependent contrast inversion of the apparent moiré corrugation in STM images, the STM contrast is mainly determined by electronic effects, despite the considerable geometric corrugation. Combining I(z) spectroscopy with field emission spectroscopy, a work function modulation of roughly 0.5 eV within the moiré unit cell was estimated. The pore regions - defined as the rather circular areas of the moiré superstructure - correspond to areas of lowest local work function, an assignment confirmed by DFT modeling [247] (Fig. 5(f–h)). At the same time, the pore regions correspond to strongly bound *h*BN in a $B_{hcp}N_{top}$ registry, featuring a small adsorption height and a large XPS binding energies [250] (Fig. 5 (k)). The work function gradient between pores and wires leads to an electric field in the order of 0.1 V/nm at the edge between these two regions [251].

Recently, Schulz et al. demonstrated the identification of B and N sites in *h*BN/Ir(111) by combining nc-AFM imaging (Δf, with CO functionalized tips), KPFM mapping and nc-AFM image simulations (based on a DFT optimized interface geometry) [253]. This study not only shows that the B sublattice dominates the nc-AFM image contrast at large tip-*h*BN distances (with a CO tip carrying a positive partial charge), but also provides a mapping of the vertical electric field near the surface featuring atomic-scale and moiré-related variations [253].

In summary, *h*BN/Ir(111) is a comprehensively characterized interface providing both a considerable electronic and geometric corrugation with a superstructure periodicity of 2.91 nm, which makes it interesting as template.

2.2.9. Nickel(111), (110), (100)

Ni(111). A first quantitative structure determination of the *h*BN/Ni(111) interface based on a LEED intensity analysis was reported by Gamou et al. in 1997 [255]. The *h*BN forms a commensurate 1 × 1 monolayer on Ni(111), featuring a $B_{fcc}N_{top}$ registry (Fig. 6 (b)). Overall, the *h*BN sheet is planar (Fig. 6 (a)), but the B and N atoms are not placed at the exactly same height due to the different binding of the two species and the lattice mismatch, leading to an atomic-scale corrugation (Fig. 6 (b)). Atomically resolved STM images typically represent the N lattice [259,350]. The LEED study of Gamou et al. yielded an adsorption height of 2.22 ± 0.07 Å for the N atoms with respect to the Ni surface layer, the B species reside 0.18 Å below the N. Angle-scanned XPD experiments combined with single- and multiple scattering calculations [262] by Auwärter et al. and Muntwiler et al. gave both a smaller adsorption height for N (1.95 ± 0.16 Å) and a smaller corrugation (0.07 ± 0.06 Å) [259,351]. A PhD study, again by Muntwiler et al., yields an adsorption height of 2.11 ± 0.02 Å and a distance of 1.99 ± 0.04 Å between the two top most relaxed Ni layers [269]. Finally, recent NIXSW experiments by Ohtomo et al. gave a corrugation of 0.15 Å with adsorption heights of

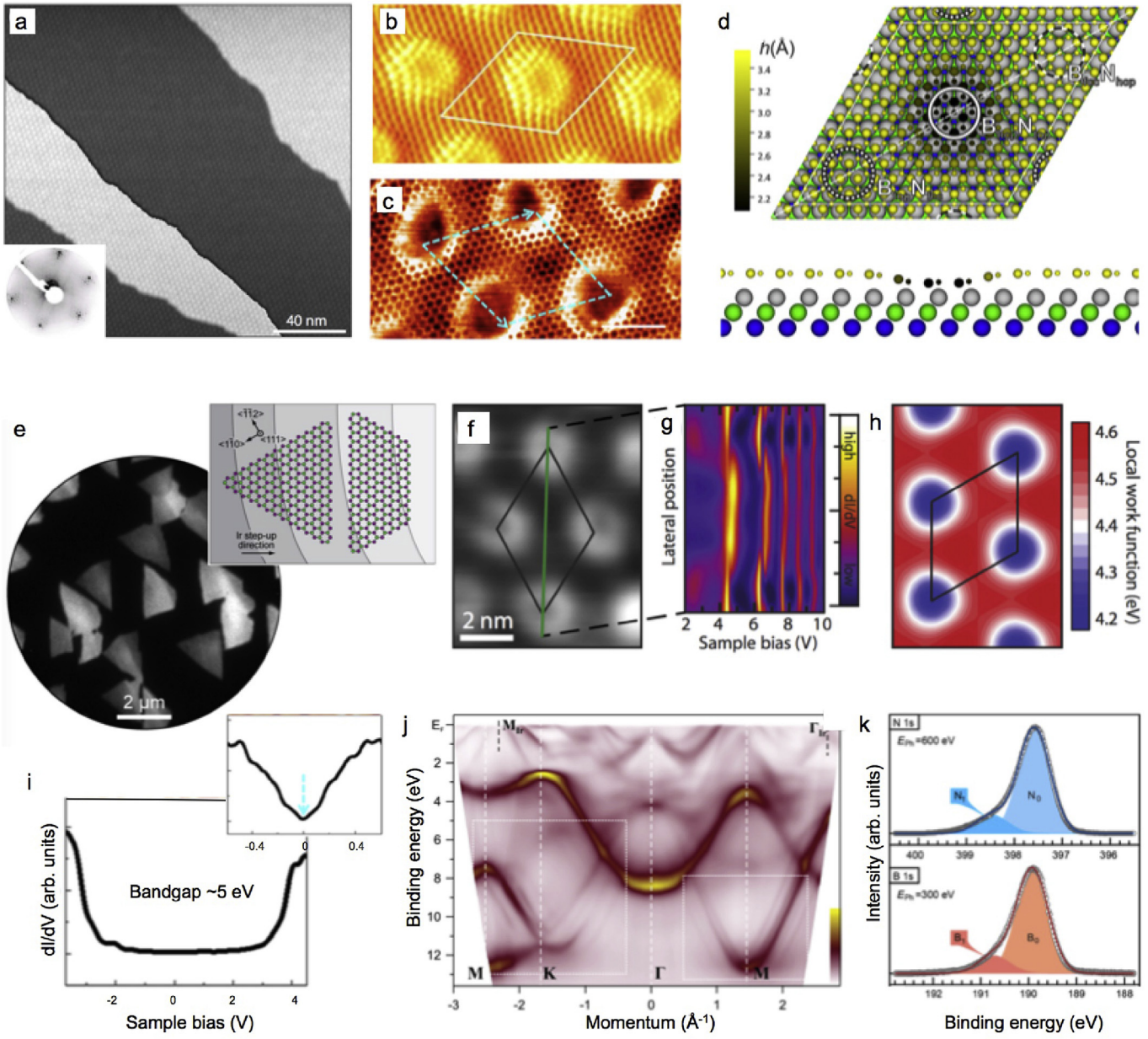

Fig. 5. *h*BN/Ir(111). (a) Large-scale STM image and LEED pattern (inset). (b,c) Atomically-resolved STM image featuring different contrast. (d) DFT-optimized structural model of the interface: Top view (top panel) and side view (bottom panel). (e) PEEM image of *h*BN islands, showing different, work function related intensity for the two island types, which are sketched in the inset. (f) STM image of the moiré superstructure across which the FER map (g) was recorded. (h) Local work function map calculated from DFT. (i) dI/dV spectrum. In contrast to graphene/Ir(111) (inset) a large gap is observed. (j) ARPES map of the band structure. (k) N 1s (top panel) and B 1s (bottom panel) XPS signals. (a,f-h) Adapted with permission from Ref. [247] © (2014) American Physical Society. Inset in (a) adapted from Ref. [250], (b,d,k) Adapted with permission from Ref. [250] © (2016) American Chemical Society, (c,i) Adapted with permission from Ref. [249] © (2014) American Chemical Society, (e) Adapted with permission from Ref. [252] © (2017) Elsevier, (j) Adapted with permission from Ref. [246] © (2012) American Physical Society.

2.13 Å (N) and 1.98 Å (B), respectively [275]. Despite some scatter in these experimental values, the published data consistently point to a small adsorption height of *h*BN on Ni(111), indicating considerable attractive interactions.

Besides the dominating $B_{fcc}N_{top}$ domain, a combined XPD and STM study revealed an additional possible domain, featuring a $B_{hcp}N_{top}$ registry, where the balance between the two domain types was guided by subtle influences in the sample preparation [261]. At *h*BN sub-monolayer coverages, triangular shaped *h*BN islands, rotated by 180° relative to each other, reflect these two domain structures. Intriguingly, such *h*BN islands grew either on Ni(111) terraces [261,266] or were embedded therein [273]. In a recent study, Yang et al. observed two types of (triangular) *h*BN islands on Ni(111) by LEEM and μ-LEED, identified as epitaxial, strongly bound and non-epitaxial, weakly bound species, respectively [277]. While the epitaxial islands cover the two registries discussed above, the non-epitaxial ones show a variation of azimuthal alignments between the *h*BN and Ni(111) lattices. Indeed, two N1s species are observed by XPS (BE 398.8 eV epitaxial component, see below and BE 397.9 eV). Compared to the Ni(111) work function, the one for epitaxial *h*BN is reduced by 1.6 eV while the one for non-epitaxial *h*BN only decreased by 0.9 eV (see below). DFT yields an adsorption height

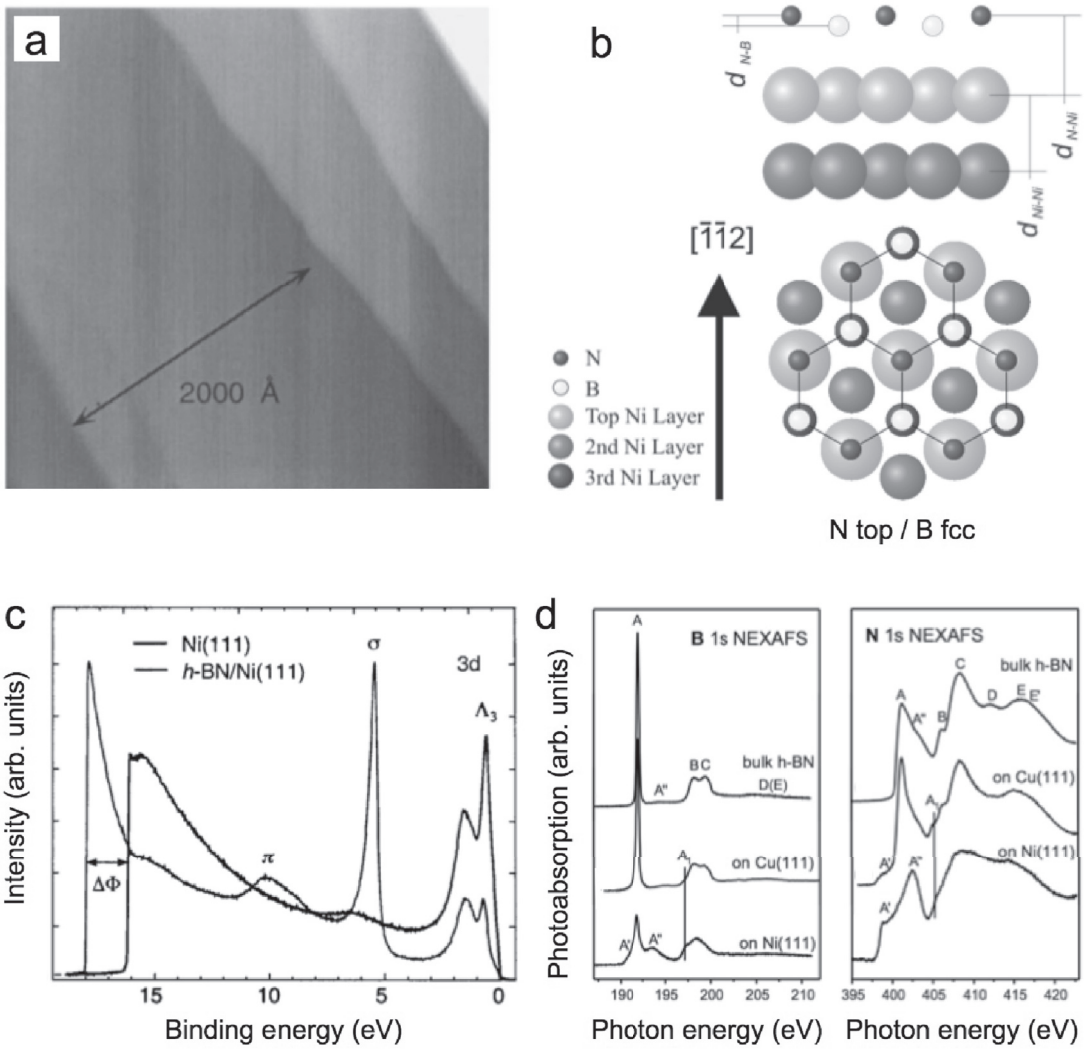

Fig. 6. *h*BN/Ni(111). (a) STM image. (b) Structural model of the interface: Side view (top panel) and top view (bottom panel). (c) UPS spectrum of *h*BN/Ni(111), showing contributions from the σ and π bands. The comparison to the Ni(111) spectrum reveals a work function reduction ($\Delta\phi$) on the *h*BN-covered surface. (d) K-edge NEXAFS spectra for B (left panel) and N (right panel), including comparison to bulk *h*BN and *h*BN/Cu(111). (a) Adapted with permission from Ref. [259] © (1999) Elsevier, (b) Adapted with permission from Ref. [351] © (2001) Elsevier, (c) Adapted with permission from Ref. [264] © (2002) Royal Society of Chemistry, (d) Adapted with permission from Ref. [265] © (2005) Elsevier.

of 2.0 Å for the epitaxial and 2.9 Å for the non-epitaxial structure. The emergence of non-epitaxial *h*BN domains not recognized in other studies might be attributed to the relatively low growth temperature [277]. Indeed, theoretical modeling predicted both a chemisorbed (energy minimum) and physisorbed state (local energy minimum) for *h*BN/Ni(111) [189,330,352] - similar to the graphene/Ni(111) system [353].

The electronic structure of *h*BN/Ni(111) is rather multifaceted and not all reported findings can be detailed in this review [231,267,268,270,274,354]. The experimental valence- and conduction band structure was provided first in 1997 by Nagashima et al., concluding that the *h*BN band structure was not severely deformed on Ni(111) [254]. Nevertheless, based on phonon spectra, Rokuta et al. inferred some hybridization between the Ni d and *h*BN π electrons [256,260]. Indeed, later NEXAFS, XPS, RAS, and XES experiments by Preobrajenski et al. showed that *h*BN is chemisorbed on Ni(111), featuring considerable Ni 3d - *h*BN π hybridization and in-gap states [231,263,265] (Fig. 6 (d)). The latter show a positive spin polarization as inferred from SPMDS experiments [274]. Laskowski et al. calculated and analyzed the B and N K-edge NEXAFS spectra by DFT, providing an interpretation of the key features observed in the experiments by Preobrajenski et al. [347]. The *h*BN-Ni interaction involves a charge redistribution at the interface, with minute electron transfer to the metal [187]. The reported experimental work function values for *h*BN/Ni(111) range from 3.5 to 3.62 eV and are thus considerable reduced compared to bare Ni(111) (5.23–5.3 eV) (Fig. 6 (c)) [257,264,265]. XPS binding energies for the B 1s and N 1s core levels are reported in a considerable range from 190.47 to 191.2 and 398.5–399.1 eV, respectively [189,254,258,263].

Following the first theoretical study focused on *h*BN/Ni(111) by Grad et al. in 2003 that identified the $B_{fcc}N_{top}$ registry as favorable [350], a series of DFT studies addressed this interface, e.g., Refs. [187,189,200,330,347,355–361]. While a consensus about the preferential adsorption configuration is reached, adsorption energies and distances, as well as the level of hybridization and charge redistribution naturally depend on the level of theory employed. Unfortunately, a further discussion of such effects including the type of functional or dispersion correction employed is beyond the scope of this

review. However, it should be noted that DFT-based reactive molecular dynamics simulation can yield detailed insight into the nucleation and growth of *h*BN/Ni(111) [362].

In summary, *h*BN on Ni(111) represents a chemisorbed, geometrically planar, commensurate overlayer with a prevalent $B_{fcc}N_{top}$ registry featuring a small height difference between B and N atoms.

Ni(110). Greber et al. comprehensively characterized a *h*BN monolayer on Ni(110) in a combined LEED and ARPES study. The data revealed the coexistence of a 1 × 6 and a 7 × 5 superstructure, with the former being more abundant. Interestingly, the *h*BN units cells are rotated by 90° in the two structures which is reflected in k-space maps recorded at an energy probing the *h*BN σ_2 band [278].

Ni(100). Already in 1997, Desrosiers et al. provided a characterization of *h*BN/Ni(100). Based on LEED imaging revealing a 1 × 7 pattern, a strained *h*BN monolayer geometry - where the hexagonal lattice is slightly stretch in one direction - was proposed [214]. It was also reported that the LEED pattern could be fully recovered by slight annealing after storing *h*BN/Ni(100) in atmosphere for several days, signaling a low reactivity and high stability of *h*BN on Ni(100) [214].

Varia. To complete this discussion on *h*BN monolayers on different Ni crystal faces, it should be noted that *h*BN growth is typically accompanied by Ni mass transport. Thus, attempts to prepare 1D-superstructured, grating-like *h*BN/Ni interfaces employing vicinal Ni(223) supports failed due to a reconstruction of the surface upon *h*BN growth [363]. Beyond the *h*BN monolayer systems on Ni single crystals discussed so far, Ni foils and films are frequently applied as substrate for *h*BN growth. In APCVD or LPCVD systems, mostly Ni foils are employed, opening pathways for *h*BN transfer to other substrate via etching of the Ni (e.g., Refs. [364–370]). Recently, however, the APCVD growth of centimeter-sized, single domain *h*BN films on a Ni(111) crystal was reported, followed by bubble-type transfer (i.e., applying an electrochemical delamination protocol using hydrogen bubbles), allowing for a re-use of the Ni(111) support [371]. Single-crystal *h*BN domains with edge length up to 0.6 mm were synthesized by ion beam sputtering deposition on Ni(111) films [319]. Furthermore, Tonkikh et al. applied an MBE technique to grow highly-ordered *h*BN multilayers on Ni(111). An ARPES and NEXAFS characterization revealed bulk-like *h*BN properties in such 10-ML films [200]. Previously, the MBE approach was employed on Ni foils by Nakhaie et al. [199]. In a recent multimethod study including LEEM, μLEED, XPS, and STM, Ismach et al. explored the influence of the environment - especially carbon sources - on the LPCVD growth of single and bilayer *h*BN on Ni foils [372].

2.2.10. Palladium(111), (110)

Pd(111). The first experimental description of *h*BN/Pd(111) was provided by Nagashima et al. in 1995, yielding the valence band structure (σ and π bands) by ARPES, highlighting a weak *h*BN/Pd interaction [257] and reporting a work function reduction to 4 eV upon *h*BN monolayer formation. A real space characterization by STM, complemented by LEED and ARPES was contributed later by Morscher et al. [279]. STM images revealed different coexisting moiré patterns with periodicities ranging from 1.1 to 2.75 nm that were attributed to different rotation angles between *h*BN domains and the Pd(111) lattice. Indeed, LEED images show a ring-like structure [279]. However, unlike in the Ag cases discussed below, this ring is not homogeneous and the LEED images additionally exhibit superstructure spots. Thus, *h*BN/Pd(111) features prevailing *h*BN orientations. One of those was assigned to a coincidence lattice where 11 × 11 BN units adsorb on 10 × 10 Pd unit cells, while another one represents a R30° structure that appears to be incommensurate [279]. XPS measurements yielded a B 1s BE of 190.46 ± 0.25 eV and a N 1s BE of 398.05 ± 0.27 eV [326]. Normal emission valence band spectra show a single component for the σ and π bands, thus precluding a heavily corrugated *h*BN nanomesh structure featuring strongly- and weakly-bound *h*BN areas [279]. Accordingly, the large apparent moiré corrugations observed in STM images (up to 1.6 Å) were not attributed to a real geometric corrugation, but electronic effects due to changes in the local work function were considered (average work function: 4.26 eV). This study furthermore successfully introduced the use of thin Pd(111) films grown on a sapphire (0001) support as substrates for *h*BN synthesis, highlighting the reduced preparation efforts [279].

Pd(110). Corso et al. combined STM with LEED to characterize the *h*BN/Pd(110) interface. Ring-like structures in LEED and coexisting moiré patterns with different periodicity and symmetry resolved in STM show rather weak site-specific interactions between the *h*BN sheet and the Pd(110) support. The geometric corrugation of *h*BN/Pd(110) was estimated to be 0.5 Å. The moiré patterns could be modeled well by only considering one atomic species in the *h*BN layer, which was assigned to N dominating the STM contrast. Intensity variations along the rings visualized in LEED changed considerably within different sample preparations, indicating subtle influences of the preparation conditions on the *h*BN domain composition. Judging from LEED data, the *h*BN/Pd(110) system was stable up to at least 950 K [280].

2.2.11. Platinum(111)

The interaction of borazine with Pt(111) was first described by Simonson et al. in 1990 by IRAS [281], followed by a combined HREELS, UPS, and TDS study [86]. The decomposition of borazine - oriented with its molecular ring perpendicular to the surface - starts at 170 K and proceeds at higher temperature to yield *h*BN. Paffett et al. characterized the resulting *h*BN monolayer grown on Pt(111) at 1000 K by a multi-method approach including EELS and LEED also in 1990, proposing a structural model for the interface with a 10-on-9 superstructure [85]. Here, the B and N sublattices are aligned with the Pt(111) substrate (Fig. 7 (b, d)). The valence band structure of *h*BN/Pt(111), i.e., the dispersion of the σ and π bands was provided by Nagashima et al. in 1995 using ARPES together with the work function (4.9 eV), concluding that the *h*BN sheet is physisorbed [257]. This finding was supported by measurements of the phonon spectra [256]. More than a decade later, this picture was refined by a series of papers from Preobrajenski et al. comparing *h*BN/Pt(111) to other *h*BN transition metal interfaces that clearly advanced the understanding of this system [88,192,231]. A rather weak interaction between *h*BN and Pt(111) (including Pt *d, s* - *h*BN π orbital mixing) was inferred from XAS, XES, XPS, and UPS measurements [88,192]. This interaction was classified as physisorption or very weak chemical bonding, resulting in a low density of adsorption-induced gap states [88]. Furthermore, the first real space characterization of *h*BN/Pt(111) by STM was provided, complemented by LEED imaging [192]. Atomically resolved STM images reveal a moiré pattern with 2.5 nm periodicity consistent with a 10-on-9 coincidence lattice (Fig. 7 (a)). A significant geometric corrugation of the *h*BN was judged unlikely based on STM data, N 1s XP spectra, and normal emission valence band spectra. *h*BN/Pt(111) is thus considered a “nearly flat” monolayer [88,192]. However, Cavar et al. pointed out that minor geometric corrugations - likely present in the *h*BN/Pt(111) system - can not be quantified by the methods applied (standard LEED, STM) [282]. The atomic contrast in STM images is assigned to the N species as NEXAFS spectra show that the N LDOS at E_F clearly exceeds the B one, thus corroborating an earlier assignment in the *h*BN/Ni(111) system [350]. Calculated NEXAFS spectra were reported by Laskowski et al. [347].

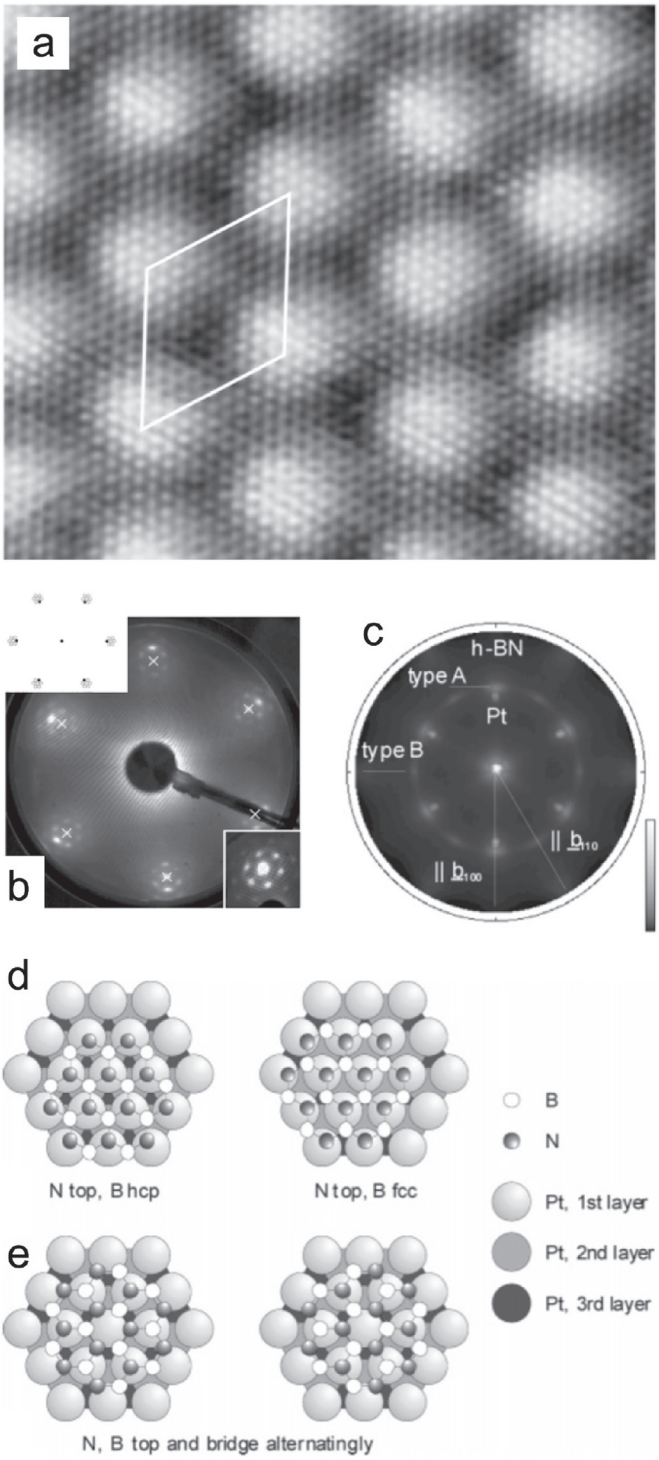

Fig. 7. *h*BN/Pt(111). (a) Atomically resolved STM image. The white rhombus highlights the moiré superstructure. (b,c) LEED images for *h*BN/Pt(111) prepared from borazine (b) and B-trichloroborazine (c). The latter shows contributions from type A and type B registries. (d) A-type domain structure and (e) B-type domain structure, with 30° rotation of the *h*BN sheet. (a,b) Adapted with permission from Ref. [192] © (2007) American Physical Society, Inset in (b) reproduced with permission from Ref. [85] © (1990) Elsevier. (c–e) Adapted with permission from Ref. [211] © (2005) American Chemical Society.

Interestingly, a LEED study by Müller et al. based on a B-Trichloroborazine precursor demonstrated the existence of additional *h*BN domains where the B and N sublattices are rotated by 30° with respect to the Pt(111) lattice (Fig. 7 (c, e)) that were not recognized before, thus highlighting subtle influences of the preparation procedure (including precursor) on the *h*BN monolayer structure [211]. LEEM measurements performed for borazine exposures between 1×10^{-8} and 1×10^{-6} mbar at 1073 K revealed larger and more regular islands at lower borazine pressure [282]. Zhang et al. confirm a single orientation for *h*BN domains on Pt(111) by LEEM and μLEED measurements and report a *h*BN growth dominated by the downhill direction across the Pt(111) steps. After cooling to rt, defects as wrinkles, domain boundaries and vacancies were observed, potentially influencing adsorption and intercalation processes (see 3.2.2) [283].

As a side note, it should be mentioned that also Pt foils were successfully employed for the growth and subsequent transfer of *h*BN. Two studies submitted nearly simultaneously applied APCVD and LPCVD to synthesize *h*BN on Pt foils [63,373]. Kim et al. showed that the Pt foil can be re-used after a bubble-type transfer of the *h*BN sheet, thus offering means for repeated, cheap fabrication of highly-crystalline *h*BN monolayers [63]. Gao et al. also repeatedly used the Pt foil after the transfer and showed in addition that besides *h*BN monolayers, also bilayer and few-layer films can be achieved by changing the concentration of the borazane precursor introduced in the APCVD system [373].

2.2.12. Copper(111), (110)

Cu(111). Compared to the vast amount of literature about *h*BN on polycrystalline copper supports such as foils and films (e.g., Refs. [11,13,56,301,374–397]), reports on *h*BN/Cu(111) interfaces are scarce. In 2005, Preobrajenski et al. provided a combined NEXAFS and photoelectron spectroscopy characterization, reporting low Cu 3d - *h*BN π interaction (compared to the *h*BN/Ni(111) case) resulting in weak chemisorption (see Fig. 6 (d)) [265]. Two important aspects of *h*BN growth on Cu(111) were highlighted in this early study. First, relatively high borazine precursor doses (≈2000 L) need to be applied to achieve a monolayer. Second, the substrate temperature is critical. Optimal growth was reported in a temperature window between 1023 and 1073 K, higher temperature might damage the Cu(111) surface. Based on LEED imaging, a commensurate 1×1 overlayer structure was reported. Formation of the *h*BN sheets lowered the work function by 0.24 eV to 4.73 eV, B 1s and N 1s binding energies correspond to 190.45 and 398.0 eV, respectively. Additional B 1s features at lower BE are indicative of defects, as B dissolved in Cu(111) [265].

In 2012, Joshi et al. provided a first real space characterization of *h*BN/Cu(111) by low-temperature STM and STS [284]. In a wide bias voltage range around E_F, the *h*BN sheet is transparent in STM under regular tip/scanning conditions. This allows to access and spatially map an electronic interface state, upshifted by ≈ 0.1 eV from the native Cu(111) Shockley-type surface state (Fig. 8 (j)). Consequently, an insulating character and a weak interaction (≈60 meV/unit cell) of *h*BN with Cu(111) was inferred. At bias voltages well above 3 V, when tunneling into field emission resonances (FERs) is operational, pronounced moiré-like superstructures were resolved (Fig. 8 (a)). As the moiré contrast inverts in a small bias voltage range (Fig. 8 (f)), the superstructure was assigned to an electronic and not topographic effect. Indeed, STS measurements in the FER regime yield a local work function reduction of ≈300 meV on the pore or hill regions (3.8 eV) of the superstructure compared to the wire or valley regions (4.1 eV) (Fig. 8 (h)) [284,398]. Recently, Zhang et al. showed that this local work function variation decreases with decreasing moiré periodicity (Fig. 8 (l)) [289]. The coexisting moiré patterns featuring periodicities from 1 to 14 nm emerge from minute rotational misalignments of *h*BN domains with the Cu(111) lattice [284,287] and are thus not consistent with a commensurate 1×1 structure. Comparison to DFT calculations indeed showed that a lateral variation of the *h*BN - Cu adsorption registries resulting in varying distances between B,N and the topmost Cu atoms cause

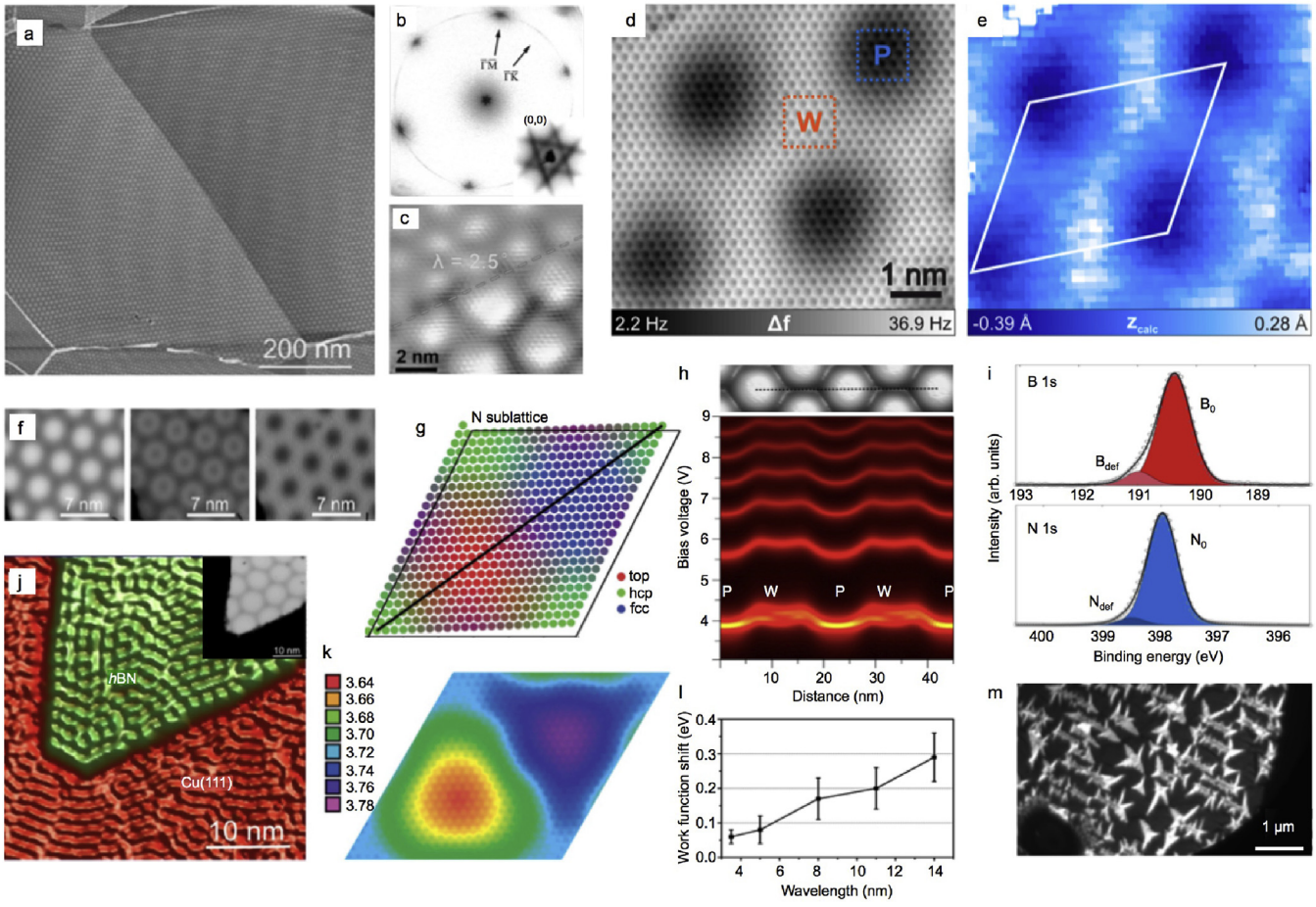

Fig. 8. *h*BN/Cu(111) (a–l) and *h*BN/Cu(110) (m). (a) Large scale STM image. (b) SPA-LEED pattern. The inset shows a zoom-in of the central (0,0)-spot. (c) Atomically-resolved STM image of a domain boundary. (d) Constant height AFM image (Δf). (e) Height map extracted from an analysis of the atomic corrugation. (f) Voltage-dependent moiré contrast in STM images (3.7, 4.25, 4.9 V). (g) Registry of the N atoms of *h*BN to the Cu lattice (color-coded). (h) FER map (bottom panel) recorded along a line across the moiré superstructure (top panel). (i) B 1s (top panel) and N 1s (bottom panel) XPS signals. (j) dI/dV map of interface state below *h*BN island. Inset: Topographic STM image of the area. (k) Lateral map of the calculated electrostatic potential. (l) Work function variation as a function of the moiré wavelength. (m) Bright field LEEM image of *h*BN islands on Cu(110). (a,f,j) Adapted with permission from Ref. [284] © (2012) American Chemical Society, (b) Adapted with permission from Ref. [288] © (2017) American Chemical Society, (c) Adapted with permission from Ref. [290] © (2015) American Chemical Society, (d,e,i) Adapted with permission from Ref. [287] © (2017) American Chemical Society, (g,k) Adapted with permission from Ref. [399] © (2013) Royal Society of Chemistry, (h) Adapted with permission from Ref. [398] © (2014) American Chemical Society. (l) Adapted with permission from Ref. [289] © (2018) American Chemical Society. (m) Adapted with permission from Ref. [291] © (2018) Elsevier. (For interpretation of the references to color in this figure legend, the reader is referred to the Web version of this article.)

this electronic superstructure (Fig. 8 (g)), with a topographically rather flat overlayer structure [284,399]. An STM study by Hwang et al. confirmed the appearance of moiré patterns and reports a temperature window from 1020 to 1100 K for good quality *h*BN growth via regular CVD - similar to the values reported above. Interestingly, the growth temperature can be lowered by about 100 K by ionizing and/or exciting the borazine precursor gas with an electron beam [285].

Aiming for the fabrication and characterization of grain boundaries (GB) in *h*BN/Cu(111), Li et al. chose a two-step growth method with low-temperature precursor adsorption (typically 600 K) yielding a high nucleation density followed by prolonged annealing (1000 K, up to 6 h). Hereby, an Ostwald ripening of *h*BN grains was observed. Atomically resolved STM images of the *h*BN lattices across different grain boundaries directly yielded the tilt angles between adjacent domains and allowed to propose structural models for distinct grain boundaries, including square-octagon pairs (4|8 GB) and pentagon-heptagon pairs (5|7 GB) (Figs. 8 (c) and Fig. 9 (h,i)) [290]. While STS measurements on regular *h*BN patches yielded a band gap of ≈5 eV, which is reduced to ≈4.3 eV at 4|8 GB, 5|7 GB feature distinct in-gap peaks and thus demonstrate how GB can be used to tailor the electronic properties of *h*BN/Cu(111). Based on a comparison of the experimental dI/dV spectra with the DFT-calculated LDOS, distinct types of grain boundaries could be assigned [290].

A recent study by Hwang et al. used a submonolayer *h*BN/Cu(111) as a template for graphene growth, yielding distinct surface areas representing *h*BN/Cu(111), graphene/Cu(111) and graphene/*h*BN/Cu(111), respectively [286]. An upshift of ≈0.2 eV for the interface state in *h*BN/Cu(111) - about twice the value reported in Ref. [284] - was related to a charge transfer from Cu to *h*BN and a band gap of ≈4 eV was extracted from the STS data [286]. On the other hand, a (moiré-pattern dependent) band gap of ≈6.65 eV was proposed by Zhang et al. based on STS data [289]. These examples show the difficulties of a quantitative band gap determination in *h*BN/metal systems by STS.

Feigelson et al. used grazing-incidence infrared reflection absorption spectroscopy (IRRAS) to characterize vibrational modes in *h*BN/Cu(111) in direct comparison to other Cu supports [400]. The position of one of the two observed A_{2u}(LO) phonon peaks - characteristic for the *h*BN/metal interaction - indicated an interaction

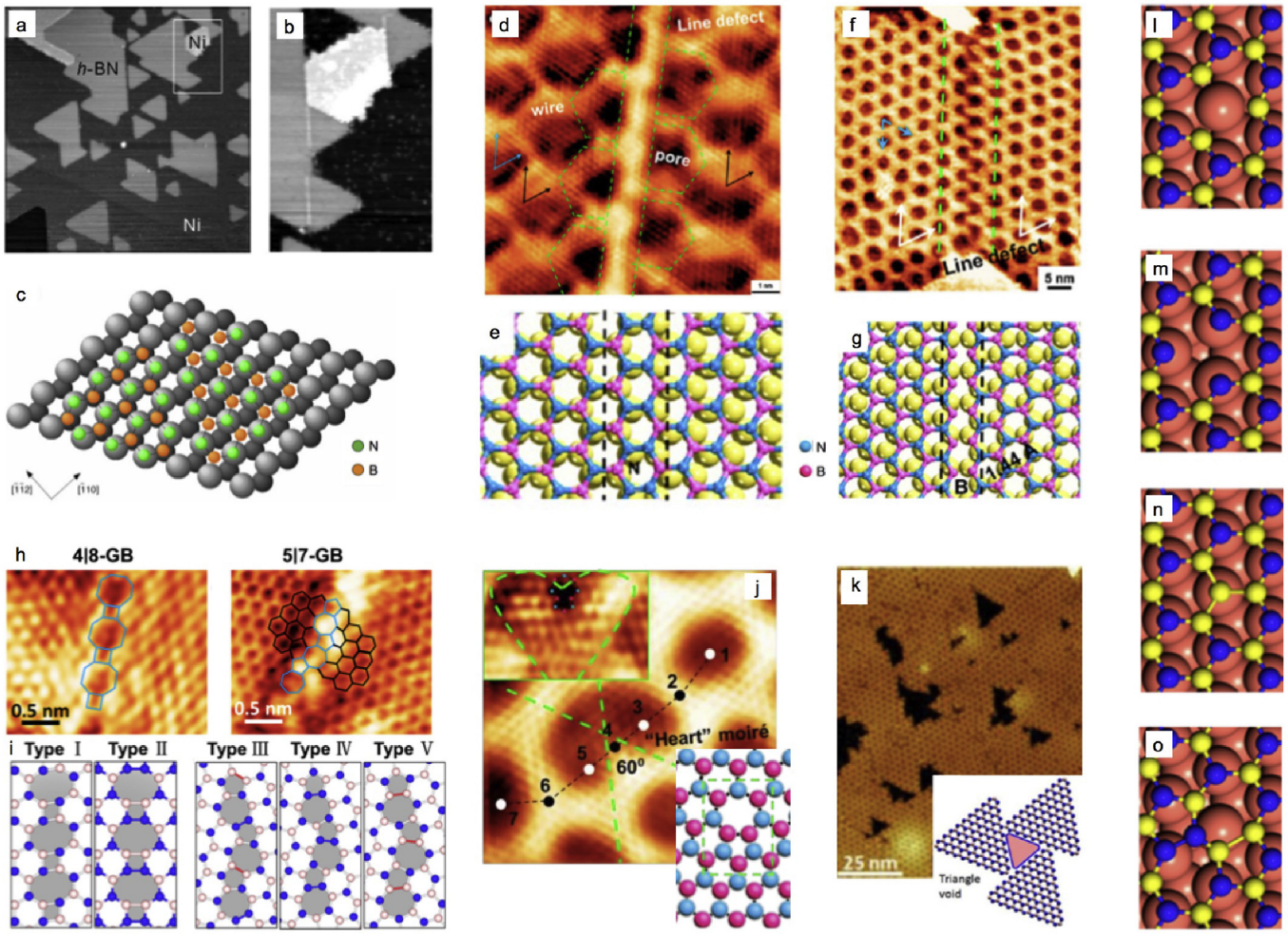

Fig. 9. Characteristic defects in *h*BN monolayers on metal single crystals. (a–c) Defect lines between two *h*BN domains on Ni(111). (a) Overview STM image. (b) Zoom-in and (c) structural model. (d–g) Defect lines between *h*BN domains on Re(0001). STM image of bonding patching defect (d) with DFT model (e) and STM image of non-bonding patching defect (f) with DFT model (g). (h,i) Aligned defects in *h*BN/Cu(111). (h) STM image of 8|4 and 7|5 grain boundaries and possible structural models (i). (j) Heart-shaped distortion in the moiré pattern of *h*BN/Re(0001) related to a 7|5 defect. (k) Triangular voids in *h*BN/Ru(0001) with scheme (inset). (l–o) DFT modeling of local defects in *h*BN/Cu(111). (l) N vacancy, (m) B vacancy, (n) Boron impurity, (o) Stone-Wales-type defect. (a–c) Adapted with permission from Ref. [261] © (2003) Elsevier, (d-g, j) Adapted with permission from Ref. [219] © (2017) American Chemical Society, (h,i) Adapted with permission from Ref. [290] © (2015) American Chemical Society, (k) Adapted with permission from Ref. [222] © (2013) American Chemical Society, (l–o) Adapted with permission from Ref. [361] © (2016) American Chemical Society.

exceeding the one on (110) and (100) Cu facets. Furthermore, an absence of a blue shift in this phonon band upon exposing *h*BN/Cu(111) to air for 3 months indicated that Cu oxidation was prevented, in contrast to the other *h*BN/Cu systems explored [400].

A recent x-ray standing wave (XSW) study by Schwarz et al. determined a mean adsorption height of 3.38 ± 0.06 Å for *h*BN/Cu(111). This value, close to the bulk *h*BN interlayer separation, confirms a weak coupling of the sp^2 sheet to the Cu(111) support [287]. A sophisticated non-contact AFM height distribution analysis based on the atomic contrast of *h*BN yielded a geometric corrugation of several tens of picometer across distinct moiré superstructures in the *h*BN, consistent with the coherent fraction extracted from the XSW data (0.65 and 0.71 for B and N, respectively) [287] (Fig. 8 (d,e)). This classifies *h*BN/Cu(111) as an electronically and topographically corrugated interface, where the latter finding was not recognized by the previous studies. Intriguingly, a combined XSW and SPA-LEED study by Brülke et al. published in the same month provides different findings. The XSW analysis yields a mean adsorption height of 3.24 ± 0.03 Å and a significant corrugation related to the moiré pattern (exceeding a buckling amplitude of 5 pm) is excluded from the SPA-LEED analysis [288]. Furthermore, the coherent fraction reported in the latter report, representing static or dynamic disorder, is distinctly different for the B and the N species (0.57 and 0.8, respectively) [288]. Thus, while both XSW studies agree on a large vertical separation of *h*BN from Cu(111), no consensus is reached about the corrugation, the exact mean adsorption height and the differences between B and N contributions. Subtle differences in sample preparation and properties, e.g., reflected in the domain composition of *h*BN/Cu(111), might be a source of these discrepancies - thus leaving room for further experimental studies. Indeed the possible coexistence of *h*BN domains nearly aligned with the Cu lattice and rotated by about 30° is recognized by both studies [287,288] (see Fig. 8 (b)).

Systematic DFT modeling summarized in the work of Schwarz et al. showed how calculated mean adsorption heights, local work functions, and geometric corrugations sensitively depend on the choice of the functional [287]. Indeed, several studies employing different levels of theory and/or different system sizes to describe *h*BN/Cu(111) yielded adsorption heights ranging from 2.65 to 3.33 Å [187,188,289,361,383,399–404].

Siegel et al. introduced a heterogeneous pyrolysis approach to grow not only a single ML of *h*BN on Cu(111), but also bi-, and trilayers [296]. Hereby, the *h*BN sheets are in registry with each

other and TEM evidences a parallel alignment. The growth mode was rationalized by DFT and MD simulations, confirming a reduction of the second layer growth rate compare to the first one by about two orders of magnitude. AFM images reveal an apparent corrugation reflecting moiré superstructures with periodicities from 8 to 12.5 nm for the first layer, which is absent in the second layer. These data - recorded in air - indicate a considerable stability of the interface. Assuming a planar geometry of *h*BN/Cu(111), the AFM contrast was rationalized by electrostatic effects emerging from laterally modulated interfacial dipoles, as calculated by DFT [296].

In summary, *h*BN/Cu(111) represents an electronically superstructured interface with a small geometric corrugation, despite the rather weak *h*BN - Cu interaction.

Cu(110). Herrmann et al. followed the *h*BN sub-monolayer growth on Cu(110) by LEEM (Fig. 8 (m)) [291]. Importantly, *h*BN synthesis was only achieved after inducing a Cu reconstruction by annealing in H_2. Following the nucleation of triangular *h*BN islands, merged stripe and star-like flakes formed, featuring an epitaxial match between *h*BN and Cu as inferred from LEED [291].

2.2.13. Silver(111), (100)

Ag(111). The first experimental study of *h*BN growth via CVD on silver dates back to 2010 and was performed by Müller et al. As naively expected, the study revealed a very low sticking coefficient of *h*BN precursors calling for high dose to grow a *h*BN monolayer on Ag(111). The weak interaction between Ag(111) and *h*BN, anticipated from early DFT investigations [187], is furthermore reflected in coexisting, azimuthally arbitrary orientated rotational *h*BN domains, resulting in a continuous, ring-like feature in LEED images. This ring is separated by about 15% from the first-order spots from Ag(111), matching the lattice misfit between silver and unstrained *h*BN. The XPS binding energies of the B 1s and N 1s core levels are 190.8 and 398.3 eV, respectively [292].

A recent study by Garnica et al. applied ion-gun assisted CVD to grow *h*BN sub-monolayers on Ag(111) and characterized the interface structure by low-temperature STM. The *h*BN reduces the work function by ≈ 0.35 eV and upshifts the Ag(111) surface state by 119 meV, indicating a moderate *h*BN-Ag interaction as confirmed by DFT modeling [293]. Even if the *h*BN atomic lattice could be resolved and moiré superstructures were visualized, this procedure did not prove suitable to synthesize high quality *h*BN monolayers and Ag intercalation was chosen as an alternative approach (vide supra) [293].

Ag(100). The growth of *h*BN/Ag(100) was explored by Müller et al. employing XPS and LEED. Again, a homogeneous ring reveals the absence of preferred *h*BN orientations and the XPS binding energies (B 1s: 190.8 eV, N 1s: 398.4 eV) are consistent with the *h*BN/Ag(111) case, evidencing that the surface symmetry of Ag has no distinct influence on the *h*BN overlayer structure [294].

2.2.14. Gold(111)

In contrast to Ag(111), *h*BN growth on Au(111) (performed via reactive magnetron sputtering) resulted in two distinct azimuthal orientations of *h*BN flakes. STM data showed a preference for triangular shaped islands rotated by 60° relative to each other. Besides additional *h*BN shapes like “butterflies” or six-apex stars, the growth of second- and third-layer *h*BN islands was observed - before completion of the first layer. The formation of well-defined *h*BN islands featuring a specific orientation relative to the Au(111) lattice was tentatively attributed to strong interactions between the *h*BN island edges and the Au support - locking the *h*BN nuclei into a geometry where the dangling bonds of edge atoms efficiently interact with Au atoms, thus resulting in *h*BN edges aligned with dense-packed Au(111) directions upon further growth [295].

2.2.15. Alloys and other supports

Stania et al. explored the interface structure of *h*BN on a PtRh(111) intermetallic compound by a multi-method experimental approach including XPS, XPD, SXRD, LEED and STM [405]. As evidenced by SXRD, *h*BN forms an 11-on-10 nanomesh structure similar to the Rh(111) case, but with a smaller lattice constant (2.73 nm). Interestingly, upon *h*BN formation, the interfacial layer gets enriched with Rh, while the second layer is depleted from Rh. This interaction with *h*BN imposes a lateral surface segregation profile: The pore regions of the nanomesh structure are bound to Rh patches, while the wire regions occur on Pt regions [405]. Gubó et al. studied the growth of *h*BN on Au/Rh surface alloys by XPS, STM, low energy ion scattering (LEIS), and DFT, covering different Au contents (0–1.5 ML) [243]. The nanomesh structure is observed up to large Au amounts (0.9 ML) featuring its intrinsic periodicity, but the pore diameter is decreasing while the number of defects increases with increasing amount of Au. At higher Au content, flat and corrugated *h*BN areas coexist, indicating that pure and bimetallic regions occur below the *h*BN sheet [243]. Large single crystal *h*BN grains on a Cu—Ni alloy foil were reported by Lu et al. [406,407]. Here, the engineering of the alloy support, i.e., the choice of the Cu:Ni ratio, helped to minimize the *h*BN nucleation density and thus to increase the average grain size to up to 7500 μm^2 [406]. The potential of alloys as substrate for 2D materials was furthermore demonstrated by Ni_xPd_{1-x}(111) films featuring a tunable lattice constant [408].

Even if not in the focus of this review, we briefly mention recent efforts to extend *h*BN monolayer growth to non-metallic supports. For example, a *h*BN layer was grown by CVD on the wide-band gap semiconductor SiC(0001) by Shin et al. [409]. The epitaxial growth of highly aligned, large area *h*BN monolayers on Ge(100) and Ge(110) surfaces by LPCVD was reported by Yin et al. [410]. On Ge(110) only two - coorientated and antiorientated - *h*BN domains were observed, whereas Ge(100) supports four domains [410]. In experiments aiming for the coating of SiBNC fibers, Ye et al. explored the CVD synthesis of *h*BN on Si(100) using borazine and ammonia [411]. The wafer-scale, multilayer *h*BN growth on sapphire by LPCVD was recently demonstrated by Jang et al., who successfully applied the *h*BN film as an insulating substrate for a graphene FET [412]. Li et al. used metal-organic vapor phase epitaxy for *h*BN synthesis on 2-inch sapphire wafers, reporting a strong absorption at the bandgap of 5.87 eV and near-bandgap light emission at 5.73 eV, corroborating *h*BN's potential use in deep UV devices [413]. Furthermore, high-temperature MBE was employed for *h*BN growth on sapphire and HOPG, with the latter support being beneficial for deep UV emission [203]. *h*BN prepared by plasma-assisted MBE on HOPG revealed moiré-modulated conductance when probed by conductive AFM [414]. Asides HOPG, also graphene (supported on Co foils) served as substrate for plasma-assisted MBE growth of few-layer *h*BN films (e.g., Ref. [415]).

2.3. Defects

Asides the properties of ideal *h*BN/metal interfaces discussed above, defects in the sp^2 sheet can play a relevant role for the interaction with adsorbates. On the one hand, imperfections in real systems might hamper the performance of *h*BN sheets as templates. On the other hand, deliberate modifications of the *h*BN lattice open pathways to engineer the properties of *h*BN/metal supports, beyond the choice of the metal substrate. Both effects will be briefly touched in section 3.1.

Within the experimental characterization of *h*BN/single crystal interfaces summarized above, mainly defect lines at domain boundaries were discussed. These include bonding and non-bonding patching defects in *h*BN/Ni(111) [261] (Fig. 9(a–c)), *h*BN/Ru(0001) [222], and *h*BN/Re(0001) [219] (Fig. 9(d–g)) or aligned 8|4 and 7|5 defects

in continuous *h*BN sheets on Cu(111) [290] (Fig. 9(h and i)). In addition, characteristic "heart-shaped" distortions of the *h*BN moiré on Re(0001) were assigned to 7|5 pair-like defects [219] (Fig. 9(j)), which were identified previously in *h*BN/Ru(0001) near lateral interfaces to graphene [416]. Triangular voids remaining upon merging of *h*BN islands were reported for example on Ru(0001) [222] and Cu(111) [314] (Fig. 9(k)), especially on samples featuring a high nucleation density. Such openings in *h*BN films might persist also at high precursor dose [222]. Atomic-scale protrusions were detected centered on the wire-regions of *h*BN/Ir(111) by STM and tentatively assigned to point defects (e.g., N vacancies) in the *h*BN sheet [190].

Furthermore, a multitude of theoretical studies focused on point-like defects in *h*BN monolayers, covering single atom vacancies (B or N), divacancies, Stone-Wales-like defects, homonuclear bonds (B—B, N—N) or substitutional heteroatoms (e.g., Refs. [249,361,417–425,425–433]) (Fig. 9(l–o)). These modeling efforts - and scarce experimental endeavors - highlight the pivotal role of such structural modifications for the engineering of electronic, magnetic, and catalytic *h*BN properties, as briefly discussed in sections 3.1 and 3.2. Additionally, modeling of distinct grain boundaries in *h*BN on Ni(111) and Cu(111) - featuring continuous rows of repeating 5–7 ring pairs - highlighted the impact of such extended defect structures on the electronic and topographic interface structures [434].

From an experimental perspective, local defects can be created site-selectively by ion bombardment of surface-supported *h*BN nanomeshes (see section 3.1) or in free-standing sheets by a high-energy electron beam (e.g., Ref. [435]). HRTEM imaging of isolated *h*BN sheets gave direct access to the atomic structure of defects within regular domains or at grain boundaries (e.g., Refs. [435–439]). Alternatively, etching processes can yield well defined openings in surface-supported *h*BN films (e.g., Refs. [385,393], see section 3.2).

A distinct type of "defect", namely atomically-defined lateral interfaces between *h*BN monolayers and graphene on single crystals (e.g., Refs. [218,249,273,322,416,421,440–443]) is omitted here. Recent reviews summarize the synthesis and properties of such sp^2 heterostructures [444–447]. However, the outlook (see chapter 4) will allude to the relevance of such well-defined in-plane heterostructures and BNC networks (e.g., Refs. [224,423,448–450]). Also for free-standing *h*BN graphene hybrid systems, theoretical studies addressed defects, such as nanopores (e.g., Ref. [451]).

A quantification of defects in CVD grown *h*BN monolayers - albeit being of high importance in view of potential applications - is rarely provided in literature. As an exception, Mertens et al. applied copper underpotential deposition to quantify defects in *h*BN/Rh(111), reporting an upper limit for total defective areas of 0.7% of the geometric sample area and suggesting a primary defect area as low as 0.08% [452]. Furthermore, Gubó et al. used LEIS to determine an upper limit for uncovered metal areas after *h*BN formation on Rh(111), amounting to 0.0005 ML of Rh [243].

For completeness, it should be noted that the energetics, shapes, and edge-structures of free-standing *h*BN flakes were addressed theoretically, e.g., revealing a preference for N-terminated zig-zag edges [453,454], thus providing some hints for the interpretation of experimental data on sub-ML *h*BN islands.

2.4. Comparison and discussion

This section provides a discussion and comparative assessment of *h*BN/metal systems - based on the information collected in the previous paragraphs. Specifically, the following aspects are considered: Categories of *h*BN/metal systems, distinction from graphene, superstructures, homogeneity, XPS signatures, and work function.

Categories of hBN/metal systems. In the following, we attempt to classify the *h*BN/metal interfaces regarding their interactions strength, in analogy to categories of graphene/metal interfaces introduced by Batzill [455]. Weakly interacting systems (colored yellow in Fig. 10) are defined by a large average *h*BN-metal separation comparable to the *h*BN bulk interlayer spacing of 3.33 Å (see Table 1) and/or the persistence of the electronic surface state of the supporting metal. Strongly interacting systems (colored red in Fig. 10) are defined by one or more of the following characteristics: (i) the smallest *h*BN-metal separation is around 2.2 Å, (ii) formation of a single domain structure in CVD growth, (iii) appearance of a nanomesh structure, *i.e.*, emergence of a superstructure with a corrugation typically exceeding 1 Å. This assessment summarized in Fig. 10 bears pronounced similarities to the graphene case - despite the significant difference in the electronic structure of *h*BN (insulator) and graphene (conductor). *h*BN interacts strongly with nearly lattice matched Co and Ni(111) surfaces, forms corrugated, nanomesh-like structures on Re(0001), Ru(0001), Rh(111), Ir(111), and shows weak adsorption on Cu(111) and Ag(111). While a fully reliable comparison between the different systems is hampered by the considerable scatter in experimentally and theoretically determined adsorption distances and corrugation values, two trends are clearly discernible from the information reviewed in this chapter. First, the *h*BN/metal interaction increases from Pt(111) via Ir(111), Rh(111) to Ru(0001) and Re(0001) [88,218]. Second, the heavily corrugated superstructures emerge in lattice mismatched systems with strong *local* *h*BN/metal interactions, which depend on the position of the B and N atoms relative to the outermost metal atoms (see introductory paragraph of this chapter) [192]. Throughout the ((111)-terminated) systems discussed, the strongly interacting regions within the superstructure, featuring the smallest *h*BN-metal separation are typically assigned to approximate $B_{hollow}N_{top}$ registries, constituting the specific pore areas. As in the case of graphene/metal interfaces [455], the *h*BN-metal distance in the areas of strong interaction (1.9–2.2 Å) is similar to the separation in the commensurate *h*BN/Ni(111) case. In the complementary "non-bonding" areas and registries in the superstructure, the *h*BN adsorption heights (3.1–3.7 Å) can locally exceed the bulk interlayer spacing. These findings are corroborated and rationalized by DFT modeling including dispersion corrections, where recent reviews and articles provide a systematic screening of properties of *h*BN/metal interfaces (e.g., Refs. [188,403]), complementing earlier methodic achievements [187,456]. Among these contributions, the study by Bokdam et al. also characterizes *h*BN/Ti(0001) and *h*BN/Al(111) interfaces that were - to this author's knowledge - never explored experimentally [188]. While *h*BN is predicted to be chemisorbed on Ti(0001) at a distance of 2.17 Å with a work function of only 3.65 eV, *h*BN physisorbs on Al(111) featuring an adsorption distance and work function of 3.55 Å and 3.84 eV, respectively [188].

Interestingly, the different interaction strengths between *h*BN and the elements summarized in Fig. 10 open up pathways to nanostructure multi-component metals by the *h*BN overlayer, using the *h*BN to template its support via segregation [405].

Distinction from graphene. Despite some striking similarities to graphene/metal interfaces (e.g., Refs. [186,455,457–459]), the binary elemental nature of *h*BN introduces distinct differences compared to its carbon relative. Importantly - in view of the templating properties - *h*BN nanomesh structures typically present an inverted topography. For example, in graphene on Ru(0001) both $C_{fcc}C_{top}$ and $C_{top}C_{hcp}$ registries lead to strong interaction with the metal, while *h*BN is strongly interacting only for $B_{fcc}N_{top}$ [89] (see Fig. 11). A similar inverted topography, namely an array of depressions (pores, holes) in *h*BN versus protrusions (mounds, hills) in graphene, was recently also observed for the weakly bonded sp^2 sheets on Cu(111) and quantitatively assessed by non-contact AFM [287,460].

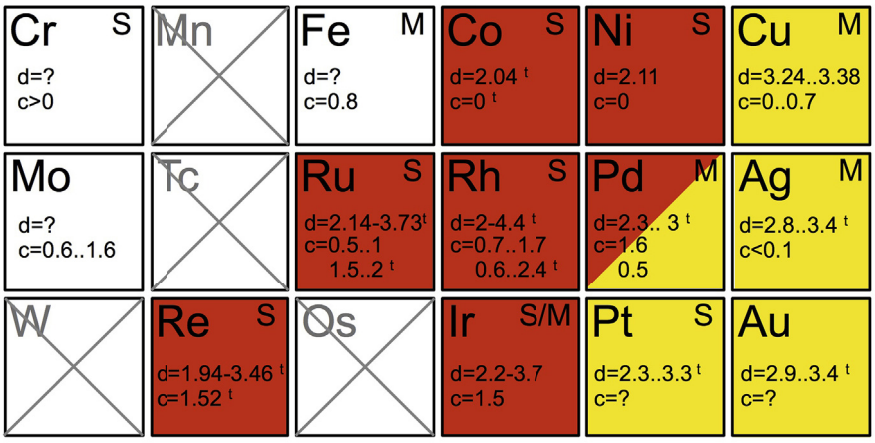

Cr	Cr(110) STM [191]
Fe	Fe(110) STM [220]
Co	DFT d: 2.03 Å [330], 2.05 Å [328]
Ni	PhD [269]
Cu	XSW d: 3.24 Å [288], 3.38 Å [287] , SPA-LEED c: $<$ 5 pm [288], AFM $\approx$ 50 pm [287]
Mo	c: STM (depending on tip condition) [217]
Ru	DFT d: average: 2.60 Å [224], 2.14 - 3.73 Å [225], STM c: 0.5 Å [226], 1 Å [224], DFT: 1.5 Å [224], 1.67 Å [225], 2 Å [89]
Rh	DFT d: 2-4.4 Å [337], 2.17-2.72 Å [333], 2.1-3.1 Å [338], STM c: 0.7 Å [233], 1.7 Å [442], DFT 1.24 Å [442], 2.4 Å [346]
Pd	DFT d: 2.25 Å [187], 2.47 Å [188], 3.0 Å [188], STM c: 1.6 Å [279], Pd(110) 0.5 Å [280]
Ag	DFT d: 2.78 Å [187], 3.2 Å [188], 3.37 Å [188], STM c [293]
Re	STM & DFT [218]
Ir	XSW [250]
Pt	DFT d: 2.30 Å [187], 3.04 Å [188], 3.27 Å [188]
Au	DFT d: 2.93 Å [187], 3.24 Å [188], 3.37 Å [188]

Fig. 10. Summary of the interaction of *h*BN monolayers and transition metals (in analogy to the graphene case presented in Fig. 5 in Ref. [455]). Elements in red are metals that interact strongly with *h*BN and elements in yellow are those that interact weakly. "S" or "M" indicates if *h*BN forms single or multiple rotational domains. "d" is the *h*BN-metal separation in Å, "c" the corrugation (and not the atomic buckling) as well in Å. "t" marks values obtained from DFT. ".." indicates a range of distinct values, which are listed in the table below, while "-" describes the continuous adsorption height variations in corrugated, nanomesh-like structures. For clarity, only representative values are selected (see table for details). If available, results from experiments sensitive to vertical interface structures are used (XSW, PhD). In other cases, experimental (STM - not providing true topographic information) and theoretical values are combined (highlighting values obtained by the most suitable calculation schemes). Thus, this schematic classification should be taken with a grain of salt. (For interpretation of the references to color in this figure legend, the reader is referred to the Web version of this article.)

The chemical composition of the sp^2 sheet (all C versus B and N) is also reflected in different superstructure periodicities of graphene and *h*BN on the same metal support. E.g., the graphene nanomesh on Rh(111) shows a smaller periodicity (2.90–2.96 nm) [461–463] compared to its *h*BN counterpart (3.2 nm, see paragraph 2.2.7), with the pore areas however matching quite well in both systems [463]. Also for Ir(111), the graphene superstructure features a smaller periodicity (2.46 nm [464]) than the *h*BN one (2.91 nm [250]). Moire periodicities exceeding 13 nm were occasionally observed for *h*BN/Cu(111) [284], whereas such large values were not reported for graphene/Cu(111) [465,466]. In addition, the dielectric character of *h*BN can induce more pronounced local work function variations than graphene for the same substrate (e.g., Ir(111) [247,467], Cu(111), and Rh(111) [339,468]). Furthermore, *h*BN interacts stronger with distinct supports than graphene. For example, (using borazine or ammonia borane as precursors), a single *h*BN domain orientation prevails on Pt(111) with a growth in the downhill direction over Pt steps dominating (i.e., "downhill growth"), while multiple domains and both downhill and uphill growth are reported for graphene on the same surface [283]. In view of its applicability as a structurally regular template, *h*BN might thus be favored over graphene on these specific substrates. However, it should be mentioned that also opposite situations are reported, e.g., in the weakly bound sp^2/Ag(111) systems. Here, graphene was found to interact stronger with its support than *h*BN, as reflected in charge transfer from Ag to graphene and more pronounced surface state upshifts [293]. In addition, graphene islands interact stronger with Ru(0001) than *h*BN islands, due to interactions of edge atoms with the metal [228].

Superstructures. Reverting to *h*BN/metal interfaces, this chapter revealed that depending on the choice of the *h*BN/substrate pair, a wealth of surface morphologies are achieved. As anticipated in Fig. 2, homogeneous, "flat" layers with a minor buckling between B and N atoms in a 1 × 1 commensurate structure are reported for the systems with small lattice mismatch ($\leq$1%) and considerable *h*BN-metal bonding, such as Co and Ni(111). Adopting a 30° rotation of the *h*BN on the substrate lattice could also bring systems featuring a considerable lattice mismatch in a 0° rotation to (near-)commensurabilty (e.g., Ag, Au, Al(111)) [188] and - based on theoretical modeling - thus could be considered as candidates for homogeneous overlayers. However, in the case of Au(111) edge effects fix *h*BN islands to a 0° rotation while the weak *h*BN - Ag interaction results in manifold rotational domains. With most systems being severely lattice-mismatched ($\geq$2%) and/or showing modest *h*BN-metal bonding, superstructured *h*BN/metal interfaces prevail, representing a continuously varying registry of B and N versus the outermost metal atoms. Hereby, with studies on fcc(111) and hcp(0001) surfaces being most abundant, 2D-nanostructures stand out. Only considering the apparent periodicity of the superstructure, values reported range from about 1 to 15 nm. Both these extreme values were observed on a Cu(111) support, providing coexisting moiré-like patterns serving as variable platform for local adsorption studies, similar to the case of Pd(111) featuring superstructure periodicities from 1.1 to 2.75 nm. Considering only systems where single domain

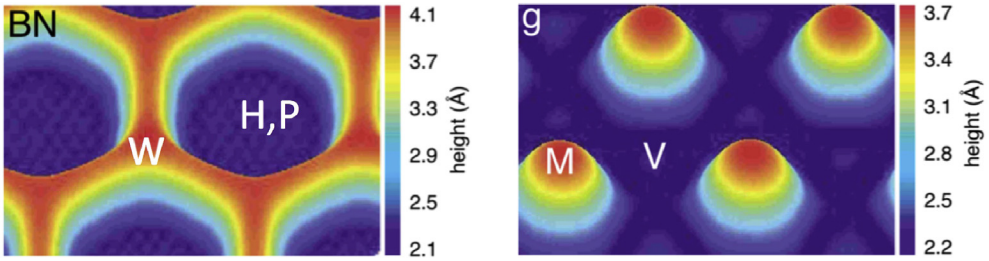

Fig. 11. Illustration of the inverted topography of *h*BN (left panel) and graphene (right panel) nanomesh structures on Ru(0001), obtained from DFT calculations. The *h*BN case is characterized by an array of holes (H) or pores (P) embedded in continuous wire regions (W), whereas the graphene case reveals an array of hills or mounds (M) embedded in continuous valley (V) regions. Adapted with permission from Ref. [89] © (2009) American Physical Society.

structures can be achieved, which are highly relevant as long-range ordered templates addressable by space-averaging techniques, the range of superstructure periodicities is considerably smaller, as summarized in the following series: 2.5 nm (Pt) - 2.91 nm (Ir) - 3 nm (Re) - 3.22 nm (Rh) - 3.5 nm (Ru). The overall trend expressed by these values (from large superstructure periodicities in Ru and Rh to small periodicities in Pt) relates reasonably well to the behavior expected from a superstructure model based on the lattice mismatch in the respective *h*BN/substrate pairs: A large lattice mismatch relates to small moiré periodicities (surface lattice constants: 2.775 Å (Pt) - 2.76 Å (Re) - 2.715 Å (Ir) - 2.70 Å (Ru) - 2.689 Å (Rh)). At the same time, the above series is reminiscent of the increasing interfacial interaction strength (see above) and the increasing *h*BN XPS binding energies (see below).

1D-nanostructured *h*BN/metal interfaces received less attention and were explored employing the (110) surfaces of Cr, Mo, Fe, Rh and Pd. The respective superstructure periodicities range from about 0.9 nm (Cr) to beyond 4 nm (Pd) with intermediate values of 1.26 nm (Mo), 1.3 nm (Rh), and 2.6 nm (Fe). While a real-space characterization of *h*BN/Cr(110) is lacking, Mo, Fe, and Pd reveal a coexistence of superstructures with different appearance in STM data, whereas Rh supports a unique superstructure. As the experimental and theoretical characterization of these systems is less developed than for the 2D-nanostructured cases, the following discussion will focus on the latter. Nevertheless, it should be noted that the very small apparent corrugation in *h*BN/Rh(110) (compared to *h*BN/Rh(111)) was assigned to the lack of periodically distributed regions with significant size featuring highly symmetric binding landscapes - highlighting that the "flatness" of *h*BN can sensitively depend on the crystallographic orientation of the substrate [244].

Apart from the periodicity of the superstructure, its corrugation - both in geometric and electronic terms - is highly relevant. While the "geometric corrugation" is intuitively understood as the maximum separation of BN units in the direction along the surface normal within a continuous *h*BN sheet, the term "electronic corrugation" is less used. It reflects an electronic superstructure, i.e., a periodic variation of the surface potential or the local work function (see Fig. 12). As such, it is experimentally mainly accessible by local probes, i.e., STS, KPFM, and the PAX method [341]. The geometric corrugation on the other hand can be addressed in a quantitative manner by XSW - at least if chemical components representing strongly and weakly bound areas are resolvable. While a recent study suggests the use of atomically resolved nc-AFM images to quantify minute height variation in *h*BN [287], corrugation values extracted from regular AFM and STM measurements are largely unreliable due to interference of electrostatic or mechanical interactions and the convolution with the sample electronic structure, respectively [235,287]. Accordingly, apparent corrugation inversions can occur, depending on the experimental conditions (e.g., Ref. [458]). DFT modeling on the other hand also struggles in providing precise, clear-cut information on the geometric corrugation, e.g., as the results depend on the applied functional - with the choice of the optimal functional potentially depending on the exact system characteristics (see Fig. 10). It also should be noted that XSW and DFT do not necessarily provide the same measure for the geometric corrugation. While DFT indeed yields the vertical separation between a B/N atom and the outermost metal atom, XSW determines the B/N separation from a mean metal reference plane following bulk periodicity [287,349]. Thus, in case of frequent (local) relaxation of the outermost metal layer, differences between XSW and DFT results are expected. Furthermore, XSW probes the systems at finite temperature, whereas DFT calculations are performed for 0 K [469]. To cut a long story short, for the reasons just outlined, a comprehensive characterization of both geometric and electronic structure is very rare, which unfortunately prevents a conclusive comparative assessment of *h*BN/metal systems. Nevertheless, two conclusion can be drawn from the information in this chapter. First, all 2D-superstructured systems where height variations were quantitatively explored seem to indeed feature a geometric corrugation (see Fig. 10 for values), even if the *h*BN/Cu(111) case is still disputed [287,288]. Second, the electronic corrugation in *h*BN/metal systems can be pronounced, with experimental values for local work function differences ranging from about 0.3 eV (*h*BN/Cu(111), *h*BN/Rh(111)) to about 0.5 eV (*h*BN/Ir(111)) (see Fig. 13(c)), which are reasonably well reflected by the DFT calculated electrostatic potential variation [287,338]. In these systems, the regions of lower local work function correspond to the supercell areas featuring stronger *h*BN - metal interaction and smaller adsorption distance [247,287] (see Fig. 12). The size of these pore areas depends strongly on the *h*BN/metal interface, showing more pronounced variations than the corresponding superstructure periodicities (Pore diameters: *h*BN/Ir(111) $<$ 1.5 nm [349], *h*BN/Rh(111) $\approx$ 2.1 nm [337], *h*BN/Ru(0001) $\approx$ 2.34 nm [88], *h*BN/Cu(111) from $<$1 nm to $>$7 nm [284,287]).

As exemplified for *h*BN/Rh(111) and *h*BN/Ir(111), the electronic corrugation induces considerable lateral electric fields and so-called dipole-rings, which are relevant for the templating functionality of these interfaces. The comparable electronic corrugation in geometrically clearly distinct systems (e.g., *h*BN/Cu(111) versus *h*BN/Rh(111)) shows that the correlation between local work function variations and geometric corrugation might not be obvious, at least when considering absolute numbers of these quantities. Nevertheless, it should be noted that such geometric and electronic corrugations can induce a chemical corrugation of *h*BN/metal, e.g., a site-selective reactivity. This phenomenon is reminiscent of the influence of local electric fields (arising form surface potential differences) on the electronic structure and stability of CO chemisorbed on metals, which was described by Gumhalter et al. introducing the concept of a "lateral surface Stark effect" [470].

Furthermore, B—N bond length variations between strongly- and weakly-interacting areas in nanomesh-like structures were reported. For example, a stretched bond length (up to 1.48 Å, exceeding the equilibrium B—N distance by about 2%) was calculated for the pores

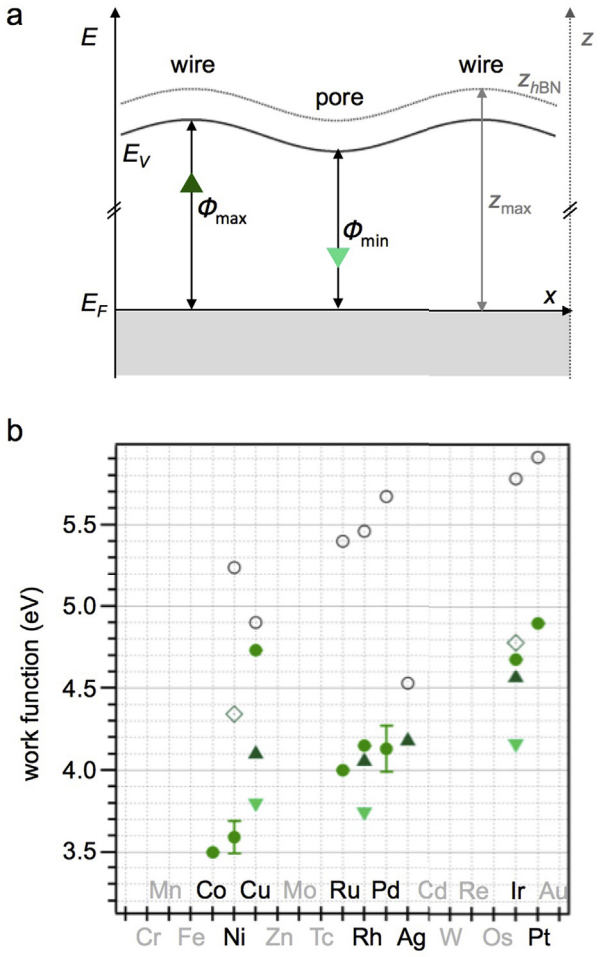

Fig. 12. (a) Schematic illustration of electronic and geometric corrugation in a superstructured *h*BN/metal interface. The electronic corrugation is represented by a modulation of the local work function (ϕ, E_V, solid line; left ordinate). The geometric corrugation is given by a variation of the adsorption height (z_{hBN}, dotted line; right ordinate). The abscissa represents the distance (x) along a line in a horizontal plane. In typical systems such as *h*BN/Rh(111), *h*BN/Ir(111), and *h*BN/Cu(111), the areas of lower local work function (ϕ_{min}) correspond to the supercell regions with smaller adsorption distance, i.e., the "pore" regions. (b) Compilation of (local) work function values ϕ for distinct *h*BN/metal interfaces. See respective paragraphs for references. The graph includes reference values for selected bare metal surfaces (black open circles [473]), space-averaging values (filled circles), and spatially-resolved values (triangles). In electronically corrugated systems, the dark up-pointing triangles represent the higher local work function, whereas the brighter, down-pointing triangles indicate the lower local work function (compare triangles in (a) and color-scheme in Fig. 13. The open squares for Ni and Ir reflect island types with different epitaxy. Asides the value for *h*BN/Co, the graph bases on experimental data. Note that relative local work functions were converted to absolute ones by reference to the bare metal surface or by matching the mean calculated value (in the case of Rh(111) [338]). Thus, the absolute numbers should be taken with care. The error bars added for selected elements indicate the range of reported values. (For interpretation of the references to color in this figure legend, the reader is referred to the Web version of this article.)

of *h*BN/Rh(111) [337]. With strain predicted to sensitively affect the band gap of free-standing *h*BN [471,472], also subtle B—N bond length changes might contribute to electronic structure variations in corrugated *h*BN/metal interfaces.

Homogeneity. Beyond a suitable superstructure periodicity and corrugation, a high structural quality and homogeneity, e.g., a single domain orientation with low defect density, is beneficial for the use of *h*BN/metal interfaces as templates. Also in this respect, the choice of the substrate and the preparation conditions can be relevant. For example, an early comparative study of *h*BN on Rh(111) and Ru(0001) reported a reduced structural regularity with frequent distortions for the *h*BN nanomesh on Ru(0001) [226]. The *h*BN nanomesh only overgrows step edges on Rh, an observation rationalized by the 60° rotation of the surface unit cell of neighboring terraces on hcp-like Ru(0001), which is absent in fcc-like Rh(111) [226]. Structural defects obviously can influence the templating quality of *h*BN/Ru(0001), e.g., facilitating intercalation processes [228]. Thus, it is important to note that high quality nanomesh structures with a perfect azimuthal *h*BN alignment were later also achieved on Ru(0001) [221,225]. Aiming for large, regular *h*BN domain sizes, also foils - despite their structural quality being inherently inferior to single crystals - can offer interesting perspectives. For example, *h*BN growth on molten foils - an approach rather avoided with expensive single crystals - can drastically reduce the *h*BN nucleation density and thus increase the domain size [391]. Besides the role of the substrate element, this chapter also revealed the potential impact of sample preparation procedures for the *h*BN overlayer perfection. As reported for Ni(111), Cu(111), and Ir(111) substrates, two *h*BN islands types can coexist on the very same support, featuring distinctly different work functions and adsorption heights [252,277,474]. At least for the Ni case, the emergence of such "physisorbed" areas in addition to the regular "chemisorbed" *h*BN regions was related to a relatively low sample temperature during CVD growth. Due to their distinct interfacial structures, such coexisting *h*BN patches induce an inhomogeneity beyond the coexistence of rotational domains with similar properties that might be induced by minute amounts of surface contaminants [261]. On the other hand, the control over both "chemisorbed" and "physisorbed" *h*BN areas opens fascinating routes to engineer *h*BN/metal interfaces and to synthesize multilayer structures [277].

XPS signatures and work function. As a last endeavor in this comparative section, we address the B 1s and N 1s XPS binding energies and work function values ϕ of selected *h*BN/metal interfaces (see Figs. 13 and 12(b)). The *h*BN-related core-level spectra contain two levels of information. First, the BE of the B 1s and N 1s signature reflects the interaction of *h*BN with its environment. Second, the shape of these spectral features allows for conclusions about the homogeneity of the *h*BN/metal interface. For example, the coexistence of strongly- and weakly-bound *h*BN areas in nanomesh-like structures is reflected in a high- and low-BE component in the core levels, whereas a homogeneous *h*BN layer is described by a single component. Accordingly, a high BE reflects a strong *h*BN interaction with its support. One however should be aware that this assignment bases on three assumptions: All B and N related XPS signatures emerge from a chemically intact, i.e., sp^2 bonded *h*BN lattice (and for example not from individual B atoms or sp^3 coordinated fragments) [287], the peak shifts are related to interfacial charge redistribution, and the screening ability of the support is similar in all cases. For example, the relatively high binding energies reported for multilayer *h*BN or bulk-like *h*BN (Fig. 13) do not signal strong interaction of the individual *h*BN sheets with the adjacent layers, but rather the poor screening of the core holes by the dielectric *h*BN compared to the metal supports. Focusing only on the values for *h*BN/metal interfaces presented in Fig. 13, one realizes that a direct correlation or "translation" of BE values to *h*BN - metal interaction strength, even though often employed in literature, is not conclusive - and thus should be taken with care. For example, *h*BN/Ni(111) and *h*BN/Cu(111) reveal very similar XPS binding energies, despite representing most strongly and most weakly bound systems, whereas Ag and Au, both part of the latter class, show distinctly different binding energies (compare Fig. 10). Nevertheless, some trends are discernible. Following for example the low BE N 1s component through the (Ru - Rh - Ir - Pt) series, a decrease in BE is observed reflecting the above discussed tendency in interaction strength [88] - whereas Re

Table 4
Atomic species interacting with *h*BN/metal supports. Abbreviations: ann. = annealed, inter. = interaction, intercal. = intercalation, facil. = facilitated.

Element	Substrate	Temp.	Technique(s)	Comment	Refs.
H	*h*BN/Ni(111)	rt	XPS, NEXAFS	hydrogenation, intercal.	[189,271,275]
	*h*BN/Rh(111)	350 K	STM, TDS, XPS, UPS, DFT	intercal.	[308]
	*h*BN/Rh(111)	–	DFT	includes C-doped *h*BN	[503]
D	*h*BN/Ni(111)	–	PSID, NEXAFS	deuteration.	[272]
	*h*BN/Rh(111)	350 K	STM, TDS, XPS, UPS, DFT	intercal.	[308]
Li	*h*BN/Au/Ni(111)/W(110)	ann. to 673 K	STM, UPS, XPS, DFT	–	[475]
	*h*BN/Ni(111)	–	DFT	–	[504]
C	*h*BN/Cu(111)	–	DFT	–	[383]
	*h*BN multilayer/Co(0001)	800 K	XPS, TEM, LEED	–	[230]
	*h*BN/Ir(111)	400 K	STM	–	[190]
O	*h*BN/Ir(111)	rt	XPS, NEXAFS	–	[498]
	*h*BN/Ni(111)	–	DFT	–	[358,505]
	*h*BN/Cu(111)	–	DFT	–	[402,505,506]
	*h*BN/Rh(111)	–	DFT	includes C-doped *h*BN	[503]
Si	*h*BN/Pt(111)	rt	STM, DFT	sub-ML *h*BN, intercal.	[507]
Ar, Ar^+	*h*BN/Rh(111)	rt	STM, XPS, UPS, DFT	low-energy implantation	[497,508–510]
K	*h*BN/Au/Ni(111)/W(110)	ann. to 673 K	STM, UPS, XPS, DFT	intercal.	[475]
Sc	*h*BN/Ni(111)	–	DFT	–	[504]
Ti	*h*BN/Ni(111)	10 K	STM	inter. with H_2	[511]
	*h*BN/Ni(111)	–	DFT	–	[504]
	*h*BN/Rh(111)	10 K	STM	inter. with H_2	[511]
Mn	*h*BN/Rh(111)	10 K	STM	ring state	[512]
	*h*BN/Rh(111)	rt	STM	intercal. at 653 K	[513]
Fe	*h*BN/Rh(111)	10 K	STM	ring state	[512]
Co	*h*BN/Ni(111)	210–575 K	STM, XPS	intercal. at higher T	[305]
	*h*BN/Ni(111)	–	DFT		[504,514]
	*h*BN/Cu(111)	–	DFT		[514]
	*h*BN/Rh(111)	10 K	STM	ring state	[512]
	*h*BN/Rh(111)	rt, ann. to 723 K	STM, XPS, NEXAFS	O_2 facil. intercal. upon ann.	[310]
CoH_x	*h*BN/Rh(111)	20 K	STM, DFT	Co deposition	[515]
Ni	*h*BN/Ni(111)	–	DFT	–	[504]
	*h*BN/Rh(111)	rt	STM, TPD	inter. with CO	[516]
	*h*BN/Rh(111)	–	DFT	–	[517]
Cu	*h*BN/Ni(111)	–	DFT	–	[504]
	*h*BN/Rh(111)	–	DFT	–	[517]
Ge	*h*BN/Ni(111)	ann. to 450 K	XPS, NEXAFS, ARPES	intercal.	[306]
Br	*h*BN/Ni(111)	–	DFT	–	[518]
Rb^+	*h*BN/Rh(111)	rt	STM	implantation, 100 eV	[496]
Pd	*h*BN/Rh(111)	–	DFT	–	[517]
	*h*BN/Ru(0001)	rt - 1050 K	STM	–	[519]
Ag	*h*BN/Rh(111)	rt	STM, DFT	–	[517]
Xe	*h*BN/Rh(111)	5 K, ann. to 86 K	STM, ARPES, DFT, MD	–	[339,520]
Xe^+	*h*BN/Ir(111)	rt	STM, XPS, DFT	3 keV irradiation, implantation	[521]
Ir	*h*BN/Ir(111)	250–900 K	STM, DFT	intercal. at higher T	[190]
Pt	*h*BN/Rh(111)	rt	STM, DFT	–	[517]
Au	*h*BN/Ni(111)/W(110)	773 K	XPS, ARPES, NEXAFS, LEED	intercal.	[318]
	*h*BN/Ru(0001)	rt - 1050 K	STM, XPS, AES	intercal. at higher T	[226,522]
	*h*BN/Ru(0001)	–	DFT	–	[523]
	*h*BN/Rh(111)	rt, ann. up to 873 K	XPS, ARPES, NEXAFS	–	[524]
	*h*BN/Rh(111)	–	DFT	–	[525]
	*h*BN/Rh(111)	rt	STM, DFT	–	[517]
	*h*BN/Rh(111)	77 K, 115 K, rt, ann. to 600 K	STM, TPD, XPS, HREELS, DFT	inter. with CO	[346,526]
	*h*BN/Rh(111)	rt	STM, TPD	inter. with CO	[516]
	*h*BN/Rh(111)	rt - 1200 K	LEIS, XPS, STM	intercal. at higher T	[243]
	*h*BN/Ir(111)	300 K	STM	–	[190]
	*h*BN/Pt(111)	rt	XPS, ARPES, NEXAFS	–	[524]
Pb	*h*BN/Ni(111)	130–300 K	STM	–	[495]

Table 5
Metal clusters on *h*BN/metal supports. Abbreviations: ann. = annealed, inter. = interaction.

Element	Substrate	Temp.	Technique(s)	Comment	Refs.
Co	*h*BN/Rh(111)	ann. to rt	STM	Xe buffer layer	[499]
Pd_{19}	*h*BN/Rh(111)	rt, ann. to 700 K	STM, DFT	soft-landed	[502]
Sn	*h*BN/Rh(111)	ann. to rt	STM	Xe buffer layer	[501]
Au_n	*h*BN/Rh(111)	–	DFT	n = 2–4	[527]
Au_n	*h*BN/Rh(111)	–	DFT	n = 7,19,30,51	[346]
Au_{30}	*h*BN/Rh(111)	–	DFT	inter. with CO	[526]
Au_8	*h*BN/Au(111)	–	DFT	–	[528]
Pb	*h*BN/Rh(111)	ann. to rt	STM	Xe buffer layer	[500,501]

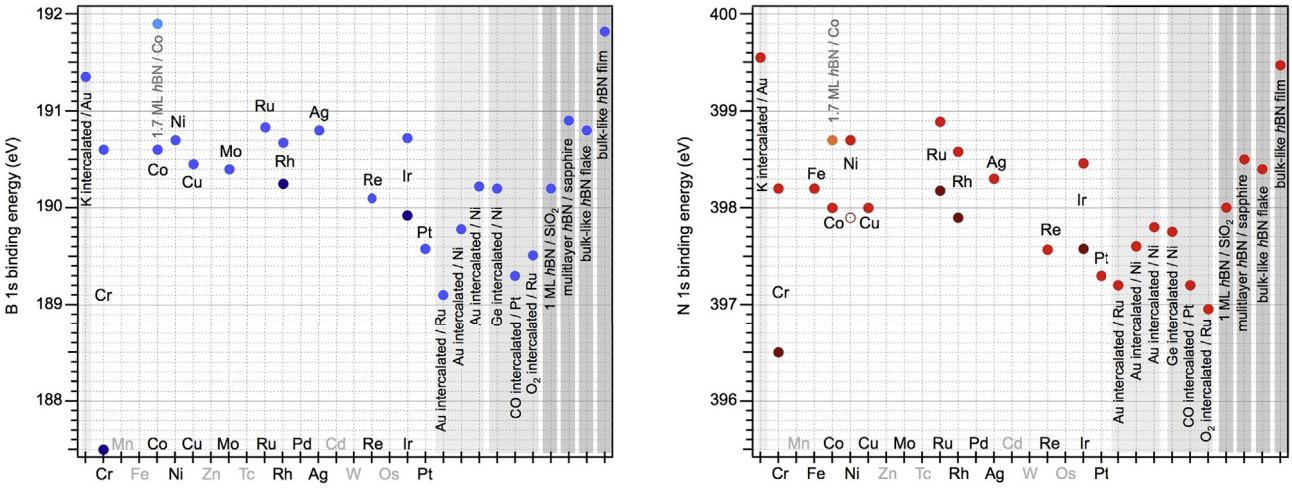

Fig. 13. Compilation of B 1s (left panel) and N 1s binding energies (right panel) for distinct *h*BN/metal interfaces. See respective paragraphs for references. Selected intercalated systems are included for comparison (see chapter 3, [228,283,306]), comprising Au films [276,318,321,475]. Values for a *h*BN ML on SiO_2 [395], a *h*BN multilayer on sapphire [412], a bulk-like *h*BN flake [476], and a thick bulk-like *h*BN film [263] are added as reference. In systems revealing a peak splitting due to strongly and weakly interacting *h*BN areas, the low BE component is colored darker (compare Fig. 12 (b)).

breaks ranks. In summary, only limited conclusions about the interfacial interaction can be drawn based on absolute binding energies. While the peak splitting in systems where two components are identified in the XPS analysis can indicate a corrugated *h*BN structure featuring strongly and weakly bound areas, the precise relation of peak splitting and geometric corrugation remains elusive [287]. Nevertheless, based on the intensity ratio of the two components, the ratio between the two areas (i.e., pore and wire regions) can be estimated [88].

The work function ϕ of surfaces can influence the electronic level alignment and charge state of adsorbates [477] and thus is of relevance for the *h*BN's templating functionality (e.g., see paragraph 3.3.7). In addition, work function changes ($\Delta\phi$) occurring upon *h*BN termination of the metal support reflect interfacial charge redistribution processes and accordingly are of interest as such. The compilation of (local) work functions for selected *h*BN/metal systems in Fig. 12(b) reveals three findings. First, *h*BN reduces the work function compared to the bare metal surface considerably. Second, by selecting an appropriate *h*BN/metal pair, the work function can be tuned from roughly 3.5 to about 5 eV. Third, some discrepancies occur between work function measurements based on space-averaging methods and local probe estimations, with the latter usually providing lower values (for both the wire and pore position). While this last observation relates to methodological issues, the first two represent interfacial properties. The work function reduction is related to the formation of an interfacial dipole, which - depending on the interaction strength between *h*BN and the metal - can be dictated by the exchange repulsion between electrons in *h*BN and the metal ("push-back" or "pillow" effect) analogous to the situation for noble gas adlayers, or be ascribed to interfacial charge redistributions upon hybridization, mimicking electron transfer from *h*BN to the metal [188,247,265,287,293,350]. Larger work function changes thus signal stronger interaction. Indeed, DFT modeling of a series of *h*BN/metal interfaces on the optB88-vdW-DF level reveals a work function reduction with decreasing *h*BN adsorption height [188]. Accordingly, Fig. 12(b) shows for example a larger work function reduction in the strongly bond *h*BN/Ni(111) system compared to the weakly bond *h*BN/Pt(111) system, irrespective of the relevant differences in work function of the two bare metal surfaces.

3. Adsorption on hexagonal boron nitride/metal

The application of the manifold *h*BN/metal structures discussed in section 2.2 as templates for adsorbates opened up exciting opportunities not available on conventional surfaces as metal single crystals, bulk insulators or semiconductors. The following features highlight key advantages of *h*BN templates in surface and nanoscience addressed over the last two decades both in experimental studies and theoretical endeavors:

- As highlighted in section 2.4, nanostructures of distinct symmetries and periodicities are achievable by a deliberate choice of the *h*BN/substrate pair. This modulation - featuring periodicities from 1 to 15 nm - might be of topographic, chemical or electronic origin and can induce site-selective adsorption, gating, and charging.

- *h*BN spacer layers considerably reduce the electronic "disturbance" of adsorbates, but enable high-resolution single atom and molecule studies by scanning tunnelling microscopy. This opened up pathways not only to recover intrinsic functionalities of complex molecules and supramolecular architectures, but also to deliberately tune them.
- A chemical functionalization and doping of the sp^2 sheets with heteroatoms, vacancies, or out-of-plane "defects" introduces active sites for catalytic processes and the tethering of adsorbates via specific terminal groups. Similar surface modifications are well studied in related BN nanomaterials, including flakes and nanotubes (e.g., Ref. [478]).
- A carpet-like growth mode of *h*BN upon CVD on metallic supports can yield continuous sheets extending over defects as atomic steps and thus is not restricted to expensive single crystal supports, but is regularly applied to low-cost foils and thin films. Adsorption of adsorbates on such systems thus opens up perspectives for large-scale and low-cost architectures, e.g., for technologically relevant functional surfaces.
- *h*BN monolayers are chemically stable in air, liquid water and perchloric acid and can withstand high temperatures (see examples in chapters 1 and 2). Accordingly, they can be reversible modified by molecular adsorption/desorption cycles, an important feature in view of sensing capabilities.
- Intercalation processes, well established in bulk-like sp^2 compounds (e.g., Refs. [315–317,479–483]), are applicable for a tailored modification of *h*BN/metal interfaces. From a different perspective, intercalation gave access to nano-reactors between the *h*BN sheet and the metal support, where chemical processes proceed under confinement.

3.1. Atoms and clusters

Pioneering physical adsorption studies on *h*BN date back to the late 1950s, both involving experiments on bulk BN and theoretical modeling [484,485]. Specifically, noble gases interacting with *h*BN continued to attract considerable interest over the following decades (e.g., Refs. [486–492]). The exploration of adsorption on surface-supported monolayer *h*BN model systems however only developed in the late 1990s. The motivations to explore the interaction of deposited atoms with such *h*BN sheets are as manifold as the available templates. Three selected key objectives are listed in the following:

- It was anticipated early on that corrugated *h*BN layers could provide a template for the site-selective positioning of individual atoms and the self-assembly of clusters featuring uniform size, thus yielding highly-ordered adsorbate arrays. Two main goals are the control of magnetic and catalytic properties of such systems. To this end, both adsorbate-adsorbate as well as adsorbate-substrate interactions need to be comprehensively characterized and controlled.
- Atomic adsorbates are used to engineer the electronic and/or structural properties of the *h*BN/metal interface, maintaining however the native chemical composition of the sheet. Here, adsorption of atoms on *h*BN, as well as intercalation below *h*BN are employed. On the one hand the intercalation can reduce the sp^2-metal interaction, approaching quasi-freestanding *h*BN or switching the sp^2 sheet's texture. On the other hand a charge redistribution at the interface of adsorbate and the sp^2 layer can be deliberately induced and exploited to gate the *h*BN sheet. Furthermore, H uptake by *h*BN sheets offers potential for efficient hydrogen storage.
- Atoms can be employed to modify the structure and chemical composition of the sp^2 sheet itself, aiming for *h*BN functionalization or doping. From an experimental perspective, ion implantation at *h*BN/metal interfaces provides routes to defect and nanostructure formation. In addition to vacancy defects, substitutional heteroatoms embedded in the sp^2 sheet offer means to engineer the (opto)electronic, magnetic, and catalytic properties of *h*BN and are a potential basis for a subsequent functionalization of *h*BN by out-of-plane tethering of adsorbates.

Table 4 summarizes a selection of elements combined as atomic adsorbates with distinct *h*BN/metal systems to address one of the above objectives. Besides experimental studies, complementary theoretical approaches are covered. After briefly addressing experimental aspects of single atom and ion deposition in the next paragraph, we will review the interaction of adsorbates for one (class of) *h*BN/metal system after the other, loosely following the chronological sequence.

Experimental aspects of atom and cluster deposition. Depending on the element one of the following methods of choice is typically employed to dose single atoms. Most experiments with transition metals involve the sublimation via e-beam evaporation from rods or crucibles or resistive heating of a coated filament (e.g., Ti, Mn, Co, Fe, Au). The former method can also provide C [230,493,494] and Ge [306], whereas Pb was deposited by the latter [495]. Alkali metals (K, Li, Rb) are dosed form dispensers [475,496], whereas tailor-made sources were developed to control ions (Rb^+) [496]. Noble gases as Xe and Ar can be dosed through leak valves onto the h-BN held at low temperature. Ionized species are typically generated by commercial sputtering sources used for UHV sample preparation [497]. The atomic deposition of H, D or O is achieved by cracking the diatomic molecule using hot tungsten filaments or capillary tubes upon dosage [189,308,498]. The deposition of clusters (see Table 5) relies on more advanced procedures as Xe buffer-layer assisted growth (Co, Pb, Sn) [499–501] or the use of dedicated sources providing true size-selectivity (Pd_{19}) [502].

3.1.1. hBN/Nickel(111)

Given the commensurate *h*BN overlayer structure on Ni(111) providing a laterally homogeneous platform for adsorbates, this system was mainly chosen with the perspective to fabricate sandwich-like structures featuring stacked layers with atomically defined interfaces. Compared to the corrugated nanomesh topography, the interpretation of space-averaging data is facilitated and the small unit cell reduces the efforts for computational modeling. The first study on the interaction of atoms with h-BN monolayers was published in 2002 reporting on Co adsorption on *h*BN/Ni(111) [305]. In this early work, the influence of characteristic properties of the h-BN/metal interface as the low surface energy and domain boundaries (cf. paragraph 2.2.9) on the adsorption behavior of metals was highlighted. Rt deposition of atomic Co resulted in the formation of three-dimensional (3D) clusters with an apparent height of about 6 Å weakly coupled to the h-BN support as evidenced by controlled removal via STM manipulation (Fig. 14 (a)). In addition, the thermally activated intercalation of Co under the h-BN monolayer was reported and related to the efficient trapping of diffusing Co by defect lines at domain boundaries (Fig. 14 (b)). Intercalation at defects was observed after rt deposition and prevails above 500 K. Co 2p XPD patterns revealed a very similar six-fold symmetry for both rt and high-temperature Co deposition, preventing a discrimination of the two growth scenarios [529]. An XPS based analysis of the growth kinetics showed a pronounced reduction of the Co sticking coefficient on *h*BN at high substrate temperatures. Even exposure of *h*BN/Ni(111) to Ti at 10 K revealed a sticking coefficient below one [511]. Individual Ti atoms randomly adsorbed on the surface readily take up hydrogen, as every H_2 molecule impinging on a Ti atom dissociates without activation barrier. Hydrogenation doubles the apparent height in STM images to roughly 300 pm and can be reversed by STM-

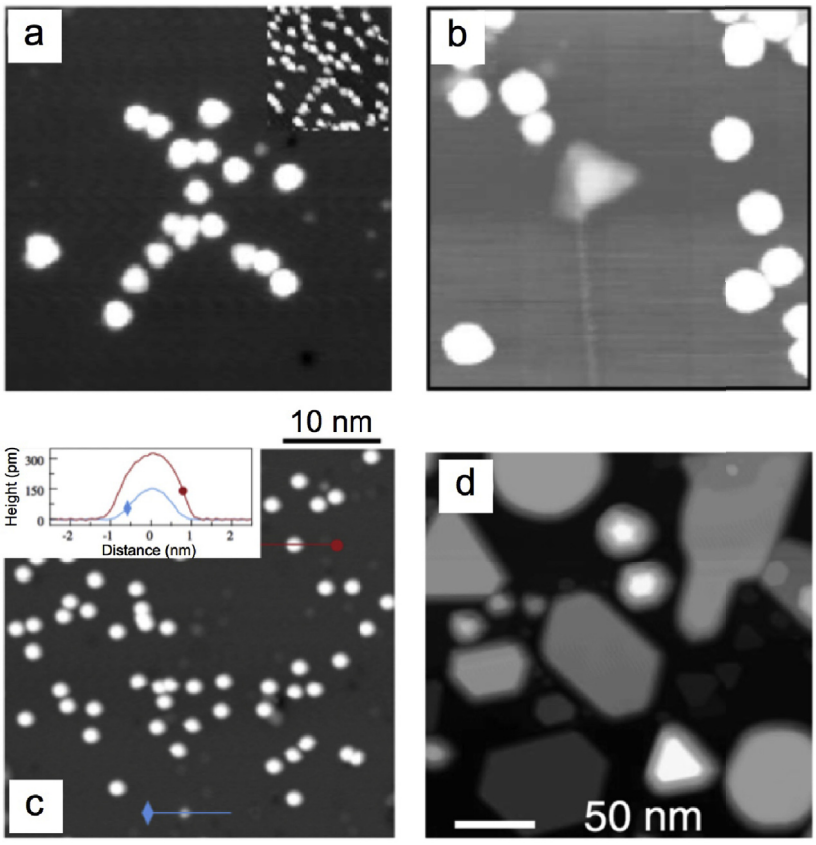

Fig. 14. STM images of metal adatoms and islands on *h*BN/Ni(111). (a) "Soccer player" composed of Co clusters. The inset shows the same sample area before removing selected clusters by STM manipulation. (b) Coexistence of 3D Co cluster on *h*BN and a 2D Co island intercalated at a *h*BN defect line. (c) Clean (blue) and hydrogenated (red) Ti adatoms. The inset shows line profiles for the two species. (d) Planar, multilayer Pb islands. (a,b) Adapted with permission from Ref. [305], (c) Adapted with permission from Ref. [511] © (2013) Elsevier, (d) Reproduced with permission from Ref. [495] © (2012) American Physical Society. (For interpretation of the references to color in this figure legend, the reader is referred to the Web version of this article.)

induced desorption (Fig. 14 (c)) [511]. Pb deposition on *h*BN/Ni(111) yielded planar, multilayer Pb islands (Fig. 14 (d)) [495]. A dynamic Coulomb blockade was observed by conductance measurements on these Pb islands and a decrease of the resistance (capacitance) with increasing (inverse) area was demonstrated in these nanocontacts on *h*BN [495]. From a theoretical perspective, the electronic transport properties through sandwich-like Ni/*h*BN/Ni(111) structures were addressed, covering different numbers of *h*BN layers [530,531].

Deposition of Ge on *h*BN/Ni(111) followed by annealing to 723 K resulted in an intercalated atomically thin Ge layer, where the interface is characterized by a p($\sqrt{3} \times \sqrt{3}$)-R30° surface reconstruction as visualized by LEED [306]. Upon intercalation, the B1s and N1s core levels are shifted to lower binding energies by 0.3 and 0.75 eV, respectively. Furthermore, Ge intercalation leads to a shift of the *h*BN π and σ bands towards E_F. Based on these XPS and ARPES results (see Fig. 15), Verbitskiy et al. concluded that a quasi-free-standing *h*BN layer is achieved, where the Ni 3d - *h*BN π hybridization is reduced by the Ge intercalation. It should be noted that the annealing temperature has to be carefully chosen. Heating to 823 K leads to Ge-Ni alloying, enhancing the substrate-*h*BN interaction [306].

Au deposition on *h*BN/Ni(111)/W(110) results in disordered Au clusters on *h*BN. Upon annealing to 773 K the Au intercalates inducing a quasi-free state of the *h*BN sheet as evidenced by NEXAFS and XPS that goes in hand with a decrease of its lattice constant [318]. Au intercalation on *h*BN/Ni(111) was also applied by Cattelan et al., who further employed the *h*BN/Au/Ni(111) as support for WS_2 synthesis (see section 3.4) [276]. LEED indicated the formation of a 9 × 9 moiré superstructure representing the *h*BN/Au interface and photoemission experiments showed a shift of the B and N 1s core levels - as well as of the π and σ bands - to lower BE upon Au intercalation [276], confirming earlier results by Usachov et al. [318]. In an attempt to further tailor the structural and electronic properties of *h*BN by ionic functionalization, Fedorov et al. exposed this layered material to K and Li dopants [475]. Interestingly, the response of *h*BN/Au is distinctly different for the two alkali metals. Li resides on *h*BN, while K intercalates in between *h*BN and Au/Ni(111), lifting the sp^2 sheet by about 2.36 Å. This behavior was tentatively assigned to different preferences in forming surface alloys. Importantly, the combination of XPS, ARPES, NEXAFS and complementary DFT modeling revealed that the dopants induce pronounced charge redistribution at the respective interfaces. In the Li case, this results in an electric field embedding the *h*BN sheet, shifting the π and σ bands away from E_F and enhancing the corrugation in the layer to 0.25 Å. For K, *h*BN is placed outside this interface capacitor and the energy shift of its band is explained by the potential difference (see Fig. 16) [475]. As a side remark, hybrid Hartree-Fock DFT calculations revealed no adsorption of isolated Li on a free-standing *h*BN sheet (see paragraph 3.1.7) [532].

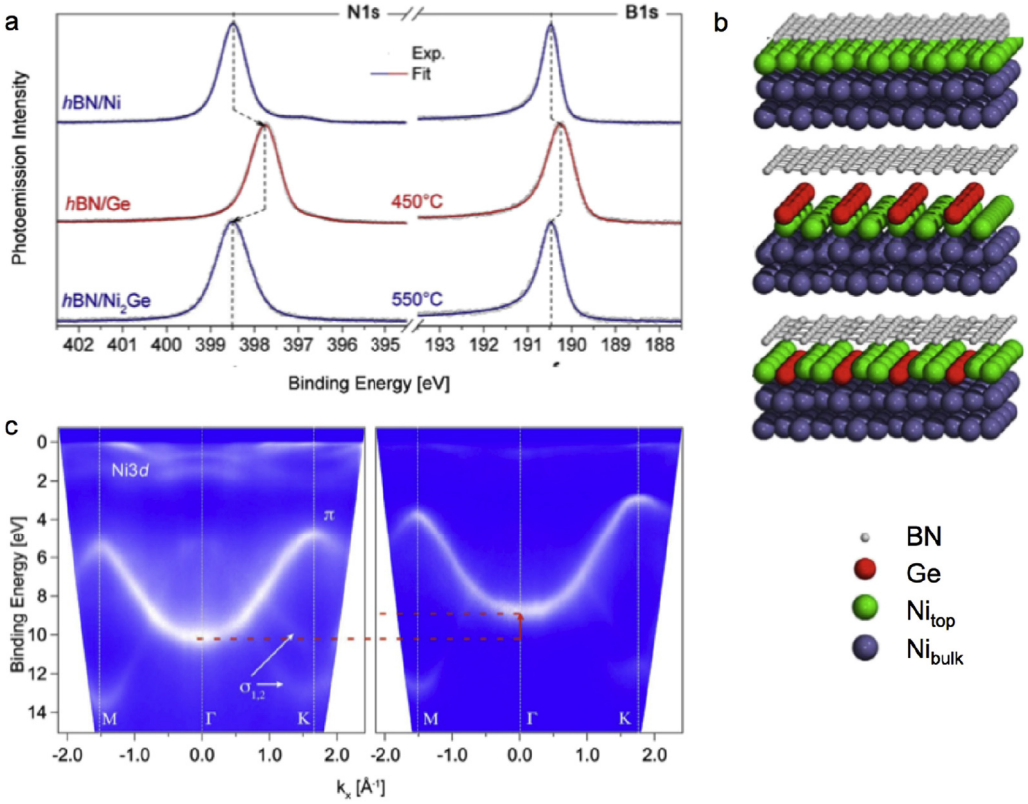

Fig. 15. Ge/*h*BN interfaces on Ni(111). (a) B1s and N1s XPS spectra before and after Ge intercalation. The structural models in (b) describe the respective interface structures. (c) ARPES maps of *h*BN/Ni(111) (left panel) and *h*BN/Ge/Ni(111) (right panel). Adapted with permission from Ref. [306].

We now return to the basic *h*BN/Ni(111) system and review experimental findings on its interaction with atomic hydrogen. In 2011, Koswattage et al. proposed a site-selective adsorption mechanism, with deuterium preferentially adsorbing on B sites, as inferred from XPS and NEXAFS measurements, complemented by spectral modeling using the discrete variational Xα method [271]. In addition, this preferred deuteration at B sites was corroborated by photon-stimulated ion desorption [272]. Annealing to 473 K confirmed the stability of the deuterium functionalization and thus a covalent binding [271,272]. Two recent publications - both combining (synchrotron-based) experiments with DFT modeling - refined the understanding of hydrogen interaction with *h*BN/Ni(111) [189,275]. Ohtomo et al. applied NIXSW, LEED, UPS, NEXAFS, and SPMDS to characterize the geometric structure and the (spin-dependent) band structure of hydrogenated *h*BN/Ni(111). The NIXSW data confirm a site-selective H adsorption on B sites (Fig. 17(a)), with a H presence up to 673 K, while SPMDS shows a magnetic moment on the hydrogenated *h*BN, rationalized by a re-hybridization of the σ and π orbitals together with back-donation from Ni 3d states [275]. Späth et al. explored the reactivity of *h*BN/Ni(111) towards atomic hydrogen over a wide exposure range with exquisite detail, applying (temperature-programmed) XPS, NEXAFS, TPD, and UPS complemented by DFT calculations. With increasing hydrogen exposure, two competing processes were identified: First, as described in the previous studies, hydrogenation of the *h*BN occurs. In this regime, the interaction of *h*BN with Ni(111) is increased. At higher hydrogen exposure, intercalation prevails, decreasing the *h*BN - Ni(111) interaction [189]. Fig. 17(b and c) shows selected XPS and NEXAFS data, representing these exposure-dependent effects. The two phases show different thermal stabilities, with de-intercalation occurring at 390 K, whereas de-hydrogenation proceeds at 550 K (Fig. 17(b)). Interestingly, both hydrogenation and intercalation reduce the n-doping of the surface, either by charge redistribution and buckling upon B—H bond formation (hydrogenation) or by an increased adsorption distance (intercalation) - and thus modify the interface structure and properties in distinct ways (Fig. 17(e–h)) [189].

Also the interaction of O with *h*BN/Ni(111) attracted considerable interest. Lyalin et al. calculated (DFT, WC functional) the optimized geometric structure for an adsorbed oxygen atom and compared it to the situation on a free-standing *h*BN sheet [358]. While O binds on both surfaces, the adsorption sites and binding energies are distinctly different, highlighting the promotion of oxygen binding by the interaction of *h*BN with the Ni support. The most stable structure of O/*h*BN/Ni(111) corresponds to adsorption on a bridge position between two B atoms with a binding energy of 3.35 eV. Without support, O resides above a BN bond (binding energy 1.67 eV). Considering vdW interaction, Guo et al. found two stable adsorption sites for O on *h*BN/Ni(111): O positioned on a B site (binding energy 5.57 eV) and on the bridge site of the B—N bond (binding energy 2.21 eV) [505]. Furthermore, the O modification enables the hydroxylation of the *h*BN sheet (vide infra, section 3.2). Similar results were found for O on *h*BN/Cu(111) [505]. For comparison, selected theoretical studies on atomic O interacting with free-standing *h*BN sheets will be briefly discussed in paragraph 3.1.7.

3.1.2. *hBN/Rhodium(111)*

Of course, the nanomesh structure of *h*BN/Rh(111) attracted considerable interest regarding the adsorption of atoms in the quest to assemble arrays of isolated monoatomic units or clusters with a

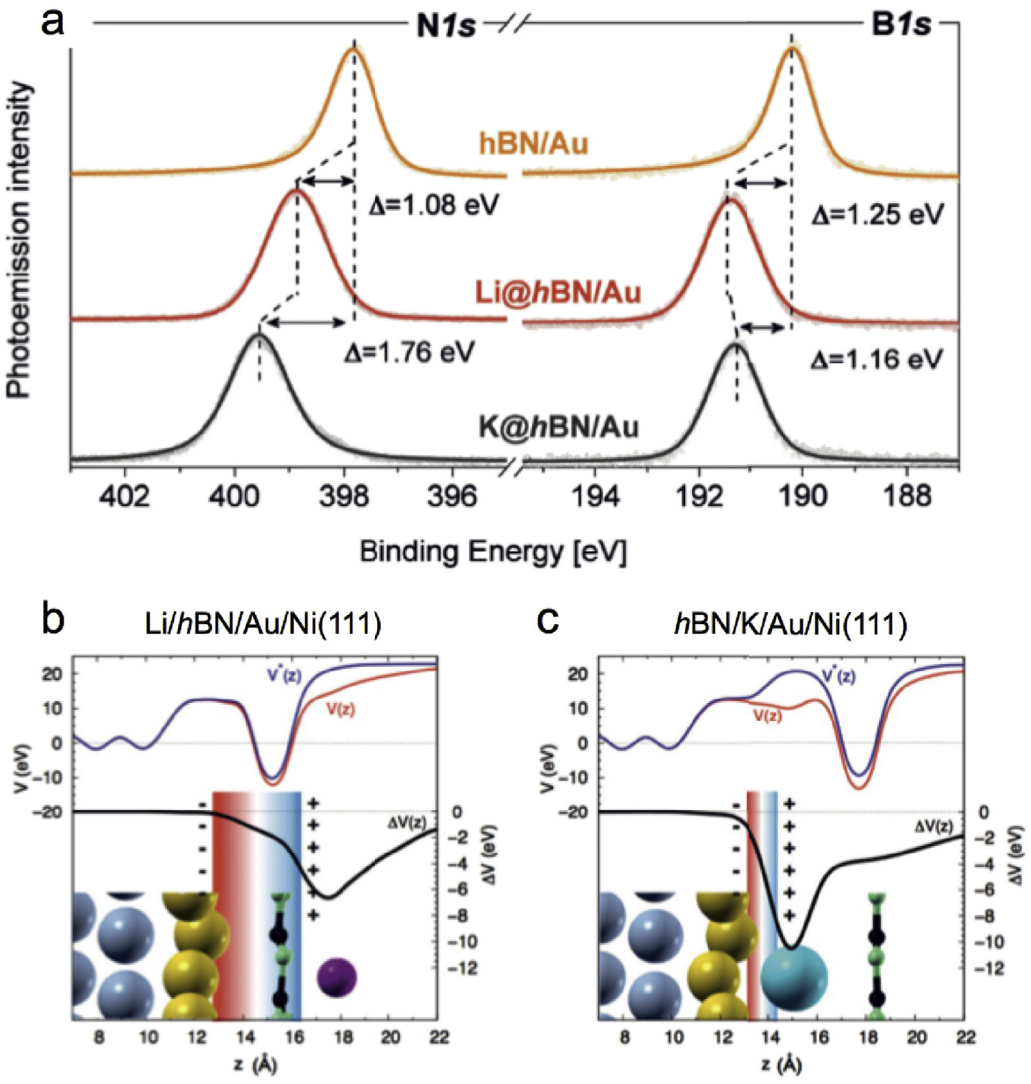

Fig. 16. Interface engineering by K and Li dopants at Au-intercalated *h*BN/Ni(111)/W(110). (a) B1s and N1s XPS spectra of *h*BN/Au, Li/*h*BN/Au, and *h*BN/K/Au, respectively. (b) and (c): DFT calculated potential along the direction perpendicular to the surface combined with capacitor model of the interface for Li/*h*BN/Au (b, Li: purple ball) and *h*BN/K/Au (c, K: azure ball). Adapted with permission from Ref. [475] © (2015) American Physical Society. (For interpretation of the references to color in this figure legend, the reader is referred to the Web version of this article.)

homogeneous size distribution. Special focus lies on magnetic materials (Co), metals with promising catalytic properties at the nanoscale (Au, Pd), or small atoms (H) triggering morphological changes upon intercalation. In addition to the dosing of atoms, clusters were deposited [499–502]. Complementary to the experimental studies, the binding of single atoms and clusters on the *h*BN nanomesh on Rh(111) was comprehensively modeled by first-principle calculations.

From an experimental perspective, one can distinguish three approaches for the deposition of atoms, which we will address sequentially: Aiming mostly for individual atoms on *h*BN/Rh(111) atoms are deposited at low temperature to prevent intercell diffusion ($T_{substrate}$ typically < 35 K [512]). To assemble clusters or burried layers, atoms are added at rt, frequently followed by annealing to trigger or enhance diffusion, ripening or intercalation processes. Finally, accelerated ions and atoms are used to promote implantation below the *h*BN sheet.

Atom deposition. We start our discussion on single atoms interacting with nanomesh structures by the smallest possible adsorbate, atomic hydrogen (H). Interestingly, exposure of *h*BN/Rh(111) to H (or D) induces a pronounced change in surface texture and electronic structure [308]. STM imaging revealed a flattening of the nanomesh structure yielding domains without apparent corrugation. Indeed, UPS spectra showed the quenching of the σ- and π-based spectral features characteristic for the pore regions upon H dosage. These effects were assigned to H intercalation between the *h*BN sheet and the Rh support (Fig. 18). DFT modeling reveals a subtle balance between H—Rh and BN—Rh bonding. With 1 ML H atoms intercalated, the mean BN-Rh separation increases to 3.4 Å (compared to 2.9 Å for the pristine case) and the nanomesh corrugation is reduced to 0.2 Å. Modest annealing (600 K) triggers de-intercalation and desorption of hydrogen (or deuterium) and thus switches the sp^2 sheet back to the initial nanomesh state [308]. Interestingly, such a reversible switching could not only be triggered and followed in an electrochemical scanning tunneling microscopy setting, but also induced a switching of static friction and adhesion, detected on a macroscopic scale on a liquid drop [335].

The low-temperature deposition approach of atoms on *h*BN nanomeshes was applied for Co, Fe, Mn, Ti, Cr, Cu, Au, and Xe

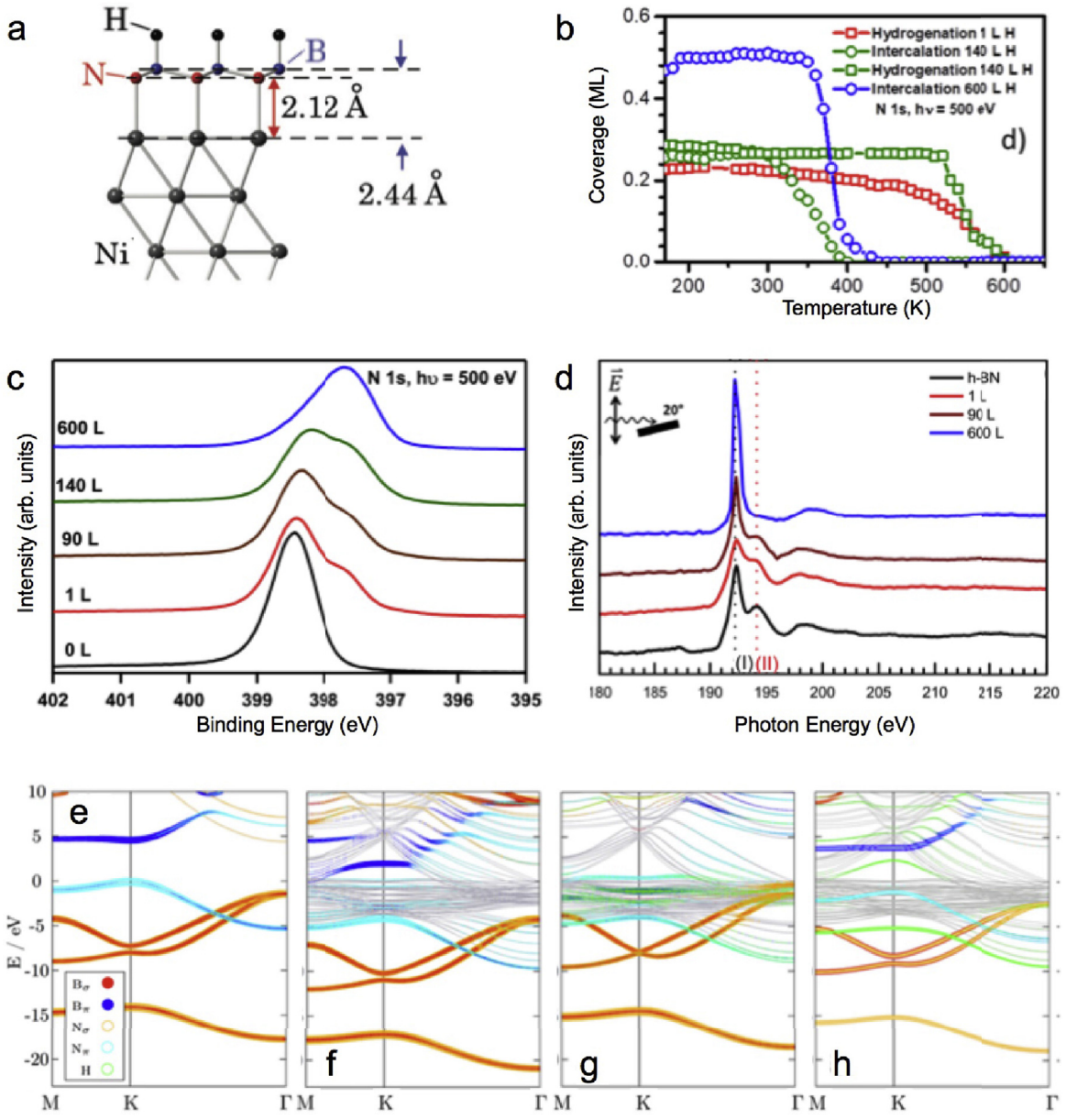

Fig. 17. Interaction of atomic hydrogen with *h*BN/Ni(111). (a) Geometric interface structure of H on *h*BN/Ni(111) reflecting NIXSW data. Note that the buckling is inverted compared to bare *h*BN/Ni(111) (compare Fig. 6(b)). (b) Coverage versus temperature for chemisorbed and intercalated H. (c) N1s XPS and (d) B K-edge grazing-incidence NEXAFS spectra for increasing H exposure. Feature (II) reflects *h*BN - Ni(111) interactions. (e–h) Calculated band structure for (e) free-standing *h*BN, (f) bare *h*BN/Ni(111), (g) hydrogenated *h*BN/Ni(111), and (h) H-intercalated *h*BN/Ni(111). A comparison of (e) and (h) suggests a quasi-free standing character of *h*BN. (a) Adapted with permission from Ref. [275] © (2017) Royal Society of Chemistry, (b–h) Adapted with permission from Ref. [189] © (2017) IOP Publishing.

[511,512,515,520]. For all these elements, adsorption in the pore regions of the nanomesh structure prevails. Only a minority of adatoms is observed on the wire regions. Fig. 19 highlights this templating effect for Ti, Co and Xe. To mainly deal with individual metal adatoms, the coverage is usually kept low with a typical fraction of occupied pores below 20% [511,512]. At higher coverage, the formation of dimers and clusters following a Poisson statistics is anticipated, as the incoming adatoms are randomly distributed and confined to one nanomesh cell.

Despite the shared site-specific adsorption in the nanomesh pores, distinct differences in the bonding configuration and the trapping mechanism of individual adatoms on *h*BN/Rh(111) were reported, which are discussed in the following. The off-center adsorption frequently observed at low occupancies of the pores was rationalized by the trapping of polarizable units by the dipole rings inherent to the nanomesh structure [339] (see section 2.2.7) and visualized in real space by imaging 12-membered Xe rings on *h*BN/Rh(111) by STM at 5 K (see Fig. 19 (c)) [520]. The latter study, combining STM data with DFT and classical MD modeling, showed that both vdW- and electrostatic polarization interactions need to be considered to describe the site-specific adsorption. The MD simulations however did not reveal static Xe rings, but showed a dynamic motion of Xe rings along the rim consistent with STM data recorded at 86 K. For the case of Au adatoms, it was concluded that strong covalent interactions dominate the adsorption behavior [525]. Specifically, the binding mechanism involves hybridiza-

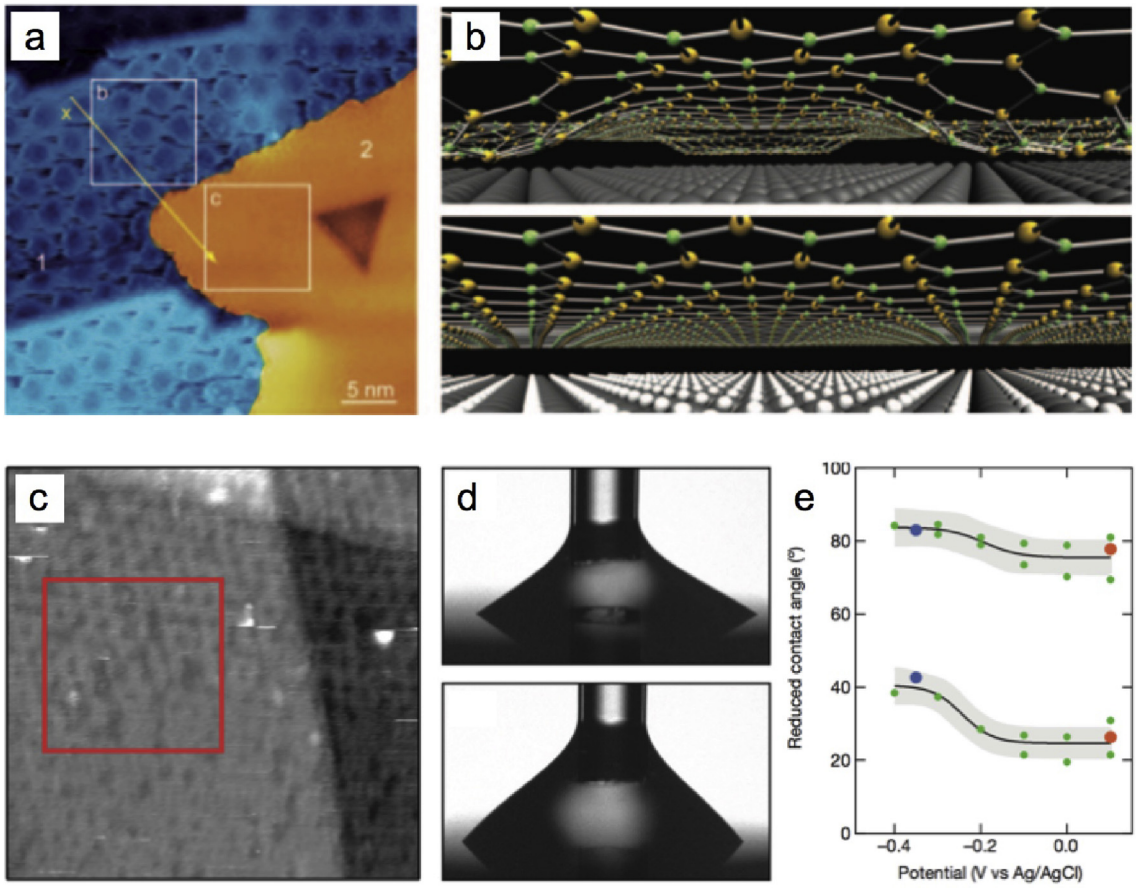

Fig. 18. H intercalation in *h*BN/Rh(111). (a) STM image after exposure to atomic H. *h*BN/Rh(111) nanomesh regions (left) coexist with planar, H-intercalated areas (right). (b) Structural models of the corrugated (top) and planar interface structure (bottom). (c) Electrochemical STM image after hydrogen desorption. (d) Pictures of liquid drop on corrugated (top) and planar (bottom) *h*BN configuration. (e) Contact angles for different applied potentials. Hydrogen intercalation occurs at about −0.2 V. (a,b): Reproduced with permission from Ref. [308] © (2010) John Wiley and Sons, (c–e): Adapted with permission from Ref. [335] © (2016) Springer Nature.

tion of Au-d_z^2 with B-p_z states and charge transfer to Au. Again, the pore regions are clearly preferred over the wire regions. However, the binding energy in the center of the pore (2.4 eV) was calculated (WC-GGA) to be favorable over the rim-adsorption by 0.4 eV. Recent DFT results by McKee et al. - using an averaged lattice constant approach - reveal important differences regarding the adsorption of Ni, Pd, Pt, Cu, Ag and Au on *h*BN/Rh(111) [517]. While all these metal atoms are covalently coupled to *h*BN receiving negative charge (Ni on N sites, Pd, Pt, Ag, and Au on B sites), their preference for the pore regions varies considerably. Au and Pt strongly prefer adsorption in the pore regions, with a pore-to-pore diffusion barrier predicted to exceed 1.2 eV, thus presumably hampering inter-pore diffusion at rt. Ag and Cu still favor adsorption in the pores but feature a lower inter-pore diffusion barrier (≈0.5 eV). Finally, Pd and Ni do not discriminate between pore or wire regions. These theoretical findings considering individual adatoms were corroborated by STM experiments evidencing distinct differences in the cluster morphologies resulting from rt deposition of Pt, Au and Ag (see below) [517].

Interestingly, specific elements (Co, Fe, Mn) destabilize the *h*BN/substrate bonding, resulting in a bistable adsorption complex when probing the surface by STM. In one state, the adatom is imaged as an individual protrusion in the pore, in the other state, it is represented by a characteristic ring-like feature [512]. For Ti, Cr, Cu or Au adatoms, this effect was not observed [512]. The appearance of the ring-like state is reminiscent of the circular feature observed upon Xe adsorption (compare Fig. 19 (b) and (c)). Nevertheless, a comparative study revealed that they indeed base on different phenomena - either single (Mn) or multiple atoms (Xe) [533]. The interaction with hydrogen on the surface readily converts Co to CoH or CoH_2 species. DFT calculations reveal that the hydrogenation goes in hand with a change in adsorption site. While bare Co prefers the adsorption in the center of a *h*BN hexagon, CoH_x resides on N sites [515]. Furthermore, Jacobson et al. exploited the lateral superstructure of *h*BN/Rh(111) to engineer the Kondo exchange interaction between the single spin CoH and the support - thus modulating the magnetic anisotropy of the complex (see Fig. 20). In a follow-up study, the spin state of such a CoH complexes was reversibly switched by approaching it with a H-functionalized STM tip. At large tip-sample distance (low conductance of $6.45 \times 10^{-4} G_0$), a spin 1 state with magnetic anisotropy is observed, while at small distances (high conductance of $12.9 \times 10^{-4} G_0$)), a spin 1/2 Kondo peak emerges in the dI/dV spectra. Hereby, the position of the H in the junction determines the total spin of the complex [534].

Cluster formation. After mainly focusing on individual adsorbates in a nanomesh pore - with the exception of the confined Xe islands in Fig. 19 - we now describe systems where cluster formation was operational *on* *h*BN. This implies that the substrate temperature in the experiment was high enough to enable diffusion of the adsorbates and that the coverage exceeds the single atom limit discussed above.

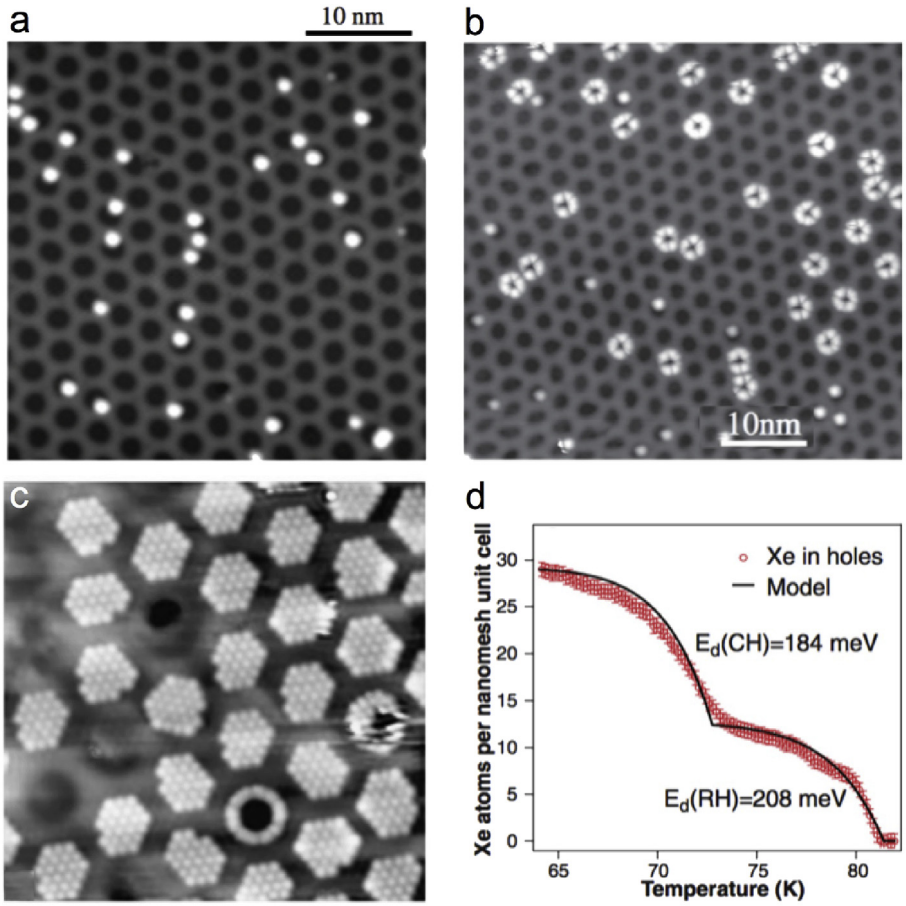

Fig. 19. Adatoms on *h*BN/Rh(111): (a) STM image of individual Ti atoms. (b) STM image of Co atoms in both the ring- and individual protrusion state. (c) Islands of Xe atoms. (d) Number of Xe atoms in nanomesh pore as function of temperature. Two distinct desorption energies of Xe in the pore are used to rationalize the data. (a) Reproduced with permission from Ref. [511] © (2013) Elsevier, (b) Reproduced with permission from Ref. [512] © (2012) American Physical Society, (c) Adapted with permission from Ref. [520], (d) Adapted with permission from Ref. [339] © (2008) AAAS.

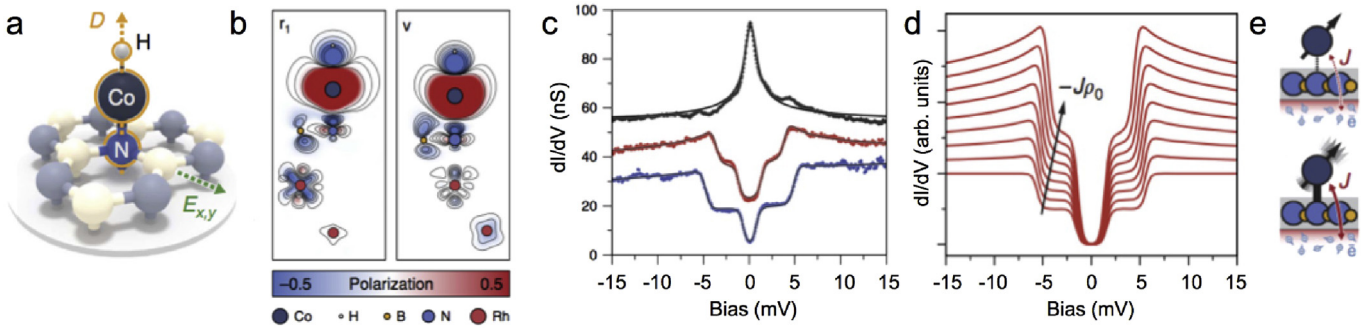

Fig. 20. Quantum engineering of Co spins on *h*BN/Rh(111): (a) Model of CoH adsorbed on *h*BN. (b) Asymmetry between majority and minority PDOS on wire (left) and pore regions (right). (c) dI/dV spectra for three CoH_x species featuring spin 1/2 (grey) and spin 1 (red, blue). (d) Computed dI/dV spectra for increasing coupling between the localized spin and support electrons. (e) Schematic diagrams showing the effect of weak (top) and strong exchange (bottom). Adapted with permission from Ref. [515]. (For interpretation of the references to color in this figure legend, the reader is referred to the Web version of this article.)

In case adsorbate-adsorbate interactions prevail over adsorbate-*h*BN interactions 3D clusters are preferred over 2D islands [523]. Fig. 21 summarizes results for the adsorption of Au, Pt, Co, Ag, Mn, and Ni on *h*BN/Rh(111).

Upon low coverage deposition at rt (typically 0.07–0.2 ML), Pt and Au clusters nucleate preferably at the pore areas of the nanomesh structures, where mono- or bilayer islands are confined [243,516,517,524,535]. ARPES and XPS experiments indicate a rather narrow size distribution of small, mainly 2D Au islands [524]. Au deposition at 115 K followed by STM measurements at 115 K or rt also confirms the aggregation in the pores, but reveals differences in the distribution of monolayer versus bilayer or larger clusters [346]. 5 ML Au dosed at 115 K yields 3D clusters after warming to rt, which feature a cluster density *n* (i.e., number of clus-

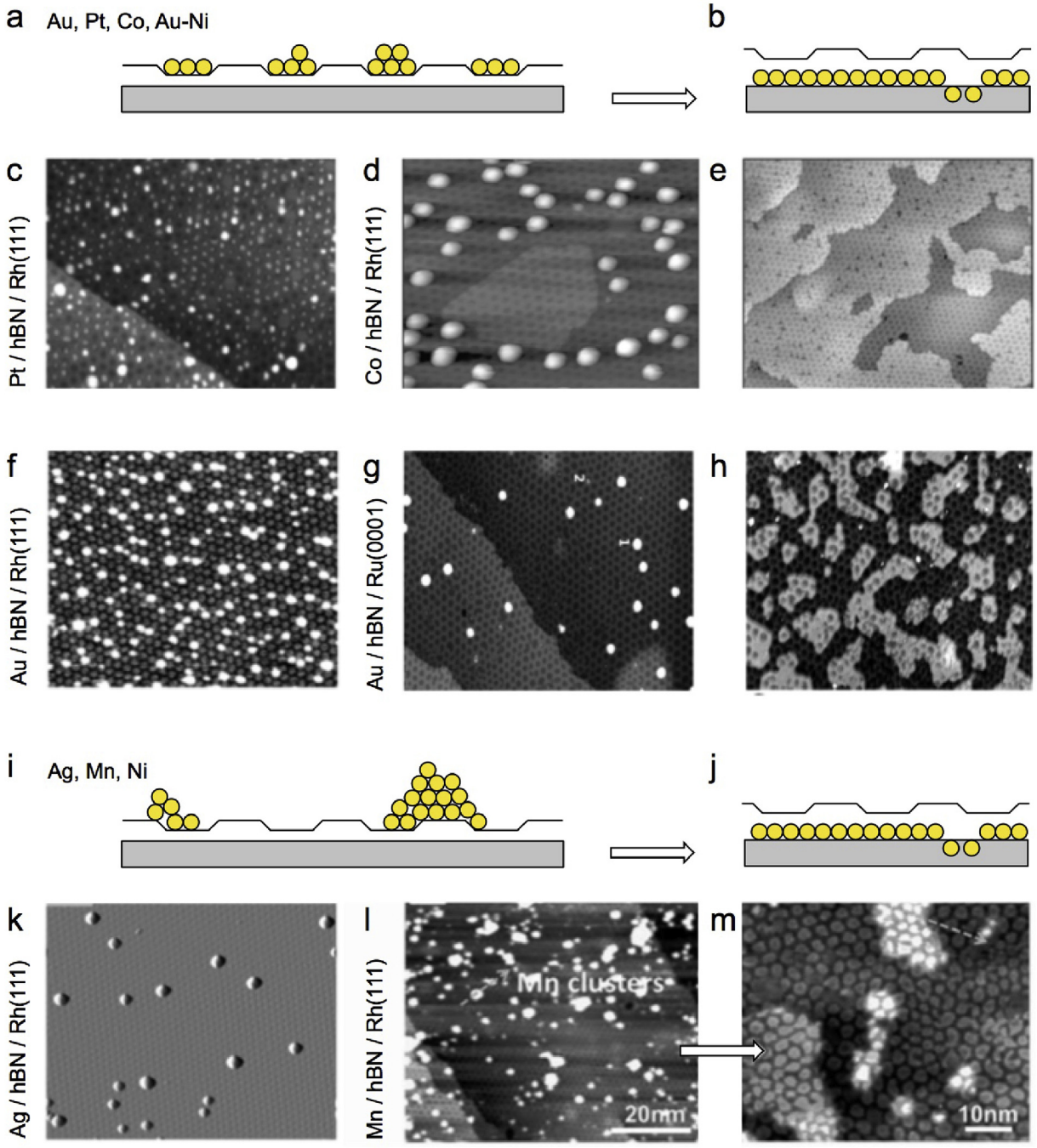

Fig. 21. (a) Site-selective cluster formation on *h*BN. (b,j) Intercalation below *h*BN. (c) Pt/*h*BN/Rh(111) (rt, 0.4 ML) [517]. (d) Co/*h*BN/Rh(111) deposited in the presence of O_2 after annealing at 557 K (0.2 ML Co). (e) after annealing at 723 K (0.5 ML Co) [310]. (f) Au/*h*BN/Rh(111) (rt, 0.16 ML) [517]. (g) Au/*h*BN/Rh(0001) annealed at 900 K [226]. (h) after annealing 1 ML at 1050 K [321]. (i) Adsorption on *h*BN. (k) Ag/*h*BN/Rh(111) (rt, 0.15 ML) [517]. (l) Mn/*h*BN/Rh(111) (rt) and (m) after annealing at 573 K [513]. (c,f,k) Adapted with permission from Ref. [517]) © (2016) Elsevier, (e) Adapted with permission from Ref. [310] © (2009) American Chemical Society, (g) Adapted with permission from Ref. [226] © (2007) American Chemical Society, (h) Adapted with permission from Ref. [321] © (2008) American Chemical Society, (l,m) Adapted with permission from Ref. [513] © (2013) Springer Nature.

ters/pore) of about 0.7 [346]. LEIS and STM results confirm a 3D growth of Au clusters at high coverage [243]. The low Au $4f_{7/2}$ XPS BE (83.55 eV) prevailing at low coverage ($\Theta_{Au} = 0.045$ ML) was assigned to a negative charging of the small Au aggregates by Gubó et al., who also showed that Au intercalation is not significant at rt [243].

The growth of Ag, Mn, and Ni clusters on the other hand does not exclusively follow the nanomesh template, 3D clusters with a broad height distribution can laterally extend over multiple pores [513,516,517]. For Co supplied in the presence of molecular oxygen the situation is not clearcut, but the island distribution rather resembles the Au and Pt cases, with Co particles centered in the nanomesh pores [310]. The trends discussed here follow the predicted element-specific affinity for selected regions of the nanomesh (pore, wire, none) and the calculated inter-pore diffusion barriers (vide supra) [517], even though an adatom exchange between pores

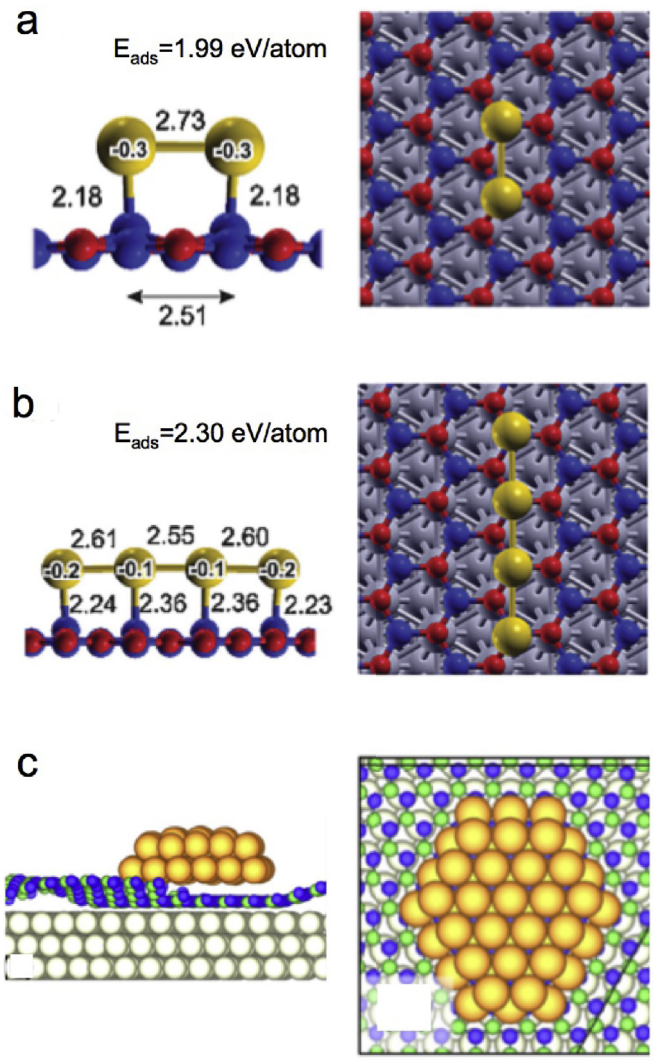

Fig. 22. DFT modeling of Au clusters in *h*BN/Rh(111) pores: (a) Side (left) and top view (right) of a Au_2 cluster. Adsorption energies and bond distances are given in the figure (Blue: B; red: N; yellow: Au; grey: Rh). (b) Chain-like Au_4 cluster. (c) Bilayer Au_{51} cluster (Green: B; blue: N; yellow: Au; white: Rh). (a,b) Adapted with permission from Ref. [527] © (2012) American Physical Society, (c) Adapted from Ref. [346] © (2014) American Physical Society. (For interpretation of the references to color in this figure legend, the reader is referred to the Web version of this article.)

(e.g., in the case of Au) is hard to exclude from the available analysis of the experimental data. A recent study by Wu et al. explored the growth of bimetallic clusters on *h*BN/Rh(111) by means of STM, TPD, and AES [516]. Specifically, the influence of the deposition sequence of Au and Ni was addressed. Bimetallic Ni—Au clusters were successfully formed in the nanomesh pores when first depositing Au, followed by Ni. Here, the charged Au islands serve as nucleation sites for the Ni. Applying a reversed deposition order (first Ni, than Au), bimetallic clusters could not be formed, as Au islands nucleated and grew between Ni clusters [516]. Interestingly, the Ni—Au clusters feature a stronger interaction with CO than pure Ni clusters as judged from TPD, indicating that charge redistribution might promote the catalytic activity of bimetallic clusters on *h*BN/Rh(111) [516].

Thermal annealing induces morphological changes, as exemplified by agglomeration of Au above ≈500 K, forming larger, 3D-like clusters with a reduced cluster density [243,524], e.g., affecting the interaction with CO [526]. Furthermore, it activates intercalation processes, resulting in extended 2D islands buried below *h*BN. Surprisingly, the nanomesh structure persists on the intercalated Mn and Co islands and ML films, despite the differences in bulk lattice constants of these elements in comparison to Rh (see Fig. 21 (e, m)) [310,513]. Also for Au (where intercalation sets in at 700 K and is completed at 1050 K, coming along with considerable Au desorption), the nanomesh structure was still observed after intercalation of significant amounts of Au below *h*BN [243]. Similar observations were reported for Au intercalation in *h*BN/Ru(0001) (see paragraph 3.1.3 and Fig. 21 (h)). Three suggestions were brought forward to solve this puzzle: (i) The formation of a surface alloy [524] (e.g., Au-Rh, compare paragraph 2.2.15 and Ref. [243]), (ii) the assembly of a pseudomorphic layer [321], or (iii) a rigid attachment of the intercalated atoms to the corrugated nanomesh structure. For the case of Co, XPS measurements support the third explanation [310]. Despite the common conservation of the nanomesh superstructure, the Mn, Co and Au systems show distinct differences. In contrast to Mn (and Au), Co intercalation is only triggered when oxygen is supplied, weakening Co—Co bonds and suppressing Co agglomeration on *h*BN [310]. This observation is in line with the Au—Au interaction energy being smaller than the Co—Co one [523]. Annealing Mn intercalated *h*BN/Rh(111) at 773 K resulted in a shrinking of buried islands which was assigned to Mn de-intercalation and desorption [513].

Au agglomerates on *h*BN/Rh(111) were also addressed theoretically by DFT calculations, covering $Au_n(n = 2, 3, 4)$ [527] and $Au_n(n = 1, 7, 19, 30, 37, 51)$ [346] in the pore of the 13-on-12 nanomesh structure. As mentioned above, atoms in the clusters are negatively charged. Thus, chain-like structures are preferred for small clusters to reduce the interatomic Coulomb repulsion [527] (Fig. 22). The adsorption energy is above 2 eV/atom with the Au atoms binding to the B sites. The intermediate clusters up to 37 atoms were modeled as flat, single-layer hexagonal islands. Around a critical size of 30 atoms, the calculated average Au chemical potential gets lower for bilayer instead of monolayer islands, thus indicating a transition to bilayer clusters consistent with experimental observations (see above) [346]. A comparison to calculations on a free-standing *h*BN bilayer once again exemplifies the role of the metallic substrate. Here, Au and Au_2 adsorbs on top of N sites with calculated adsorption energies of 0.25 eV and 0.77 eV, respectively [536]. On a free-standing *h*BN monolayer, individual Au atoms were found to adsorb with adsorption energies of 0.1 eV and 0.11 eV on N and B sites, respectively [537].

Cluster deposition. Pre-assembled metal clusters were deposited on *h*BN/Rh(111) either by buffer layer assisted growth (BLAG; Co, Sn, Pb) [499,501,538] or soft-landing of size-selected clusters from a designated source (Pd_{19}) [502] (see Table 5). In the first approach, metal is deposited on a Xe layer typically adsorbed at 50 K (e.g., 0.5 ML Pb with 3000 L Xe). Clusters are formed during deposition and further grow through coalescence upon desorption of the buffer layer by warming up to rt [500]. For Co, this procedure yielded hexagonal arrays of particles. The clusters present some scatter in size - with a typical diameter of 2.7 nm - and follow the nanomesh periodicity, being placed on the pores (Fig. 23 (a)). By repeated BLAG cycles, filling factors up to 70% were achieved. Higher occupancies are hampered by attractive cluster-cluster interactions and the cluster mobility, yielding larger aggregates consistent with Monte-Carlo modeling [538]. This merging might occur during the BLAG process, as Pd clusters of similar size deposited without buffer layer did not show a pronounced cluster mobility (see below). In contrast to adsorption on bare Rh(111), where the clusters flattened due to the large interfacial energy, the clusters on *h*BN appeared with a nearly (hemi)spherical shape [499,500]. STS

recorded at 4.2 K on individual clusters revealed an electronic gap of ≈160 meV that was assigned to Coulomb blockade (Fig. 23 (b)) [499]. The superconducting energy gap of Sn and Pb clusters with an apparent height between 1 and 35 nm was recorded by STS at approximately 1 K. For Sn, giant oscillations in the gap with cluster size provided evidence for coherent shell effects in nanoscale superconductors [501] (Fig. 23 (c)). The absence of such gap variations for the Pb case was assigned to a suppression of shell effects for shorter coherence lengths (Fig. 23 (e)). On the other hand, small Pb clusters (height ≤ 13 nm) showed a finite energy gap even above the critical temperature T_C, providing evidence for the important role of thermal fluctuations in superconducting nanostructures approaching the zero-dimensional limit (Fig. 23 (d)) [500].

The deposition of size-selected clusters on h-BN/Rh(111) and the subsequent tracking of temperature-induced modifications of the apparent cluster size by STM allowed Fukamori et al. to assess the ripening mechanism [502]. After rt deposition, clusters of uniform size are centered in the nanomesh pores. Annealing up to 700 K, the clusters still follow the template: clusters of increased size centered in the pores coexist with single-layer clusters adsorbed at the rim. The modified size distribution of the Pd clusters upon annealing was exclusively assigned to Ostwald ripening, apparently a diffusion of Pd clusters across the nanomesh is hindered by the site-specific cluster-substrate interactions, preventing a Smoluchowski ripening [502].

Ion implantation. After discussing the adsorption of atoms and clusters on nanomesh structures, we now proceed to ion implantation at the *h*BN/Rh(111) interface. This peculiar procedure can yield three distinct structures: (i) Individual atoms immobilized at rt, (ii) highly curved BN domes, so-called nanotents housing one or more atoms, and (iii) vacancies and regular voids in the *h*BN sheet [497,508–510,539] (see Fig. 24). First, we review the experimental findings focusing on Ar. Similar results were achieved for Ne [508] and Rb [496], as well as for epitaxial graphene on Rh(111) and Ru(0001) suggesting a general applicability of the procedure [540]. Upon irradiating *h*BN/Rh(111) with low-energy Ar^+ ions (typical sputtering charge density 1.6×10^{12} e/cm^2) [508] or neutral hyperthermal Ar atoms [497], protrusions preferably located at the wire crossing regions of the nanomesh structure are observed at rt, together with small irregularities assigned to vacancy defects (Fig. 24 (b)). The former are identified as individual Ar atoms, sandwiched between the deformed sp^2 sheet and the Rh support [508]. The resulting local distortions - named nanotents - are imaged as dome-like structures with apparent heights around 1.8 Å in STM. Annealing at moderate temperatures enables the diffusion and aggregation of Ar below *h*BN, resulting in larger nanotents hosting Ar agglomerates [509]. After heating to 900 K, a new type of regular defect structure was observed in the sp^2 sheet. These 2 nm voids appear at the former pore areas of the nanomesh, and can reach a density of up to 5% of these sites (Fig. 24 (c)). As the mechanism was attributed to sequential bond scission and cut *h*BN nanoflakes complementary to the voids were observed on the surface, the process was named “can-opener effect” [541]. Above 1000 K, the voids disappear indicating a self-healing of the *h*BN to the expense of formation of larger holes (Fig. 24 (d)). Interestingly, centimeter-sized single-orientation *h*BN sheets perforated by the 2 nm voids could be prepared on Rh films, followed by transfer to arbitrary substrates, including TEM grids [239]. Using this protocol, the membrane functionality of such “voidal *h*BN (*v*BN)” monolayers was recently demonstrated in aqueous solution [239].

Theoretical modeling gave exquisite insight into the complex implantation process - including its dynamics - and the resulting structures. Here, we summarize some of the most recent results of Iannuzzi based on the PBE + D3 functional [510]. Indeed, the buried Ar favors adsorption below the wire crossing regions with an implantation energy of 1.38 eV (compared to 6.62 eV at the pore center). In the nanotent, the BN reaches a maximum separation of 5.3 Å from the Rh. The interfacial electron density redistribution includes charge transfer from Ar to Rh and a concomitant polarization of the closest B and N atoms. This local modification stabilizes the implanted species and the nanotent (Fig. 24 (f)). NEB calculations revealed that individual Ar units diffuse below the wire regions with an energy barrier of about 1 eV. Including two atoms, the implantation energy

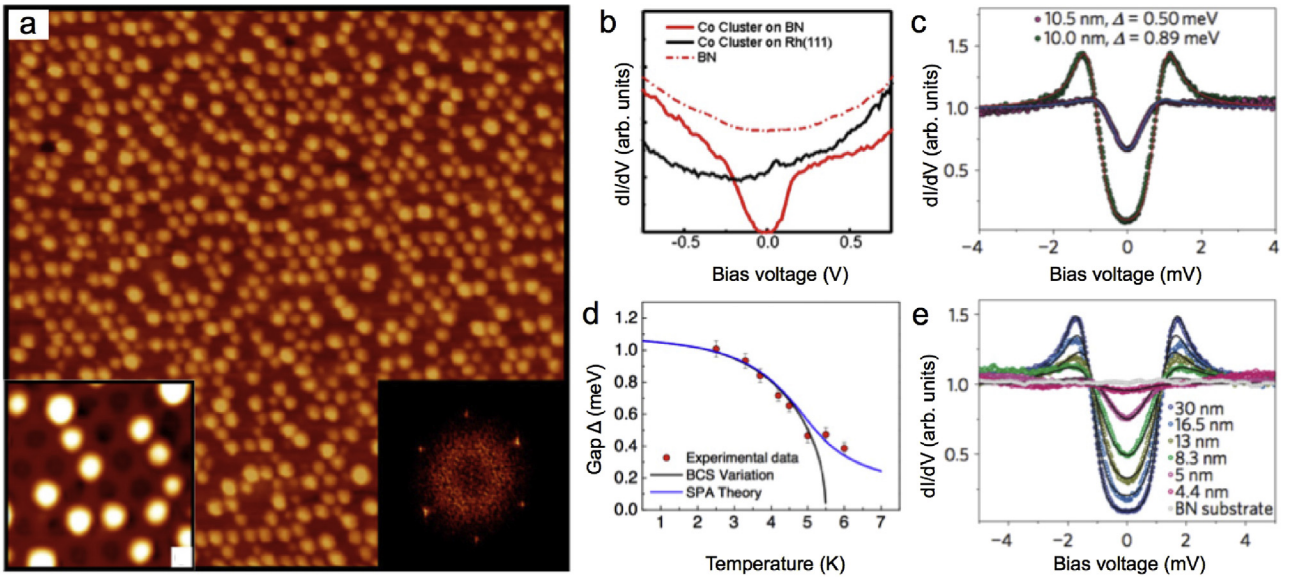

Fig. 23. Quantum effects on clusters confined on *h*BN/Rh(111): (a) Co clusters deposited by three BLAG cycles. The insets show a zoom-in (left) and a FT image (right). (b) dI/dV spectra comparing a Co cluster on *h*BN (red) with one in contact with Rh(111) (black). (c) dI/dV spectra on two small Sn nanoparticles of similar height. (d) Superconducting gap (Δ) versus temperature for a Pb cluster with 8 nm height. Data: red markers, BCS theory: black line, Model including thermal fluctuations: blue line. (e) dI/dV spectra on Pb clusters of different heights. (a,b) Adapted from Ref. [499] © (2008) Elsevier, (d) Adapted from Ref. [500] © (2011) American Physical Society, (c,e) Adapted from Ref. [501] © (2010) Springer Nature. (For interpretation of the references to color in this figure legend, the reader is referred to the Web version of this article.)

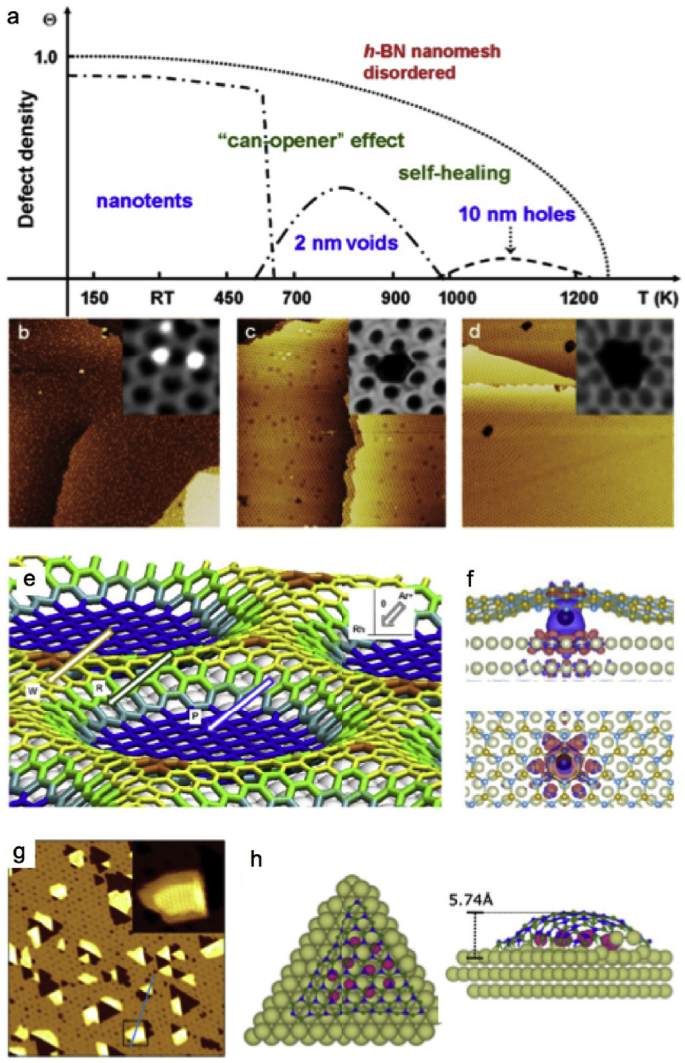

Fig. 24. Ion implantation in corrugated *h*BN structures: (a) Temperature-dependent "phase" diagram of *h*BN/Ar/Rh(111). (b–d) STM images showing the three different "phases": Nanotents (b), 2 nm voids (c), and larger holes (d). (e) DFT structure of *h*BN/Rh(111). The arrows indicate the approaching directions of the Ar ions impacting on three distinct regions of the nanomesh (W: Wire, R: Rim, P: Pore). (f): Structural model of Ar ion implanted between *h*BN and Rh(111) with superimposed charge density difference map (charge accumulation: red, depletion: blue). (g) STM image of *h*BN/Ir(111) annealed to 1300 K after exposure to 3 keV Xe ions. (h) Relaxed DFT structure of *h*BN blister hosting 10 Xe ions (pink balls. Left panel: top view, right panel: side view). (a–d) Adapted with permission from Ref. [541] © (2014) American Chemical Society, (e,f) Adapted with permission from Ref. [510] © (2015) American Chemical Society, (g,h) Adapted with permission from Ref. [521] © (2017) American Physical Society. (For interpretation of the references to color in this figure legend, the reader is referred to the Web version of this article.)

is reduced if the units are placed at the same wire crossing site, as the distortion energy of the *h*BN is reduced compared to the formation of two nanotents. The implantation process itself was explored by ab initio MD calculations revealing the highest success rate for Ar implantation if the ion impinges on the curved rim of the pore (Fig. 24 (e)).

As mentioned above, the ion irradiation induces vacancy defects in the *h*BN sheet triggering structural modifications upon annealing. It should be pointed out that individual N and B vacancies or combinations thereof are of high interest as they offer means to functionalize *h*BN. Several theoretical studies focusing on free-standing *h*BN sheets or bilayers revealed how such defects can radically modify the electronic, magnetic properties and the reactivity of the material (e.g., Refs. [420,542,543]) (see discussion in paragraph 3.1.7). Coming back to *h*BN/Rh(111), DFT modeling showed that the formation energy of vacancy defects in the surface supported *h*BN sheet are lower than in the free-standing monolayer, as the substrate can partly compensate the dangling bonds created upon atom removal [539]. In addition, the nanomesh structure is reflected in a higher stability of the vacancies in the pore or at the rim compared to the wire. In most cases, the boron vacancies are more stable than the nitrogen ones [539].

3.1.3. *hBN/Ruthenium(0001)*

Complementing *h*BN/Rh(111) as a template, the structurally closely related *h*BN/Ru(0001) nanomesh attracted some attention regarding adsorption and intercalation of metal atoms. Specifically, Goriachko et al. reported the exclusive nucleation of Au islands in the nanomesh pores of *h*BN/Ru(0001) at low coverage (0.07 ML) [226] (see Fig. 21 (g)). Even after annealing 0.2 ML Au to 1050 K, individual Au clusters were observed in the pores. Already at 0.3 ML however, Au additionally formed so called "replica islands" on *h*BN/Ru(0001), displaying the same pore-wire morphology in STM images as the original *h*BN/Ru(0001) nanomesh [321]. These islands extend over several nanomesh periods and were assigned to Au on

*h*BN/Ru(0001) [321]. Deposition of large Au amounts ($\Theta \geq 0.3$ ML) followed by annealing to 1050 K resulted in intercalated Au films (see Fig. 21 (h)) [321]. Similar to the Mn and Co intercalation in *h*BN/Rh(111) discussed in paragraph 3.1.2, the nanomesh structure prevails on the intercalated regions. For the Au case, the formation of a pseudomorphic layer was favored as explanation for this observation [321]. The intercalation of thicker Au films (14 ML) at 1050 K in *h*BN/Ru(0001) removes the nanomesh structure and induces substantial (≈2.5 eV) downshifts of the B1s and N1s peaks in XPS [321]. *h*BN/Ru(0001) was also applied as template for the growth of Pd clusters at low coverage. In contrast to the Au case, Pd particles showed some coalescence upon annealing at elevated temperatures [519].

From the modeling perspective, a systematic DFT (PBE-GGA) study by Wang and Bocquet comparing transition metal adsorption on sp^2 templates reports a preferred Au adsorption in the pore of the *h*BN/Ru(0001) nanomesh structure. Here, the binding energy of a single Au atom in the pore was calculated to be 1.9 eV [523] (compare calculation on Au/*h*BN/Rh(111) in paragraph 3.1.2).

3.1.4. *h*BN/Platinum(111)

Ng et al. applied *h*BN/Pt(111) as support for Au [524]. Based on XPS and ARPES experiments, the authors conclude that upon rt deposition, Au forms 3D clusters of irregular size. The Au $4f_{7/2}$ core level signal shows two components, assigned to Au surface and bulk contributions, respectively - consistent with a 3D cluster morphology. In contrast, Au adsorption (in the sub-ML regime) directly on Pt(111) results in 2D island growth, as inferred from the absence of the bulk-related Au peak. The ARPES data of Au/*h*BN/Pt(111) show smeared out Au 5d bands, signaling Au islands being irregular in size and shape. In contrast, sharp, non-dispersing Au 5d bands were observed for a comparable Au coverage on *h*BN/Rh(111), indicating smaller Au islands with a rather narrow size distribution [524].

Recently, Rose et al. reported the growth of Si chains embedded in Pt(111) after atomic Si deposition on sub-ML *h*BN/Pt(111) at rt [507]. The Si intercalates below the *h*BN islands to form chains, which are protected by the *h*BN cover: In contrast to similar Si chains embedded in Pt(111) in the absence of *h*BN, the intercalated chains featured a high stability, e.g., sustaining an exposure to air (dose: 6×10^{11} L). From an analysis of STM images showing the position of chains relative to *h*BN island edges and grain boundaries, the authors concluded that Si intercalation does not happen at these “defects”, but proceeds via diffusion through the *h*BN [507].

3.1.5. *h*BN/Copper(111)

As will be discussed in paragraph 3.2.3, *h*BN/Cu(111) is a promising system regarding catalytic activity, with several reports focusing on its interaction with molecular oxygen. Regarding monoatomic adsorbates however, literature is scarce. A first principles study by Guo et al. using the DFT-D2 method addressed the adsorption of atomic O on a Cu(111) supported *h*BN sheet [506]. Two stable adsorption sites were found, with the strongest interaction (5.29 eV) for O on a B site and a weaker for O above a B—N bond (3.29 eV). In the former configuration, the oxygen is stabilized by charge transfer from the metal substrate to the O atom, rendering the oxidized *h*BN metallic. Interestingly, the adsorption site and the energy barriers for migration between the two sites is controlled by charge injection. For example, addition of one electron would promote motion of the O atom from a B—N position to a B site, thus switching the electronic properties of the *h*BN sheet [506].

Preliminary experiments on adsorption of single Co atoms on *h*BN/Cu(111) performed in the author’s group reveal the coexistence of Co species featuring different apparent heights, presumably due to interaction with hydrogen, and show a high mobility of the Co adatoms under influence of the STM tip at 5 K. Thus, *h*BN/Cu(111) seems less suitable as support for spectroscopic studies on single (Co) atoms than for example *h*BN/Rh(111) (see paragraph 3.1.2).

3.1.6. *h*BN/Iridium(111)

Compared to the many studies addressing adsorption on *h*BN/Rh(111) (see paragraph 3.1.2) the interaction of atomic species with *h*BN/Ir(111) is less explored. Recently, Will et al. studied Ir, C, and Au on *h*BN/Ir(111) and addressed the formation and stability of cluster superlattices by means of STM and complementary DFT modeling (for the Ir case) [190]. For Ir, the substrate templated a very regular cluster superlattice with a cluster density n (i.e., number of clusters/moiré unit cell) of ≈1, where the average cluster size can be controlled from about 65 to 175 atoms by the amount of deposited Ir. The Ir cluster superlattice does not degrade up to 700 K. A gradual decay of the array sets in around 800 K, with clusters coalescing (Smoluchowski ripening) and intercalation starting at higher temperature (see Fig. 25(a–c)). The site-specific cluster growth in the pores of *h*BN/Ir(111) and the high thermal stability was rationalized by DFT calculations, which show that in the pore areas, the *h*BN can adopt an sp^3 hybridization in the presence of an Ir heptamer, forming strong Ir-cluster-atom - B bonds and enhancing Ir-substrate-atom - N bonds [190]. For the C case (Fig. 25 (d)), cluster arrays formed that can sustain temperatures up to 1350 K. For the Au case (Fig. 25 (e)), deposition of 0.3 ML at rt resulted in cluster arrays with $n = 0.9$ including monolayer to trilayer clusters [190].

Simonov et al. used a multi-technique approach (PES, NEXAFS, LEED) to characterize the rt adsorption of atomic oxygen on *h*BN/Ir(111), dosed at 3×10^{-8} mbar [498] (see Fig. 25 (f)). Interestingly, the O mainly incorporates into the sp^2 sheet, replacing N. Only a minority of O atoms intercalates. The O embedding results in four distinct B environments ($BN_{3-x}NO_x$, x = 0,1,2,3) that are reflected in four π^* resonances in the B K-edge adsorption spectrum, thus resolving some ambiguity in the interpretation of previous NEXAFS data on bulk *h*BN [498]. Post-annealing to 873 K results in a further decomposition of the *h*BN lattice, i.e., an irreversible etching in contrast to the situation for graphene/Ir(111).

A recent STM, XPS, and DFT study by Valerius et al. explored the impact of 3 keV Xe^+ ion bombardment on the integrity of *h*BN/Ir(111), highlighting interesting structural phenomena emerging upon annealing the system [521]. Specifically, triangular shaped voids were created at specific locations within the moiré superstructure and Xe could be sealed in (standalone) *h*BN blisters even at rt, an effect attributed to the strong interaction of B-terminated *h*BN zigzag edges with Ir (see Fig. 24 (g,h)) [521]. Furthermore, *h*BN/Ir(111) is one of the interfaces successfully applied for the intercalation of thick Au films [322] (see paragraph 2.1.2).

3.1.7. Comparison and discussion

This section revealed the influence of the metal-supported *h*BN sheets on the physicochemical properties of atomic adsorbates and agglomerates thereof. The templating effect of the nanomesh-like systems was demonstrated for individual atoms and clusters of selected elements. The resulting arrays of nanoparticles represent model systems to explore, e.g., catalytic or magnetic functionalities - and complement arrangements achieved by other means, such as colloidal self-assembly or the diblock copolymer micelle method [544]. Aiming for regular, monodisperse metal cluster arrays on *h*BN, deposition of clusters (Co, Sn, Pd, Pb) pre-fabricated either by BLAG or site-selective cluster sources provided good results [499,501,502,538], offering alternatives to the formation of Au or

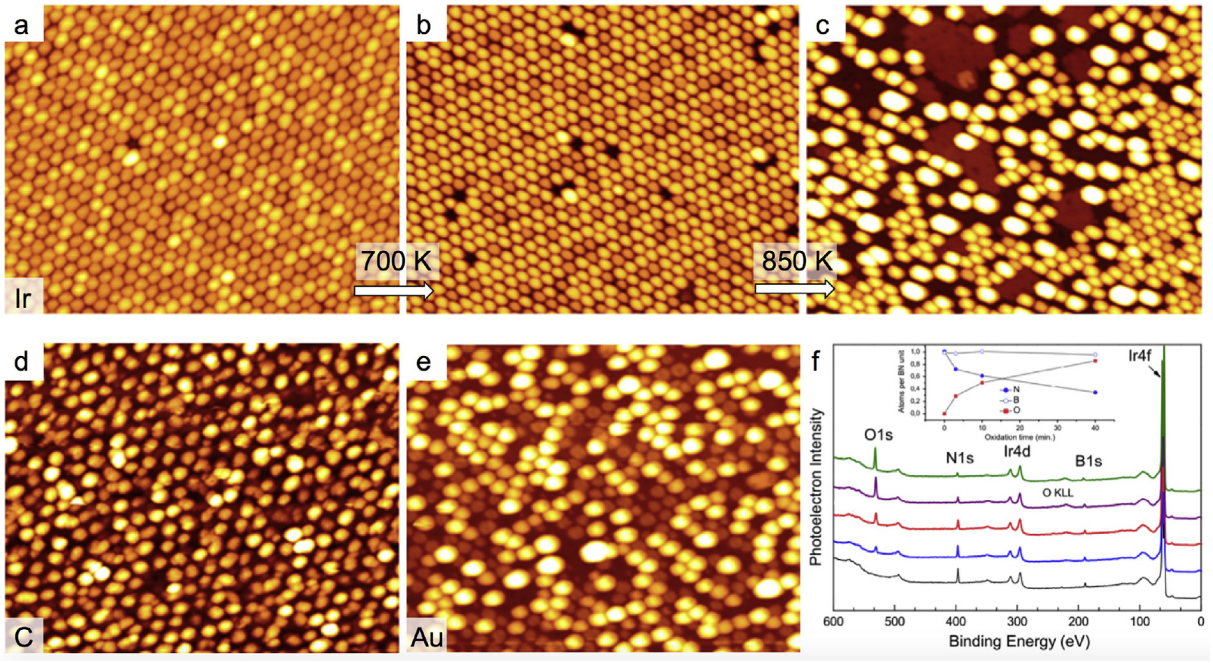

Fig. 25. Atom deposition (Ir, C, Au, O) on *h*BN/Ir(111). (a) STM image of regular Ir cluster superlattice after deposition of 0.57 ML Ir at 350 K. (b) Same sample after annealing to 700 K and (c) 850 K, where intercalated islands are observed. (d) C cluster array after deposition of 0.3 ML C at 400 K. (e) Au clusters after deposition of 0.3 ML Au at 300 K, imaged at 40 K. (f) Overview XPS data with increasing atomic O exposure (Black curve: pristine *h*BN/Ir(111); Blue, red, purple: increasing O treatment; Green: after subsequent annealing to 873 K). The inset shows the overlayer composition with increasing O treatment. (a–e) Adapted with permission from Ref. [190] © (2018) American Chemical Society, (f) Adapted with permission from Ref. [498] © (2012) Elsevier. (For interpretation of the references to color in this figure legend, the reader is referred to the Web version of this article.)

Ir islands via atomic deposition (see below). As discussed for the case of Pd, the *h*BN layer guarantees the integrity of the 3D clusters, which would flatten in contact with Rh(111) [499,500]. The distinct environment on *h*BN gave access to quantum effects, including dynamic Coulomb blockade (in Pb/*h*BN/Ni(111) [495]) or spin state engineering (in Co/*h*BN/Rh(111) [534]). Furthermore, it allowed for the observation and tuning of quantum size effects in Pb and Sn clusters [500,501]. Planar supports (*h*BN/Ni(111) or *h*BN/Co(0001)) might additionally be implemented in well-defined magnetoresistive junctions [545].

Differences between hBN supports*: Au as a case study*. The adsorption behavior was shown to sensitively depend on the element used and the specific properties of the *h*BN/metal support. Here, Au serves as an instructive example, which is also of practical relevance in view of the catalytic activity of (*h*BN-)supported Au clusters [546]. The adsorption energy of a single Au atom on a free-standing *h*BN sheet was calculated to be about 0.1 eV [537]. Upon introducing a Rh(111) support for the *h*BN layer, the adsorption energy is predicted to rise above 1.5 eV [346,517] - highlighting the important role of the metal. Models of small Au aggregates on *h*BN/Rh(111) show peculiar chain-like structures [527]. Experimental data reveal Au aggregates confined to the pores of *h*BN/Rh(111) even at coverages above 1 ML, while some Au islands extend beyond the pore regions on *h*BN/Ru(0001) [321,346], despite some templating functionality providing stable Au cluster on *h*BN/Ru(0001) even at high temperatures [519]. The growth of "replica islands" only reported for *h*BN/Ru(0001) - and reminiscent of Au island growth on graphene/Ru(0001) - was tentatively rationalized by the weaker interaction of *h*BN with Rh(111) compared to Ru(0001) [346] (cf. paragraph 2.2.5). Based on this information - highlighting the influence of the substrate - *h*BN/Rh(111) seems the more suitable template for fabrication of Au cluster arrays. Indeed, Au/*h*BN/Rh(111) was employed to study the response of Au nanoparticles to CO exposure [526]. Hereby, a combined DFT and TPD effort showed that small Au islands bind CO more strongly than bulk Au or larger Au clusters supported on *h*BN/Rh(111). This effect was assigned to CO binding at the periphery of the negatively charged Au islands [526]. Au clusters on *h*BN/Rh(111) also promoted acetaldeyde (CH_3COH) adsorption, which did not occur on bare *h*BN/Rh(111) [535]. The adsorption saturated at about 2 ML of Au, suggesting that the active sites of Au clusters on *h*BN are possibly edge and corner atoms and that the negative charge on the clusters enhances their reactivity [535]. Furthermore, a DFT study based on the WC functional revealed that Au_8 clusters on *h*BN/Au(111) stabilize the O intermediate in the ORR by 1.6 eV compared to the bare *h*BN/Au(111) support. This makes the dissociation of OOH a downhill process, opening a 4-electron reduction pathway of oxygen to H_2O, rationalizing experimental findings on Au-BNNS coated electrodes [528].

Recently, *h*BN/Ir(111) was introduced as an additional template for Au clusters arrays [190]. Whereas the resulting cluster height distribution was rather inhomogeneous, a larger Au cluster density ($n \approx 0.9$) was achieved on *h*BN/Ir(111) [190] than on *h*BN/Rh(111) ($n \approx 0.7$) [346]. Au deposition on *h*BN/Pt(111) at rt yielded 3D clusters with irregular size distribution [524]. This growth mode - differing from the situation on *h*BN/Rh(111) - was rationalized by kinematic effects, such as a larger diffusion length on *h*BN/Pt(111) due to the weaker corrugation [524]. It comes as little surprise that no ordered Au clusters were reported on a smooth *h*BN/Ni(111) support [318].

Finally, Au intercalation was reported at 1050 K for *h*BN/Ru(0001) [321] and at 755 K for *h*BN/Ni(111) [318], whereas it set in at 700 K for *h*BN/Rh(111) [243]. However, as systematic, temperature- and coverage-dependent measurements are only reported for

*h*BN/Rh(111) [243], no conclusion on *h*BN/substrate interaction and *h*BN quality can be deduced from these values.

Comparison to graphene templates. Additionally, the example of Au shows that *h*BN and graphene overlayers on the very same metal support might yield distinctly different adsorbate topologies, as *h*BN/Ru(0001) and graphene/Ru(0001) nanomeshes feature an inverted topography (see paragraph 2.4): While the diffusion of Au adatoms is predicted to be restricted to the confined pore regions in *h*BN/Ru(0001) at rt, the low-lying valley regions in graphene/Ru(0001) are connected to form a continuous domain enabling adatom diffusion over large distances [523]. Experiments on Au sub-ML coverages deposited on graphene/Ru(0001) indeed reveal 2D islands extending over multiple nanomesh cells [547]. The island morphology however resembles the situation for Au/*h*BN/Ru(0001), which is not reflected in the calculations. The comparison of morphology and stability of Au clusters on *h*BN/Ir(111) [190] and graphene/Ir(111) [548] reveals the benefits of the *h*BN/Ir(111) support, that can template cluster superlattices at rt whereas Au clusters are unstable on graphene/Ir(111) and can only be templated by cooling to about 90 K [190]. Nevertheless, it should be emphasized that graphene/Ir(111) acts as a suitable template for other elements as Ir, Pt, W, and Re [548,549]. Nonetheless also the Ir case highlights advantages of the *h*BN/Ir(111) template. Due to the larger moiré periodicity, a larger maximum cluster size is achieved before coalescence sets in Ref. [190]. Furthermore, defect free *h*BN/Ir(111) provides a unique pinning site per moiré cell, whereas graphene/Ir(111) offers two sites [190].

Regarding intercalation, a direct comparison of *h*BN/Rh(111) and graphene/Rh(111) for the case of Mn revealed stronger interactions in the former system, e.g., exemplified by an intercalation threshold temperature exceeding the one of graphene/Rh(111) by about 80 K [513].

The temperature stability of clusters is affected by ripening processes that can considerably differ between *h*BN and graphene overlayers on the very same metal support (see discussion of Au diffusion above). For example, it was shown that Pd clusters on *h*BN/Rh(111) feature an increased stability compared to graphene on Rh(111) or Ru(0001) [502]. It should be noted that the stability of *h*BN/metal interfaces including the nanomesh structures in liquid environments (see section 2.2) opens up fascinating options for cluster-based heterogeneous catalysis beyond the UHV scenario described in this review. For example, a recent study by Fu et al. demonstrates the formation and immobilization of Pd—Fe core shell nanoclusters on BNNS efficiently catalyzing a Suzuki-Miyaura coupling reaction [550].

Intercalation and ion implantation. The above results show that intercalation is applicable in a variety of *h*BN/metal system including *h*BN/Ni(111), *h*BN/Rh(111), and *h*BN/Ru(0001). Here, the focus was not set on the intercalation of thick metal films, mimicking a "new" *h*BN/metal system (see paragraph 2.1.2), but rather on the use of (sub)monolayer amounts of intercalated atoms to engineer the properties of *h*BN and the interface. As the above three interfaces fall into the category of strongly interacting systems (see Fig. 10), intercalation might be operational for most of the systems discussed in chapter 2.2. Indeed, intercalation is well-known from bulk-like *h*BN featuring weak interlayer coupling (e.g., Refs. [315,317,481–483]). This apparently opens pathways to control the electronic structure and the texture of *h*BN terminated supports. Interestingly, experimental and theoretical studies on H intercalated nanomesh structures revealed that structural modifications at the nanoscale can affect the macroscopic (wetting) behavior of the *h*BN materials [335,551]. Complementing intercalation protocols, ion implantation adds the possibility to immobilize noble gases at rt and to create well-defined voids and nano-tents in *h*BN sheets. This strategy was successfully applied on *h*BN/Rh(111) (for Rb, Ar) [496,509,510] and *h*BN/Ir(111) (for Xe) [521]. Thus, *h*BN/metal systems might complement 2D zeolite layers as nanoscale materials for rt noble gas storage [552].

Effects of atomic adsorbates on hBN properties. Complementing the use of the *h*BN to support thin films, decouple and confine atoms, and tune their interaction with the support by site-selective positioning, adatoms in return might be applied to engineer the *h*BN properties. Indeed, theoretical predictions for free-standing *h*BN sheets envision, e.g., a pronounced effect of atomic adsorbates on the (opto)electronic, magnetic, and catalytic properties of the material. A comprehensive summary of such theoretical studies and a discussion of predicted interface properties is beyond the scope of this review. Nevertheless, Table 6 presents a selection of DFT studies addressing the interaction of atomic species with free-standing *h*BN. It is not meant to be complete, but the list of elements and the corresponding literature might serve as helpful reference for (future) experiments on surface anchored or quasi free-standing *h*BN or even motivate such experimental endeavors.

A few selected examples are discussed in the following. H or F functionalization is expected to reduce the *h*BN band gap to about 3 eV [64], with F inducing a considerable magnetic moment (of 0.44 μ_B) on the N sites [553,554]. F is predicted to strongly bind to the B atoms in *h*BN [532,553], in contrast to isolated Li, which is not expected to adsorb on free-standing *h*BN [532]. A considerable magnetic moment on N (1 μ_B) was also calculated by the GGA approximation (PBE functional) for F adsorbed on B sites of a free-standing *h*BN sheet [554]. While a ferromagnetic ground state was deduced in the former study [553], the latter found nearly degenerate ferromagnetic and antiferromagnetic states [554]. Atomic O on free-standing *h*BN sheets attracted also some interest regarding the magnetic properties in these model systems [553,555] and in view of oxidation and bond-rupture in *h*BN [556]. The first principles calculations of Zhou et al. revealed strong bonding of O on top of N atoms and above BN links (adsorption energy exceeding 2 eV). The binding of one O on a B atom or the center of a B_3N_3 ring in a 2 × 2 cell is weaker, but the latter configuration induces a metallic character of the O-BN system featuring a magnetic moment of 2.0 μ_B [555]. At high coverage ($\Theta = 1/8$) Ataca et al. determined a preferred O adsorption on top of B with a ferromagnetic ground state. O was the only species of all evaluated adatoms (bonding: Sc, Ti, V, Fe, Pt, C, Si, B, O, Cu, Pd, and Ni; non-bonding: Cr, Mn, Mo, W, H, N, Ca, and Zn) to show a FM ground state [557]. For an O coverage of 0.5 ML in a 2 × 2 cell, the calculations of Yang et al. in the FLAPW framework yielded preferred O adsorption on top of B atoms and also predict a ferromagnetic ground state for O/BN with a spin magnetic moment of 0.91 (O) and 0.4 μ_B (N) and a Curie temperature well above rt [553]. The optimized structure for a single O atom chemisorbed on *h*BN reported by Zhao et al. is characterized by an adsorption energy of 2.13 eV for O on a BN bond, weakening the latter. Computing the minimum-energy path for O diffusion revealed a motion via N sites.

Systematic DFT calculations of Yazyev et al. - albeit not including a proper description of weak vdW interactions - highlight some trends in adsorption energy and diffusion barriers for adatoms on *h*BN (and graphene) across the periodic table [514].

Additionally, it should be noted that *h*BN decoration offers a basis for subsequent anchoring of adsorbates, as exemplified theoretically by trichloroethylene adsorption on hydrogenated *h*BN [558].

Substitutional heteroatoms. Beyond the functionalization of *h*BN by adatoms, the incorporation of heteroatoms in the sp^2 lattice provides additional means to control interface properties. Vacancy defects - experimentally producible via ion impact as discussed above - can readily interact with atomic adsorbates and dopants [559,560]. For example, Loh et al. modeled the adsorption of hydro-

Table 6
Selected (DFT) calculations for adatoms and their aggregates on free-standing *h*BN sheets and *h*BN bilayers.

Element	Comment	Refs.
H	–	[64,417,583–587]
	no adsorption	[557]
	on *h*BN cluster	[588]
	on $B_{27}N_{27}H_{18}$	[271]
	H, H^+	[589]
Li	–	[504,560,590]
	no adsorption	[532]
Be	–	[590,591]
B	–	[557]
C	–	[383,557,592,593]
N	–	[594]
	no adsorption	[557]
O	–	[358,553,555–557]
F	–	[64,532,553,554]
	on *h*BN cluster	[588]
Na	–	[560,590]
Mg	–	[590,591]
Si	–	[557]
K	–	[560,590]
	very weak binding	[514]
Ca	–	[514,590,591]
	no adsorption	[557]
	very weak binding	[514]
Sc	–	[504,514,557,595]
Ti	–	[504,514,557,595]
V	–	[514,557,595,596]
Cr	–	[595]
	no adsorption	[557]
	very weak binding	[514,596]
Mn	–	[595]
	no adsorption	[557]
	very weak binding	[514,596]
	on armchair nanoribbon	[597]
Fe	–	[514,557,595,596,598]
	on nanoribbon	[599]
Fe_2	–	[598]
Co	–	[504,514,595,596,598,600]
Co_2	–	[598]
Ni	–	[504,514,557,595,596,598,601]
Ni_2	–	[598,601]
Cu	–	[504,514,557,595,602,603]
Zn	–	[595]
	no adsorption	[557]
	very weak binding	[514]
Ga	–	[514]
Rb	–	[560]
Sr	–	[591]
Y	–	[595]
Zr	–	[595]
Nb	–	[595]
Mo	–	[595]
	no adsorption	[557]
Tc	–	[595]
Ru	–	[595]
Rh	–	[514,595,601]
Rh_2	–	[601]
Pd	–	[514,557,595,603]
Pd_6	–	[604]
Ag	–	[580,595]
	very weak binding	[514]
Cd	–	[595]
La	–	[595]
Hf	–	[595]
Ta	–	[595]
W	–	[595]
	no adsorption	[557]
Re	–	[595]
Os	–	[595]
Ir	–	[514,595]
Pt	–	[514,557,595]
PtAg	–	[605]
Au, Au_2	–	[514,536,537,543,581,595,603,606]
	on nanoribbon	[607]
Hg	–	[595]

gen and oxygen on a C-doped nanomesh/Rh(111) by DFT [503]. The atomic species can bind to the modified *h*BN sheet, with the preferred adsorption region (pore, rim, wire) depending on the substituted species (B or N). Furthermore, it was shown that the adsorbate binding energy, which is directly related to the work function, can be modified by an external electric field applied to the nanomesh [503].

Most theoretical reports on substitutional heteroatoms are restricted to free-standing *h*BN. Asides C [561–564] (see paragraph about controlled *h*BN modifications in chapter 4), the substituting elements covered in literature include Be [561,565], O [566], Mg [561,565], Al [567–569], Si [561], Ca [565], Ti [570], V [570], Cr [570], Mn [570–572], Fe [570,571,573,574], Co [570,571,573–575], Ni [570,574], Cu [573], Ga [568], Sr [565], Y [576], Mo [577], Ru [578], Rh [573], Pd [573,579], Ag [573,580], Ba [565], Ir [573], Pt [573], and Au [537,573,581].

A few examples are highlighted in the following, starting with the case of Au: Gao et al. calculated a binding energy increase of a Au adatom from 0.25 eV on pristine *h*BN to 3.48 eV at a nitrogen vacancy [581]. The concomitant charge redistribution at such "impurities" affects the reactivity towards gases and the catalytic properties of doped *h*BN sheets, as we will discuss in paragraph 3.2.6. A recent first-principle study of Mao et al. confirms the strong adsorption of Au in *h*BN vacancy defects (3.17 eV and 3.45 eV for N and B vacancies, respectively), thus approaching the average cohesive energy of Au bulk [537]. Y-doping of a free-standing *h*BN sheet was proposed as a pathway to He sensing, with distinct changes in the UV–Vis adsorption (reflecting the pronounced band gap increase upon He attachment) signaling the interaction with He gas [576]. Edge hydroxylation and O functionalization of *h*BN (i.e., replacing N by O) were predicted to reduce the optical bandgap, and to induce paramagnetism and photoluminescence - effects indeed confirmed by experiments on BNO nanosheets [566]. Incorporation of 3d transition metals (Mn, Fe, Co) into a *h*BN sheet opens pathways to controlled spin state switching via H and F adsorption [571]. Additionally, the 3d dopant's magnetic and charge states can be controlled via external electric fields [582]. An ab initio study by Mitran et al. found that different magnetic ordering (ferromagnetic, anti-ferromagnetic, spin glass) can occur in Mn-doped *h*BN, dictated by the type of substitution [572]. Magnetism can also be introduced to *h*BN by doping with alkaline earth metals (Be, Mg, Ca, Sr, Ba), which additionally increases the optical absorption coefficient in the energy region between 0 and 5 eV [565]. In a recent study, Weston et al. report the formation of small hole polarons upon Be or Mg substitution of B, whereas N replacement by C or Si introduces atomic-like levels in the *h*BN band gap [561,562]. The substitutional doping of *h*BN by Al can introduce metallic behavior in case N is replaced [567]. Furthermore Al - and Ga as another trivalent element - increases the binding energy of glucose and glucosamine by about 1 eV compared to the intrinsic *h*BN sheet [568]. Also regarding thymine adsorption, Al-doping was reported to considerably increase the reactivity of *h*BN [569].

In a comparative DFT assessment, Meng et al. demonstrated that transition metal oxide clusters ($TMO_{3/4}$) are easier to embed in a free-standing *h*BN sheet than the corresponding individual transition metal atoms (TM: Co, Cr, Fe, Mn, Ni, Ti, V), offering means to tune the band gap and the magnetic properties [570].

3.2. Di-, triatomic, and other "small" molecules

Already in the last section few di- and triatomic species (such as CoH and CoH_2) were discussed. These complexes were formed directly on the *h*BN support by hydrogen uptake of individually deposited metal atoms. In contrast, we focus in the following on the adsorption of small molecular entities. For completeness, it should be noted that molecular adsorption studies date back to the 1990s (e.g., Refs. [608,609]) - however using bulk-like *h*BN, featuring a lower binding energy than graphite for most rare gases [608,610]. Compared to the extensive literature on atoms and larger organic molecules, less studies address the interaction of di- and triatomic molecules with *h*BN monolayers on metal single crystals. As evidenced by the selection provided in Table 7, many of these reports base on theoretical efforts, experimental findings are rather scarce. Nevertheless, these systems feature distinct properties and thus deserve a short, dedicated section. Importantly, such model systems can provide a basis for the comprehensive understanding of *h*BN related materials (BNNS, nanotubes, fullerenes, hybrid structures) and their interaction with gaseous species [478]. Specifically, the research on small molecules interacting with *h*BN monolayers on metal crystals is motivated by the following fields:

- As for the case of nanoclusters addressed in the last section, the combination of small molecules with *h*BN has a genuine relation to heterogeneous catalysis. *h*BN/metal interfaces attract interest as potential catalysts, e.g., for oxygen activation and the oxygen reduction reaction.
- The stability of surface-supported *h*BN monolayers in gaseous atmospheres and their resistance towards oxidation and etching needs to be characterized to identify optimized systems for potential applications beyond an UHV environment, specifically in view of catalysis and protective encapsulation.
- (Superstructured) *h*BN/metal interfaces provide templates for spatially confined chemical reactions, either "under cover" after intercalation below the sp^2 sheet or in arrays of "Petri dishes" represented by the nanomesh pores.
- The interaction of water with *h*BN and the corresponding wetting behavior is of general interest in view of the applicability of *h*BN in ambient or liquid environments. While those are explicitly excluded from this review, we nevertheless cover related experimental surface science studies in UHV and summarize the theoretical modeling.
- In addition, small carbon-based molecules attract considerable interest as precursors for graphene synthesis on or below *h*BN sheets. Selected examples of CVD-based graphene growth on *h*BN will be discussed in a dedicated chapter (3.4).

Experimental aspects of gas dosing. From an experimental perspective, high purity gases are usually dosed directly in-situ via leak valves. Water (Milli-Q) was purified by several freeze-and-pump cycles and also dosed via leak valves ([616]). Optionally, thin capillaries terminating in proximity of the sample are applied. For species with low affinity to *h*BN such as H_2 or water, deposition at low sample temperatures is applied. In contrast to the content of the other chapters that focus on experiments performed in a UHV environment, some studies reviewed here were performed at (near-)ambient conditions and thus rely on dedicated setups as ambient atmosphere XPS (e.g., Ref. [228]). In addition, the influence of air exposure on in-situ synthesized *h*BN/metal was checked by prolonged sample storage in ambient air before re-introduction to UHV systems for characterization (e.g., Ref. [301]).

3.2.1. hBN/Nickel(111)

Natterer et al. adsorbed molecular hydrogen on *h*BN/Ni(111) at 10 K and subsequently addressed it at 4.7 K by STM and STS (see Fig. 26 (a,c)) [611]. At low coverage, H_2 readily diffuses and molecular islands only condense at co-deposited Ti adatoms. Upon saturation coverage, H_2 forms a commensurate overlayer with a $\sqrt{3} \times \sqrt{3}$)-R30° structure, with H_2 centered on the *h*BN hexagons. STS dI/dV spectroscopy showed two pairs of conductance steps on the H_2 monolayer, which were assigned to rotational excitations based

on comparative measurements on the H_2 isotopes (HD, D_2) and reported gas phase values of the excitation energies. As the allowed rotational transitions of homonuclear diatomic molecules depend on the nuclear spin state, the STS experiments made it possible to identify para and ortho species of hydrogen and deuterium, respectively, highlighting nuclear spin selectivity in a very small ensemble of molecules [611]. The comparison to H_2/Ni(111) revealed that the decoupling by the *h*BN spacer is required to extract this valuable information by STM-RES. In a follow-up study, Natterer *et al*. extended their work to graphene/Ru(0001, graphene/Ni(111) and *h*BN/Rh(111), validating the applicability of their method to different substrates. The distinct variations in the spectral line shape depending on the surface used (compare Fig. 26 (c) and (d)) were rationalized by a molecular resonance-mediated tunneling mechanism and it was pointed out that local variations in the surface potential - characteristic for the nanomesh structure - gate the molecules and thus shift the resonance [612]. It should be noted that low-temperature adsorption is necessary to confine H_2 to *h*BN/Ni(111): For example, no H_2 adsorption could be detected at 180 K and a hydrogen pressure of 1×10^{-6} mbar [189].

In view of the importance of catalytic reactions involving oxygen (oxidation, oxygen activation, oxygen reduction reaction (ORR)), the interaction of O_2 with *h*BN/Ni(111) was addressed theoretically by several groups (e.g., Refs. [330,358,360,505,614]), with two studies submitted nearly simultaneously ([358,360]). The first study by Kim et al. reports an optimized structure where the O_2 bridges two B atoms, featuring a binding energy of 1.725 eV and relates this considerable interaction strength to electron transfer from *h*BN/Ni(111) to the oxygen [614]. A similar mechanism was operational for NO_2, both on *h*BN/Ni(111) and *h*BN/Co(0001) [614]. Lyalin et al. discuss three adsorption configurations: O_2 placed on top of a B site (binding energy 0.64 eV, Fig. 27(a)), bridging two B atoms (BE 1.51 eV, Fig. 27(b)), and dissociative adsorption with O again on B positions (0.6 eV) [358]. Compared to O_2 on free-standing

Table 7
Di-, triatomic and other "small" gaseous molecules interacting with *h*BN/metal supports. Abbreviations: ann. = annealed, inter. = interaction, intercal. = intercalation, ads. = adsorption, a.a. = ambient air.

Molecule	Substrate	Temp.	Technique(s)	Comment	Refs.
H_2	*h*BN/Ni(111)	10 K	STM	includes HD and D_2	[611,612]
	*h*BN/Rh(111)	10 K	STM	includes HD and D_2	[612]
	*h*BN/Rh(111)	–	DFT	unstable	[539]
	*h*BN/Pt(111)	rt	XPS, UPS, STM	intercal. at 0.1 Torr H_2	[613]
CH	*h*BN/Cu(111)	–	DFT	–	[383]
CO	*h*BN/Ru(0001)	rt	XPS, UPS, STM	intercal. for 0.5 ML *h*BN	[309]
	*h*BN/Co(0001)	–	DFT	–	[614]
	*h*BN/Rh(111)	rt	XPS, NEXAFS, STM, LEED	intercal. at 0.008 Torr, not for H_2, H_2O, O_2	[313]
	*h*BN/Rh(111)	rt	HREEL	no ads. (10 L)	[535]
	*h*BN/Pt(111)	rt	XPS, LEEM	intercal. at 0.1 Torr for ML *h*BN	[283]
	*h*BN/Pt(111)	rt	XPS, LEEM	intercal. at 10^{-8} Torr CO for *h*BN islands	[283]
	*h*BN/Ni(111)	–	DFT	no adsorption	[360]
	*h*BN/Ni(111)	–	DFT	–	[614]
	*h*BN/Cu(111)	–	DFT	–	[402]
NO	*h*BN/Co(0001)	–	DFT	–	[614]
	*h*BN/Ni(111)	–	DFT	–	[614]
O_2	*h*BN/Ru(0001)	rt	LEEM, PEEM	intercal. at 0.1 Torr O_2	[228]
	*h*BN/Ru(0001)	–	STM, AES, LEEM	etching at elevated T	[522]
	*h*BN/Co(0001)	–	DFT	–	[330,614]
	*h*BN/Ni(111)	–	DFT	–	[330,358,360,505,614]
	*h*BN/Pt(111)	rt	XPS, UPS, STM	intercal. at 0.1 Torr O_2	[283,311]
	*h*BN/Cu(111)	–	DFT	–	[330,361,402]
	*h*BN/Cu(100)	rt, ann. at 873 K	STM, XPS, DFT	intercal. after a.a. exposure	[312]
	*h*BN/Cu foil	rt	XPS, SEM	intercal. upon a.a. exposure	[301]
	*h*BN/Au(111)	–	DFT, SEM	experiments on BNNS in solution	[615]
Air	*h*BN/SiO_2/Si	673–1123 K	AFM, Raman	ann. in a.a.	[14]
OH	*h*BN/Ni(111)	–	DFT	–	[358]
CH_2	*h*BN/Cu(111)	–	DFT	–	[383]
OOH	*h*BN/Ni(111)	–	DFT	–	[358]
H_2O	*h*BN/Rh(111)	34–52 K	STM, DFT	–	[616,617]
	*h*BN/Rh(111)	–	DFT, MD	–	[338,551,618,619]
	*h*BN/Ni(111)	–	DFT	–	[358,614]
	*h*BN/Ni(111)	–	DFT	O/*h*BN/Ni(111)	[505]
	*h*BN/Co(0001)	–	DFT	–	[614]
CO_2	*h*BN/Co(0001)	–	DFT	–	[614]
	*h*BN/Ni(111)	–	DFT	–	[614]
	*h*BN/Cu(111)	–	DFT	–	[402]
N_2O	*h*BN/Co(0001)	–	DFT	–	[614]
	*h*BN/Ni(111)	–	DFT	–	[614]
NO_2	*h*BN/Co(0001)	–	DFT	–	[614]
	*h*BN/Ni(111)	–	DFT	–	[614]
CH_3	*h*BN/Cu(111)	–	AFM, Raman, DFT	experiments on Cu foil	[620]
	*h*BN/Cu(111)	–	DFT	–	[383]
NH_3	*h*BN/Co(0001)	–	DFT	–	[614]
	*h*BN/Ni(111)	–	DFT	–	[614]
	*h*BN/Cu(111)	–	DFT	includes NH_2, NH radicals	[296]
C_2H_4	*h*BN/Ni(111)	823 K	LEEM, PEEM	intercal.	[277]
CH_4	*h*BN/Cu(111)	–	DFT	–	[383]
CH_3OH	*h*BN/Rh(111)	140 K	HREEL	–	[242]
CH_3COH	*h*BN/Rh(111)	170 K	HREEL	no ads. (5 L) without Au decoration	[535]
BH_3NH_3	*h*BN/Ni(111)	843 K	LEEM, PEEM	intercal.	[277]

*h*BN/Ni(111) (binding energy 0.06 eV), the considerable interaction with *h*BN/Ni(111) reduces the adsorption distance of the O_2 to half (≈1.5 Å) and weakens the O—O bond resulting in an activation of the molecule. Guo et al. also report a most favorable adsorption configuration where O_2 bridges two adjacent B atoms (binding energy 2.12 eV) and calculated a barrier of 0.83 eV for the dissociation of O_2. Despite the low stability of the resulting O adsorption on B, these sites can promote the dissociation of H_2O, resulting in a hydroxylation of *h*BN/Ni(111) with the OH units bound to adjacent B sites [505]. From an experimental perspective, no reaction of O_2 with *h*BN/Ni(111) was observed at 170 K under UHV conditions [189].

Similar to oxygen, the Ni substrate promotes the binding of two other ORR intermediates (OOH, OH) on *h*BN. In contrast, water - as the final product of the ORR - interacts extremely weakly with *h*BN/Ni(111), exhibiting a calculated binding energy of 0.02 eV that is below the value for free-standing *h*BN [358]. Kim et al. reported a slightly stronger binding for H_2O on *h*BN/Ni(111) (0.061 eV). This weak interaction is in line with the physisorption of CO, CO_2, NH_3, N_2O and NO and strongly contrasts the cases of O_2 and NO_2 discussed above, thus highlighting the selective adsorption of gas molecules on *h*BN/Ni(111) [614]. Abdul Wasey et al. also pointed out the important role of the Ni support and found a favored adsorption configuration with the O—O bond aligned parallel to the surface, bridging two B sites, resulting in an activation of O_2 [360]. Furthermore, they explored the reactivity of the oxygenated *h*BN/Ni(111) by modeling its interaction with CO. To mimic CO oxidation through the Eley-Rideal (ER) mechanism, the geometry of adsorbed O_2 interacting with CO was optimized. Indeed, a spontaneous rupture of the O—O bond and the formation of CO_2 was observed. In a subsequent process exposing the remaining O to CO, another CO_2 unit was formed, recovering a pristine *h*BN/Ni(111) surface (see Fig. 27(b)). Interestingly, according to this study neither CO nor CO_2 bind to bare *h*BN/Ni(111), thus ruling out the Langmuir-Hinshelwood (LH) mechanism for CO oxidation based on co-adsorption of CO and O_2 [360].

Koitz et al. studied the adsorption of the ORR intermediates (OOH, OH, H_2O) on *h*BN/Ni(111) and compared it to the cases of *h*BN/Co(0001) and *h*BN/Cu(111) [330]. In consistency with the earlier studies, the intermediates are found to bind to B sites, with OH adsorbing strongly, preventing the ORR reaction from proceeding (Fig. 27(c)). While the Co case yielded similar results, *h*BN/Cu(111) is particular as the intermediates are bound weaker, yielding energy differences between the different ORR steps that are more favorable for the reaction to occur, thus making *h*BN/Cu(111) a promising candidate for catalyzing the ORR reaction [330]. However - as the authors point out - solvation effects by the water layer, which are not included in this description might sensitively affect the performance of a real system.

Besides the influence of the supporting metal, structural defects can drastically affect the reactivity and catalytic activity of *h*BN, as discussed later for some exemplary cases of free-standing *h*BN sheets. For *h*BN/Ni(111) (and *h*BN/Cu(111)), a first principles DFT study by Gao et al. indeed revealed the important role of B or N vacancies and Stone-Wales defects for the adsorption of O_2 [361]. While N vacancies considerably increase the binding energy of O_2 by about 1 eV, B vacancies slightly decrease it. At most defects, O_2 adsorbs with its molecular axis aligned parallel to the surface, as discussed above for defect-free *h*BN/Ni(111) (see Fig. 27). A boron impurity (replacing N) however induces the dissociation of O_2. These findings highlight the selective interaction of specific defects with oxygen, dictated by charge transfer and the formation of gap states. For example, B vacancies are suggested to be potential active sites for the ORR process discussed above, while N vacancies or SW defects present too large binding energies for O_2. The sensitivity to the defect type was further corroborated by modeling CO oxidation on *h*BN/Ni(111) [361].

In an experimental study combining XPS, LEEM and PEEM, Yang et al. addressed the response of a Ni(111) surface partially covered by *h*BN islands to ammonia borane (BH_3NH_3) and ethylene (C_2H_4) at high temperatures [277]. While no adsorption of the molecular precursors on *h*BN/Ni(111) was reported under these conditions, precursor fragments (B, N, C) were shown to intercalate below non-epitaxial *h*BN islands. These adspecies in contact with the Ni support can than form an sp^2 layer below the initial *h*BN sheet, thus forming a bilayer heterostructure on Ni(111) [277]. This approach comple-

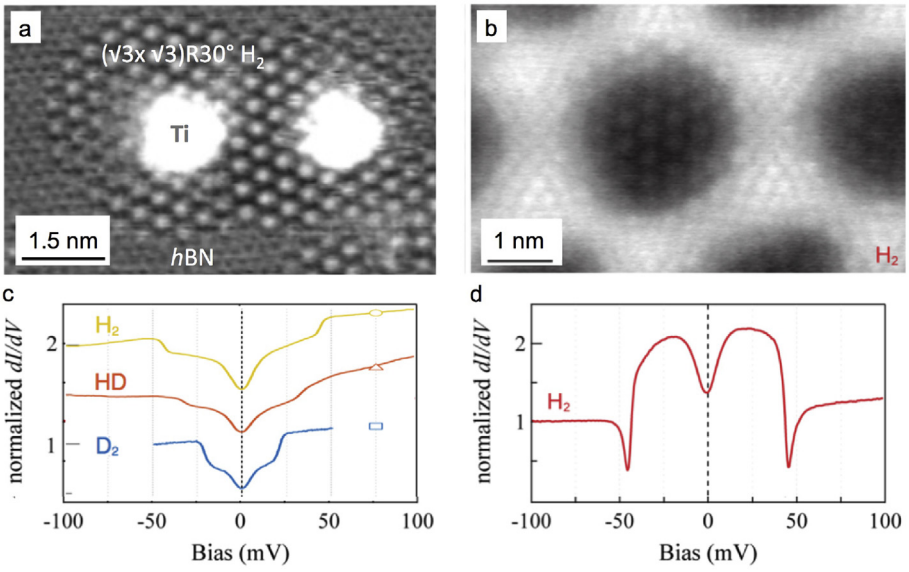

Fig. 26. Molecular hydrogen and its isotopes on *h*BN/Ni(111) and *h*BN/Rh(111). (a) STM image showing a H_2 superstructure around Ti adatoms on *h*BN/Ni(111). (b) STM image resolving H_2 molecules trapped in a nanomesh pore. (c) dI/dV spectra on H_2, HD, and D_2 revealing rotational excitations. (d) Average of dI/dV spectra recorded at the center of an H_2-filled nanomesh pore. Note the distinct differences to the H_2/*h*BN/Ni(111) case. (a,c) Adapted with permission from Ref. [611] © (2013) American Physical Society, (b,d) adapted with permission from Ref. [612] © (2014) American Chemical Society.

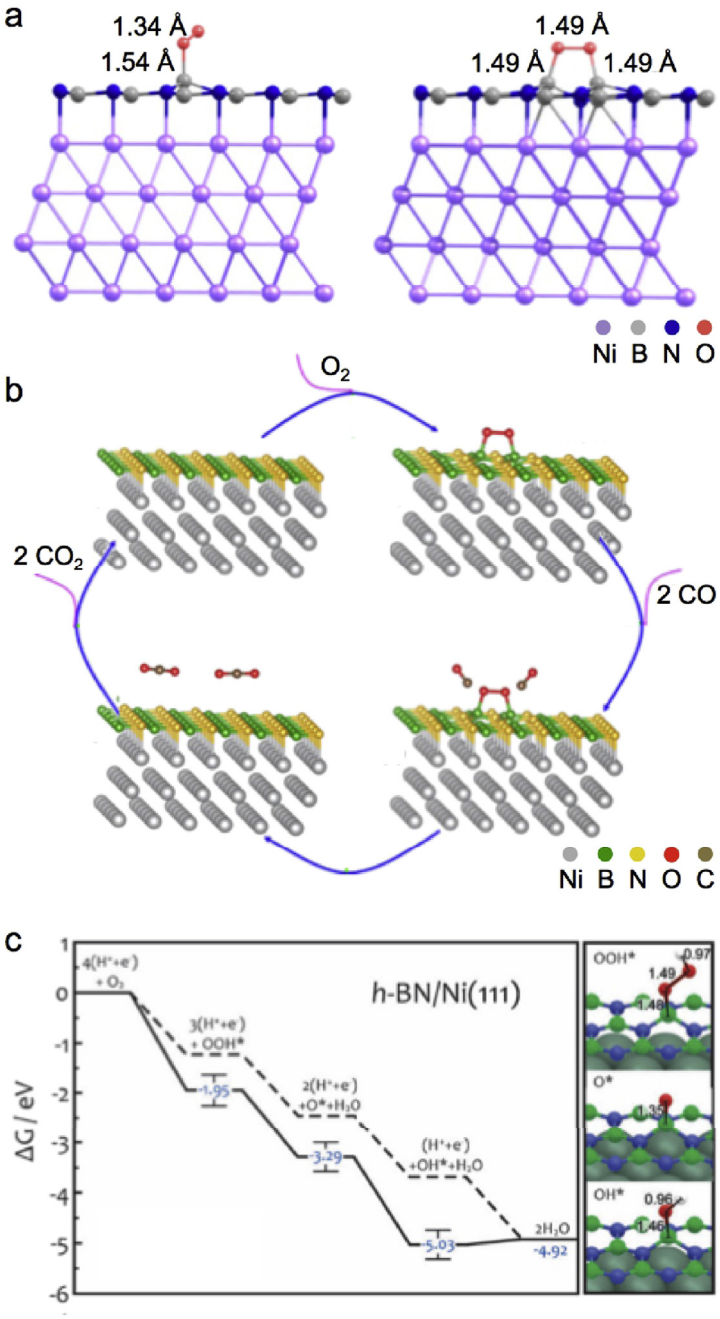

Fig. 27. Theoretical modeling of O_2 interacting with *h*BN/Ni(111). (a) O_2 adsorbed on top of a B site (left panel) and bridging two B atoms (right panel). (b) O_2 adsorption and oxidation of CO. (c) Energy profile of the ORR and optimized adsorption structures of OOH, O and OH intermediates. (a,b) Adapted with permission from Refs. [358,360], respectively © (2013) American Chemical Society, (c) Adapted with permission from Ref. [330] © (2015) Royal Society of Chemistry.

ments studies on *h*BN growth on graphene supported on thin films or foils (e.g., Refs. [621,622]). Heterostructures featuring the inverse sequence, i.e., graphene sheets grown on metal-supported *h*BN will be discussed in chapter 3.4.

3.2.2. hBN/Platinum(111)

Given the importance of Pt for heterogenous catalysis, surprisingly few studies address the interaction of *h*BN/Pt(111) with gaseous adsorbates. Wei et al. used XPS and UPS to characterize the response of *h*BN/Pt(111) to molecular hydrogen [613]. H_2 exposure at low pressure (1×10^{-5} Torr) and rt revealed no modifications of the Pt, B, and N core level signals, evidencing that H_2 does not adsorb dissociatively as on bare Pt(111). Exposure of *h*BN/Pt(111) to high H_2 pressure (0.1 Torr) at rt resulted in a negative shift of the N and B 1s binding energies, which was assigned to hydrogen intercalation, lifting the *h*BN from the support (see Fig. 28 (a)). A hydrogenation of the sp^2 sheet was excluded, as it should result in pronounced positive BE shifts. Heating *h*BN/Pt(111) in 0.1 Torr H_2 at 473 K results in almost complete desorption of hydrogen [613]. Zhang et al. provided insight into the interaction of CO with *h*BN/Pt(111) [283]. Based on LEEM, μ-LEED and STM data they showed that CO intercalates below *h*BN islands at rt already at low CO pressure (5×10^{-8} Torr),

lifting the *h*BN and removing the moiré patterns. On contrary, no CO intercalation was detected at these conditions for a full *h*BN monolayer. Only when applying 0.1 Torr of CO, intercalation was achieved (Fig. 28 (b)). In contrast, CO intercalation was observed already above a threshold pressure of about 5.3×10^{-6} Torr by Ng et al. [313] (see discussion). Interestingly, the CO intercalation is fully reversible around rt when the CO supply is stopped (Fig. 28 (c,d)) [283]. The calculated CO adsorption energy decreases from 1.99 eV on bare Pt(111) to 1.48 eV when adding the *h*BN. This effect was attributed to the confinement effect of the *h*BN cover on the CO, exceeding the one of graphene. The confinement of CO in the "nanoreactor" can thus modify chemical reactions. Indeed, when adding O_2 by intercalation at 0.1 Torr, the CO oxidation reaction proceeds with a lower activation energy than on the Pt(111) surface [283].

3.2.3. *hBN/Copper*

The effects of ambient air exposure were explored for *h*BN on polycrystalline copper [301] and on the (100) surface of a Cu foil [312]. The former study by Kidambi et al. combined XPS and SEM to address sub-ML *h*BN/Cu and a multilayer hBN film on Cu. After prolonged air exposure (4 days or 10 months, respectively) XPS revealed an oxidation of Cu indicating oxygen intercalation even for the multilayer film. Typical XPS binding energies for the *h*BN islands after air exposure are 190.6 eV (B 1s) and 398.1 eV (N 1s), thus presenting a negative shift compared to pristine *h*BN/Cu (B 1s: 191.1, N 1s: 398.6). For the *h*BN islands on Cu, the oxygen intercalation was reversible upon heating to 923 K in vacuum (10^{-6} mbar). Subsequent re-exposure to air for 2 days again oxidized the Cu. Besides intercalation, oxygen interaction with the island edges and defects might play a role in this process. However, if the accumulated oxygen dose was sufficiently high in both systems, annealing to 973 K induces oxygen-mediated etching and disintegration of *h*BN [301] (see Fig. 29 (a,b)). Also for *h*BN/Cu(100) ambient air exposure (20 h or 1 month, respectively) induces the intercalation of oxygen through defects and domain boundaries. Upon annealing to 873 K, three surface structures are visualized by STM. Their area ratio depends on oxygen exposure and annealing time. Besides *h*BN/Cu(100) regions, stripe-like patterns identified as oxygen intercalated *h*BN featuring a $p(2 \times 2)$-O superstructure, and areas where the BN was etched away, exposing $p(2 \times 2)$-O terminated Cu patches were characterized (Fig. 29 (c)). STS showed an increase of the apparent *h*BN band gap to about 5.3 eV in the oxygen intercalated regions, evidencing an electronic decoupling. Accordingly, STS and a comparison to the calculated DOS allowed to distinguish the *h*BN-covered $p(2 \times 2)$-O areas from the "uncovered" $p(2 \times 2)$-O patches, corroborating the assignment by STM [312].

In a DFT approach including dispersion corrections, Lin et al. addressed the interaction of O_2 with *h*BN/Cu(111) and explored its potential for CO oxidation [402], thus also considering O, CO and CO_2 adsorption. O_2 was found to adsorb with its axis parallel to the surface, bridging two adjacent B atoms. Compared to adsorption on a free-standing *h*BN sheet, the binding energy is increased (from 0.11 to 1.17 eV), while the adsorption distance is drastically reduced (from 3.1 to 1.49 Å) and the O_2 is activated, reflecting similar findings on *h*BN/Ni(111) (vide supra). On the other hand, a first principle study by Guo et al. reports the desorption of O_2 formed from two O atoms on *h*BN/Cu(111) [506]. In the study of Lin et al. the oxygen binding goes in hand with a deformation of the *h*BN sheet, approaching the B and N atoms to the Cu support and inducing a charge transfer of about 1.5 electrons to the oxygen. The calculated barrier for the O capture by CO is 0.51 eV. CO and CO_2 do not bind strongly to *h*BN/Cu(111), suggesting that CO_2 can desorb easily from *h*BN/Cu(111) after the reaction. Also the remaining O can be readily removed by an additional CO molecule (barrier 0.07 eV). Thus, the catalyst can be recovered [402]. Along with the results of Koitz et al. discussed above, this highlights the special role of Cu as a *h*BN support for potential catalytic applications [330]. Furthermore, the DFT study by Gao et al. addressed above in the *h*BN/Ni(111) paragraph revealed that distinct defects in *h*BN/Cu(111) might be used to engineer the interaction with molecular oxygen, CO and ORR intermediates [361]. Specifically, B vacancies are suggested as good candidates for ORR catalysis, corroborating the relevance of Cu supported *h*BN sheets.

The work of Wang et al. showed that a Cu foil can catalyze the decomposition of methane - even when covered with several *h*BN layers - thus enabling the CVD growth of graphene on *h*BN [620,623]. In this context, the adsorption configuration of a CH_3 radical on *h*BN/Cu(111) was determined by DFT-D2 calculations (Fig. 29 (d)) and compared to the cases of bare Cu(111), a free-standing *h*BN sheet, and *h*BN bi- and trilayers, respectively. While the radical only shows a very modest binding energy on free-standing *h*BN, the addition of the Cu(111) support leads to strong binding with an energy of approximately 1.7 eV that was rationalized by charge transfer from Cu to C through the

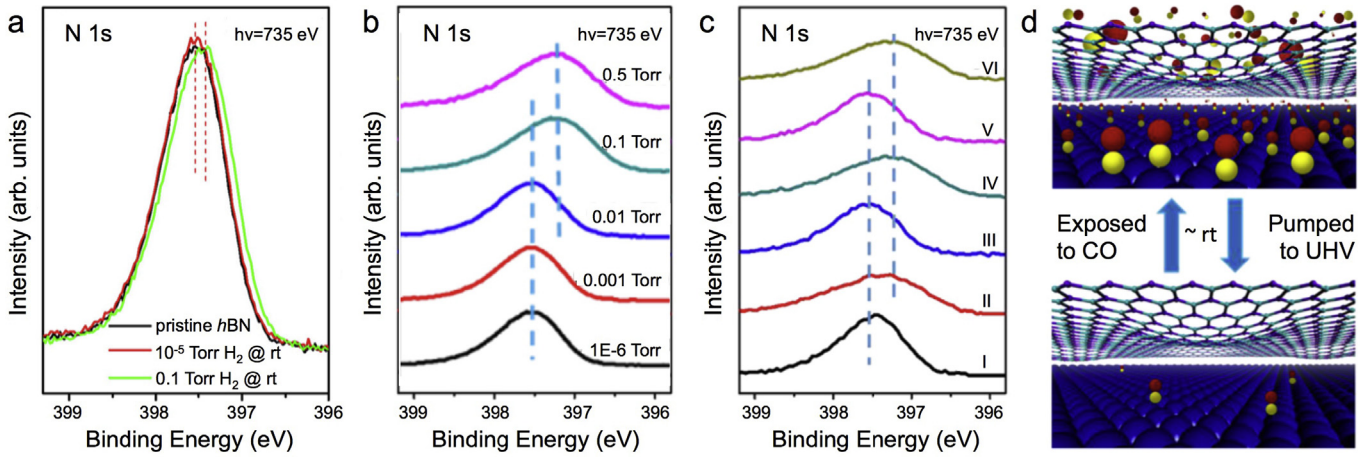

Fig. 28. N 1s XPS signatures of H_2 and CO intercalation in *h*BN/Pt(111). (a) H_2 exposure. (b) CO exposure. (c) Spectral series showing the reversibility of CO intercalation in three exposure-pumping cycles (I-VI). (d) Schematic illustration of the CO intercalated (top panel) and bare *h*BN/Pt(111) interface (bottom panel). (a) Adapted with permission from Ref. [613] © (2015) Springer Nature, (b–d) Adapted with permission from Ref. [283] © (2015) American Chemical Society.

*h*BN spacer (Fig. 29 (e)). Accordingly, the binding energy of the CH_3 radical decreases when additional *h*BN sheets are included [620].

Rationalizing their heterogenous pyrolysis approach introduced to grow *h*BN mono, bi- and tri-layers on Cu(111), Siegel et al. performed DFT calculations on the adsorption of NH_3 and its radicals (NH_2, NH) on *h*BN/Cu(111) and on a free-standing *h*BN sheet [296]. The adsorption of NH_3 on *h*BN/Cu(111) (0.167 eV, adsorbed above a B_3N_3 hexagon) is clearly weaker than on bare Cu(111) (0.819 eV, top site). The radicals however adsorb well on *h*BN/Cu(111) (NH_2: 2.651 eV, on B; NH: 4 eV, on N), suggesting that the dehydrogenation reaction can proceed if NH_3 stays adsorbed, in agreement with the experiment. The adsorption of NH_3 and its radicals on the second *h*BN layer on Cu(111) - described by a free-standing *h*BN sheet (compare Table 8) - is even weaker and the successful *h*BN growth thus relies on coadsorption [296].

3.2.4. hBN/Rhodium(111)

The influence of the *h*BN/Rh(111) nanomesh structure on the low-temperature adsorption and rotational spectra of H_2 was detailed by Natterer et al. [612], as already discussed above in comparison to the *h*BN/Ni(111) case (paragraph 3.2.1, see Fig. 26(b,d)). Next, we address *h*BN/Rh(111) exposed to CO. An in-situ study by Ng et al. using ambient pressure XPS and NEXAFS covering the pressure range from UHV up to 0.2 mbar revealed that at rt CO intercalation sets in at a CO threshold pressure of 0.01 mbar [313]. Once intercalated, the CO remains trapped below *h*BN even after cutting the CO supply. Similar to the systems discussed above, the intercalation induces a negative BE shift of the N 1s core levels. Additionally, the nanomesh corrugation is lifted upon intercalation resulting in a mostly flat layer and the work function is increased by 1.2 eV (Fig. 30(a–f)). The similarity of NEXAFS spectra of bulk *h*BN and *h*BN/CO/Rh(111) further confirm the electronic decoupling by the CO. Annealing to 600 K induces desorption of CO and restores the *h*BN/Rh(111) structure. Interestingly, this study highlighted the chemical selectivity of the intercalation process in *h*BN/Rh(111): Contrary to CO, the molecules H_2, O_2, and H_2O do not intercalate, showing the protective properties of the *h*BN cover for specific gases [313].

The direct observation of water with molecular resolution on *h*BN/Rh(111) reported by Ma et al. in 2010 [616] was followed by a series of experimental and theoretical investigations [338,551,617–619]. STM images recorded after dosing 2 L of H_2O at 52 K showed protrusion forming a hexagonal lattice filling all nanomesh pores, while no ordered structures were detected on the wire regions. The assemblies stabilized in the pores were identified as ice clusters featuring a H_2O bilayer structure fulfilling the ice rules. Based on the dipolar character of H_2O, dI/dz mapping - sensitive to the tunneling barrier and thus to local variations in the electrostatic potential - was applied to access the structure of the clusters assembled from about 40 molecules [616]. DFT-PBE calculations including vdW dispersion corrections screened several distinct structural models for H_2O clusters on a planar, free-standing *h*BN sheet [619]. One structure was favored as it minimizes the total dipole in the assembly. When optimizing the geometry of this structure including the nanomesh support and simulating the corresponding STM image, the main features of the experimental observations were reproduced (Fig. 31 (e,f)) [619]. A follow-up study applied a considerably lower water dose (0.001 L at 34 K), where only parts of the pores hosted H_2O assemblies [617]. The most abundant ice clusters feature three protrusions forming a triangle that can be distorted (see Fig. 31 (a,b)). Based on the lateral dimensions, the considerations of the ice rules (where every molecule provides a proton for a hydrogen bond to an adjacent molecule), and complementary DFT modeling, the majority of these triple-protrusion-clusters was assigned to ice hexamers [338,617,618] (Fig. 31(b–d)). The distorted clusters can reflect pentamers. Within these bilayer-like structures, three of the H_2O molecules adsorb closer to the *h*BN and surprisingly dominate the STM contrast as confirmed with TH modeling, while the others are vertically and laterally offset. Besides the hexamers, also trimers, dimers and individual water molecules were theoretically characterized [338].

A recent study following a hybrid quantum mechanics/molecular mechanics (QM/MM) approach compared H_2O adsorption on

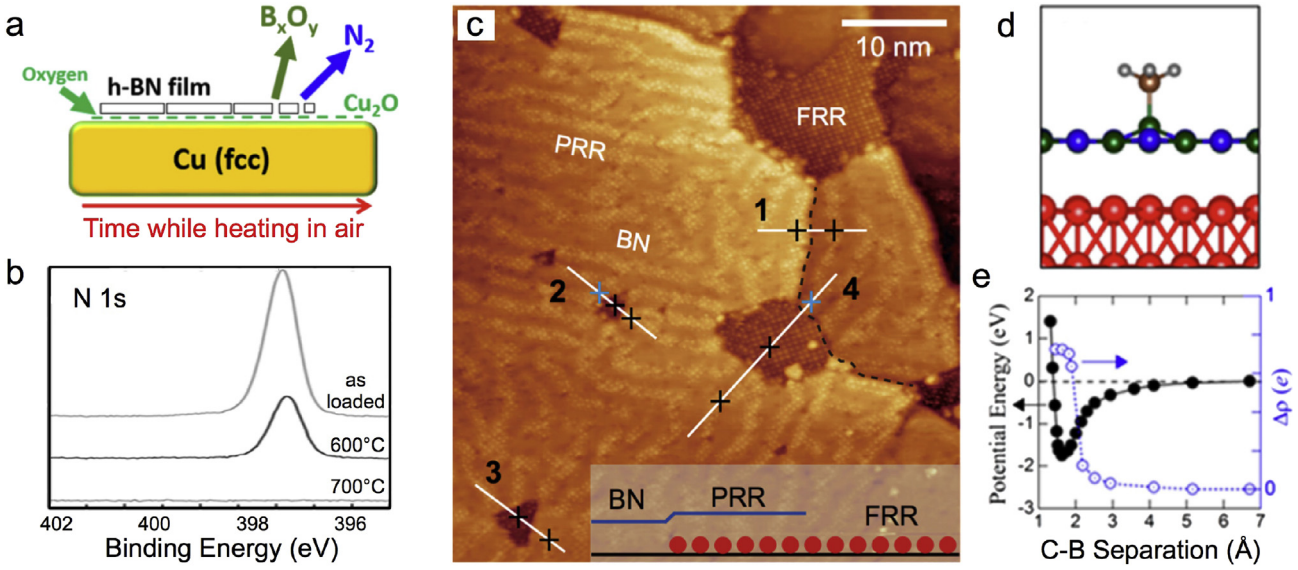

Fig. 29. Interaction of *h*BN/Cu with O_2 and CH_3. (a) Schematic illustration of an oxygen-mediated catalytic dissociation of *h*BN on Cu upon heating. (b) N1s XPS spectra revealing the disintegration of air-exposed *h*BN upon heating in 1×10^{-4} mbar O_2. (c) STM image showing different superstructures after annealing an air exposed sample. The inset depicts cross-sections of three typical regions (Red dots: oxygen atoms). (d) DFT-optimized geometry of CH_3 on *h*BN/Cu(111). (e) Potential energy (black) and charge difference (blue) versus the distance of the CH_3 carbon to the underlying B atom of *h*BN. (a,b) Adapted with permission from Ref. [301] © (2014) American Chemical Society, (c) Adapted with permission from Ref. [312] © (2016) American Physical Society, (d,e) Adapted with permission from Ref. [620] © (2014) American Chemical Society. (For interpretation of the references to color in this figure legend, the reader is referred to the Web version of this article.)

Table 8
A selection of DFT calculations for di- and triatomic molecules on free-standing *h*BN sheets. Please note that the absolute value of the binding energy (rounded to three digits) is listed, as in the text. For further information (e.g., methods, definition of binding energy, adsorption sites, coverage dependence, etc.), the reader is referred to the original publications.

Molecule	Binding energy	Refs.
H_2	no binding	[539,583]
	0.04 eV	[417]
	0.07	[627]
	0.08 eV	[628]
	0.09 eV	[629]
	0.13 eV	[630]
N_2	0.24 eV	[630]
NH	2.26	[296]
	2.42 eV	[594]
NH_2	0.24 eV	[631]
OH	–	[539]
	2.47 eV (on N)	[64]
OH	0.88 eV (radical)	[632]
OH^-	2.3 eV	[633]
CH	2.42 eV	[383]
CO	0.02 eV	[614]
	0.06 eV	[634]
	0.1 eV	[628]
	0.13 eV	[402]
	0.26 eV	[630]
CH_2	2.1 eV	[383]
CHO	2.3 eV (on B)	[64]
CHO radical	coverage dependent	[635]
CO_2	0.02 eV	[614]
	0.05 eV	[636]
	0.10 eV	[628]
	0.19 eV	[402,627]
	0.2 eV	[563]
	0.44 eV	[630]
COOH	no binding	[64]
C_2H_2	0.92 eV (on B)	[637]
CN	4.52 eV (on B)	[64]
NO	0.12 eV	[628]
	0.07 eV (PBE), 0.16 eV (DFT + D)	[634]
N_2	different theory levels	[638,639]
N_2O	0.03 eV	[614]
NO_2	0.03 eV	[614]
	0.13 eV	[628]
	0.55 eV	[563]
O_2	no binding	[360,543]
	0.03 eV	[614]
	0.06 eV	[634,640]
	0.08 eV	[556]
	0.11 eV	[402]
O_3	0.41 eV (on $B_{12}N_{12}H_{12}$)	[641]
I_2	0.47–1.15 eV (on $B_{33}N_{33}H_{22}$), different theory levels	[642]
H_2O	no binding	[64,539]
	0.03 eV	[614]
	0.04 eV (PBE), 0.17 eV (DFT-D2)	[643]
	0.08 eV	[644]
	0.14 eV	[628]
	0.18 eV	[630]
H_2S	0.11	[563]
NH_2	0.33 eV	[594]
	0.86 eV (on B)	[296]
	1.05 eV (on $B_{12}N_{12}H_{12}$)	[645]
	2.58 eV (on B)	[64]
NH_3	0.03 eV	[614]
	0.1 eV	[628]
	0.14 eV	[296]
	0.16 eV (PBE), 0.25 eV (DFT + D)	[634]
	0.41 eV	[471]
	0.48 eV	[646]
CH_3	0.28 eV	[383]
	2.32 eV (on B)	[64]
CH_4	0.16 eV	[627]
	0.27 eV	[383]
	0.33 eV	[630]
SO_4	1.46 eV	[647]
CH_3SH	binds to Al-doped and B-vacancy-defected *h*BN	[648]
CH_2CH_3SH	binds to Al-doped and B-vacancy-defected *h*BN	[648]
NH_2NO_2	0.30 eV (on $B_{24}N_{24}H_{182}$)	[649]
NH_3BH_3	0.32 eV	[650]

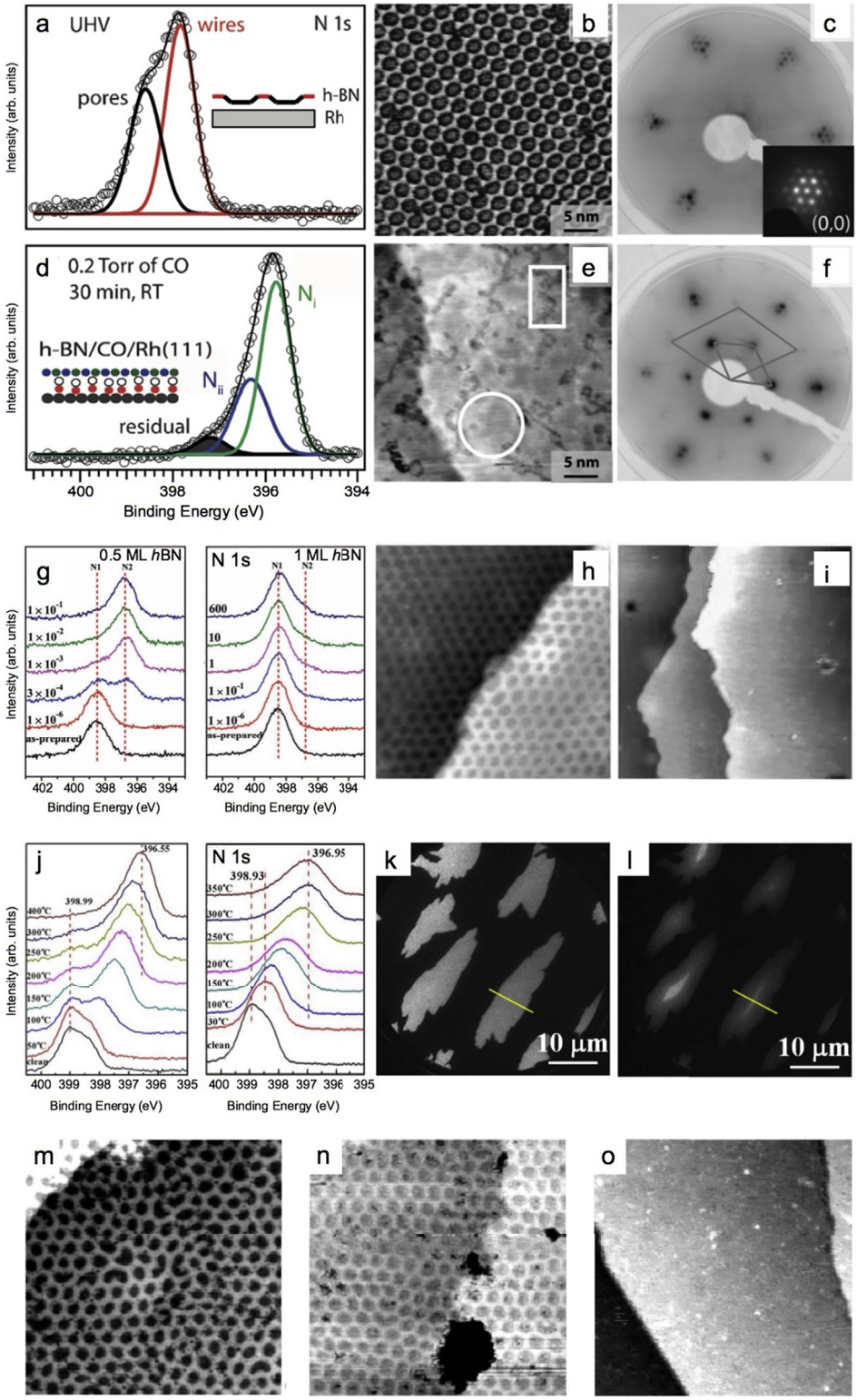

Fig. 30. Interaction of CO and O_2 with *h*BN/Rh(111) and *h*BN/Ru(0001). All the shown XPS data represent the N 1s core level. (a) XPS, (b) STM and (c) LEED data of the bare *h*BN/Rh(111) in UHV. (d) XPS, (e) STM and (f) LEED data after rt CO exposure and intercalation. (g) XPS as a function of CO exposure for a sub-ML *h*BN/Ru(0001) (left panel) and a ML *h*BN/Ru(0001) (right panel). (h) STM image before and (i) after CO intercalation on *h*BN/Ru(0001). (j) XPS under O_2 exposure as a function of temperature for a sub-ML *h*BN/Ru(0001) (left panel) and a ML *h*BN/Ru(0001) (right panel). (k,l) PEEM images during O_2 intercalation showing the initial situation (k) and partial intercalation (l). (m–o) A series of STM images representing bare *h*BN/Ru(0001) (m) and the etched surface after an O_2 exposure of 100 L (n) and 600 L (o) at 873 K. (a–f) Adapted with permission from Ref. [313] © (2015) John Wiley and Sons, (g–i) Adapted with permission from Ref. [309] © (2016) Royal Society of Chemistry, (j–l) Adapted with permission from Ref. [228] © (2015) Springer Nature, (m–o) Adapted with permission from Ref. [522] © (2008) American Chemical Society.

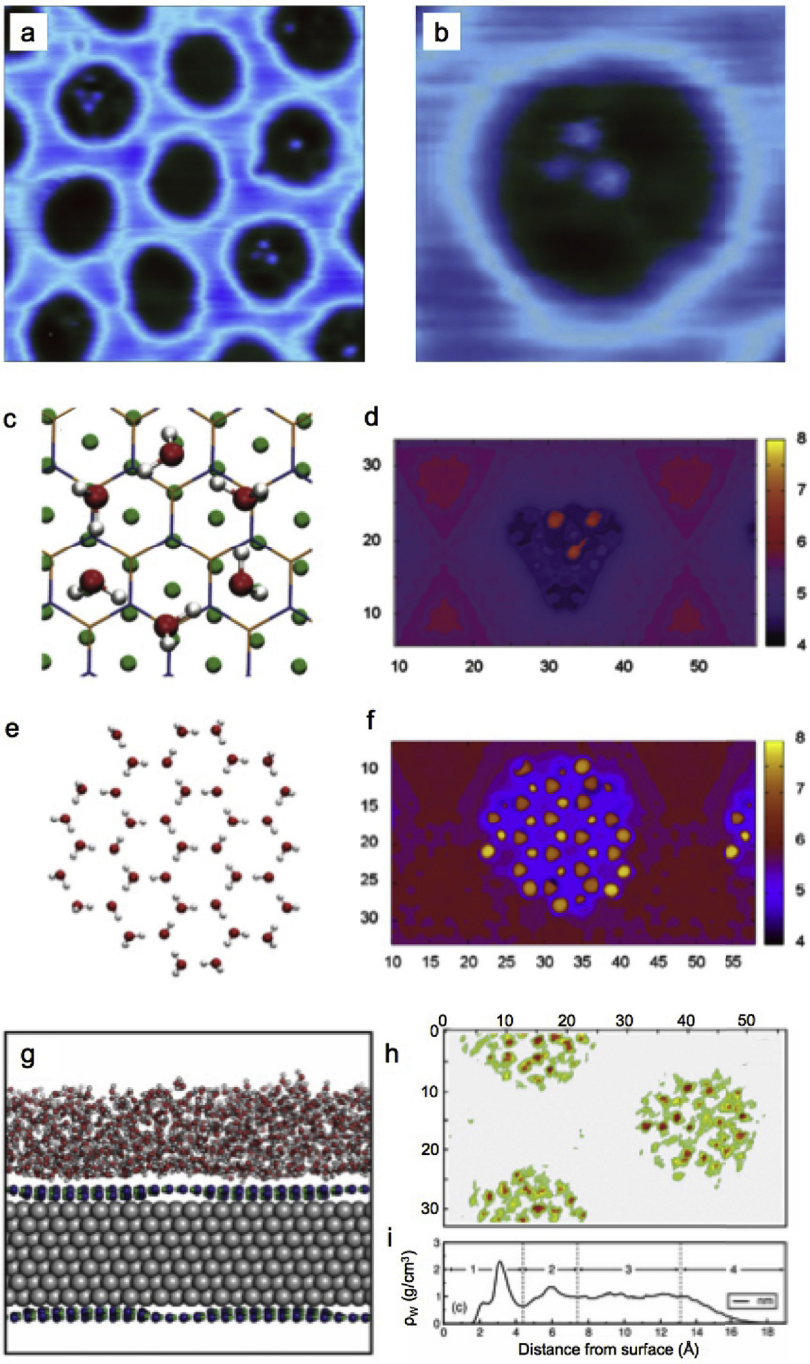

Fig. 31. Water interaction with *h*BN/Rh(111). (a) STM image of ice clusters featuring single- or triple-protrusions. (b) STM zoom-in on a single hexamer. (c) Corresponding structural model and (d) simulated STM image. (e) Structural model of 38 water molecules optimized in a nanomesh pore. (f) Corresponding simulated STM image. (g) Snapshot of the simulation cell of a water film on *h*BN/Rh(111). (h) Spatial distribution of O atoms at a height of 2.3 Å above the nanomesh wire. (i) Plane-averaged water density ρ_W along the surface normal. All numbers in (d,f,h), representing lateral or vertical distances, are in Å units. (a,b) Adapted with permission from Ref. [617] © (2012) American Chemical Society, (c,d) Adapted with permission from Ref. [338] © (2011) American Chemical Society, (e,f) Adapted with permission from Ref. [619] © (2012) IOP Publishing, (g–i) Adapted with permission from Ref. [551] © (2015) Royal Society of Chemistry.

the pristine nanomesh and on the H intercalated, near-planar *h*BN/H/Rh(111) structure (see paragraph 3.1.2), discussing the wetting behavior of these surfaces including structural and dynamic properties [551] (Fig. 31(g–i)). It was found that the nanomesh is slightly more hydrophilic than the *h*BN/H/Rh(111) system. Transferred to a macroscopic scale, these findings predict a smaller contact angle for a water droplet on *h*BN/Rh(111) compared to the H intercalated system [551]. Finally, Farkas et al. addressed the interaction of methanol (CH_3OH) with *h*BN/Rh(111) by HREELS [242]. At 140 K, methanol adsorbs molecularly, but the majority of the molecules desorb at 160 K as inferred from TPD. However, a small part of the molecules - assigned to its metoxy form - stayed stable up to 400 K, in contrast to adsorption on bare Rh(111), where the detection of CO signaled a decomposition of the molecule [242].

3.2.5. hBN/Ruthenium(0001)

Similar to the *h*BN/Rh(111) case discussed above, CO intercalation was explored for (sub-)ML coverages of *h*BN on Ru(0001) [309]. For 0.5 ML *h*BN, rt intercalation proceeded at a CO pressure of 3×10^{-4} mbar. To intercalate a (nearly) full layer (0.9, 1 ML), a CO pressure of 600 mbar was required. Upon intercalation, the B 1s and N 1s core levels shift to lower BE by 1.6 and 1.8 eV, respectively and STM data evidence the disappearance of the nanomesh superstructure (Fig. 30(g–i)). Compared to Ru(0001), CO desorbs from *h*BN/CO/Ru(0001) at a lower temperature and more abruptly, which was assigned to confinement effects as discussed above for CO in *h*BN/Pt(111) [309]. In line with the results for CO, oxygen intercalation below a full *h*BN layer on Ru(0001) requires harsher conditions than in the sub-ML case. *h*BN islands got intercalated at an O_2 pressure of 6.7×10^{-8} mbar at 423 K while 0.133 mbar O_2 were required at rt to intercalate 1 ML *h*BN/Ru(0001) [228]. Here, the negative BE shifts in XPS were measured to be 1.88 eV for B 1s and 2.44 eV for N 1s, exceeding the ones reported for CO intercalation [309]. In addition to XPS (Fig. 30 (j)), the intercalation process was directly tracked in PEEM image series (Fig. 30 (k,l)). An early study by Goriachko et al. combining XPS, AES, LEEM, and STM revealed etching of *h*BN/Ru(0001) by exposure to O_2 at elevated temperatures [522]. On a mesoscopic scale explored by LEEM (with the O_2 pressure restricted to 5×10^{-8} mbar), *h*BN etching sets in at a temperature of 1023 K, starting from macroscopic defects. On a microscopic scale addressed by STM in combination with AES (with the O_2 pressure set to 1×10^{-6} mbar), the threshold temperature was about 873 K. In both cases, the *h*BN was completely dissolved and removed from the Ru support, presumably by forming volatile BO_x and NO_y compounds [522] (Fig. 30(m–o)). The etching must rely on atomic O, thus the dissociation of O_2 which can only occur on Ru and not on *h*BN areas is a prerequisite for the process to happen. This points to the important role of defects in *h*BN to trigger the etching [522]. Indeed, deposition of small amounts of Au on the nanomesh - presumably saturating defect sites - considerably increased the stability of *h*BN/Ru(0001) towards oxygen etching [522].

3.2.6. Comparison and discussion

Two distinct approaches to “small” molecules interacting with *h*BN were represented by the studies summarized above. On the one hand, the specific properties of the *h*BN/metal interfaces were applied to achieve a given process by the molecules adsorbed *on* the *h*BN. Such as, for example, the assembly of supramolecular structures under spatial constraints (e.g., water clusters in nanomesh pores [616,617]), the control of molecular dynamics of physisorbed molecules (e.g., H_2/*h*BN/Ni(111) versus H_2/*h*BN/Rh(111) [611,612]), a selective adsorption [313,614], or the activation and reaction of adsorbates (e.g., oxygen activation and ORR). The majority of such studies relied on low-temperature deposition in a UHV environment or theoretical modeling. On the other hand, harsher conditions including exposure to air and selected gases at (or near) ambient pressure combined with annealing protocols gave valuable insights into the stability of *h*BN/metal interfaces and introduced (reversible) molecular intercalation as a tool to achieve quasi-free standing *h*BN sheets or 2D nanoscale reactors. In the following, we attempt a comparative discussion of selected cases, providing a somewhat more detailed summary of both approaches.

Selective adsorption behavior. From a general perspective, this chapter highlighted the important role of the supporting metal for the reactivity and catalytic activity of *h*BN monolayers. Thanks to the metal - *h*BN interaction, an inert material might be even turned into an active one. For example, according to DFT calculations, O_2 shows a negligible adsorption energy on free-standing *h*BN sheets, but binds considerably on *h*BN/Ni(111) and *h*BN/Cu(111). Interestingly, such an enhancement of the adsorption energy by the underlying metal support is not a general rule, but only affects selected molecules [614]. CO, CO_2 or H_2O are predicted to interact very weakly both with free-standing and metal (Cu, Ni) supported *h*BN. H_2O also desorbs from *h*BN/Rh(111) below rt. Moreover, a selective adsorption was revealed in intercalation experiments on *h*BN/Rh(111): While CO intercalates at given conditions, O_2, H_2, and H_2O do not [313].

In addition, the nature of the metal itself affects the adsorbate - *h*BN interaction, thus influencing predicted reaction pathways. For example, *h*BN/Cu(111) is a promising candidate as ORR catalyst, while *h*BN/Co(0001) or *h*BN/Ni(111) seem less suitable due to strong binding of hydroxyl intermediates [330,358,361,402]. Nevertheless, calculations for O_2 indicate that the difference in adsorption behavior between certain bare metal surfaces might be reduced when covering them with *h*BN. On *h*BN/Cu(111) and *h*BN/Ni(111) O_2 favors bridging two B atoms with a B—O distance of 1.49 Å and similar adsorption energy [358,402]. The adsorption behavior of O_2 on bare Cu(111) and Ni(111) (with its axis aligned parallel to the surface - as in the *h*BN cases) however shows distinct differences. The most stable precursor adsorption sites differ between the two metal supports, so do the adsorption heights and energies [624].

As a word of caution, it should be noted that the level of theoretical modeling and subtle differences in the calculations might affect the results and conclusion, as already discussed in the characterization of *h*BN/metal interfaces (e.g., paragraph 2.2.12). Especially for weakly interacting systems, the range of adsorption energies reported seems considerable (see Table 8). Thus, an experimental implementation and confirmation of the theoretically predicted adsorption and reaction processes is rewarding - notably as studies on *h*BN/metal single crystal samples are rather scarce. While DFT results on model systems nicely match experimental observations for example regarding the successful use of *h*BN covered Au as electrocatalyst for ORR [615] and HER [625] or the parallel orientation of the O_2 axis to a *h*BN support [626], such experiments rely on BN powder or film-supported BNNS.

Interface stability. A comparative assessment of the stability of the diverse *h*BN/metal interfaces based on the experimental reports summarized in this section is tempting. However, this section has revealed that processes like intercalation and oxidation sensitively depend on the structural quality of the *h*BN sheets (completeness of the layer, domain boundaries, wrinkles, etc.). Thus, subtle differences in sample preparation and quality might hamper the recognition of trends and explain some of the apparent discrepancies, especially as different studies rely on complementary (i.e. space averaging versus local) characterization techniques. Nonetheless, some insight might be gained from the following cases. For example, the threshold pressure for CO intercalation in *h*BN/Rh(111) is orders of magnitude higher than on *h*BN/Pt(111), consistent with the stronger interaction of *h*BN with Rh(111) compared to Pt(111) (see section 2.4) [313]. Here, the chemical potential of the gas at a given pressure and temperature indicates if the energy cost for lifting the *h*BN might be overcome, thus enabling intercalation [313]. Accordingly, rather subtle variations in the binding energies of adsorbed *h*BN sheets can translate into pronounced changes of intercalation threshold pressures [313]. Within the same system (e.g., *h*BN/Pt(111), paragraph 3.2.2), the considerable differences in reported pressures applied for CO intercalation are nevertheless not easily rationalized. Under the conditions CO intercalation was observed in *h*BN/Ru(0001) [228], it did not occur in *h*BN/Rh(111) [313]. This is not in line with the interaction strength of *h*BN with Ru(0001) exceeding the one of Rh(111) (see section 2.4). However, an inferior structural quality of *h*BN/Ru(0001) might explain this effect (see paragraph 2.2.5) [226], as the important role of defects in *h*BN/Ru(0001) was recognized,

e.g., in oxygen etching processes [522]. In addition to the adsorption energy of *h*BN, the interaction of *h*BN edges with the metal support influences the intercalation processes for incomplete *h*BN layers. For example, the easier oxygen and CO intercalation under *h*BN islands on Ru(0001) compared to their graphene counterparts was tentatively attributed to B and N edge atoms binding weaker to Ru than the corresponding carbon atoms [228,309]. Furthermore, the interfacial interaction energies of the gas, as well as kinetic factors and entropic contributions would need to be considered for a complete description of the intercalation process (and the threshold pressures).

Naturally, also the oxidation resistance of *h*BN at elevated temperature is reduced by the metal support. Etching of *h*BN/Cu, *h*BN/Ir, and *h*BN/Ru(0001) was reported at temperatures as low as 873 K [312,498,522], whereas free-standing *h*BN monolayers and multilayers can sustain temperatures up to 1123 K. Also in this respect, defects in the *h*BN sheets, e.g., exposing bare metal surface and providing atomic adsorbates via dissociation are relevant.

The above discussion demonstrates that *h*BN/metal interfaces might readily be modified by rt exposure to air and other selected gases. However, the threshold parameters for such modifications, their magnitude, and their impact on the nanoscale structure seem ambiguous. For example, the *h*BN/Rh(111) nanomesh superstructure was shown to survive in ambient atmosphere up to 60 h (XRD, STM) [232], while it vanished after only 30 min at 0.2 Torr CO (LEED, STM) [313] - with the CO partial pressure being comparable in both situations. Importantly, part of these exposure-induced effects are reversible when a UHV environment is restored. In these cases the initial *h*BN/metal structures can be recovered, often requiring a thermal annealing step (e.g., CO de-intercalation occurs from *h*BN/Pt(111) at rt, from *h*BN/Ru(0001) at 500 K [309], and from *h*BN/Rh(111) above 600 K [313], respectively). The conditions for an activation of irreversible *h*BN modifications following O_2 exposure seem less clearcut. For example, oxygen intercalation in *h*BN islands on Cu was reversible when annealing to 923 K as long as the previously accumulated O_2 dose was sufficiently low - otherwise etching occurred [301]. Unfortunately, based on the experimental evidence available, it is thus hard to precisely and reliably position the distinct *h*BN/metal interfaces on an imaginary scale ranging from “absolutely inert” to “highly (re)active”.

Effects of molecular adsorbates on hBN properties. Importantly, beyond the choice of the support, the electronic and magnetic properties as well as the catalytic activity of the *h*BN sheet *itself* might be tuned by molecular adsorbates, similar to the modifications by atoms discussed in paragraph 3.1.7. Numerous studies mainly applying first principle calculations to free-standing *h*BN explored such protocols, including functionalization by adsorbates, doping, application of strain, or the use of electric fields - often in comparison to related low-dimensional BN materials as nanotubes and fullerene-like BN cages (e.g., Refs. [478,651–654]). A comprehensive coverage of this field is beyond the focus of this review. Nevertheless, we list a selection of reports on “small” molecules interacting with free-standing *h*BN sheets in Table 8. These examples should highlight the potential of molecular adsorbates to modify *h*BN, also in view of potential future experimental endeavors on surface supported model systems. Several of these theoretical studies were already addressed above in direct reference to experimental findings and are not discussed again. Here, we briefly cover two additional cases. Bhattacharya et al. applied DFT to systematically explore the band gap engineering of *h*BN by a variety of groups including OH, CN, NH_2, CH_3, CHO, where particularly the latter two resulted in a pronounced reduction of the electronic gap (to about 0.3 eV for CHO) [64]. Tang et al. addressed modifications of *h*BN induced by NH_x (x = 0,1,2) adsorption, revealing impurity levels in the gap, charge transfer towards the adsorbates and the emergence of a magnetic moment of 1 μ_B for the N and NH_2 cases [594].

Modification of the hBN sheet. Beyond such modification of intact *h*BN sheets, structural defects in the free-standing *h*BN layer (e.g., vacancies or heteroatoms) can play a pivotal role (see section 2.3 and paragraph 3.1.7). For example, B vacancies in *h*BN promote the adsorption, activation and subsequent dissociation of CO_2 [636] or can bind mercaptans that do not adsorb on pristine *h*BN sheets [648].

N doping of *h*BN yielded adsorption energies for ORR intermediates that are quite similar to the case of Pt(111), thus suggesting promising catalytic properties [655]. The influence of C atoms either replacing B or N on the activity of *h*BN was explored for O_2 activation [564], CO oxidation [656], and the adsorption of H_2S and NO_2 [563]. While the C substitution at B sites was found to be energetically less favorable compared to the N sites [563], it induces electron doping of the *h*BN sheet turning it into an n-type semiconductor-like material promoting O_2 activation [564] and a CO oxidation activity superior to Au_{55} or Pt_{55} clusters [656]. C substitution at N sites on the other hand greatly enhanced the adsorption energies of H_2S and NO_2 to 0.55 and 2.4 eV, respectively (compare Table 8) [563]. Deng et al. showed a selective enhancement of molecular adsorption energies on C-doped *h*BN. Specifically, the C defects enhanced the binding of O_2, NO, NO_2, CO_2, and SO_2, but did not affect the adsorption of H_2, N_2, CO, NH_3 [657]. Si substitution was found to occur most likely at B sites, inducing a magnetic moment of 1 μ_B and enhancing the reactivity of the *h*BN towards CO, NH_3, O_2 and NO [634]. Furthermore Lin et al. showed how a Si impurity at a B position activates O_2 and offers prospects for CO oxidation [658]. All these examples highlight the potential of engineered *h*BN sheets for metal-free catalysis.

In addition, substitutional doping by a series of metal atoms (Cu, Ag, Au, Pt, Rh, Pd, Fe, Co, Ir) was explored by Lin et al. revealing for example the adsorption of CO and O_2 - activating exclusively the latter - on a Co impurity [573]. Recently, Lu et al. described the catalytic oxidation of CO on such Co sites in detail, highlighting that ER, LH and TER processes might occur at low temperature [575]. The ER reaction barrier was found to be similar than for Fe-doped *h*BN [659], but considerably smaller than for the Cu [602] and Pt [602] incorporation. Additionally, CO oxidation mechanisms were evaluated for Ag- [580], Pd- [579] and Ru-doped [578] *h*BN sheets. The interaction of O_2 and CO with Au atoms embedded in a *h*BN monolayer was explored by Gao et al., addressing adsorption, activation and dissociation processes [536,581,606]. A recent first-principle study of Mao et al. reported a novel trimolecular ER mechanism for the CO oxidation involving two CO molecules bound to a Au defect [537]. Screening the potential of a series of metal dopants (Sc to Zn, Mo, Ru, Rh, Pd, Ag) for the electrochemical N_2 reduction reaction, Zhao et al. showed that Mo-decorated B monovacancies reveal the highest catalytic activity for N_2 fixation at rt [577]. Al doping opens routes to mercaptans (CH_3SH, CH_2CH_3SH) adsorption, which does not occur on pristine, N-vacancy, or SW-defected *h*BN [648].

Besides doping, strain in *h*BN islands might be used to tailor the adsorption energies of small molecules, as exemplified by Neek-Amal et al. for NH_3. A strain of 10% roughly doubled the calculated binding energy [471]. In view of strongly distorted *h*BN structures as nano-domes (see paragraph 3.1.2) achieved experimentally, such a finding is interesting. Finally, Guo et al. predicted that the adsorption of CO_2 can be selectively enhanced when applying an external electric field normal to the *h*BN plane, thus proposing pathways for field-controlled CO_2 capture and release [630]. However, the considerable field strength might impose some challenges for an experimental implementation. Sun et al. theoretically investigated the adsorption of CO_2, H_2, and CH_4 on charged (and neutral) *h*BN sheets [627]. A charge density in the order of $10^{13}cm^{-2}$ on *h*BN drastically

enhances the adsorption of CO_2 and should be applicable to separate CO_2 from its mixtures with H_2 and CH_4. Switching to neutral *h*BN, the adsorbed CO_2 can be released from *h*BN without reaction barrier [627].

In addition to adsorption on free-standing *h*BN sheets, first principles modeling efforts also addressed the interaction of molecules with isolated *h*BN/graphene double-layers, e.g., covering H_2O and TMA [643].

3.3. Larger (metal-)organic molecules

Based on their relevance in biological and artificial systems, "large" (metal-)organic molecules are key elements in surface-, material- and nanoscale-science with prospects for fields as diverse as molecular electronics, heterogeneous catalysis, sensing, or light harvesting. Typical representatives include tetrapyrroles [660,661], fullerenes [662,663], oligophenylenes [664–668], and polyaromatic hydrocarbons [669–675]. Fig. 32 and Table 9 provide an overview of species studied on *h*BN/metal single crystal supports. Their interplay with 2D materials offers tremendous opportunities to design and engineer assemblies with novel functionalities and to tune molecular properties. Naturally, *h*BN sheets were considered early on as spacer layers separating individual molecules or self-assembled structures from metallic supports, complementing graphene as template for molecular self-assembly (e.g., Refs. [90–92,676,677]). The following phenomena - mostly not accessible on metallic supports - were explored on surface-supported *h*BN monolayers [91]:

- Electronic decoupling. Relevant in all the systems studied.
- Site-selective adsorption. Prominent on the topographically and/or electronically nanostructured templates, i.e., *h*BN/Rh(111), *h*BN/Ir(111), and *h*BN/Cu(111).
- Orientational switching with increasing sub-ML coverage. Reported on *h*BN/Rh(111).
- Site-selective gating and charging. Explored on *h*BN/Ir(111) and *h*BN/Cu(111).
- Tip-gated charging. Studied on *h*BN/Rh(111) and *h*BN/Cu(111).
- Intercalation. Reported for *h*BN/Cu(111).

In addition, self-assembly and on-surface reaction protocols - well established on metals - were adapted to *h*BN terminated supports.

Experimental aspects of molecule deposition. Experimentally, the deposition of large (metal-)organic molecules mainly relies on organic molecular beam epitaxy using crucibles filled with high-purity molecular powder heated in UHV or - in case of large and fragile species - electrospray deposition applying dedicated sources [692,693].

3.3.1. hBN/Nickel(111)

The first experiments with "large" molecules on epitaxial *h*BN sheets were performed by the author in the Greber/Osterwalder group in 2002 using C_{60} on *h*BN/Ni(111) [694]. After rt deposition, C_{60} (#6 in Fig. 32) initially forms extended single layer islands with a hexagonal packing representing a 4×4 superstructure with a nearest neighbor separation of 1 nm (Fig. 33 (a,b)). At higher coverages, a layer-by-layer growth was observed. To readily prepare a complete C_{60} monolayer, multilayers were annealed. From the C_{60} desorption temperature from *h*BN/Ni(111) (520 K), a binding energy of ≈1.5 eV was inferred [682]. Upon cooling to 160 K Muntwiler et al. observed a transformation to a $4\sqrt{3} \times 4\sqrt{3}$)-R30° structure by LEED (Fig. 33 (c)). Interestingly, this transition representing a freezing of molecular rocking motion goes in hand with a decrease of the LUMO occupancy of C_{60}. At rt, the LUMO is partially filled by ≈ 0.5 electrons while at low temperature it is almost empty (0.08 e^-) (Fig. 33 (d)). This effect was rationalized by orientation-dependent tunneling between the support and the LUMO combined with electron-phonon coupling stabilizing the charge [682]. A theoretical description of C_{60}/*h*BN/Ni(111) by first-principles calculation showed a most favor-

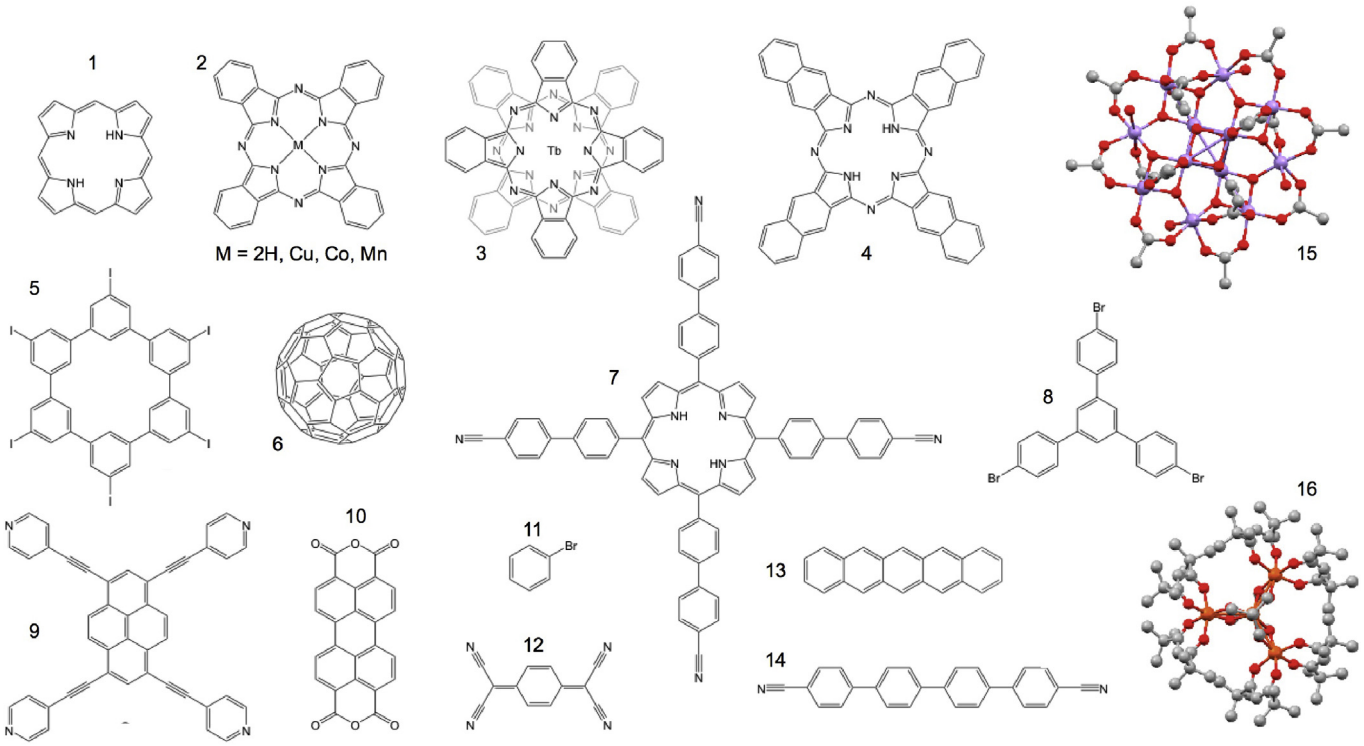

Fig. 32. Chemical structures of selected (metal-)organic molecules studied on *h*BN/metal supports. Compare to Table 9.

Table 9
(Metal-)organic molecules on *h*BN/metal supports. The corresponding chemical structures are displayed in Fig. 32. Abbreviations: P: porphine, Pc: phthalocyanine; NC: naphthalocyanine; CHP: 5,5′,5″,5‴,5⁗,5⁗′-hexaiodocyclohexa-m-phenylene; TPCN: tetra[-(4-cyanophenyl)phen-4-yl]porphyrin; TBB: 1,3,5-tris(4-bromophenyl)-benzene; PTCDA: 3,4,9,10-perylene tetracarboxylic dianhydride; TCNQ: 7,7′,8,8′-tetracyanoquinodimethane; qdc: quaterphenylene dicarbonitrile; Mn_{12}: manganese-12-acetate; Fe_4: $C_{74}H_{128}Fe_4O_{18}$.

# (cf. Fig. 32)	Molecule	Substrate	Technique(s)	Comment	Refs.
1	2HP	*h*BN/Cu(111)	STM, DFT	–	[398]
2	2HPc	*h*BN/Rh(111)	STM, DFT	–	[337]
	CuPc	*h*BN/Rh(111)	STM, DFT	–	[337,339]
	MnPc	*h*BN/Rh(111)	STM	–	[678]
	CoPc	*h*BN/Ir(111)	STM, DFT	–	[251,679]
3	$TbPc_2$	*h*BN/Ru(0001)	XMCD	–	[680]
4	NC	*h*BN/Rh(111)	STM	–	[240]
5	I_6CHP	*h*BN/Rh(111)	STM, DFT	–	[681]
6	C_{60}	*h*BN/Rh(111)	STM	–	[87]
		*h*BN/Ni(111)	STM, UPS, LEED	–	[682]
		*h*BN/Ni(111)	DFT	–	[356]
		*h*BN/Ni(111)	DFT	Fe-doped C_{60}	[683]
		*h*BN/Pd(110)	STM	–	[280]
7	TPCN	*h*BN/Cu(111)	STM	Co metalation	[684]
8	TBB	*h*BN/Ni(111)	STM	dehalogenation	[518,685]
9	Pyrene	*h*BN/Cu(111)	STM	–	[686]
10	PTCDA	*h*BN/Rh(111)	STM, DRS	–	[687,688]
		*h*BN/Pt(111)	STM, DRS	–	[687,688]
11	Bromobenzene	*h*BN/Ni(111)	DFT	dehalogenation	[518]
12	TCNQ	*h*BN/Cu(111)	STM	–	[398]
	F_4TCNQ	*h*BN/Rh(111)	STM, XPS, UPS, DFT	–	[689]
13	Pentacene	*h*BN/Rh(111)	STM, NEXAFS, LEEM, LEED	–	[690]
14	qdc	*h*BN/Cu(111)	STM, MD	–	[691]
15	Mn_{12}	*h*BN/Rh(111)	STM	–	[692]
16	Fe_4	*h*BN/Rh(111)	STM, DFT	–	[693]

able adsorption configuration with a C_{60} bottom hexagon placed on a N site (Fig. 33 (b)). A cage orientation exposing a pentagon towards BN was slightly less stable (0.1 eV). While the calculated adsorption energy of 0.47 eV considerably exceeds the experimental value listed above, the energy difference for rocked C_{60} is very small (0.1–0.2 eV) [356]. Che et al. calculated a minor charge transfer of 0.13 electrons from *h*BN/Ni(111) to the fullerene, being fairly consistent with the experimental low-temperature situation (Fig. 33 (e)). In contrast to the experimental findings, the calculated charge transfer between *h*BN/Ni(111) and C_{60} did not depend on the orientation of the molecule. This discrepancy was tentatively attributed to the role of electron-phonon coupling that can not be treated exactly in the applied calculation scheme. Additionally, vdW interactions were not accounted for in this GGA based theoretical approach, albeit considered to play a relevant role in such interface structures. In any case, compared to C_{60} adsorption on metal surfaces, the calculations confirm a weak interaction with little charge transfer for the fullerenes on the *h*BN terminated surface. Low-temperature STM data recorded on C_{60} monolayer islands on *h*BN/Cu(111) reveal that the fullerene preferably exposes a hexagon to the *h*BN, in line with the theoretical findings discussed above for *h*BN/Ni(111) [695]. Li et al. extended the DFT studies on C_{60}/*h*BN/Ni(111) to explore effects of Fe doping [683]. The interaction of Fe adatoms with (metal-)organic films can be used to tailor the structural, electronic and magnetic properties of such bi-component adsorbate layers [117]. Indeed, the formation of Fe_n-C_{60} complexes with n = 1–4 and n = 15 showed a monotonically increasing charge transfer from Fe to the fullerene with increasing number of Fe atoms. Furthermore, a magnetic moment is induced in C_{60} that aligns antiparallel to the Fe ones. Fig. 33(f–h) represents the Fe_1-C_{60} case featuring a charge transfer of about one electron, highlighting the PDOS, the most stable structure, and the electron density difference, respectively. Generally, the considerable interaction between Fe and C_{60} bases mainly on an ionic character and hybridization between HOMO/HOMO-1 and Fe *s* and *d* orbitals, thus introducing a covalent character [683].

Morchutt et al. used *h*BN/Ni(111) as a platform for dehalogenation reactions yielding covalent assemblies [518]. Deposition of TBB (#8 in Fig. 32) at a substrate temperature of 413 K resulted in dense-packed islands with an oblique unit cell containing four molecules, which is stabilized by close contacts between Br and H (Fig. 34 (a)). This behavior contrasts the adsorption of TBB on bare Ni(111), thus highlighting the influence of *h*BN. On Ni(111), the molecules partially debrominate upon rt deposition and no long-range ordered assemblies are achieved. To induce TBB dehalogenation on *h*BN/Ni(111), the samples were annealed (523–573 K). Indeed, the cleavage of C—Br bonds was achieved, resulting in small oligomers upon covalent bond formation. Long-range order or the formation of extended oligomers was not observed (Fig. 34 (b,c)). This limitation was assigned to considerable interactions between dehalogenated terminal sites with the *h*BN support limiting the mobility. Indeed, DFT modeling yields a diffusion barrier of 1.9 eV for fully debrominated TBB (Fig. 34 (e)). Furthermore, the debromination reaction pathway calculated for bromobenzene - mimicking the TBB's terminal moieties - shows a strong coupling (≈2.5 eV) between C and B atoms [518].

In an attempt to lower the substrate temperature necessary for successful debromination and covalent bond formation, Zhao et al. explored the catalytic effects of Cu and Pd on the Ullmann reaction of TBB on *h*BN/Ni(111) [685] (Fig. 34 (d)). Indeed, adding Cu and Pd lowered the onset temperature of the reaction considerably (by 70 K for Cu, down to rt for Pd) (Fig. 34 (f)). For the latter case, organometallic intermediates were observed after annealing to 453 K, which assemble into regular arrays based on dimeric units. No such intermediates were found for the Cu-catalyzed reaction, reflecting distinctly different reaction pathways for the two metals [685].

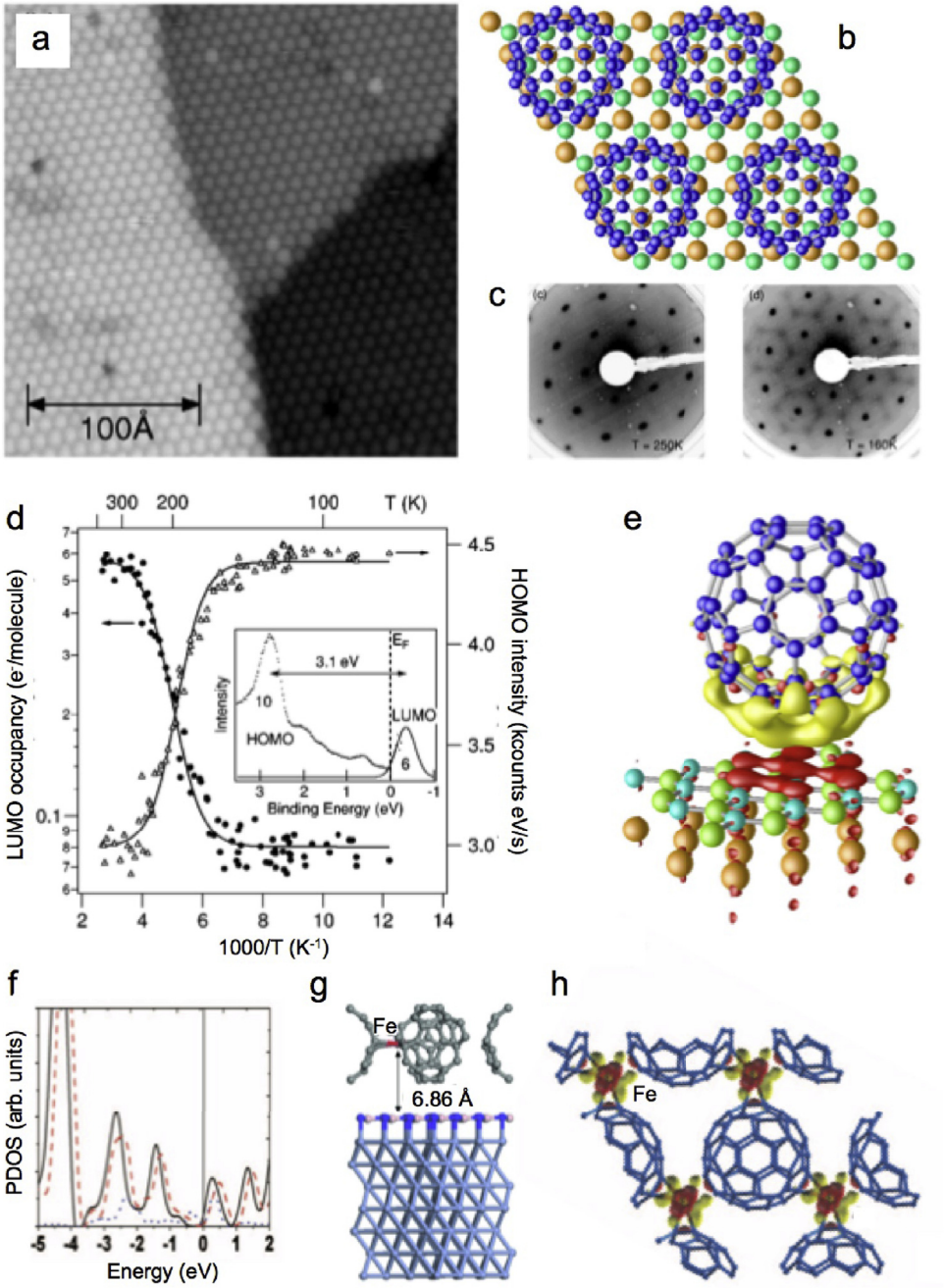

Fig. 33. C_{60}/*h*BN/Ni(111). (a) STM image of C_{60} monolayer at rt. (b) Corresponding structural model of the 4 × 4 superstructure. (c) LEED images at 250 K (left panel) and 160 K (right panel). (d) Occupancy of the frontier orbitals (HOMO, LUMO) versus temperature. (e) Charge transfer plot at the interface (yellow: electron accumulation, red: electron depletion). (f) PDOS of C_{60} (black: GGA, red: LDA) and Fe (blue: GGA) (g) DFT model of Fe_1-doped C_{60} monolayer (side view) (h) Corresponding top view including electron density difference contours (yellow: electron accumulation, red: electron depletion) (a,c,d) Adapted with permission from Ref. [682] © (2005) American Physical Society, (b,e) Reproduced with permission from Ref. [356] © (2005) American Physical Society, (f–h) Reproduced with permission from Ref. [683] © (2010) AIP Publishing. (For interpretation of the references to color in this figure legend, the reader is referred to the Web version of this article.)

In the context of the TBB experiments by Morchutt et al., J. Björk explored the interaction of bromobenzene (#11 in Fig. 32) with *h*BN/Ni(111) by DFT calculations using the rev-vdWDF2 functional. The molecule adsorbs with the benzene ring aligned parallel to the *h*BN surface. Several configurations with very similar adsorption energies (0.65–0.69 eV) and average adsorption heights (3.36–3.29 Å) were reported [518].

3.3.2. hBN/Palladium(110)

C_{60} adsorption on *h*BN/Pd(110) was explored by Corso et al. using STM and LEED [280]. Dense-packed C_{60} monolayers with an intermolecular distance of 9.7 ± 0.7 Å revealed a moiré-like contrast variation. The apparent corrugation at bias voltages between 1 and 2 V (i.e., the height difference between brightest and dimmest C_{60} units) amounts to 0.53 ± 0.12 Å, reflecting the non-planarity of the

*h*BN/Pd(110) template, where different domains coexist (see paragraph 2.2.10). Thus, the corrugation of the template is conserved upon adsorption of one ML C_{60}. Interestingly, C_{60}/*h*BN/Pd(110) is stable even after air exposure [280].

3.3.3. *hBN/Copper(111)*

The topographically weakly corrugated, but electronically superstructured *h*BN/Cu(111) system was used by the author's group as support for tetrapyrroles, pyrenes, oligophenylenes, fullerenes and helicenes. At rt, all individual species are highly mobile on *h*BN/Cu(111), enabling successful self-assembly. The simplest tetrapyrrole - free-base porphine (2HP, #1 in Fig. 32) as a parent compound of the porphyrin family - provided interesting insights regarding the interaction of macrocyclic molecules with *h*BN/Cu(111). First, STM experiments showed a trapping of individual 2HP units and small agglomerates on the low work function areas of the surface upon rt deposition and subsequent cooling to 5 K (Fig. 35 (a)). At intermediate porphine coverage, ordered arrays of 2HP assemblies self-organize on *h*BN/Cu(111) (Fig. 35 (e)). Finally, at high coverage extended layers featuring a porous chiral Kagomé architecture cover all areas of the *h*BN/Cu(111) superstructure (Fig. 36(a)) [398]. Throughout this coverage range, the porphine assemblies base on the same intermolecular arrangement characterized by a nearest neighbor separation of 11.3 Å - in striking difference to adsorption on coinage metal surfaces as Cu(111) and Ag(111), where repulsive interactions induced by charge transfer prevent the assembly of ordered structures at low coverage [696,697]. Second, STS reveals sharp molecular resonances assigned to the HOMO and LUMO, respectively, separated by an electronic gap, evidencing a reduced coupling of the porphines to metallic states (Fig. 36(c)). Third, the lateral modulation of the *h*BN/Cu(111) electronic structure translates to a periodic modulation of the energy of the 2HP frontier orbitals, as visualized by STM, STS, and corroborated by DFT calculations [398]. Interestingly, the electronic decoupling and level alignment induced by *h*BN was operational for all large molecules studied on *h*BN/Cu(111) (see below), while the site-selective adsorption prevails only for selected systems. Specifically, a templated growth following the *h*BN/Cu(111) electronic superstructure upon rt deposition was reported for 2HP, CoP, F_{16}CoPc, and TCNQ (#1,2, and 12, respectively in Fig. 32. See Fig. 35), while extended islands expanding over the different superstructure areas evolved for TPCN, qdc, and C_{60} (#7,14, and 6, respectively in Fig. 32).

The trapping of molecular adsorbates on *h*BN/Cu(111) was tentatively attributed to enhanced molecule-metal interactions in the regions of a low local work function. Indeed, the gap between occupied and unoccupied frontier orbitals is reduced in these area, in line with an enhanced screening by the support. Calculations including DFT-D3 dispersion correction however did not show a relevant difference in binding energy for 2HP on low- and high local work

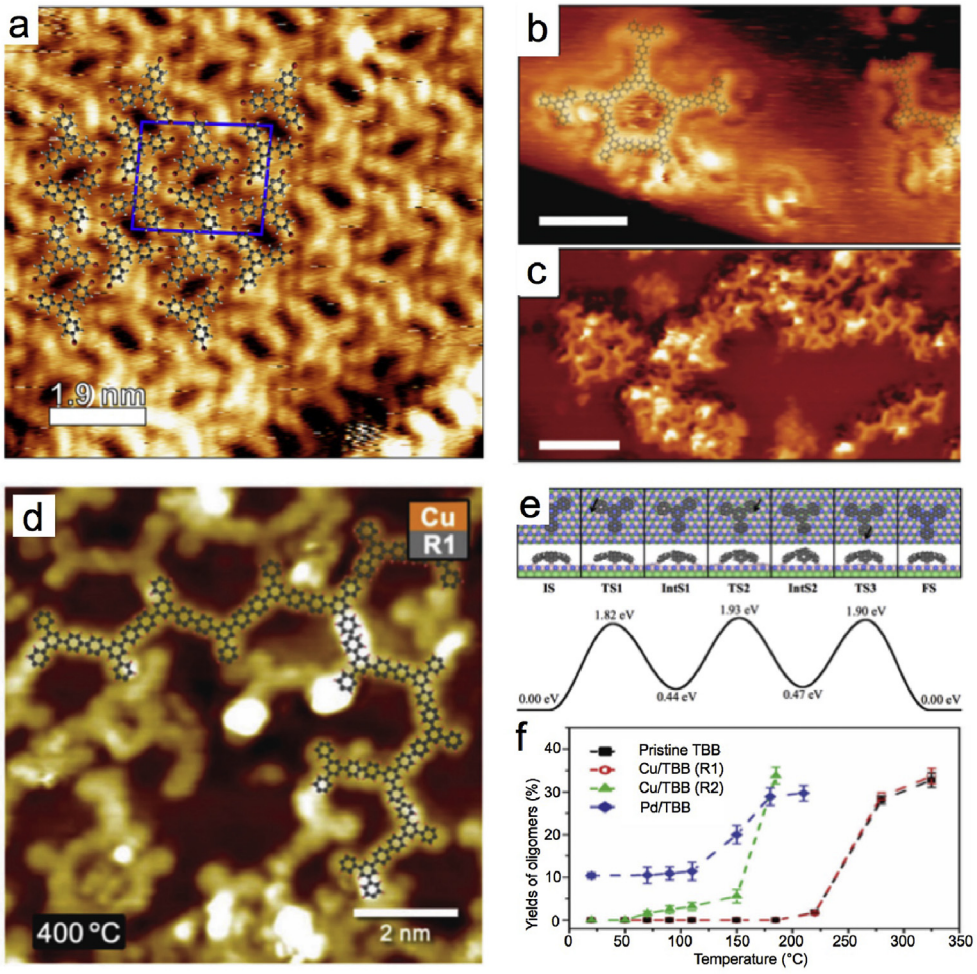

Fig. 34. Covalent coupling reactions on *h*BN/Ni(111). (a) Self-assembled array of TBB (b,c) Reaction products of TBB: Pentagon shaped (b, scale bar 2.6 nm) and extended oligomers (c, scale bar 6 nm). (d) TBB oligomers after rt Cu-deposition and annealing to 673 K. (e) Calculated diffusion path for TBB radical. (f) Oligomer yield versus temperature with and without Cu or Pd adatoms. (a-c,e) Adapted from Ref. [518] © (2015) Royal Society of Chemistry, (d,f) Adapted with permission from Ref. [685] © (2016) Royal Society of Chemistry.

function areas of *h*BN/Cu(111) [398]. Irrespective of the specific trapping mechanism, the lateral confinement of molecules only prevails if attractive inter-molecular interactions are not dominant. Naturally, un-functionalized planar molecules as porphines or phthalocyanines interacting via vdW forces fall into this category. Stronger inter-molecular interactions as H-bonding mediated by terminal pyridyl or cyano groups on the other hand promote the assembly of extended islands (TPCN, qdc). Clearly, the trapping of TCNQ on *h*BN/Cu(111) does not follow this simplistic rule. Here, charge transfer to the well-known electron acceptor TCNQ might play a role. Indeed, a theoretical study on the interaction of TCNQ with a free-standing *h*BN sheet reported a transfer of 0.12 electrons from *h*BN to TCNQ, affecting not only the molecule, but also reducing the band gap of *h*BN. In the lowest energy configuration, TCNQ is placed 3.49 Å above the sp^2 sheet with a binding energy of 0.112 eV [699]. Besides attractive inter-molecular interactions, a molecular coverage approaching the ML limit can be applied to promote the assembly of extended molecular films. While the trapping mechanism is overruled in this situation by the additional adsorption energy, the electronic superstructure of *h*BN/Cu(111) still prevails, being imprinted in the molecular layer as briefly mentioned above. Fig. 36 highlights this site-selective gating effect - i.e., the dependence of the frontier orbital's energy on the lateral position of the molecule on *h*BN/Cu(111) - for four distinct systems, namely 2HP, TPCN, qdc, and pyridyl-functionalized pyrene. In a rough approximation, the periodic energy shift of the molecular orbitals can be related to the periodic variation of the local work function (see discussion). For 2HP, this correspondence was confirmed by DFT calculations. However, this simple vacuum-level-alignment model would yield a rigid shift of the frontier orbitals and thus a constant HOMO - LUMO gap. The experimentally observed gap variations thus indicate that additional mechanisms as site-selective screening might be operational. Furthermore, the spread of the LUMO energies is fairly similar for distinctly different systems, but sometimes exceeds the estimated local work function variations. It is important to note that STM only provides a fingerprint on the electronic superstructure if the frontier orbitals are selectively involved in the tunneling (Fig. 36(b,e,h,k)): Images recorded at bias voltages below the LUMO onset show an identical contrast for all molecules on *h*BN/Cu(111) (Fig. 36(a,d,g,j)) [398,684,691]. Beyond the characteristic variation of the LUMO energy on the length scale of several nm, STM and STS experiments on qdc/*h*BN/Cu(111) revealed a second-level spatial modulation of conductance on the molecular scale. Based on DFT calculations, this bias- and position-dependent submolecular contrast was assigned to excitations of librational modes in qdc during vibronic conductance on *h*BN/Cu(111) [691]. Furthermore, the zigzag shape of given qdc molecules in high-resolution STM images directly indicates a considerable non-planar, chiral conformation, in contrast to qdc in contact with metal, where small interphenylene torsion angles (below 10°) are characteristic [668]. Indeed, MD simulation of a qdc adlayer on *h*BN yield a torsion angle of ≈ 40° and show that one chirality is promoted in a qdc assembly [691].

Deposition of 2HTPCN on *h*BN/Cu(111) yielded regular arrays with a square unit cell containing one molecule, reminiscent of the packing scheme on Ag(111) [701,702]. Exposure to an atomic beam of Co induced both the metalation of the porphyrin macrocycle yielding CoTPCN and the formation of metal-organic coordination networks [684]. The metalation readily occurred at rt while the formation of the coordination architecture was more efficient at elevated temperature (350 K). CoTPCN is characterized by a sharp unoccupied electronic resonance emerging from Co states, giving rise to a characteristic central protrusion in STM images at selected bias voltages. The metal-organic network has a periodicity of 24.1 Å and bases on a distinct 4-fold coordination motif (Fig. 37). In contrast, 3-fold motifs dominate for Co-carbonitrile complexes on metal surfaces. Furthermore, the spectral fingerprints of Co in the porphyrin center and in the coordination node are distinctly different, pointing

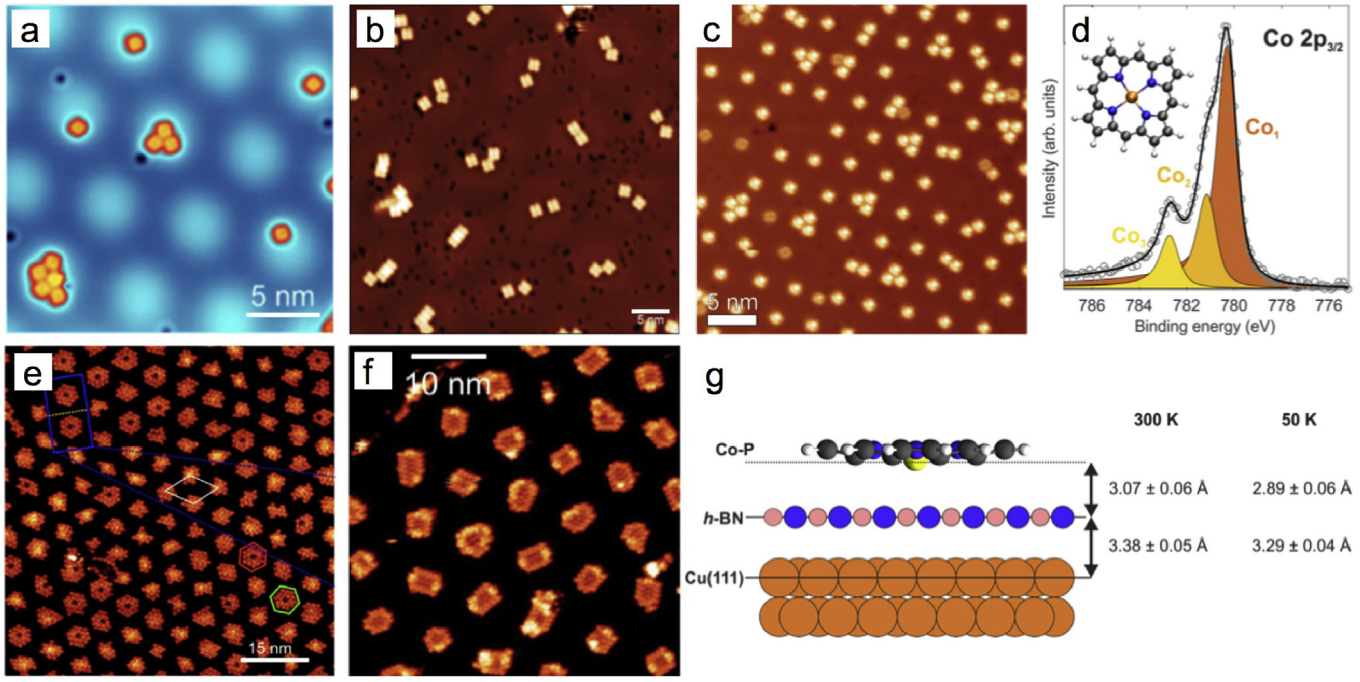

Fig. 35. Trapping of individual molecules and molecular assemblies on *h*BN/Cu(111). (a) Low coverage of free-base porphines (2HP). (b) Low coverage of F_{16}CoPc. (c) Low coverage of CoP with corresponding Co $2p_{3/2}$ XPS signature (d). (e) Intermediate 2HP coverage. (f) Intermediate TCNQ coverage. (g) Average vertical separations in the CoP/*h*BN/Cu(111) structure determined by XSW at two distinct temperatures. (a,e,f) Adapted with permission from Ref. [398] © (2014) American Chemical Society, (b) Adapted from Ref. [698], (c,d,g) Adapted from Ref. [469].

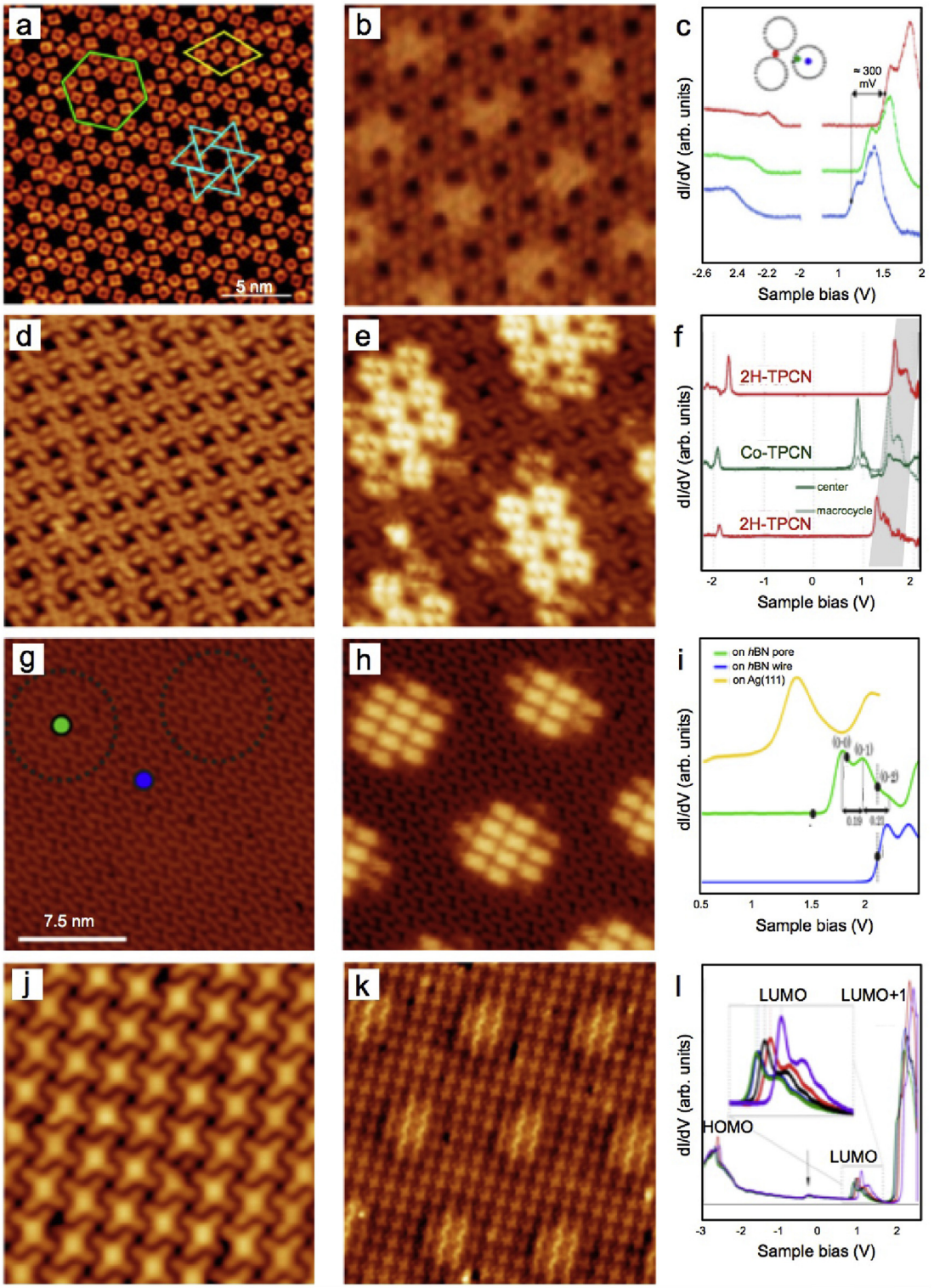

Fig. 36. Electronic patterning of molecular films on *h*BN/Cu(111). Left panels (a,d,g,j): STM imaging in the gap. Central panels (b,e,h,k): STM imaging selectively accessing the LUMO in the pore regions. Right panels (c,f,i,l): Representative dI/dV spectra on characteristic positions of the superstructure, highlighting the shift of molecular resonances depending on the lateral position of the molecule. (a–c) Porphine (2HP). (d–f) TPCN. (g–i) Qdc. (j–l) Pyridyl-functionalized pyrene. (a–c) Adapted with permission from Ref. [398] © (2014) American Chemical Society, (d–f) Adapted with permission from Ref. [684] © (2014) American Chemical Society, (g–i) Adapted with permission from Ref. [691] © (2015) American Chemical Society, (j) Adapted with permission from Ref. [686] © (2016) American Chemical Society, (k,l) Adapted from Ref. [700].

to the formation of a mixed-valence coordination network on *h*BN/Cu(111) [684].

On a different note, *h*BN/Cu(111) was recently employed as a parent material to produce insulator/molecule/metal heterostructures via molecular intercalation [314]. Specifically, Ducke et al. exposed a (sub-)ML coverage of *h*BN/Cu(111) at 470 K to 2HP, resulting in the self-assembly of regular porphine arrays below *h*BN (see Fig. 38(a)). The intercalation was confirmed by combined STM and non-contact

AFM measurements. While the porphines burried below the insulating (and thus electron-transparent) *h*BN sheet can be imaged by STM, the AFM is sensitive to forces and images the atomic *h*BN lattice covering the porphine arrays (Fig. 38(b and c)) [314]. This protocol, reminiscent of the intercalation processes for atoms and small molecules discussed in sections 3.1 and 3.2, enabled the operation of a single-molecule tautomerization switch protected by a *h*BN cover (Fig. 38(d)) and opens perspectives to study chemical reactions in a confined space. Complementary DFT calculations revealed that a configuration based on a porphine unit sandwiched between *h*BN and Cu(111) is indeed energetically favorable compared to an initial state represented by an isolated porphine and the pristine *h*BN/Cu(111) interface (Fig. 38(e)). Accordingly, the rather weak *h*BN interaction with Cu(111) (compare paragraph 2.2.12) might be a prerequisite for the successful intercalation of large (metal-)organic molecules.

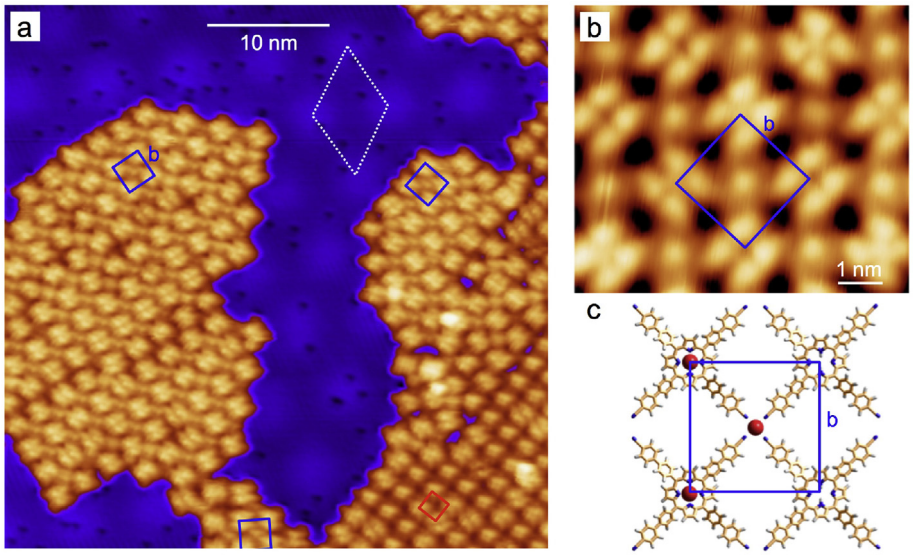

Fig. 37. Coordination network on *h*BN/Cu(111). (a) STM image showing the coexistence of a Co-coordinated TPCN networks (blue unit cells) with a TPCN array (red unit cell). (b) High-resolution STM image of the coordination network. (c) Structural model of the network featuring 4-fold coordinated Co nodes. (a–c) Adapted with permission from Ref. [684] © (2015) American Chemical Society. (For interpretation of the references to color in this figure legend, the reader is referred to the Web version of this article.)

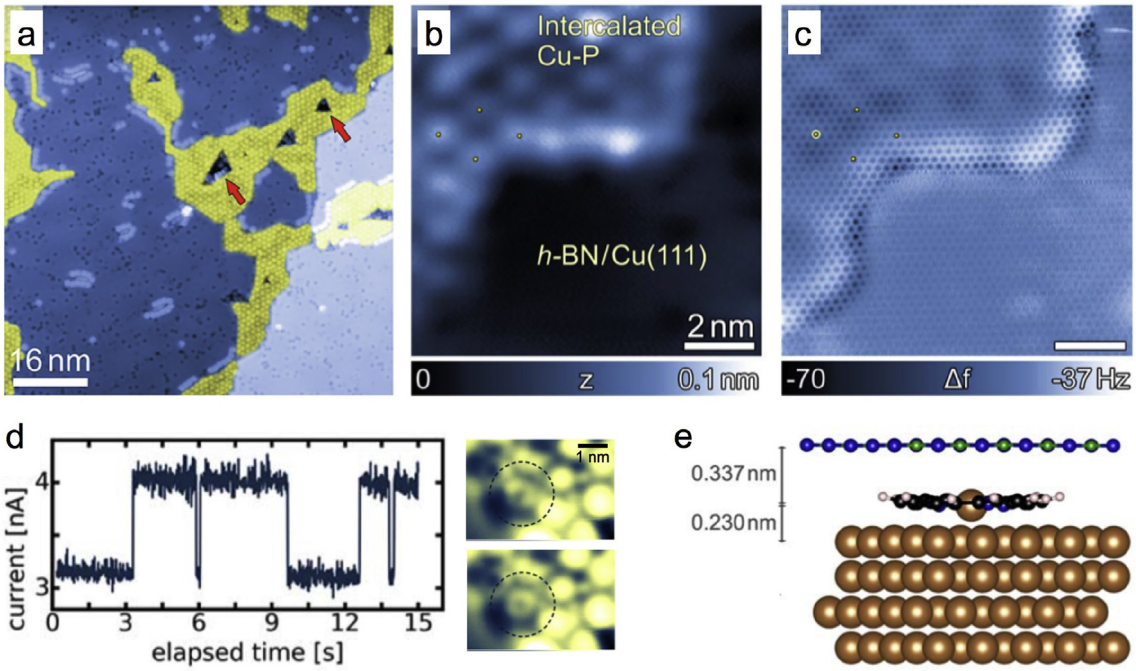

Fig. 38. Porphine intercalation in *h*BN/Cu(111). (a) Porphine arrays (highlighted in yellow) intercalated below *h*BN. Openings in the *h*BN sheet are marked by red arrows. (b) STM image resolving a porphine array below *h*BN. (c) AFM image of the identical area shown in (b) revealing the atomic contrast of the *h*BN cover. (d) Current versus time trace showing the switching between two 2HP tautomers (shown on the right) below the *h*BN. (e) Optimized DFT structure of the *h*BN/Cu-P/Cu(111) interface. Adapted with permission from Ref. [314] © (2018) American Chemical Society. (For interpretation of the references to color in this figure legend, the reader is referred to the Web version of this article.)

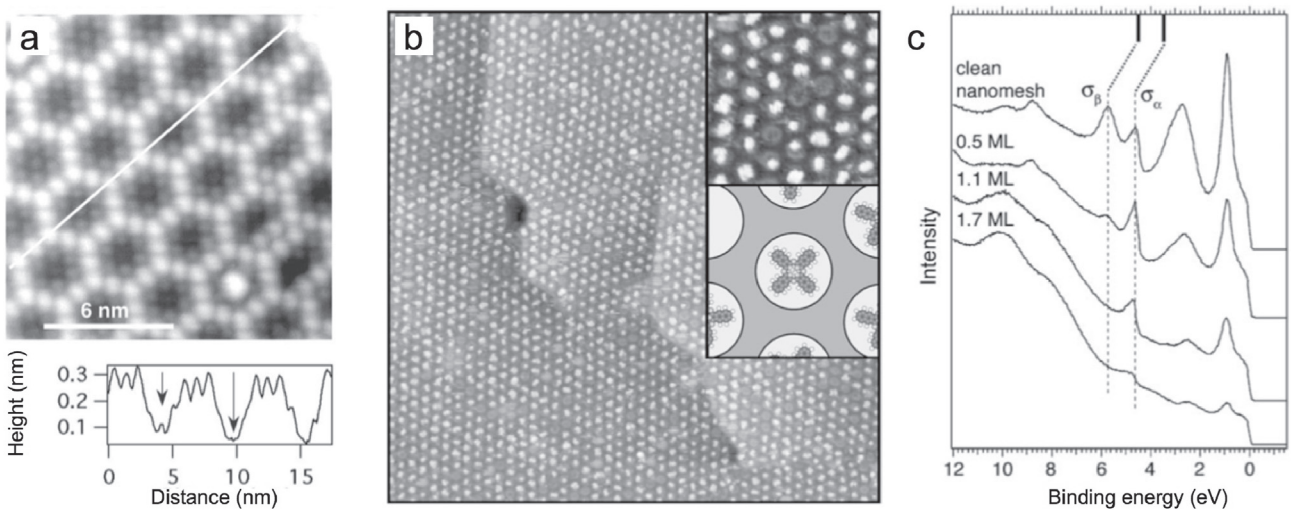

Fig. 39. C_{60} and Nc on *h*BN/Rh(111). (a) Dense-packed C_{60} monolayer. Bottom panel: height profile. (b) Site-selective adsorption of Nc molecules in the nanomesh pores. Insets: Zoom-in image and scheme. (c) UPS spectra with increasing Nc coverage show the attenuation of the pore-related σ band component (σ_β) before the wire-related one (σ_α) is affected. (a) Adapted with permission from Ref. [87] © (2004) AAAS, (b,c) Adapted with permission from Ref. [240] © (2007) John Wiley and Sons.

3.3.4. hBN/Rhodium(111)

The first experimental report on *h*BN/Rh(111) by Corso et al. included the rt adsorption of C_{60} on this nanomesh structure [87]. The periodicity of the *h*BN/Rh(111) superstructure is retained in the fullerene adlayer, where the wire regions are decorated by lines of molecules, whereas six or seven molecules were resolved in the pore areas, yielding an apparent corrugation in the C_{60} monolayer of roughly 2 Å (see Fig. 39(a)).

Berner et al. provided the first evidence for site-selective adsorption on *h*BN/Rh(111) - or more generally on a nanostructured, *h*BN terminated surface. Upon rt deposition, Naphthalocyanine (Nc, #4 in Fig. 32) molecules featuring a diameter of about 2 nm thus closely matching the pore dimensions, preferentially occupy the pore areas at low coverage. The resulting arrays of trapped Nc (see Fig. 39(b)) were reported to be stable at rt with minor inter-pore diffusion and no noticeable desorption of molecules was observed upon annealing to 650 K. Interestingly, the site-selective adsorption visualized by STM was corroborated by UPS experiments. Increasing the molecular coverage, initially exclusively the σ-band branch attributed to the pore areas gets attenuated. Only when pushing the coverage beyond a value where all the pores are occupied, the wire-related σ-band branch gets quenched (Fig. 39(c)) [240]. Also for a slightly smaller Phtalocyanine (Pc) molecule, namely CuPc, a trapping on *h*BN/Rh(111) was postulated based on rt STM data and rationalized with the dipole-ring model developed by Dil et al. for Xe adsorption (see paragraphs 2.2.7 and 3.1.2) [339]. The first clear-cut STM observation for trapping of Pcs at the rim of the nanomesh pores was provided in 2014 by the Gröning group [337]. STM data for coverages below 0.2 molecules per nm^2 recorded at 5 K show that both 2HPc and CuPc exclusively adsorb in the pore areas, with the center of the molecule displaced more than 5 Å away from the pore center (see Fig. 40(a–d)). Two distinct orientations of the Pc's relative to the *h*BN lattice coexist, where a different orientation dominates for 2HPc and CuPc, respectively (Fig. 40(e)). Both the off-center adsorption and two predominant orientation where also found for MnPc/*h*BN/Rh(111) [678]. At 77 K, the molecules moved inside the pores, toggling for example between two opposite off-center positions at a frequency considerably exceeding the STM scanning speed (Fig. 40(g)), but did not leave the pores [337]. These experimental findings were corroborated by DFT calculations addressing the potential energy surface of *h*BN/Rh(111). Iannuzzi et al. determined the off-center position to be 0.2 eV more stable than a position at the center of the pore, while different rotational configurations exhibited only minor energy differences [337] (Fig. 40(f)). The PBE-rVV10 method yielded a maximal adsorption energy of Pc at the rim of the nanomesh pore of 4.26 eV with the dispersion contribution being crucial for the binding. As discussed in paragraph 2.2.7, this theoretical study highlighted the importance of a proper choice of exchange and correlation functionals to precisely describe the *h*BN/Rh(111) structure.

Besides the site-selective adsorption, the Pc/*h*BN/Rh(111) systems revealed two additional properties, namely electronic decoupling and tip-gated charging [337,678]. Constant current STM images showed a bias-dependent intramolecular contrast that was assigned to dominant contributions of frontier orbitals (e.g., Fig. 41 (a,b) represents the HOMO of 2HPc). The 2HPc HOMO is located about 1.2 eV below E_F, the LUMO 0.2 eV above E_F thus yielding an electronic gap of 1.4 eV. For MnPc/*h*BN/Rh(111), the HOMO is observed closer to E_F (0.08 and 0.017 eV, respectively, for the two molecular orientations) and shows vibronic sub-structure with a vibrational mode of 88 meV (710 cm^{-1}) corroborating the reduced electronic coupling to the underlying Rh. Intriguingly, subtle differences in the adsorption configuration of MnPc on *h*BN/Rh(111) yield considerably different topographic and electronic fingerprints of the molecules in STM data that can be summarized in three types. This observations highlights the distinct influence of the *h*BN support on the electronic structure of the molecular adsorbates and foils the simplistic perception of *h*BN/Rh(111) as an "innocent" and inert substrate [678]. Interestingly, MnPc in one of the adsorption types shows a pronounced field-induced charging characteristic, which can be rationalized by a two-barrier model of the tunneling junction, where the applied bias drops both across the tip-molecule and molecule-metal interfaces. Applying an electric field by the STM tip, the MnPc HOMO shifts and loses an electron when energetically aligned with E_F of the Rh(111). This transformation of $MnPc^0$ to $MnPc^+$ is represented by a narrow spectral feature at positive sample bias voltage, a so-called "charging peak" (see Fig. 41 (d)). Accordingly, by changing the bias voltage, the MnPc/*h*BN/Rh(111) can be reversibly switched between a neutral and positively charged state (Fig. 41 (c)).

The electronic decoupling and templating properties of *h*BN on Rh(111) were also employed to study the optical transition ener-

gies of PTCDA (#10 in Fig. 32) for individual monomers and aggregates [687,688]. Low-temperature STM imaging of a low PTCDA coverage deposited at rt revealed the trapping of PTCDA units and small agglomerates in the nanomesh pores (Fig. 42(a)). Regular PTCDA islands were achieved at higher coverage upon annealing at 400 K (Fig. 42(b)). Submolecular contrast was assigned to the HOMO of PTCDA. Opposite to experiments on PTCDA monolayers in direct contact with metal supports, DRS measurements performed for a sub-ML and ML coverage of *h*BN on Rh(111) show vibronic progressions, and thus confirmed an electronic decoupling. More importantly, the optical absorption spectra reveal a distinct coverage dependence. While at low PTDCA coverage, the optical properties come close the ideal case of isolated monomers, molecular aggregation shifts the $S_0 \rightarrow S_1$ transition energy to lower values when approaching a ML coverage (Fig. 42(c)) [687,688].

Pentacene (#13 in Fig. 32), another prominent candidate for molecular electronic applications, was studied by Ng et al. on *h*BN/Rh(111), employing a battery of surface science techniques including NEXAFS, XPS, LEEM, μ-LEED, and STM [690]. Angle dependent C 1s NEXAFS data revealed a transition from flat lying pentacene at low coverage (0.07 ML) to rather upright molecules at higher coverage (0.35 ML) (Fig. 42(f)). Furthermore, the spectral shape resembles the one from gas phase pentacene, indicating at most a weak chemical interaction with the support. These finding were corroborated by the analysis of the coverage dependent C 1s XPS data (Fig. 42(g)). The onset of thermal desorption of pentacene from *h*BN/Rh(111) at a temperature as low as 353 K confirms the weak molecule-surface interaction. STM images recorded at rt revealed a dense, herringbone-like packing of upright pentacenes (Fig. 42 (d)), resembling the structure of upstanding pentacenes on HOPG [703]. μ-LEED patterns showed the coexistence of two distinct domains and the corresponding twins, which were attributed to two different coincidence lattices, i.e., the pentacene overlayer recognizes the hexagonal nanomesh structure of *h*BN/Rh(111) [690]. In comparison to the first pentacene layer, the second layer shows a higher nucleation density and island growth proceeds in a fractal way, indicative of considerable intermolecular interaction between the two pentacene layers (Fig. 42(e)) [690]. In contrast to some of these findings, a wetting layer formed from flat lying molecules was reported for pentacene growth on *h*BN flakes (see discussion) [704]. In this study, DFT calculations on individual pentacene molecules on a *h*BN bilayer revealed an adsorption height of 3.27 Å and an alignment of the molecular axis with the *h*BN zigzag directions [704]. A recent STM/STS study by Koslowski et al. showed a trapping of individual, flat-lying pentacene molecules in characteristic off-center positions of the nanomesh pores [705]. This site-selective adsorption, prevailing at rt, was assigned to the lateral electric fields of the nanomesh. Interestingly, the electronic gap for pentacene units on *h*BN/Rh(111) (3.39 eV), used as an indicator for molecule - support interactions, exceeds the one on a KCl monolayer on Cu(110), but is smaller than the one for bilayer KCl/Au(111) [705]. Furthermore, the trend for an increasing HOMO binding energy with increasing work function observed for the KCl systems is not shared by the *h*BN one. This finding was attributed to the in-plane electric field, enhancing molecule - substrate interactions for pentacene/*h*BN/Rh(111) [705]. Additionally, the larger thickness of a KCl bilayer compared to the *h*BN mono-

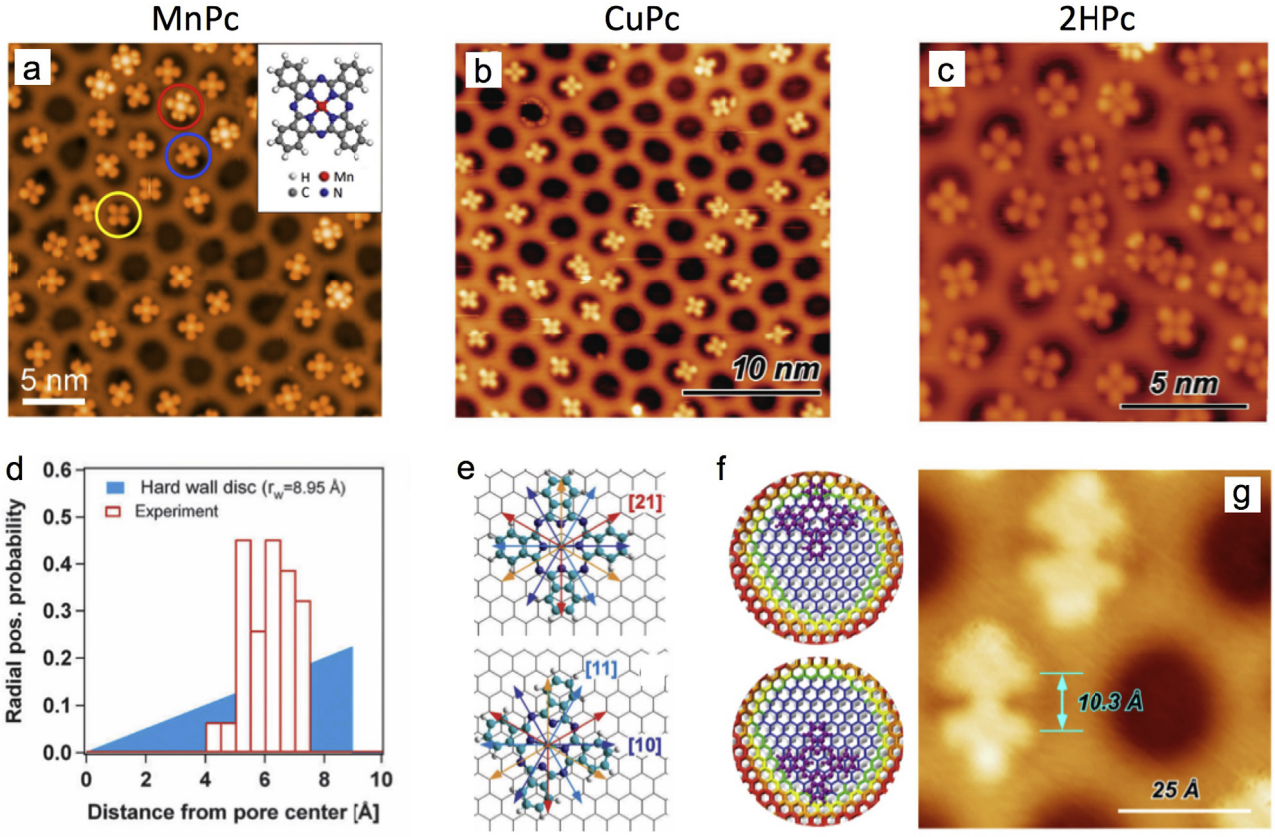

Fig. 40. Site-selective Pc adsorption on *h*BN/Rh(111). (a) MnPc. (b) CuPc. (c) 2HPc. (d) Probability distribution of the radial off-center position of CuPc. (e) Two distinct azimuthal Pc alignments on *h*BN. CuPc favors the upper orientation, 2HPc the bottom one. (f) DFT minimum energy configurations of H_2Pc in opposite off-center positions. (g) STM image recorded at 77 K showing a superposition of CuPc in two off-center positions. (a) Adapted with permission from Ref. [678] © (2015) American Chemical Society, (b–g) Adapted from Ref. [337] © (2014) Royal Society of Chemistry.

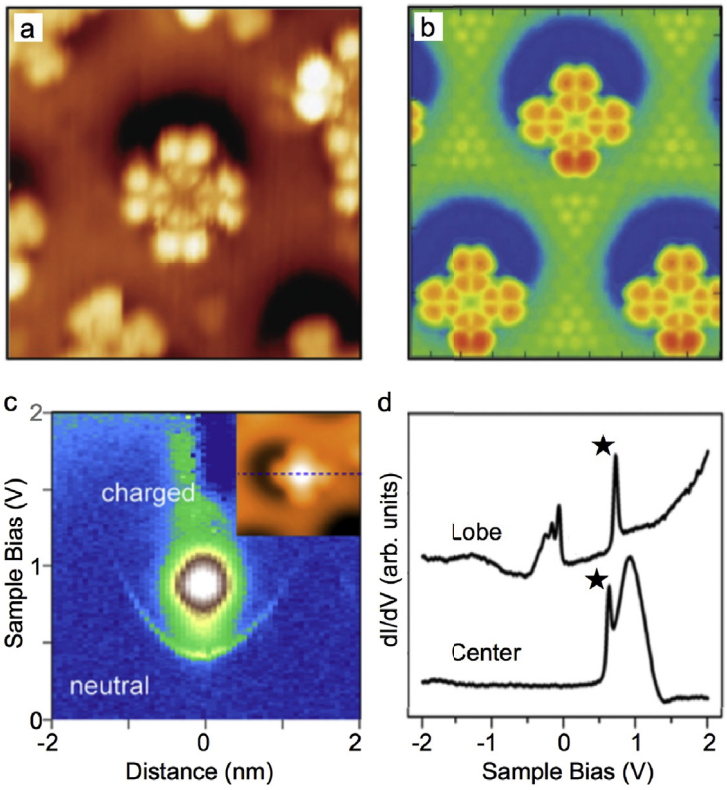

Fig. 41. Electronic structure of Pcs on *h*BN/Rh(111). (a) Experimental STM image of 2HPc featuring intramolecular contrast representing the HOMO. (b) Corresponding simulated STM image. (c) dI/dV map across a MnPc molecule (see inset) showing a parabolic signature induced by tip-gated charging. (d) Individual dI/dV spectra on Mn Pc. The ⋆ symbols mark the charging peaks. The other features are related to molecular orbitals. (a,b) Adapted from Ref. [337], (c,d) Adapted with permission from Ref. [678] © (2015) American Chemical Society.

layer might contribute to the reduced electronic gap in the latter case.

Recently, Cun et al. studied the adsorption of F_4TCNQ - a strong electron acceptor - on *h*BN/Rh(111) [689]. Coverage-dependent UPS data show a preferred adsorption in the nanomesh pore, with sequential STM images indicating that "hopping" of F_4TCNQ between neighboring pores is activated at rt. The work function of the F_4TCNQ/*h*BN/Rh(111) system increases considerably with increasing molecular coverage [689]. This effect was assigned to charge transfer from the support to the F_4TCNQ, resulting in negatively charged molecules. DFT calculations reproduce the work function shift and assign the molecules to anionic "2-" species, where the former LUMO is placed well below E_F [689].

Besides electronic and optical characteristics of molecular adsorbates on *h*BN/Rh(111), magnetic properties - specifically of single-molecule magnets - attracted special interest [680,692,693]. The first study by Kahle et al. dating back to 2012 combines electrospray deposition of fragile Mn_{12} SMMs (#15 in Fig. 32) with STM, STS experiments and DFT modeling [692]. The STM data recorded at 1.5 K show intact Mn_{12} units occupying the pores of the nanomesh, with the acetate groups dominating the submolecular contrast (Fig. 43(a)). The magnetic properties were probed by inelastic spin-flip spectroscopy without magnetic field and with a magnetic field applied perpendicular to the surface, respectively. Clearly, step-like features appearing at positions symmetric to E_F were resolved in dI/dV spectra (see Fig. 43(b)), which were assigned to spin-flip excitations in Mn_{12} based on comparison to a simplified Mn_{12}/*h*BN structure and an effective 8-spin model. Such excitations were only observed for Mn_{12} on *h*BN/Rh(111), but not on Cu or Au supports [692].

Erler et al. as well relied on the electrospray technique to deposit Fe_4H SMMs (#16 in Fig. 32) on *h*BN/Rh(111) [693]. At very low coverage (0.001 ML), individual Fe_4H units exclusively occupy the pores of the nanomesh (Fig. 43(d)). At intermediate coverage (0.06 ML) individual molecules coexist with dense-packed Fe_4H arrays covering the pore and wire regions and pointing to relevant intermolecular interactions. Two distinct periodic hexagonal Fe_4H lattices were detected in these islands, featuring a different alignment with respect to the nanomesh superstructure. At higher coverage regular, almost complete Fe_4H monolayers were achieved. Submolecular features in low-temperature STM images showed good agreement with simulated images representing a calculated adsorption geometry where the plane defined by the four Fe atoms in Fe_4H is aligned parallel to the surface. This configuration represents a perpendicular alignment of the magnetic easy axis of the SMM with respect to the surface [693]. STS furthermore revealed two pronounced molecular resonances 1.6–2.3 eV above E_F, one being centered on Fe_4H, the other contributing at the dpm ligands. By comparison to spin-polarized DFT calculations of the PDOS and the spin-split LUMO orbitals of a free Fe_4H molecule, the former was identified as the majority LUMO, while the latter was assigned to the minority LUMO (Fig. 43(g and h)). Based on the good agreement between the STS data on Fe_4H/*h*BN/Rh(111) and the spin-polarized calculations of the free molecule, the authors conclude that the Fe_4H complex not only remains structurally intact upon adsorption, but also largely retains its electronic and magnetic properties [693]. Furthermore, the experimental STS data reveal a site-selective gating of the LUMO resonances - featuring a shift of the LUMO by about 0.35–0.4 eV between pore and wire sites, which was assigned to the local work function variations on the nanomesh (≈0.31 eV), analo-

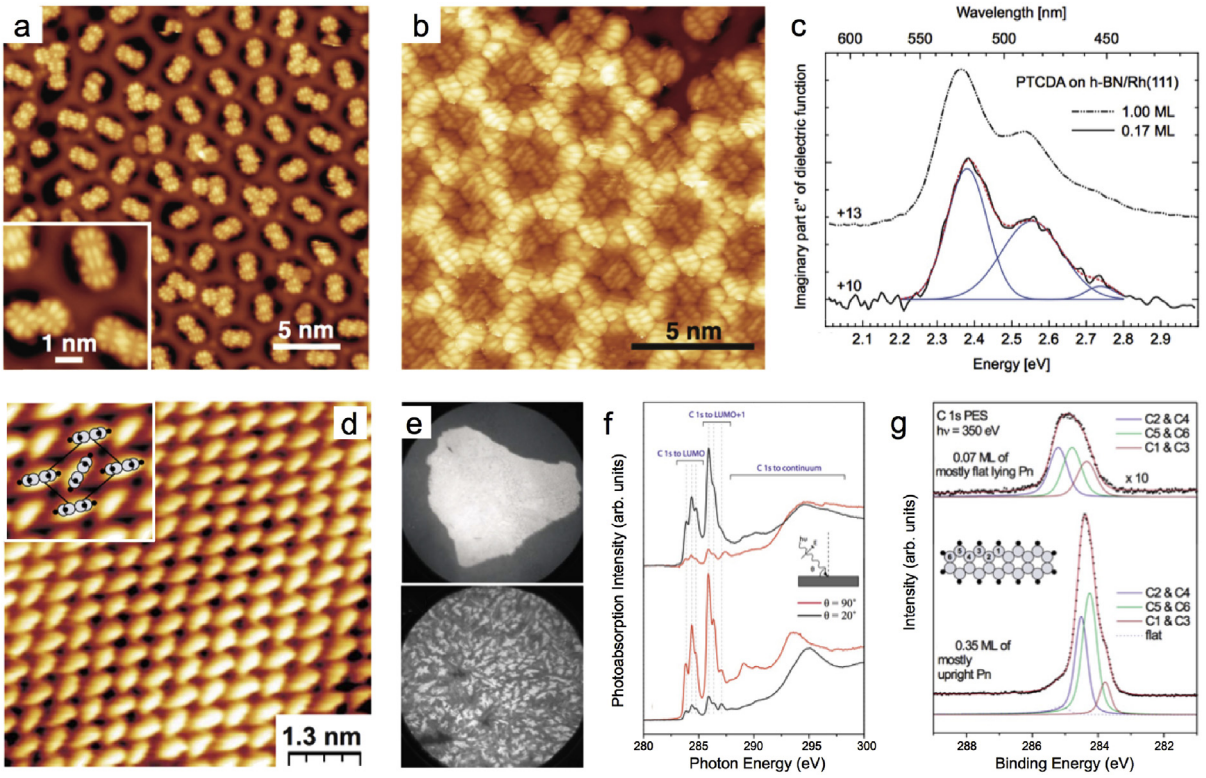

Fig. 42. (a) *h*BN/Rh(111) nanomesh pores filled with PTCDA. (b) PTCDA array on *h*BN/Rh(111). (c) Imaginary part $\epsilon^{\parallel}$ of the dielectric function extracted from differential reflectance spectroscopy measurements for two PTCDA coverages on *h*BN/Rh(111). (d) Pentacene (Pn) array on *h*BN/Rh(111). Inset: Zoom-in including structural models of the upright standing Pn molecules. (e) LEEM images of a 1-ML-thick Pn island (top panel) and fractal second Pn ML islands (bottom panel). (f) Angle-dependent C 1s NEXAFS spectra for 0.07 ML (top panel, flat lying Pn) and 0.35 ML Pn (bottom panel, upright Pn). (g) C 1s XPS spectra for the two Pn coverages highlighted in (f). (a–c) Adapted with permission from Ref. [687] © (2016) American Physical Society, (d–g) Adapted with permission from Ref. [690] © (2010) American Physical Society.

gous to the cases discussed in paragraph 3.3.3 for the *h*BN/Cu(111) system.

Finally, the first report of a dehalogenative coupling reaction performed on a *h*BN monolayer - published by Dienel et al. in 2014 - relied on *h*BN/Rh(111) as a substrate [681]. The combined STM and DFT study addressed the adsorption, dehalogenation and coupling of a polyphenylene precursor, namely I_6CHP (#5 in Fig. 32). Low-temperature STM data recorded after rt deposition of small amounts of I_6CHP (≈0.15 ML) reveal a trapping of the molecules in off-center positions in the nanomesh pores featuring a preferential orientation (Fig. 44(a)). Combining high-resolution STM imaging with DFT calculations, it was inferred that I_6CHP is centered above N atoms, reducing the apparent six-fold symmetry of I_6CHP to an effective three-fold one (A and B termini in Fig. 44(d)). This was reflected in dehalogenation experiments, where C—I bond cleavage sets in at a temperature of 500 K and gradually proceeds up to 850 K where a full dehalogenation is achieved. At intermediate temperature, a preference for a distinct I_3CHP configuration (B—B—B) was observed, reflecting the aforementioned specific adsorption configuration (Fig. 44(b,e)). Covalent coupling to extended, disordered oligomers was only realized for high molecular coverages annealed above 800 K (Fig. 44(c)). This study demonstrated that while *h*BN can promote the activity needed to trigger dehalogenation reactions of adsorbed species, it does not necessarily reflect a "smooth" support. Clearly, site-specific interactions between the precursor/the intermediates and the *h*BN/Rh(111) substrate govern the on-surface reaction [681].

3.3.5. *hBN/Ruthenium(0001)*

Recently, Wäckerlin et al. studied $TbPc_2$ SMMs (#3 in Fig. 32) on different supports, including the *h*BN/Ru(0001) nanomesh by XMCD [680]. These lanthanide-based double-decker SMMs adsorb with their macrocycles parallel to the surface plane. Importantly, the magnetization curves obtained with XMCD for 0.3 ML $TbPc_2$/*h*BN/Ru(0001) at 3 K show an opening of a hysteresis loop, with an area of the hysteresis opening exceeding the one for $TbPc_2$/Ag(100) by roughly a factor of four and the one of $TbPc_2$ multilayers by a factor of two (Fig. 43(i)). However, MgO multilayers outperform the *h*BN monolayer as insulating spacer as evidenced by the giant hysteresis observed for $TbPc_2$/MgO/Ag(100), featuring a hysteresis area more than twice as large as in the $TbPc_2$/*h*BN/Ru(0001) case [680].

3.3.6. *hBN/Iridium(111)*

The interaction of CoPc with *h*BN/Ir(111) was explored in exquisite detail by Schulz et al., employing low-temperature STM, STS and complementary DFT and TDDFT calculations [251,679]. At low sub-molecular coverage, individual CoPc units are trapped in the pore regions of the *h*BN/Ir(111) moiré (Fig. 45(b)). The STM data indicate a preferred off-center position, reminiscent of Pc adsorption on *h*BN/Rh(111), even though the pore size is considerably smaller for *h*BN/Ir(111). After saturation of the pores, the molecules occupy the wire regions, locally forming dense-packed square arrays (Fig. 45(c)). When increasing the CoPc coverage beyond one ML, second layer molecules nucleate site-selectively on pore molecules. STM

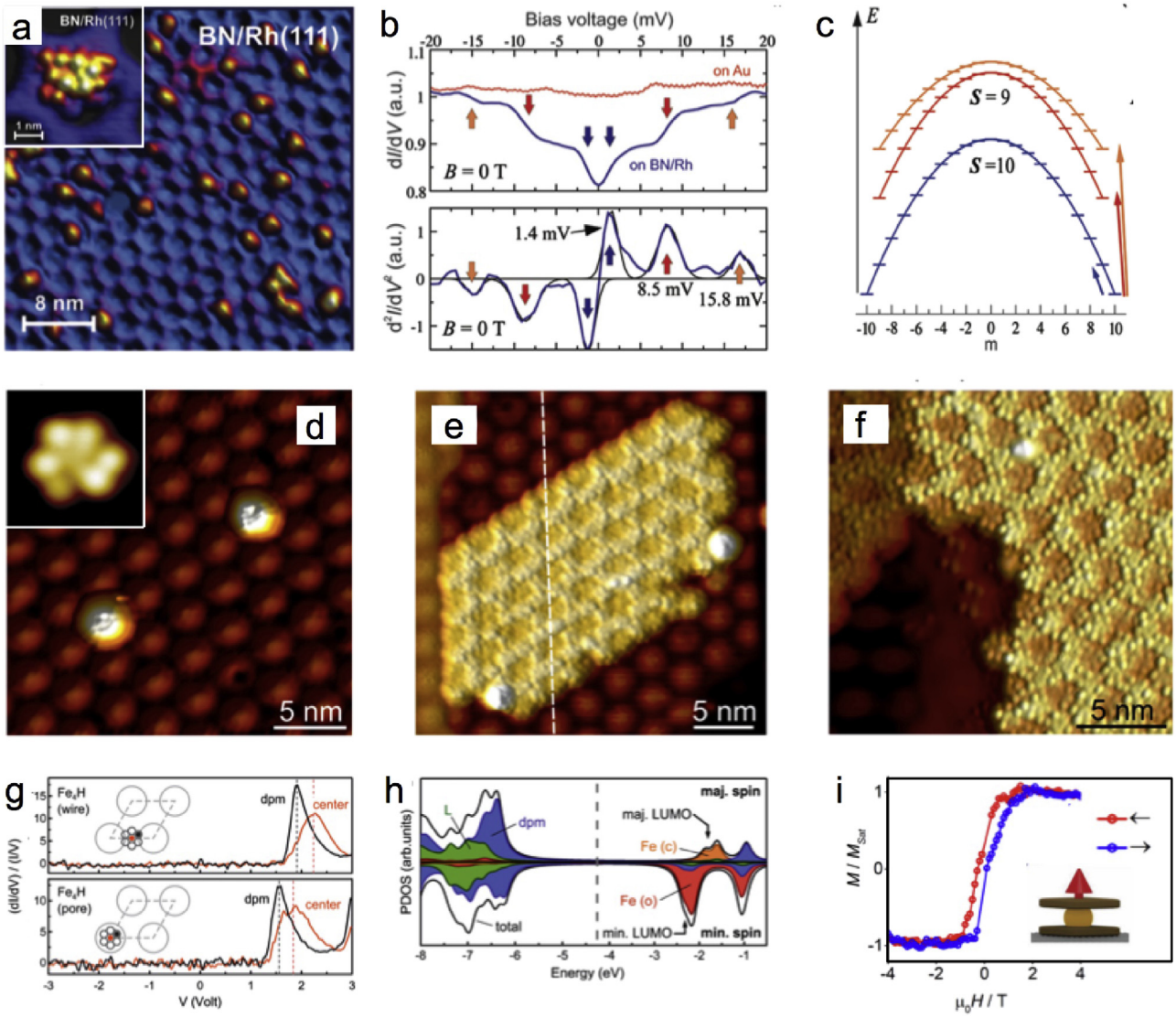

Fig. 43. Single-molecule magnets on *h*BN/Rh(111) and *h*BN/Ru(0001). (a) STM image of Mn_{12} adsorbed in the nanomesh pores. Inset: zoom-in. (b) STS data on Mn_{12} (top panel: dI/dV, bottom panel: d^2I/dV^2) showing spin-flip excitations on *h*BN/Rh(111) but not on Au(111). (c) Schematic energy diagram of Mn_{12}. The arrows indicate possible excitations (see (b)). (d–f) STM images with increasing Fe_4H coverage (d: 0.001 ML, e: 0.06 ML, f: 0.7 ML). Inset in (d): individual Fe_4H. (g) dI/dV spectra of Fe_4H on the wire (top panel) and pore (bottom panel) areas of the nanomesh. (h) Spin-dependent PDOS calculated for a free Fe_4H molecule. The colors represent projections onto distinct moieties. (i) Magnetization curves of 0.3 ML $TbPc_2$/*h*BN/Ru(0001) showing a hysteresis opening of 56 J mol^{-1}. (a–c) Adapted with permission from Ref. [692] © (2012) American Chemical Society, (d–h) Adapted with permission from Ref. [693] © (2015) American Chemical Society, (i) Adapted with permission from Ref. [680] © (2016) John Wiley and Sons. (For interpretation of the references to color in this figure legend, the reader is referred to the Web version of this article.)

and STS data on an intermediate CoPc coverage recorded at 5 K reveal a characteristic, position-dependent molecular contrast and spectral fingerprint, assigned to site-selective gating and charging. On the pore regions, the molecules get negatively charged, i.e., correspond to $CoPc^{-1}$, while remaining neutral on the wire sites ($CoPc^0$) (Fig. 45(a)). This static charging effect on the pores is reflected in a downshift of the pristine LUMO by about 1.1 eV, placing it well below E_F and thus turning it into the HOMO. This considerable energy shift includes the decrease of the local work function when going from the wire to the pore regions (≈0.4 eV) and a relevant charging energy (≈0.7–0.9 eV). The wire molecules feature a gap between occupied and unoccupied orbitals on the molecular arms of about 2.75 eV (Fig. 45(e)). In addition, the molecular resonances exhibit vibronic satellite peaks featuring a Lorentzian line shape with a width limited by the lifetime (Fig. 45(f,i)). The small average line width (37 meV on the wire and 60 meV on the pore) signals a considerably reduced electronic coupling of wire molecules to the metal support. From STS measurements of the CoPc's LUMO, a vibrational mode with an energy of 105 meV was deduced, that compares well with the uncorrected value (97 ± 5 meV) reported in Ref. [678] for the HOMO of MnPc/*h*BN/Rh(111), while an electron-vibration coupling strength of 0.4 was estimated (Fig. 45(f)). Interestingly, a description of the CoPc's electronic structure in the single-particle picture failed to correctly reproduce the orbital order and the respective energy positions. Only when including a series of many-body excitations of the different ground states, the experimental spectroscopic data could be reproduced (Fig. 45(g and h)). CoPc/*h*BN/Ir(111) thus represents a rare case where many-body effects in adsorbed molecules are experimentally pinpointed [679].

3.3.7. Comparison and discussion

Despite the large variety of *h*BN/metal interfaces (introduced in section 2.2), experimental work with large (metal-)organic molecules focused on a few systems, mainly *h*BN/Ni(111), *h*BN/Cu(111), *h*BN/Rh(111), and *h*BN/Ir(111). In the following, we comparatively assess some of the findings reported above, highlighting common aspects of molecule/*h*BN/metal structures, as well as differences between them, and peculiarities of specific systems. Furthermore, we refer to observations and predictions for related interfaces, such as molecules on graphene/metal, bulk-like *h*BN, and free-standing *h*BN sheets.

Distinction from metal supports. In all cases, the *h*BN sheet provides some electronic decoupling of the molecules form the metal, which is evidenced by the resolution of sharp molecular resonances in STS [251,398,678], the temperature-controlled switching of orbital occupancy [682], the manifestation of many-body phenomena [679], the persistence of single molecule magnet properties [680,692,693], or the access to optical transition energies [687,688]. Regarding self-assembly, a number of systems introduced in this section exhibit distinct differences to architectures in direct contact with metal surfaces. We mention three examples of molecular adsorption and assembly on *h*BN/Cu(111), where H-bonding and stronger metal-coordination interactions lead to substantially different behavior than on metal substrates. In the first case, qdc molecules formed densely-packed chevron assemblies on *h*BN/Cu(111), where the molecular conformation reflects considerable, alternating torsions of the phenylene rings. In contrast, qdc adsorption on Ag(111) results in an open-porous, rhombic packing with small interphenylene torsion angles [668,706]. In the second case, porphine units assembled into molecular aggregates on *h*BN/Cu(111) already at low sub-ML coverages, while individual molecules are observed on Ag(111) and Cu(111) due to dominating repulsive interactions [696,697]. In the third case, Co coordination of carbonitrile-terminated porphyrins (TPCN) on *h*BN/Cu(111) resulted in a four-fold motif (see paragraph 3.3.3), whereas a three-fold motif prevails for Co-coordinated carbonitriles on Ag supports, with the latter mimicking a forth ligand [684,707]. These three exemplary cases highlight that *h*BN can reduce the charge transfer between metal and adsorbates (i.e., molecules or coordination centers) and might promote assemblies driven by intermolecular interactions rather than by site-specific molecule - substrate bonds.

Nonetheless, several of the experiments touched in this section highlight that surface-supported *h*BN can not generally be considered as an inert and homogeneous platform for adsorbates. Rather, the *h*BN interaction with the underlying metal offers means to tune molecular processes such as diffusion, self-assembly, on-surface reactions, energy level alignment, and charging. Most impressively, this is demonstrated by the site-specific adsorption of archetypical π-conjugated molecules (such as tetrapyrroles, PTCDA, or pentacene) on the superstructured *h*BN/metal interfaces (see below). Specifically with superstructure pore sizes approximately matching the lateral extension of molecular adsorbates, *h*BN can sensitively affect - and guide - the assembly behavior. Furthermore, the electronically corrugated *h*BN/metal interfaces can imprint a periodic energy variation of molecular electronic levels in adsorbed monolayer films. A scheme illustrating such a site-selective gating of a molecular orbital (LUMO) is provided in the left panel of Fig. 46.

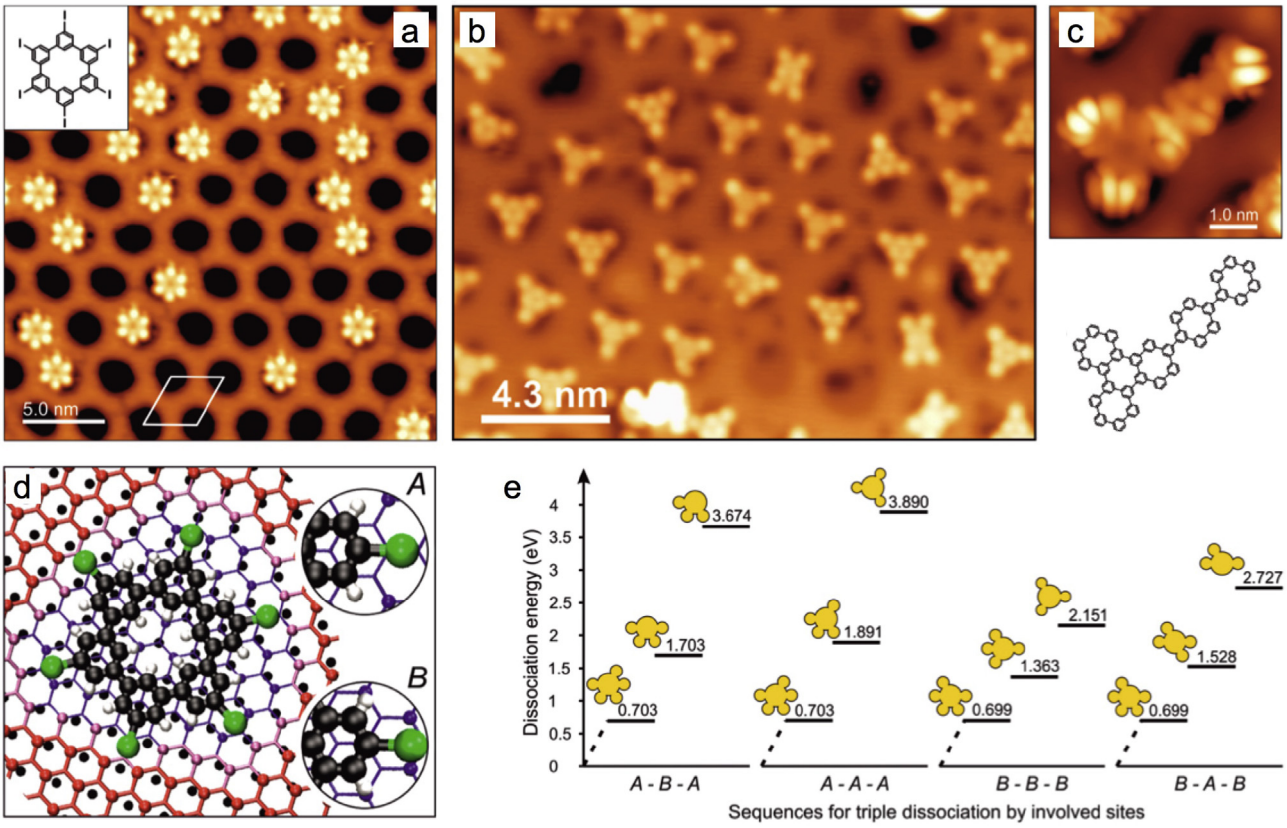

Fig. 44. On-surface reactions on *h*BN/Rh(111). (a) STM image of I_6CHP occupying off-center positions in the nanomesh pores. Inset: Molecular structure. (b) Iodine dissociation by annealing at 680 K leaving I_3CHP. (c) CHP oligomer formed upon annealing at 850 K. Top panel: STM image, bottom panel: corresponding structural model. (d) DFT model of I_6CHP on *h*BN/Rh(111) highlighting the two distinct registries of the carbon iodine bonds (A versus B). (e) Dissociation energies in four selected dehalogenation sequences resulting in I_3CHP. Adapted with permission from Ref. [681] © (2014) American Chemical Society.

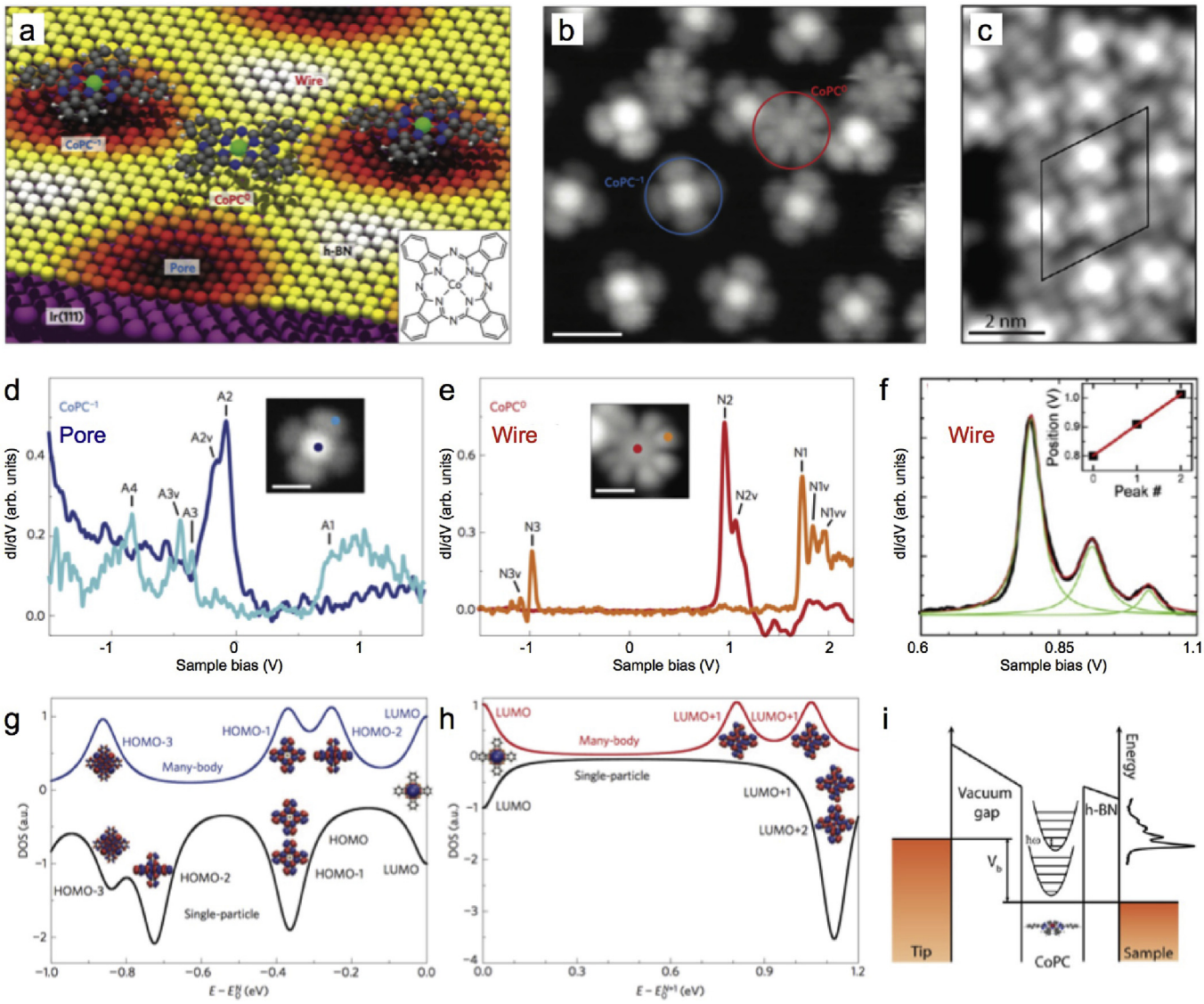

Fig. 45. CoPc on *h*BN/Ir(111). (a) Schematic illustration of CoPc in two charge states. Inset: Structural model of CoPc. (b) STM image featuring $CoPc^{-1}$ adsorbed in the pore regions and some additional CoPc species on the wires. (c) Dense-packed array at higher molecular coverage. (d) dI/dV spectra recorded on a pore molecule ($CoPc^{-1}$, center and off-center position). (e) dI/dV spectra on CoPc on the wire region. (f) High-resolution dI/dV spectrum showing the vibronic progression for a CoPc molecule. (g,h) Comparison of the calculated DOS versus energy between the many-body (top) and single-particle picture (bottom) for electron removal (from $CoPc^{-1}$, g) and electron addition (to $CoPc^{0}$, h). (i) Double-barrier tunneling model for *h*BN-adsorbed CoPc in the STM junction. (a,b,d,e,g,h) Adapted with permission from Ref. [679] © (2015) Springer Nature, (c,f,i) Adapted with permission from Ref. [251] © (2013) American Chemical Society.

The support might also induce other effects, as evidenced for example by the stabilization of specific intermediates in on-surface coupling reactions [681]. The metal supporting the *h*BN is crucial for catalytic enhancement of reactions, e.g., to perform debromination reactions with TBB on *h*BN/Ni(111) [518]. Furthermore, while generally a high mobility of (metal-)organic molecules on *h*BN is observed, it was found that radicals can have a considerable interaction with the metal-supported *h*BN lattice, inducing diffusion barriers exceeding the ones on coinage metal surfaces and thus hampering the formation of extended, regular architectures [518].

Differences between hBN templates and molecule/hBN/metal systems. Despite similarities, such as electronic decoupling and altered molecular aggregation compared to metal surfaces, it is crucial to emphasize that the characteristic nature of the manifold *h*BN/metal interfaces described in section 2.2 substantially affects the interaction with large molecular adsorbates. Distinct - but sometimes subtle - differences between the different *h*BN/metal supports are evident from the examples addressed in this section, going ways beyond the rough distinction of planar versus corrugated templates. This opens fascinating options to fine-tune structural, electronic and magnetic properties in (metal-)organic/*h*BN/metal heterostructures.

For example, the trapping mechanisms inducing site-specific adsorption reveal subtle differences between the superstructured templates. For the nanomesh structures of *h*BN/Rh(111) and *h*BN/Ru(0001), the confinement of polarizable adsorbates in off-center positions of the pores was rationalized by the existence of dipole-rings, i.e., lateral electric fields [233,339,343]. These emerge from local work function variations and result in electrostatic potential wells for polarizable atoms, molecules or negative ions (see Fig. 4 g). This trapping mechanism - originally demonstrated for Xe and CuPc on *h*BN/Rh(111) [339] - is frequently assumed as reason for

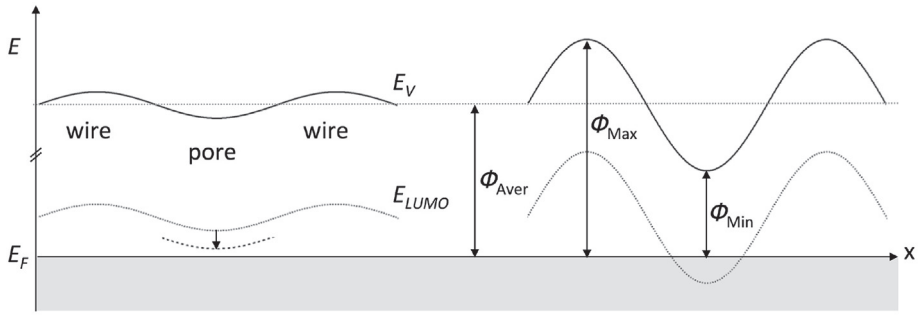

Fig. 46. Schematic illustration of site-specific gating and charging of molecular adsorbates on electronically corrugated *h*BN/metal templates (compare Fig. 12). The left panel illustrates how a pinning of the LUMO to the local vacuum level (E_V, solid line) leads to a modulation of the LUMO energy (E_{LUMO}, dotted line) with respect to the Fermi level (E_F). The LUMO of molecules trapped in *h*BN pore regions might be additionally shifted towards E_F (indicated by the arrow and the dashed line). This effect represents an increased molecule-support interaction (e.g., enhancing screening) and thus a reduction of the HOMO-LUMO gap. Pronounced work function variations combined with an energy level alignment placing a molecular frontier orbital close to E_F can result in a local charging of adsorbates. This is shown in the right panel, where the LUMO dives below E_F in *h*BN pore areas, resulting in charge transfer to the molecule. Furthermore, this figure schematically illustrates the difference between a graphene/Ir(111) (left panel) and a *h*BN/Ir(111) (right panel) template for the adsorption of CoPc. Despite a similar average work function (ϕ_{Aver}), the larger local work function modulation in the *h*BN case contributes to a charging of CoPc in the pore areas.

site-specific adsorption in corrugated *h*BN structures [705]. However, DFT modeling exploring the adsorption of 2HPc at the pore center and near the rim of pores, respectively, showed that the electrostatic contribution emerging from the lateral electric fields is not the dominant part in the adsorption anisotropy, and thus can not exclusively explain adsorption of 2HPc in off-center sites on *h*BN/Rh(111) [337]. Also the *h*BN/Ir(111) template provides site-specific adsorption in the pores, featuring strong in-plane electric fields and underlining the significance of the mutual interplay between support and molecule for the site-specific adsorption. However, the significantly smaller pore size compared to *h*BN/Rh(111) (see section 2.4) complicates the quantification of adsorption site preferences of archetypical adsorbates (such as Pcs). In addition, in contrast to the *h*BN/Rh(111) and *h*BN/Ru(0001) nanomesh supports, site-specific charging was reported on *h*BN/Ir(111) (see excursus at the end of this paragraph). For the templating functionality of *h*BN/Cu(111) - an interface with smaller geometric corrugation than its nanomesh counterparts - the local work function (and not primarily its gradient) is relevant [398]. No preferred off-center adsorption sites at the rim of the pores were observed [398,469]. Furthermore, large pores - featuring diameters exceeding 6 nm - support the formation of arrays of molecular islands [398].

The peculiarities of specific molecule/*h*BN/metal systems are reflected in the wide range of reported desorption temperatures (even though such values should be considered with care as they depend on the experimental parameters). The onset of pentacene desorption from *h*BN/Rh(111) was observed at 350 K [690], 2HP desorbed from *h*BN/Cu(111) at 470 K [314] and C_{60} desorbed from *h*BN/Ni(111) at 520 K [682], with all three cases highlighting a weak adsorbate/support coupling. On the other hand, individual Nc and I_3-CHP molecules occupied *h*BN/Rh(111) nanomesh pores even after annealing to 650 [240] or 680 K [681], respectively.

We proceed with a short excursus on charge transfer and level alignment. Static charging (excluding field-induced charging) of molecules was only reported for *some* *h*BN/metal supports (*h*BN/Rh(111), *h*BN/Ir(111), *h*BN/Cu(111)). Relevant parameters are the ionisation potential and the electron affinity of the adsorbate in comparison to the work function [689] (see compilation of work function values in Fig. 12 (b)). For the case of F_4TCNQ on *h*BN/Rh(111), the level alignment places the LUMO of the free molecule well below the Fermi level of the support (with the electron affinity exceeding the work function by more than 1 eV), resulting in charge transfer to the F_4TCNQ [689]. With molecular frontier orbital energies positioned close to the Fermi level of the support, local work function variations can induce a modulation in the charge state of adsorbed molecules. In a simplistic picture, the lateral variation of the local work function can induce a Fermi level crossing of the respective orbital - charging or discharging the molecule depending on its lateral position on the work function template (see illustration in the right panel of Fig. 46). A site-specific charging - representing an extreme case of site-specific gating (left panel of Fig. 46) - was reported for CoPc/*h*BN/Ir(111) [251,679] and recently observed for F_{16}CoPc/*h*BN/Cu(111) [698]. Such a pinning of frontier orbitals to the vacuum level - as opposed to Fermi level pinning - is reminiscent of recent findings for other vdW interfaces [708–710]. It even can occur with a charge redistribution happening upon adsorption, as known from specific organic - metal interfaces [711].

We complete the discussion about the importance of the energy level alignment for the charge state and the self-assembly properties of molecules on sp^2/metal supports by examples based on TCNQ/graphene. The deposition of F_4TCNQ at low coverage on graphene/Ir(111) results in arrays of individual, charged molecules [712], whereas TCNQ forms dense-packed islands assembled from neutral molecules [713,714]. By contrast, both TCNQ and F_4TCNQ feature site-specific adsorption on graphene/Ru(0001) with considerable charge transfer to the molecule [715]. These examples highlight how modifications - as the fluorination of TCNQ - affect the self-assembly behavior on distinct nanostructured supports and indicate the relevance of the subtle interplay between adsorbate and sp^2/metal support, including structural relaxation [712]. Such insight gained from graphene-based systems (see also next paragraph) might be applied to *h*BN templates as well, even if the charge transfer processes can be distinctly different, considering the “metallic” character of graphene and the “dielectric” character of *h*BN, respectively. E.g., the role of the adsorbates’ charge state for the self-assembly was rarely explored on *h*BN [251], leaving some room for future experiments.

Comparison to graphene templates. On first sight, many of the examples discussed in this section bear similarities to adsorbates on surface-supported graphene sheets, summarized in recent reviews (e.g., Refs. [90–92]). Site-selective adsorption at low coverage was reported for specific molecules on corrugated graphene structures (e.g., FePc/graphene/Ru(0001) [716–718], pentacene/graphene/Ru(0001) [717,719], TBPP/graphene/Ru(0001) [720], TCNQ/graphene/Ru(0001) [721], F_4TCNQ/graphene/Ir(111) [712,713]). The respective trapping mechanisms for adsorbates on graphene/metal templates were discussed in analogy to

the *h*BN/metal systems, and include lateral electric fields, local work function modulation, and molecular charging (e.g., Refs. [705,717,719]).

Nevertheless, differences between *h*BN/metal and graphene/metal systems (see section 2.4) affect the adsorption behavior. The inverted topography between *h*BN and graphene nanomesh structures (see Fig. 11) is often directly reflected in the molecular contrast mapped by STM in dense-packed molecular arrays. For example, PTCDA molecules appear brightest in the circular regions of the graphene superstructure on Ru(0001) [722], while they appear dimmest in the circular regions of the *h*BN superstructure on Rh(111) at comparable bias voltage [687]. In addition, certain aspects as site-selective self-assembly of discrete molecular aggregates - i.e., arrays of molecular arrays (reminiscent of molecular assemblies e.g. on the Au(111) herringbone reconstruction [99]) - were (to this author's knowledge) only reported for *h*BN/Cu(111), enabled by the large moiré periodicities [398].

A systematic comparison of trapping potentials and molecular properties on *h*BN and graphene spacer layers is hampered by the lack of experimental data on comparable systems. In view of the relevant roles played by the energy level alignment (see above), the sp^2/metal interface properties [723], and the chemical composition of the molecules, such a comparative assessment should base on identical adsorbate/metal single crystal pairs. For example, the functionalization of the Pc macrocycle (2H versus different metal centers) can sensitively affect the self-assembly/adsorption behavior [718,724,725]. Representing (to this author's knowledge) the only reported identical adsorbate/substrate pair, the comparison of CoPc/*h*BN/Ir(111) with CoPc/graphene/Ir(111) is instructive to work out distinct differences between graphene and *h*BN interfaces. The latter system was studied in detail by STM and space averaging techniques (e.g., Refs. [467,725–728]). At sub-ML CoPc coverage (and rt deposition followed by imaging at low temperature), only *h*BN/Ir(111) supports arrays of individual molecules [251], while dense-packed islands assemble on graphene/Ir(111) [467,727], highlighting the exclusive templating functionality of the *h*BN interface for this specific case. At high coverages, a well-ordered CoPc lattice emerges on graphene/Ir(111), whereas on *h*BN/Ir(111) translational symmetry is only seen at small scales. Such different behavior of molecules on *h*BN/Ir(111) and graphene/Ir(111) points to a subtle interplay between molecule-molecule and molecule-substrate interactions [251]. The different nature of the two sp^2/Ir(111) interfaces is reflected in the electronic structure of the adsorbed CoPc. For CoPc/graphene/Ir(111), HOMO-LUMO gaps of typically 1.75 eV were extracted from STS data. Across the moiré superstructure, the LUMO energy varies by as much as 200 meV, but the LUMO resonance is located well above the Fermi level for all molecules (independent of their lateral position). For CoPc/*h*BN/Ir(111), the site-specific gating effects are more pronounced, resulting in an occupation of the former LUMO on the pore regions. Accordingly, the LUMO energy varies by about 1.1 eV across the *h*BN/Ir(111) moiré cell. In a rough approximation, this behavior can be rationalized by the larger local work function variations on *h*BN/Ir(111) (≈500 meV [247], see paragraph 2.2.8) compared to graphene/Ir(111) (≈60–100 meV, [464,729]). While the average work function is comparable for *h*BN/Ir(111) and graphene/Ir(111), the larger variation on *h*BN yields lower absolute local work functions in the pore areas, where trapping and molecular charging occurs (see Fig. 46, where the left panel sketches the situation for CoPc/graphene/Ir(111) and the right one the CoPc/*h*BN/Ir(111) case). Obviously, this simplistic picture fails in capturing all details of the systems: the reported shifts in molecular energy levels exceed the work function variations. Thus, additional effects such as adsorption induced local modifications in the sp^2/metal interface, charging effects, and adsorption height dependent polarization screening might play a relevant role and influence the level alignment.

Even if orbital-like resolution in STM points to little hybridization of the molecular electronic states with the metals on both supports, the larger apparent electronic gaps on (the wire regions) of CoPc/*h*BN/Ir(111), and the resolution of vibronic progressions reveal an efficient electronic decoupling combined with considerable site-specificity on *h*BN - thus discriminating the *h*BN system from the graphene one.

Sticking to the Ir(111) substrate, we complete the *h*BN/graphene comparison by mentioning that a Diels-Alder-type coupling reaction resulting in C—C bonds between FePc and graphene [728] and a similar, reversible attachment of F_4TCNQ to graphene via cyano groups [712] were naturally only observed in the graphene systems. In this context, the binding of radicals to graphene and *h*BN is a topic of interest [518], as well as partial sp^3 rehybridization [712].

Summarizing this paragraph, one can conclude that despite structural similarities between the two sp^2 sheets and their interfaces with metals, the binary elemental composition of *h*BN and its direct consequences (e.g., dielectric nature) introduces distinct differences to the all-carbon graphene systems, which become apparent for molecular adsorption.

Effects of molecular adsorbates on hBN properties. Rather than employing the *h*BN support to tune the properties of molecular adsorbates, the adsorbates might be used as a tool to modify properties of the underlying *h*BN, similar to the cases of atomic and diatomic adsorbates discussed in paragraphs 3.1.7 and 3.2.6, respectively. Experiments addressing the influence of molecules on the *h*BN/metal interface however are scarce. A Raman study by Cai et al. showed pronounced shifts in the G band frequency when adsorbing R6G molecules on *h*BN/SiO_2 and on suspended *h*BN, while such shifts were absent using bulk *h*BN as support [730]. The Raman shifts (of opposite signs) are assigned to deformation in the *h*BN sheet upon R6G adsorption, building up or releasing strain in the sp^2 sheet - and not to electronic doping. This conformational adaptation increased the adsorption strength of R6G and 4-MBA molecules on *h*BN monolayers compared to *h*BN bulk. Accordingly, *h*BN nanosheets outperform *h*BN bulk particles for example in water cleaning applications [730]. The influence of the support was also highlighted in an experimental study comparing CuPc on *h*BN/SiO_2 and graphene/SiO_2. While considerable charge transfer was identified as origin of Raman enhancement effects in the graphene system, interfacial dipole-dipole interactions are dominant for CuPc on *h*BN [731]. This lack of electronic doping of *h*BN by physisorbed molecules was related to the insulating properties of the *h*BN sheet [730]. On the other hand, theoretical studies on the molecular doping of free-standing *h*BN sheets emphasize the potential to tune the electronic properties of the sp^2 layer, converting it for example into an p- or n-type semiconductor upon interaction with acceptor (e.g., TCNQ) or donor (e.g., TTF) units (see for example Ref. [699]). Corresponding experiments, adapted for example to quasi-free standing *h*BN, remain to be performed. Specifically, the fabrication and local characterization of interfaces in bi-component molecular arrays on surface-supported *h*BN seem rewarding.

Additionally, a multitude of theoretical studies explored interfaces of organic molecules with free-standing *h*BN sheets and modifications thereof (see Table 10 for selected examples). Such studies give valuable insights into important processes in model systems, including for example adsorption [732,733], nucleation and self-assembly [734], intrinsic affinity scales for different amino-acid-analogues [735], immobilization of nucleobases [736,737], work function modification [738], or power conversion [739]. However, the results summarized in this section indicate that the transfer of such functionalities to surface-supported *h*BN systems might not be straightforward and thus represents an exciting challenge.

Table 10
Selected theoretical studies addressing "large" molecules on free-standing *h*BN sheets.

Molecule	Substrate	Technique(s)	Refs.
Benzene (C_6H_6)	–	DFT	[740]
Metal-arenes (MC_6H_6, M = Ti, V, Cr, Mn, Fe, Co)	–	DFT	[640]
Triazine ($C_3H_3N_3$)	–	DFT	[740]
Borazine ($B_3N_3H_6$)	–	DFT	[740]
Trimethylaluminium (TMA)	–	DFT	[643]
Phenol (C_6H_5OH)	$B_{12}N_{12}H_{12}$	DFT	[733]
Guanine ($C_5H_5N_5O$)	$B_{27}N_{27}H_{18}$	DFT	[737]
Nucleobases (guanine, adenine, thymine, cytosine, uracil)	–	DFT	[741,742]
Nucleobase pairs	–	DFT	[736]
Amino acid analogues	–	DFT	[735,743]
Glucose ($C_6H_{12}O_6$)	–	DFT	[568]
	two sheet 19-ring model of *h*BN	DFT	[744]
Glucosamine	–	DFT	[568]
Thymine	–	DFT	[569]
Polychlorinated biphenyls (PCB)	–	DFT	[745]
Phenyl carbamate derivatives	–	DFT	[746]
Pentacene	–	MD	[704,734]
Parahexaphenyl (6P)	–	DFT	[747,748]
TTF	–	DFT	[699]
TCNQ	–	DFT	[699]
PAHs & PBDEs	–	DFT, MD	[732]
AQ & derivatives	–	DFT	[738]
PCBM	Graphene/*h*BN interface	DFT	[739]

Table 11
Selected examples of (metal-)organic molecules on bulk-like *h*BN, exfoliated *h*BN flakes, or *h*BN powders.

Molecule	Substrate	Technique(s)	Refs.
TCPP & melamine	*h*BN/SiO_2	AFM	[749]
PTCDI	*h*BN/SiO_2	AFM, Fluorescence, DFT	[177]
10,12-Nonacosadiynoic acid	*h*BN/SiO_2	AFM	[751,752]
C_8-BTBT	*h*BN/SiO_2	AFM	[753]
Rubrene	*h*BN/SiO_2	AFM, TEM, GIXD	[754]
CuPc	*h*BN/SiO_2	Raman, XPS, AFM	[731]
4-MBA	*h*BN/SiO_2	NEXAFS, Raman, DFT	[730]
R6G	*h*BN/SiO_2	NEXAFS, Raman, DFT	[730]
Alkanes (C_6H_{14}-$C_{16}H_{34}$)	*h*BN powder	XRD	[755,756]

Adsorption on bulk-like hBN. To provide a broader perspective and to establish some additional context, we will take a (superficial) look beyond single *h*BN sheets, where bulk-like *h*BN samples offer prospects to study molecular properties in a homogeneous environment without interference of a *h*BN/metal interface - excluding however the application of STM as an experimental tool (see examples in Table 11). For example, Korolkov et al. deposited PTCDI and melamine from solution on bulk *h*BN and characterized the resulting porous bi-component supramolecular networks by AFM [749]. Importantly, these architectures proved to be stable under ambient conditions. In comparison, an iso-structural hydrogen-bonded network with a periodicity of about 3.45 nm was formed from PTCDI and melamine on graphene, featuring however only limited domain sizes (40–50 nm) [750]. In a follow-up study, Korolkov et al. applied similar protocols to assemble and characterize hydrogen-bonded TCPP networks on *h*BN and resolved chromatic shifts in fluorescence spectra assigned to vdW interaction between TCPP and *h*BN [177]. Recently, the supramolecular self-assembly of bi-layer heterostructures was achieved by deposition of trimesic acid (TMA) on a hydrogen-bonded melanine/cyanuric acid network prepared on *h*BN [178].

In the context of organic devices, where interfaces between highly ordered organic semiconductor films and dielectric materials are of utmost importance, Matkovic et al. explored the epitaxy and properties of parahexaphenyl (6P) on exfoliated *h*BN by AFM and complementary DFT calculations [747,748]. Needle-like 6P crystallites pointing ±5° away from the zigzag directions of *h*BN were grown, with individual 6P units aligned along the armchair directions of *h*BN. Indeed, DFT calculation on one *h*BN layer show an azimuthal alignment of a single 6P molecule with the *h*BN lattice, featuring a planar configuration with an adsorption height of 3.33 Å. Deposition temperatures between 380 and 400 K were ideal to grow straight 6P needles, reaching lengths of several μm at heights of a few nm. Interestingly, the 6P morphology and degree of ordering depends on the separation of the molecules from the buried *h*BN/SiO_2 interface and thus on the *h*BN film thickness. A *h*BN thickness of about 1.5 nm is needed to avoid detrimental effects of interface roughness and a trapped water layer [747]. Zhang et al. grew highly ordered pentacene single crystals with a thickness of one to three layers on *h*BN flakes [704]. Based on AFM and TEM measurements, the following interfacial structure was suggested: Pentacene in direct contact with *h*BN aligns with the molecular axis parallel to the *h*BN sheet, constituting a wetting or interfacial layer. The second layer adsorbs upright, in a somewhat tilted configuration, while from the third layer on, pentacene adapts the thin-film phase with a smaller tilt. DFT calculations confirm a face-on adsorption of pentacene in the wetting layer with an adsorption energy of 2.35 eV/molecule, while the reduced interlayer interaction in the third layer (below 0.3 eV/molecule) supports the thin-film packing. It should be noted that rather upright-standing pentacene molecules

were already reported at sub-ML coverages for the *h*BN/Rh(111) substrate [690] (compare paragraph 3.3.4). An anisotropy of the optical properties related to the structure was demonstrated by polarization-dependent absorption and photoluminescence on two- and three-layer samples. Interestingly, electrical transport measurements (using a back-gated OFET geometry) showed no conductivity for the wetting layer, but revealed several features characteristic of high-quality OFETs for the bilayer system and 2D hopping-like charge transport. The three-layer system finally showed band-like transport behavior [704]. The assembly process of pentacene into ordered islands on free-standing *h*BN sheets was explored by Zhao et al. applying MD simulations [734], confirming a parallel alignment of the pentacene rings with the *h*BN plane and highlighting the crucial role of intermolecular vdW interactions in stabilizing the assemblies. By artificially reducing the pentacene-*h*BN interactions to half, the long molecular axis of pentacene is still aligned parallel to the *h*BN, the plane defined by the rings however tilts considerably [734].

Exfoliated *h*BN also served as a suitable platform for the formation of extended self-assembled monolayers of 10,12-nonacosadiynoic acid by dropcasting and spin-coating, as exemplified in Ref. [751]. Subsequent heating or ultraviolet irradiation could trigger an on-surface polymerization process yielding long polydiacetylene chains. Here, the photo-polymerization rate was two orders of magnitude higher than on graphite, reflecting the large band gap of *h*BN [752]. Aiming for quasi free-standing molecular crystals for high-performance OFETs, He et al. demonstrated the layer-by-layer growth of C_8-BTBT on exfoliated *h*BN/SiO_2. Hereby, a device based on a single molecular layer on *h*BN showed a carrier mobility of up to 10 $cm^2V^{-1}s^{-1}$ [753]. Thick, high-quality rubrene films with large single-crystalline domains were grown on *h*BN/SiO_2 by Lee et al. using vapor phase transport, evidencing high carrier mobility comparable to free-standing molecular single crystals [754]. Such studies highlight the potential of *h*BN supports exceeding the ultrathin monolayer limit for applications outside a stringent UHV environment. Indeed, as highlighted in the introduction, rubene-based OFETs including *h*BN were reported [26]. In addition, X-ray scattering techniques gave, e.g., insight into the interaction of alkanes with *h*BN powders - revealing differences to adsorption on graphite, indicating a lower enthalpy of adsorption [755,756]. Depending on the composition of bi-component adsorbate layers, partial mixing or phase separation of the molecular constituents was reported [756]. For example, n-decane can adopt two distinct adsorption structures on *h*BN (in contrast to graphite), thus resulting in an enhanced miscibility of binary mixtures including n-decane [756]. An early NMR study compared the packing and dynamics of fluorobenzene molecules adsorbed on graphite and *h*BN particles. In both cases, the experiments indicate an adsorption geometry with the molecular plane aligned parallel to the surface, with rapid reorientation about the axis normal to the surface occurring at 141 K [757].

Summarizing, these example indicate that a fabrication of well-ordered *h*BN films with precise control of the number of *h*BN sheets, thus covering the range from monolayer to bulk-like systems in a surface-science setting, which is at most partially achieved to date is a highly rewarding endeavor (compare future perspectives in chapter 4). Furthermore, some of the above findings demonstrate the potential of *h*BN applications outside stringent UHV and low-temperature settings.

3.4. Graphene and other 2D materials

Vertical vdW heterostructures - or stacks - combining *h*BN with other 2D materials attracted considerable interest over the last decade, showing a wealth of intriguing physical properties. *h*BN proved to be a suitable support for graphene [758–763], as detailed in a review by Yankowitz et al. [764]. Examples of its applications include graphene gating, doping or band (mass) engineering [765–770], valley control [771], etching [772], transistor devices [24], and light-emitting diodes [773]. Furthermore, graphene/*h*BN systems provided access to Fabry-Pérot resonances in superlattices [774] and allowed to explore the response of Dirac fermions to individual Co trimers adsorbed on gated graphene [775]. As demonstrated recently, *h*BN encapsulated twisted graphene bilayers show Mott-insulating [776] and unconventional superconductive behavior [777] for magic-angle alignment. Dynamically rotatable *h*BN/graphene heterostructures revealed how the electronic (transport) properties depend on the interlayer twist angle [778]. A free-standing vdW heterostructure consisting of an aligned graphene/*h*BN bilayer was recently characterized by Argentero et al., i.a. using TEM [779]. Interestingly, the suspended structure reveals pronounced structural out-of-plane distortions with amplitudes of ≈8.5 Å following the periodicity of the moiré pattern, thus reflecting some 3D character in intrinsically 2D materials [779]. The analysis of moiré superstructures in suspended graphene/*h*BN bilayers furthermore provided insights into the interlayer interactions [780].

Complementary theoretical efforts addressed many properties of layered hybrid systems, including for example the dispersion, absolute band gaps, and the real-space shape of the low-energy electronic states in the moiré superstructures of graphene/*h*BN [781], as well as the modification of graphene's optical properties on *h*BN [782]. Furthermore, distinct registry and stacking effects in *h*BN were explored [783,784]. Motivated by graphene-based field effect transistors, Wang et al. modeled the electronic properties of *h*BN films sandwiched between graphene layers using the DFT-based effective screening medium method, concluding that the interface with graphene only weakly affects the dielectric properties of *h*BN [65].

Getting back to experimental work, impurities at buried interfaces in vdW heterostructures were shown to segregate into isolated pockets, e.g., leaving large graphene/*h*BN areas clean and atomically flat [785]. The case of buried transition metal dichalcogenides (TMD)/*h*BN interfaces is more intricate, with pristine interfaces reported for MoS_2 and WS_2, whereas for $MoSe_2$ and WSe_2 contaminants are trapped, affecting the interface properties [786]. The role of defects in exfoliated *h*BN in the MBE growth of graphene was explored using AFM, Raman, and complementary DFT modeling [787].

Most of the heterostructures highlighted above base on exfoliation and transfer of 2D materials. In addition to the graphene-related examples, TMDs (such as WSe_2 [788]) were transferred to *h*BN supports targeting distinct functionalities, such as photoluminescence and catalytic activity. Furthermore, *h*BN encapsulation of black phosphorus or $NbSe_2$ was applied in device fabrication [31,789].

As such top-down approaches fall beyond the scope of this review, the reader is referred to recent reviews addressing the fabrication, characterization, and applications of vdW stacks (and lateral heterostructures) including *h*BN (e.g., Refs. [54,193,445,446,790–792]).

As an alternative to exfoliation and transfer protocols, graphene and TMDs were grown by CVD or MBE on *h*BN flakes. Asides graphene [761,793,794], examples include WS_2 [795] and MoS_2 [796]. A single MoS_2 layer on *h*BN revealed small azimuthal rotation angles below 5° between the two materials. The band gap of 1.89 eV - close to the one of free-standing MoS_2 - signals only minor influence of the *h*BN support [796]. Furthermore, furnace-grown ZrS_2/*h*BN

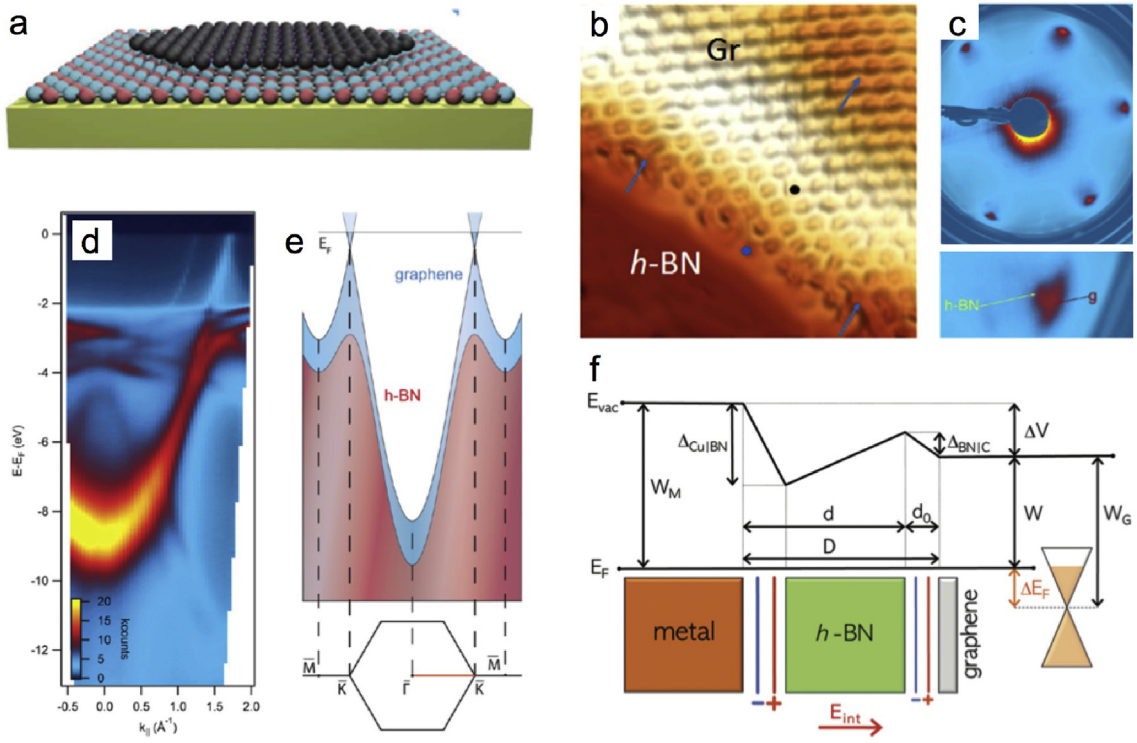

Fig. 47. vdW heterostructures: graphene/*h*BN/Cu(111). (a) Schematic illustration of a graphene sheet grown on a metal-supported *h*BN monolayer. (b) Atomically-resolved STM image of a graphene patch with an armchair-like edge termination. (c) LEED image of graphene/*h*BN/Cu(111) showing the alignment of the two sp^2 lattices. The zoom-in (bottom panel) highlights the contribution from graphene (g) and *h*BN, respectively. (d) ARPES data measured along the $\overline{\Gamma K}$ direction showing the band dispersion of graphene/*h*BN/Cu(111). (e) Scheme illustrating the dispersion relations of the π bands associated with the *h*BN and the graphene. (f) Schematic drawing of a graphene/*h*BN/metal, highlighting the electrostatic potential and interfaces across the heterostructures (compare to (d) and (e)). (a) Adapted with permission from Ref. [808], (b) Adapted with permission from Ref. [286], (c–e) Adapted with permission from Ref. [809] © (2013) American Chemical Society, (f) Adapted with permission from Ref. [767] © (2011) American Chemical Society.

was characterized by SEM, TEM, AFM, and electric measurements in devices [797,798].

Motivated by purity (see above) and scalability issues of established top-down fabrication methods, recent efforts aimed at the synthesis of vdW stacks by all-CVD processes. E.g, stacked TMD/*h*BN heterostructures were achieved in all-CVD processes for MoS_2 on few-layer *h*BN grown on a sulfide-resistant Ni-Ga alloy [799] and on SiO_2 (after transfer from Cu) [800], respectively. Furthermore, oxygen-assisted CVD-grown *h*BN films on SiO_2 served as supports for the CVD synthesis of MoS_2 and WS_2 [801]. Specifically, the MoS_2 monolayer growth on wafer-scale, CVD-synthesized *h*BN films highlights the potential to prepare extended, high-quality crystalline TMDs on *h*BN by bottom-up approaches [802]. Importantly, these examples base on *h*BN multilayers. In the following, we will get back to *h*BN monolayer systems.

3.4.1. 2D materials on hBN/single crystals

In this short paragraph, we focus on the few studies employing CVD growth of graphene and TMDs on *h*BN/metal single crystal interfaces in UHV. That is, experiments where a surface-supported *h*BN monolayer is used as substrate for graphene or TMD "assembly" (similar to the cases of atoms and molecules discussed in the previous sections) are reviewed (see scheme in Fig. 47(a)).

To this author's knowledge, the first such study was presented by Nagashima et al. in 1996, revealing the formation of a graphene overlayer on *h*BN/Ni(111) [803], followed by additional reports from the Oshima group [804–807]. In the pioneering study, a ML-equivalent of graphene was formed upon exposure of *h*BN/Ni(111) to about 10^6 L of acetylene at 873 K. Upon graphene formation, the work function increased to 4.3 eV (compared to 3.6 eV for *h*BN/Ni(111), see section 2.2.9) approaching the value of graphite (4.6 eV). Based on XPS and ARPES experiments, the interfacial electronic structure was compared to graphite and it was concluded that the interlayer interactions are weak, resulting in atomically precise spatial transitions of the electronic properties [803]. In later studies, the graphene layer was grown by exposing *h*BN/Ni(111) to about 10^6 L of benzene at 1073 K, and the resulting interface was probed by HREELS and LEED, revealing an incommensurate graphene growth. Furthermore, the interaction with the graphene overlayer reduced the *h*BN-Ni hybridization, resulting in bulk-like *h*BN properties (lattice constant, insulating character, phonons) [806]. From a theoretical perspective, Avramov et al. described geometric and electronic interface properties of graphene/*h*BN/Ni(111) and compared these to related multilayer systems [359].

In a combined experimental and theoretical endeavor, Bjelkevig et al. addressed the growth of graphene on *h*BN/Ru(0001), providing evidence for considerable interlayer charge transfer towards the graphene [327]. Usachov et al. applied a quasi free-standing *h*BN layer on Au/Ni/W(110) (see paragraph 3.1.1) as a support for nearly 0.5 ML graphene, grown at 1023 K by CVD employing acetylene ($\approx 1.2 \times 10^6$ L) [318]. ARPES data reveal a feature with linear dispersion assigned to the graphene π band, with the apex of the Dirac cone located close to E_F without indication of a gap [318]. A gap-opening was predicted for a commensurate graphene sheet on a *h*BN multilayer [765]. Also a multi-method study (LEED, STM, XPD, ARPES) by Roth et al. observed a graphene-related band with linear dispersion, crossing E_F near the $\overline{K}$ point of the surface Bril-

louin zone, lacking any indication for a gap opening, but indicating n-type doping (Fig. 47(d and e)) [809]. In this case, graphene was grown on *h*BN/Cu(111) (1100 K, 10^6 L of 3-pentanone), resulting in aligned, incommensurate heterostacks, where the mismatch between the graphene and *h*BN lattice constants is close to the one of the two free-standing layers (1.6%) (Fig. 47(c)). The resulting moiré pattern was resolved by STM [809]. The n-type doping of graphene on *h*BN/Cu(111) was also inferred from DFT modeling of this interface (Fig. 47(f)) [767]. In an attempt to apply the same approach to grow graphene on a corrugated *h*BN sheet, Roth et al. extended their experiments to *h*BN/Rh(111) [810]. In this case, the scenario was more intricate. In a first CVD step (1150 K, 3-pentanone at 2.2 mbar), carbon dissolved into the Rh support, weakening the *h*BN-metal interaction and lifting the nanomesh corrugation, together with the formation of small graphite flakes on *h*BN. In a subsequent, identical CVD step, graphene grows on the planarized *h*BN sheet - in addition to the subsurface interstitial C and the multilayer graphite flakes, resulting in a situation similar to graphene/*h*BN/Cu(111) discussed above [810]. Again, the graphene and *h*BN lattices are aligned. Such a preferred relative twist angle of 0° between the two sp^2 sheets was also inferred from thermal annealing experiments of graphene on exfoliated *h*BN flakes, where graphene patches with a twist angle below 12° rotated towards 0° upon annealing, whereas patches with an angle above 12° rotated to a metastable 30° configuration [811]. Recently, Hwang et al. reported the formation of sub-ML graphene/*h*BN/Cu(111) by exposing approximately 0.5 ML *h*BN on Cu(111) to ethylene (10^3-10^4 L) [286]. Based on STS data, it was concluded that small patches of graphene grow on *h*BN/Cu(111) - in addition to graphene islands on Cu - even before bare Cu(111) areas are fully covered. Armchair-like and zigzag edges of the *h*BN flakes, as well as their "bulk-like" regions far from boundaries were probed by STM (Fig. 47(b)) and STS, revealing distinct spectral signatures. Besides observing edge states and resonances, the authors speculate about a small (<10 meV) bandgap in graphene/*h*BN/Cu(111) based on the STS analysis [286].

Applying MBE as an alternative scalable method for 2D material synthesis, Driver et al. grew graphene on about 5 ML *h*BN/Co(0001) (compare paragraph 2.2.6). At 800 K this substrate was exposed to carbon evaporated from a graphite rod, resulting in graphene formation characterized by XPS and LEED. This method allows for the growth of graphene multilayers azimuthally aligned with the *h*BN lattice, featuring domain sizes of about 190 nm [230]. It should be noted that MBE growth of graphene was previously demonstrated on *h*BN flakes [812]. Furthermore, a recent report highlights means to generate and modify strain in graphene, grown by MBE on *h*BN flakes exfoliated from single crystals [813].

The UHV-based synthesis of 2D materials - beyond graphene - on *h*BN monolayers on metal single crystal is still in its infancy (see perspectives in chapter 4). Zhang et al. reported the successful growth of $MoSe_2$ on *h*BN/Ru(0001) by MBE [225]. The STM/STS characterization revealed a $MoSe_2$ quasi-particle band gap of 1.90 eV. Its reduction by about 0.25 eV compared to the situation on graphite or graphene supports highlights the intricate effects of band structure renormalization at such interfaces. Furthermore, the *h*BN/Ru(0001) nanomesh structure was found to imprint a potential modulation in the $MoSe_2$ [225]. Cattelan et al. studied the growth of a WS_2 monolayer on *h*BN/Au/Ni(111) [276]. Photoemission revealed an unperturbed electronic structure of WS_2, suggesting that intrinsic properties of WS_2, such as photoluminescence, can be retained on the *h*BN/Au/Ni(111) support [276].

3.4.2. Graphene on hBN/foils

Even though the results summarized in the following were achieved on metal foils in furnaces outside a UHV environment, we briefly cover them as examples of two-step CVD growth of graphene/*h*BN interfaces. Wang et al. applied *h*BN/Cu as support for CVD growth of graphene from methane [620,623,814]. Besides providing an STM/STS characterization of the interfacial structure, they showed by cross-sectional TEM measurements that the graphene/*h*BN stacks are robust enough to survive the transfer to other supports as SiO_2/Si [814]. Furthermore, the catalytic properties of *h*BN/Cu for graphene synthesis were explored as function of the number of *h*BN sheets, both in experiments and by theoretical modeling (compare paragraph 3.2.3). As the catalytic activity of the *h*BN surface is dictated by charge transfer from the underlying Cu, it is strongly suppressed with increasing film thickness, but even allows for graphene growth on *h*BN films with a thickness approaching 3 nm [620]. A non-vanishing catalytic activity of *h*BN/Cu for graphene growth was confirmed by Song et al., who furthermore demonstrated the use of PMMA seeds for the nucleation of highly ordered graphene arrays on *h*BN/Cu [383]. Kim et al. characterized graphene/*h*BN interfaces at sub-ML coverages prepared in a sequential CVD approach by AFM, KPFM, SEM, STEM, and Raman [815]. Besides lateral junctions, vertical heterostructures representing graphene patches expanding onto *h*BN flakes were observed at higher methane concentration and growth time. Here, an AA-like stacking between the sp^2 sheets with a very small azimuthal misalignment (< 1°) was identified. The contact potential difference assessed via the KPFM measurements showed a reduction of the work function for graphene/*h*BN/Cu compared to graphene/Cu (see below) [815]. A somewhat different protocol for CVD of graphene on *h*BN was introduced by Gao et al., applying benzoic acid as precursor, demonstrating the fabrication of a 4-inch wafer-scale graphene/*h*BN film. Depending on the temperature of exposure of *h*BN/Cu, either lateral or vertical interfaces can be formed. In the latter case, the temperature is kept below 1173 K to avoid etching of *h*BN by CO_2 - a decomposition product of the precursor - and graphene islands were formed on *h*BN/Cu [808]. A characterization of graphene/*h*BN/Cu by XPS, AFM and STM revealed moiré patterns with periodicities comparable to the ones described by Roth et al. ([809], see above) and confirmed an alignment of the graphene and *h*BN lattices and the integrity of the latter. In addition, work function differences were extracted from EFM measurements, yielding a lower local work function for graphene/*h*BN/Cu compared to *h*BN/Cu [808]. This finding - being in contrast to the situation for graphene/*h*BN/Ni(111) discussed above - was rationalized by an n-type doping of graphene from Cu, even through the *h*BN spacer layer [808], in-line with theoretical predictions from Bokdam et al. [767]. Replacing the CVD-synthesis step of *h*BN by ion beam sputtering deposition, Meng et al. grew graphene on ML and sub-bilayer *h*BN [816].

In addition to Cu foils, also Co films were employed for the sequential synthesis of graphene/*h*BN heterostructures. Xu et al. demonstrated that C preferentially nucleates on the Co substrate and on edges of *h*BN flakes. Higher C dosage resulted in continuous graphene sheets, eventually covering the *h*BN in a layer-by-layer fashion [331].

3.4.3. Comparison and discussion

Summarizing this short section, one can conclude that a single *h*BN layer on metal single crystals provides a stable platform for graphene synthesis, even if the catalytic activity of the *h*BN terminated templates is generally drastically reduced compared to the bare metals. Several studies indicate that charge transfer through the

*h*BN plays a relevant role for the CVD growth and the electronic properties of graphene (as n-type doping) - thus making the heterostacks distinctly different from graphene on bulk *h*BN. On the other hand, no charge transfer to graphene through *h*BN was detected when adsorbing Br_2 on *h*BN encapsulating graphene [817]. Accordingly, the situation might sensitively depend on the nature of the metal support - as discussed in the previous sections about atomic and molecular adsorbates. Detailed information on the CVD synthesis of vertical (and lateral) graphene/*h*BN heterostructures is available in a recent review article by Wu et al. [447].

Also bulk-like *h*BN and exfoliated *h*BN flakes can provide suitable supports for graphene-based architectures (see examples in the introduction of this section) and graphene synthesis [793,818–821], as evidenced for example by the plasma-enhanced CVD epitaxial growth of single-domain *h*BN [761], drastically reduced energy variations of FER in graphene/*h*BN compared to graphene/SiO_2 [822], or the epitaxy of graphene nanoribbons with widths from 15 to about 150 nm featuring high carrier mobility [823]. In addition, *h*BN model systems are applied in many theoretical studies addressing the modification of graphene-related interfaces, including for example graphene nanoribbons on *h*BN (e.g., Ref. [824]) or graphene on functionalized *h*BN (e.g., Ref. [825]).

On the next level of complexity, graphene/*h*BN stacks can themselves serve as supports for adsorbates. For example, an AFM study providing sub-molecular resolution on F_4TCNQ/graphene/*h*BN by Tsai et al. showed regular 2D islands with aligned molecules at sub-monolayer coverage - in stark contrast to F_4TCNQ adsorption on graphene/metals [826]. This peculiar self-assembly behavior was rationalized by the poorly screening graphene/*h*BN support. By implementing graphene/*h*BN stacks in devices, Riss et al. could tune the energy levels of adsorbed CVB molecules by a gate, allowing for an electronic switching between two different molecular states at fixed sample bias, visualized with sub-molecular contrast by STM and dI/dV mapping [827]. Gate-tunable charging was also reported for individual F_4TCNQ molecules on graphene/*h*BN [828] - opening prospects for charged-molecule physics [829]. Furthermore, self-assembly of CoPc on a graphene/*h*BN support resulted in extended, highly regular molecular arrays with lateral extension and electronic homogeneity exceeding the ones achieved on graphene/SiO_2 supports [830].

4. Conclusions and future perspectives

The first successful synthesis of a *h*BN monolayer on a metal single crystal more than two decades ago was the beginning of a fascinating scientific journey and an exciting, still expanding research field. In this regard - at least in the author's opinion - the appeal of atomically-thin *h*BN sheets relates to their multifaceted roles that progressed and developed with time. In the early stages, research focused on the adsorption and decomposition of borazine precursors on metals, i.e., on the elucidation of surface reaction mechanisms that resulted in *h*BN films. Soon afterwards, the potential of *h*BN as stable, insulating films interacting weakly with metals came into focus. Technological applications were envisioned, based on the abrupt change of electronic properties at the *h*BN/metal interface. A second atomically-sharp interface was then introduced by adsorption of atoms or molecules on *h*BN/metal, employing *h*BN as a passive, inert decoupling layer. Later experimental and theoretical studies recognized that *h*BN - support interactions can be exploited to turn inert *h*BN sheets into catalytically active ones, e.g., fostering site-selective on-surface reactions and providing means to steer reaction pathways for applications in heterogenous catalysis. Moreover, the rise of graphene boosted the interest in *h*BN, resulting in progress both affecting basic research (e.g., properties of heterostructures) and applications beyond model systems handled in stringent UHV environments (e.g., transfer protocols, wafer-scale synthesis, device fabrication).

In these concluding remarks we refrain from providing a somewhat repetitive summary. To recollect the key findings, the reader is referred to the résumés presented in the respective chapters. We rather turn to an outlook, compiling some open issues that might warrant further consideration and briefly outlining rewarding future research directions involving *h*BN-based model systems.

Controlled multilayer growth. As obvious from many examples discussed in this review, *h*BN monolayers can drastically reduce the electronic "disturbance" of adsorbates compared to metal supports - and thus give access to investigations of manifold physical and chemical phenomena. At the same time, as also obvious from many examples discussed in this review, they do not necessarily represent "innocent", insulating supports for adsorbates (e.g., reminiscent of findings on ultra-thin oxide films [144]). Besides the interaction with the metallic substrate, it is simply the atomically thin character of *h*BN monolayers that allows some electronic interaction including potential charge transfer, and enables for example the application of STM. Similar to the setting on ultra-thin halides (e.g., Refs. [155–158,160,161,831,832]), the STM's capabilities to probe adsorbates in a weak-coupling regime with atomic precision is expected to provide further fascinating insights into molecular properties, functionalities and on-surface chemistry. For many experiments and applications however, the *h*BN monolayer thickness of course poses a serious limitation: considerably thicker films would be needed to prevent charge tunneling [179,180] and to avoid a (spacer layer thickness dependent) influence of the buried metal on mobility and self-assembly properties [167,168]. In this respect, innovative approaches to fabricate *h*BN multilayers in-situ with controlled thickness and high structural quality in a scalable fashion need to be further developed, potentially basing on MBE protocols (see Refs. in paragraph 2.1) and progressing beyond the current state-of-the-art processes summarized in a recent review [195].

Structure determination. As emphasized in the first part of this review (chapter 2) a comprehensive characterization of *h*BN/metal interfaces is the basis for their application as templates. Indeed, considerable efforts were dedicated to structure determination throughout the last decades, with standard surface science tools (XPS, SXRD, NEXAFS, LEED, STM) yielding a wealth of information, e.g., on the electronic properties and on the *lateral* interface structure, i.e., superstructure periodicities and registries. Nevertheless, a lack of quantitative information regarding the *vertical* interface structure is apparent. For example, it is truly astonishing that experimental values for the adsorption heights and corrugation of the most widely studied nanomesh structure (*h*BN/Rh(111)) are lacking to date, or it is disappointing that no true consensus about the vertical interface structure of *h*BN/Cu(111) is reached - especially considering the plethora of studies relying on *h*BN growth on Cu. Clearly, the widely employed STM technique fails in providing this information and needs to be backed up by other methods (e.g., XSW, LEED-IV, PED). From a theoretical perspective, the challenges are as well considerable, as exemplified by the wide range of adsorption heights (2.65–3.33 Å) predicted for *h*BN/Cu(111) or by the different corrugation values reported for the nanomesh structures. As even modest changes in the vertical interface structure can severely affect its electronic properties, and thus its catalytic or templating functionalities, a precise characterization is desirable and requests further joint experimental and theoretical efforts.

Regarding the adsorbate/*h*BN/metal structures discussed in chapter 3, the lack of quantitative information about the vertical interfaces is even more apparent. Specifically, two important questions remain mainly unaddressed, at least from the experimental

perspective: What are the adsorption heights of molecules? And how do the adsorbates modify the buried *h*BN/metal interface? Again, these issues can not be solved by STM and ask for other experimental approaches. E.g., the average adsorption height of Co-Porphine on *h*BN/Cu(111) was determined recently by XSW, with no modification in the *h*BN-Cu(111) separation observed upon molecular adsorption [469]. Future research efforts will not only have to focus on modifying adsorbate's properties by the interaction with the *h*BN/metal support, but will increasingly have to deal with the engineering of *h*BN/metal properties by adsorbates [699]. Accordingly, addressing the questions above will likely be a rewarding endeavor.

Interface engineering and self-assembly. Chapter 3.3 presented a variety of well-ordered, self-assembled supramolecular nanostructures stabilized by vdW-, hydrogen-bonding- or metal-coordination-interactions, highlighting the peculiar environment provided by the *h*BN/metal supports. Nevertheless, regarding the immense possibilities of supramolecular (coordination) chemistry, these achievements can only present a starting point for more intense research efforts. So far, most of the reports describe (nearly) dense-packed homomolecular arrays, results on coordination or covalent architectures are scarce and information on advanced assemblies, introducing for example chiral building blocks or donor-acceptor pairs is largely missing. Very little is known about the thermal stability and the role of the metal centers for functionalities, e.g., in magnetism or heterogeneous catalysis. Thus, much can still be done regarding the self-assembly of specific coordination architectures and the development of covalent coupling protocols on *h*BN. Here, additional inspiration might be provided by studies on graphene, which recently served as a support for the synthesis of peculiar chain-like organometallic wires [833], 2D metal-organic networks [834], or bi-component covalent organic frameworks with pore diameters around 3 nm [835]. Regarding covalent bond formation, new, "clean" procedures beyond Ullmann coupling reactions need to be developed for the formation of well-ordered covalent nanostructures on monolayer *h*BN or its bulk compound - such as the recently reported ylide coupling mechanism [675]. In view of their promising optoelectronic and magnetic properties and their peculiar coordination ability already exploited on metal surfaces, lanthanides bear great promise as ingredients for functional coordination architectures and multi-decker complexes on *h*BN [836]. Even regarding atomic adsorbates, distinct self-assembled structures (such as Au atom chains theoretically predicted to form on *h*BN/Rh(111) [527]) deserve experimental attention.

In addition, we covered some examples highlighting how intercalation can be used to tailor the interface properties - including macroscopic parameters as wetting angles. However, there is still tremendous potential for future experiments, as indicated by studies tuning the electronic and magnetic properties of the graphene/metal interface by intercalation, selectively combined with alloy formation (e.g., Refs. [837,838]). A recent report by Bazarnik et al. showcased how Fe or Co intercalation in graphene/Ir(111) can completely alter the self-assembly of metal-organic molecules on these supports, resulting in rt stable square, honeycomb, or Kagomé lattices [307]. Au intercalation in graphene/Ni(111) quenched the magnetic coupling between $TbPc_2$ and Ni, but did not perturb the coupling for $ErPc_2$ [839]. Given the manifold reports on magnetic coupling between adsorbates (atoms or metal-organic complexes) on graphene and magnetic supports (e.g., Refs. [840–846]) - an area experimentally largely unexplored using *h*BN as spacer layer - intercalation of magnetic films will considerably expand the playground regarding modification of adsorbates' magnetic properties. The intercalation of tetrapyrroles in *h*BN/Cu(111) recently demonstrated by the author's group [314] might be extended to different functionalized molecular units, yielding (metal-)organic networks protected by the *h*BN cover, a nanoreactor-type setting for confined chemical reactions, or organic/insulator/organic sandwich structures, where intermolecular coupling effects through the ultra-thin barrier might be studied.

Controlled modification. From a surface science perspective, the study and use of deliberate structural modification of *h*BN sheets on metal single crystal supports is still in its infancy. Specifically, the potential of atomic-size defects and dopants in *h*BN to tune the systems catalytic, magnetic, and (opto)electronic properties is enormous, as many theoretical studies emphasize (see paragraphs 3.1.7 and 3.2.6). However, an experimental implementation and verification of predicted functionalities is still largely missing. Even though scarce UHV-based studies reveal the potential of dopants in sp^2 sheets to tune, e.g., the properties of large organic molecules - as exemplified by porphyrin or FePc adsorption on N-doped graphene [847,848]. Out of all the elements potentially applicable as *h*BN dopants, C naturally plays a special role, with several reports on BNC sheets available (vide infra). For example, BNC flakes showed enhanced photoelectrochemical performances that increased with increasing amount of substituted B [849] and BN doping of graphene is predicted to favor the dissociative adsorption of H_2, water, methane, and methanol [850]. Importantly, theoretical endeavors point out the relevant role of disorder, phase separation, and composition fluctuations for the properties of such BNC monolayers [851]. However, the fabrication of modified *h*BN structures with control over defect density and distribution - ideally reaching atomic precision - is a challenging tasks (see Fig. 48 (b)). In this respect, the use of self-assembly and on-surface synthesis protocols employing precursors with embedded dopants or defects might be one route to follow [448]. Specifically, BN-doped carbon scaffolds are available as promising starting materials for regular BNC nanostructures [448,449,852–861] that complement lateral *h*BN/graphene heterostructures (see below, Fig. 48 (c)) and disordered BNC sheets (Fig. 48 (a)) [443,450,862]. As highlighted by the recent use of a Au-anchored porous CN framework in electrocatalysis [863], there is also considerable potential for related systems of only bi-elemental configuration.

A further promising research area, where UHV-based experiments are emerging [189,275], is the covalent functionalization of *h*BN monolayers [864] - complementing non-covalent modification protocols of *h*BN and other 2D materials [865]. As mentioned in the discussion paragraphs 3.1.7 and 3.2.6, theoretical modeling provides predictions about the tunability of magnetic and (opto)electronic properties of *h*BN sheets by out-of-plane functionalization, which remain to be verified in experiments. As a special case, hydrogenation of *h*BN not only provides prospects for band-gap engineering, but also for application in hydrogen storage [189,275], adsorbate anchoring [558], and photocatalytic water splitting [587]. Recently, a compression-induced transformation of a silicon oxide supported *h*BN bilayer in the presence of hydroxyl ions to a conductive, sp^3-hybridized BN compound - named bonitrol - was reported [866], highlighting that the (local) application of pressure can be an additional control knob to tune properties of BN materials.

Heterostructures and interfaces. As discussed in the introduction and in section 3.4, an exciting library of 2D materials exists that can potentially be combined with *h*BN to form heterostructures (e.g., Refs. [22,23,867,868]). The near future will show if *h*BN monolayers can act as supports for the UHV synthesis of ultra-thin layers beyond graphene, e.g., other carbon allotropes as graphyne [869], silicene, germanene, borophene, stanene, phosphorene, transition-metal oxides, and dichalcogenides. For instance, recent reports show that few-layer *h*BN films are robust enough to support the CVD growth of MoS_2 crystals [799,800], whereas a *h*BN monolayer on Au/Ni(111) was employed as platform for WS_2 synthesis [276]. Triangular MoS_2 islands were grown via powder vapor transport on *h*BN flakes - achieving orientation control and thus opening up path-

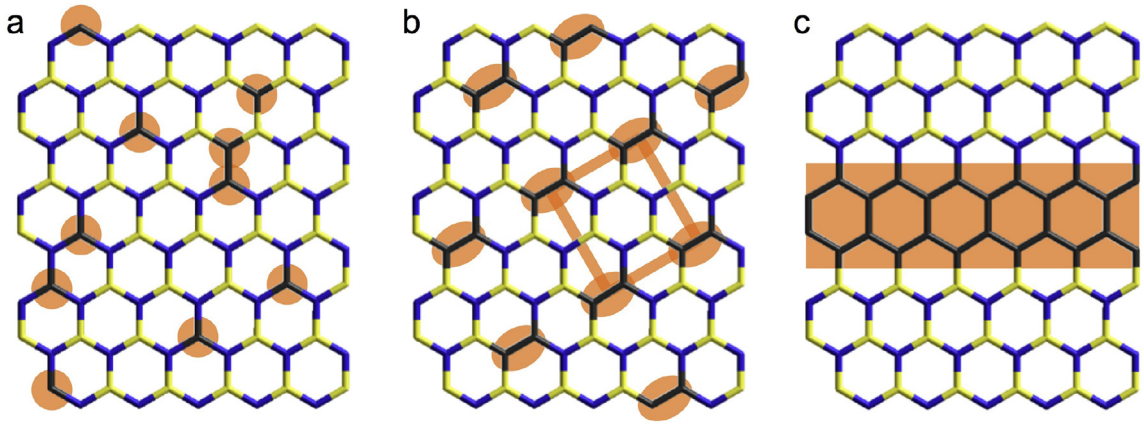

Fig. 48. Schematic illustration of substitutional heteroatoms and lateral interfaces. (a) Randomly distributed heteroatoms in a *h*BN sheet. (b) Regular doping pattern, e.g., representing C_2 units on a lattice (orange rectangle) embedded in *h*BN. (c) Atomically defined lateral *h*BN/graphene/*h*BN interface. The orange color highlights the substitutional heteroatoms and the graphene nanostructures embedded in *h*BN (blue, yellow), respectively. (For interpretation of the references to color in this figure legend, the reader is referred to the Web version of this article.)

ways to single crystal MoS_2 films without inversion domain boundaries [870]. As theoretically exemplified for the stanene/*h*BN interface, such heterostacks provide prospects for nanoelectronics and spintronic applications [871]. Intriguing topological properties are predicted for germanene/*h*BN, stanene/*h*BN, or silicene/*h*BN interfaces, which can be modified by external electric fields [872]. Furthermore, defect-engineering at phosphorene/*h*BN interfaces can be used to tune the band gap [873].

Focusing on lateral heterostructures, the combination of graphene and *h*BN (providing a close structural match) allows for the fabrication of atomically-defined interfaces on single-crystal supports [218,249,273,322,416,421,440–443,447,874], as alluded to in the paragraph 2.3 about defects. The resulting structures - reminiscent of systems on foils (e.g., Refs. [388,816,875–877]) - represent an extreme case of BNC nanostructures addressed above, featuring spatially separated, extended graphene and *h*BN patches (see Fig. 48 (c)) [878,879]. Equilibrium shapes of graphene embedded in *h*BN (or vice versa) and interface properties are rationalized by modeling efforts [453]. Even though heterostructures of distinct geometry, as regular stripe-like phases with stripe widths below 100 nm [441] could be achieved experimentally on selected substrates and uniform arrays of *h*BN/graphene "core/shell" flakes with separations in the 10 μm range were recently reported [876], a widely applicable control procedure over shape, size, and spatial order of the patches by means of bottom-up fabrication is still lacking, analogous to the above discussion about BN doping patterns in BNC structures. Importantly, as experimentally demonstrated for BNC sheets on Ru(0001) by Lu et al., dynamic mixing and demixing processes can be used to tailor the layer properties (including, e.g., the integration of GNRs), but might interfere with the stability of intended structures [443]. Furthermore, Nappini et al. reported the important role of the substrate temperature in the synthesis of BNC heterostructures on Pt(111) from a single dimethylamine borane precursor, e.g., achieving either single layers consisting of graphene and *h*BN domains or hybridized BNC films [880,881]. Recently, Petrovíc et al. showed how the BNC alloy phase in between *h*BN and graphene patches on Ir(111) can be deliberately modified by adapting the preparation conditions and discussed the effects of annealing on the *h*BN/graphene heterostructures [882].

On the other hand, by combining top-down (photolithography & reactive ion etching) with bottom-up processes (CVD) superstructures with feature sizes in the 10 μm range were achieved on a Cu foil [883]. A similar pattern/re-growth procedure was employed to create nanoscale-patterned heterostructures with stripe widths as low as 100 nm [884]. Graphene growth in etched *h*BN trenches provided individual GNR featuring widths in the 60 nm to sub-10 nm range [885]. Given the minimal structure sizes in the 10 nm range achievable by helium ion etching of graphene [886], the potential of such combined approaches is evident.

Theoretical studies on the adsorption of fullerenes and nanotubes on a 2D superlattice incorporating graphene and *h*BN stripes suggest the use of such systems in excitonic solar cells [739]. Similar stripe-like *h*BN/graphene heterostructures might provide the option of controlled CO_2 capture and release via voltage-induced charging of the *h*BN stripes [887].

Reverting to bare sheets composed of graphene and *h*BN patches, interesting properties are predicted by various theoretical studies. E.g., finite *h*BN areas embedded in a distinct graphene environment are anticipated to deliver substantial quadratic nonlinear optical activities [888], while triangular graphene patches embedded in a *h*BN matrix become ferromagnetic with full spin polarization [889] and are expected to act as spin dots operating at temperatures up to approximately 250 K [890]. Mid-gap states near E_F were predicted for graphene patches in *h*BN in case an unequal number of B and N atoms is substituted by C [891] and core (graphene)/shell (*h*BN) quantum dot properties were described in dependence of their geometric shape and extension [892]. A recent review by Kan et al. provides an overview about tunable properties in lateral heterostructures [893], including a *h*BN concentration dependent band gap [894].

Naturally, the coexistence of two chemically distinct surface terminations is appealing in view of templating applications, the most straightforward one being selective adsorption on one of the 2D constituents guided by differing adsorption enthalpies. Similar effects readily occur for submonolayer coverages of 2D materials on metal supports. For example, PTCDA was shown to interact weakly with borophene, thus preferentially forming self-assembled arrays on adjacent Ag areas, resulting in well-defined lateral PTCDA/borophene interfaces [895]. Porphines decorate Cu areas, avoiding graphene or *h*BN patches at temperatures where diffusion is operational [314]. Furthermore, selective oxygen intercalation was observed in graphene/*h*BN heterostructure islands on Ru(0001), enabling an exclusive modification of the *h*BN/Ru interface [228]. Reports on molecular decoration of 2D materials beyond *h*BN and graphene, as TMDs are currently just emerging (e.g., Refs. [896,897]). How-

ever, there is no doubt that upcoming studies will provide new insights, contributing to the fabrication of multi-component 2D templates. For instance, a recent report introduced a "sowing" mechanism applying molecules as seeds in the CVD growth of lateral heterostructures combining monolayer TMD with graphene or *h*BN [898].

Besides the distinct surface terminations, the interfaces between the 2D constituents - with current research focusing on in-plane graphene/*h*BN junctions - offer potential to modify adsorbate properties and to guide adsorption. As discussed in the introduction of Ref. [899], zigzag, armchair, or misoriented interfaces (featuring pentagons and heptagons), possess distinct characteristics, e.g., including an interface-state localized at the zigzag edge (confirmed experimentally by Drost et al. [322]) or a band-gap opening in armchair terminated graphene stripes [900]. Grain boundaries in *h*BN consisting of tetragons and octagons (4|8) are predicted to considerably enhance the adsorption energies of Co adatoms, dimers, and trimers - without affecting the magnetic properties of the Co adatoms. Furthermore, this interface induces an anisotropic diffusion behavior, with Co adatoms moving considerably faster along the 4|8 grain boundary than in the direction perpendicular to it [600]. An increased binding strength on the octagons of 4|8 defects was additionally reported for Cr, Mn, Fe, and Ni - anticipating the formation of transition metal atom chains introducing versatile electronic and magnetic properties to *h*BN [901]. Experimentally, a selective adsorption of LiF was observed at defect lines in *h*BN, resulting in a chemically and mechanically stable hybrid LiF/*h*BN film for electrochemical applications [902]. Thus, grain boundaries or lateral interfaces in *h*BN and 2D multicomponent sheets offer tremendous potential for guided self-assembly and the study of site-sensitive adsorbate properties.

Solid/liquid interfaces. Several studies reviewed in chapter 2 highlight the stability of distinct *h*BN/metal systems in water and solution (ultra-pure water [240], perchloric acid (0.01–0.1 M $HClO_4$) [240,241,335], common polar and nonpolar solvents [335]) - with the exception of hot, strongly alkaline solutions [335], suggesting their use in liquids. Indeed, pioneering studies demonstrate the applicability of *h*BN at solid/liquid interfaces, discussing the electrochemical switching of surface texture by hydrogen intercalation [335], the engineering of *h*BN wettability by covalent functionalization [903], electrocatalysis (e.g., ORR), defect decoration by Cu underpotential deposition [452], R6G adsorption from aqueous solution [730], and trapping of hydrated $(WO_3)_3$ clusters in *h*BN/Rh(111) nanomesh pores [904]. These examples not only show that *h*BN/metal model systems offer means to study the wetting behaviour, adhesion and friction [335] - connecting nanoscopic with macroscopic properties - but also highlight the potential of surface-anchored *h*BN in applications such as heterogeneous catalysis [615] or water cleaning and molecule detection [730]. Ab initio molecular dynamics simulations for instance show a friction coefficient of water on *h*BN that exceeds the one on graphene by about a factor of three, despite the structural similarity of the interfaces to the two sp^2 sheets [42].

Liquid-phase functionalization of *h*BN sheets in a bulk-like material by adenine-terminated polypropylene glycol was applied by Muhabie et al. for the exfoliation of *h*BN nanosheets in tetrahydrofuran solution, exploiting the considerable adenine-*h*BN interactions [905] and contributing to established solution-based exfoliation protocols (see Refs. in introduction of section 2.1). Also *h*BN powders are readily modified in liquids, as highlighted for example by the adsorption of saccarides on *h*BN in water [744]. While the controlled synthesis and scanning probe characterization of molecular nanostructures in solution is largely unexplored on *h*BN monolayers, related studies on graphene highlight the potential of this approach. For instance, a 2D covalent organic framework (COF) was prepared by Schiff-base coupling of benzene-1,3,5-tricarbaldehyde (BTA) and p-phenylene-diamine (PDA) in octanoic acid on copper-supported graphene. Hereby, the reaction can be limited to the interface by control of the precursor concentration and the STM allows one not only to image the porous framework with high resolution, but also to access and track dynamic processes at the interface [906]. Colson et al. reported the synthesis of nano-porous COFs with hexagonal and square symmetry on surface-anchored graphene by solvothermal condensation, employing 1,4-phenylenebis(boronic acid) (PBBA), 2,3,6,7,10,11-hexahydroxytriphenylene (HHTP), pyrene-2,7-diboronic acid, and NiPc linkers [835]. Such approaches and protocols - contributing to the overarching goal of synthesizing highly ordered 2D organic polymers [907] - still need to be implemented on *h*BN. In addition, solution-based intercalation processes, e.g., demonstrated for bulk-like *h*BN in suspensions of Brønsted acids (H_2SO_4, H_3PO_4, $HClO_4$) [317], might offer exciting possibilities for the reversible modification of interface properties or chemical reactions in a confined space providing a unique 2D environment.

Heterogeneous catalysis. Throughout this review, we repeatedly touched the potential use of surface-anchored *h*BN and its structural modifications in heterogenous catalysis. Indeed, this research field might see exciting developments in the near future, especially on the experimental side where studies on highly-defined systems are scarce to date. At this point, we refrain from repeating the most prominent systems and reactions with adsorbates, which were discussed in the respective sections. A recent review by Deng et al. comprehensively summarizes catalysis with 2D materials and their heterostructures, including the oxygen reduction reaction, water splitting, and CO_2 activation and furthermore discusses the future opportunities and challenges in this field [908]. It only should be emphasized that (carbon doped) *h*BN already has proven its ability to act as a stable and sustainable photo- and electrocatalyst (e.g., Refs. [615,625,909]). In this respect, the scalable synthesis of (doped) *h*BN on foils - either by CVD approaches or on-surface covalent coupling of tailored precursors - offers serious prospects for applications in heterogenous catalysis. The control over defect and doping structures, i.e., their density and position however remains a challenging task. Likewise, the *h*BN-substrate interaction needs to be carefully considered to enable electron transport to the catalytically active centers, which is not given for free-standing *h*BN [358,655]. The catalytic activity of metal clusters and nanoparticles adsorbed on *h*BN monolayer/metal supports also deserves more attention. For example, the catalytic activity in CO oxidation predicted for small, negatively charged Au clusters on *h*BN/Rh(111) [527] or the observation of *h*BN-supported Pd-Fe core shell nanoclusters catalyzing a Suzuki-Miyaura coupling reaction [550] give a flavor of what might be achievable when tailored cluster/*h*BN/metal architectures are systematically explored.

In addition to the synthesis procedures that might rely on a UHV environment, at least part of the experimental characterization of catalytic processes should be performed at ambient atmosphere, high-pressure, or in solution, i.e., beyond a classical UHV surface science setting. This will likely require an interdisciplinary approach combining complementary experimental instrumentation and expertise.

Acknowledgments

First and foremost, I would like to thank all team members, colleagues and project partners co-authoring cited joint publications for their dedication and contributions to the *h*BN studies. My special appreciation goes to Prof. Thomas Greber and Prof. Jürg Osterwalder for introducing me to *h*BN at times preceding the rise of 2D materials (during my PhD studies at UZH). I am grateful to Prof. Johannes V. Barth for his continuous mentorship and fruitful discussions. Prof.

Klaus Wandelt's invitation encouraged me to write this review, and I am thankful for his patience and continuous support as responsible editor of Surface Science Reports. During this work, discussions with Dr. A.P. Seitsonen, Prof. P. Liljeroth, and Dr. M. Iannuzzi were highly appreciated, and I would like to thank the many colleagues who responded promptly to inquiries for further details and clarifications on their publications. Furthermore, I am grateful to PD Dr. Florian Klappenberger for his advice regarding the handling of references. I appreciate the help of Dr. Martin Schwarz with Fig. 32 and the support by Ms. Viktoria Blaschek concerning copyright requests. I thank Dr. Manuela Garnica, PD Dr. Francesco Allegretti, and Dr. Alexander Riss for helpful feedback on selected paragraphs of this review. Furthermore, I truly appreciate the reviewer's efforts and constructive remarks. Last but not least, I acknowledge the financial support provided by the European Research Council (ERC) and the Deutsche Forschungsgemeinschaft (DFG), funding my research on *h*BN via the ERC Consolidator grant NanoSurfs (no. 615233) and a Heisenberg professorship, respectively.

References

[1] A.K. Geim, K.S. Novoselov, The rise of graphene, Nat. Mater. 6 (3) (2007) 183–191, https://doi.org/10.1038/nmat1849.
[2] A. Pakdel, C.Y. Zhi, Y. Bando, D. Golberg, Low-dimensional boron nitride nanomaterials, Mater. Today 15 (6) (2012) 256–265.
[3] G. Bhimanapati, N. Glavin, J. Robinson, 2D boron nitride: synthesis and applications, Semiconduct. Semimet. 95 (2016) 101–147.
[4] T. Hu, Y. Han, J.M. Dong, Edge reconstructions of hexagonal boron nitride nanoribbons: a first-principles study, Physica E 54 (2013) 191–196, https://doi.org/10.1016/j.physe.2013.06.028.
[5] A.I. Khan, I.A. Navid, M. Noshin, S. Subrina, Thermal transport characterization of hexagonal boron nitride nanoribbons using molecular dynamics simulation, AIP Adv. 7 (10) (2017) 105110, https://doi.org/10.1063/1.4997036.
[6] X.D. Li, X.L. Cheng, Predicting the structural and electronic properties of two-dimensional single layer boron nitride sheets, Chem. Phys. Lett. 694 (2018) 102–106, https://doi.org/10.1016/j.cplett.2018.01.043.
[7] Y.N. Zhang, J.N. Yun, K.Y. Wang, X.H. Chen, Z. Yang, Z.Y. Zhang, J.F. Yan, W. Zhao, First-principle study of graphyne-like BN sheet: electronic structure and optical properties, Comput. Mater. Sci. 136 (2017) 12–19, https://doi.org/10.1016/j.commatsci.2017.04.006.
[8] K. Watanabe, T. Taniguchi, H. Kanda, Direct-bandgap properties and evidence for ultraviolet lasing of hexagonal boron nitride single crystal, Nat. Mater. 3 (6) (2004) 404–409, https://doi.org/10.1038/nmat1134.
[9] G. Cassabois, P. Valvin, B. Gil, Hexagonal boron nitride is an indirect bandgap semiconductor, Nat. Photon. 10 (4) (2016) 262, https://doi.org/10.1038/NPHOTON.2015.277.
[10] X. Blase, A. Rubio, S.G. Louie, M.L. Cohen, Quasi-particle band-structure of bulk hexagonal boron-nitride and related systems, Phys. Rev. B 51 (11) (1995) 6868–6875, https://doi.org/10.1103/PhysRevB.51.6868.
[11] M.H. Khan, S.S. Jamali, A. Lyalin, P.J. Molino, L. Jiang, H.K. Liu, T. Taketsugu, Z.G. Huang, Atomically thin hexagonal boron nitride nanofilm for Cu protection: the importance of film perfection, Adv. Mater. 29 (4) (2017) 1603937, https://doi.org/10.1002/adma.201603937.
[12] L.H. Li, T. Xing, Y. Chen, R. Jones, Boron nitride nanosheets for metal protection, Adv. Mater. Interfaces 1 (8) (2014) 1300132, https://doi.org/10.1002/admi.201300132.
[13] F. Mahvash, S. Eissa, T. Bordjiba, A.C. Tavares, T. Szkopek, M. Siaj, Corrosion resistance of monolayer hexagonal boron nitride on copper, Sci. Rep. 7 (2017) 42139, https://doi.org/10.1038/srep42139.
[14] L.H. Li, J. Cervenka, K. Watanabe, T. Taniguchi, Y. Chen, Strong oxidation resistance of atomically thin boron nitride nanosheets, ACS Nano 8 (2) (2014) 1457–1462, https://doi.org/10.1021/nn500059s.
[15] L.H. Li, Y. Chen, Atomically thin boron nitride: unique properties and applications, Adv. Funct. Mater. 26 (16) (2016) 2594–2608, https://doi.org/10.1002/adfm.201504606.
[16] A.K. Geim, I.V. Grigorieva, Van der Waals heterostructures, Nature 499 (7459) (2013) 419–425, https://doi.org/10.1038/nature12385.
[17] K.S. Novoselov, D. Jiang, F. Schedin, T.J. Booth, V.V. Khotkevich, S.V. Morozov, A.K. Geim, Two-dimensional atomic crystals, Proc. Natl. Acad. Sci. 102 (30) (2005) 10451–10453, https://doi.org/10.1073/pnas.0502848102.
[18] Y. Liu, N. Weiss, X. Duan, H.-C. Cheng, Y. Huang, X. Duan, Van der Waals heterostructures and devices, Nat. Rev. Mater. 1 (2016) 16042.
[19] S.Z. Butler, S.M. Hollen, L.Y. Cao, Y. Cui, J.A. Gupta, H.R. Gutierrez, T.F. Heinz, S.S. Hong, J.X. Huang, A.F. Ismach, E. Johnston-Halperin, M. Kuno, V.V. Plashnitsa, R.D. Robinson, R.S. Ruoff, S. Salahuddin, J. Shan, L. Shi, M.G. Spencer, M. Terrones, W. Windl, J.E. Goldberger, Progress, challenges, and opportunities in two-dimensional materials beyond graphene, ACS Nano 7 (4) (2013) 2898–2926, https://doi.org/10.1021/nn400280c.
[20] G.R. Bhimanapati, Z. Lin, V. Meunier, Y. Jung, J. Cha, S. Das, D. Xiao, Y. Son, M.S. Strano, V.R. Cooper, L.B. Liang, S.G. Louie, E. Ringe, W. Zhou, S.S. Kim, R.R. Naik, B.G. Sumpter, H. Terrones, F.N. Xia, Y.L. Wang, J. Zhu, D. Akinwande, N. Alem, J.A. Schuller, R.E. Schaak, M. Terrones, J.A. Robinson, Recent advances in two-dimensional materials beyond graphene, ACS Nano 9 (12) (2015) 11509–11539, https://doi.org/10.1021/acsnano.5b05556.
[21] M.S. Xu, T. Liang, M.M. Shi, H.Z. Chen, Graphene-like two-dimensional materials, Chem. Rev. 113 (5) (2013) 3766–3798, https://doi.org/10.1021/cr300263a.
[22] K. Kim, H. Lee, Y. Lee, Synthesis of hexagonal boron nitride heterostructures for 2D van der Waals electronics, Chem. Soc. Rev. 47 (2018) 6342–6369, https://doi.org/10.1039/c8cs00450a.
[23] Y.B. Zhang, A. Rubio, G. Le Lay, Emergent elemental two-dimensional materials beyond graphene, J. Phys. D Appl. Phys. 50 (5) (2017) 053004, https://doi.org/10.1088/1361-6463/aa4e8b.
[24] L. Britnell, R.V. Gorbachev, R. Jalil, B.D. Belle, F. Schedin, A. Mishchenko, T. Georgiou, M.I. Katsnelson, L. Eaves, S.V. Morozov, N.M.R. Peres, J. Leist, A.K. Geim, K.S. Novoselov, L.A. Ponomarenko, Field-effect tunneling transistor based on vertical graphene heterostructures, Science 335 (6071) (2012) 947–950, https://doi.org/10.1126/science.1218461.
[25] T. Roy, M. Tosun, J.S. Kang, A.B. Sachid, S.B. Desai, M. Hettick, C.M.C. Hu, A. Javey, Field-effect transistors built from all two-dimensional material components, ACS Nano 8 (6) (2014) 6259–6264, https://doi.org/10.1021/nn501723y.
[26] S.J. Kang, G.H. Lee, Y.J. Yu, Y. Zhao, B. Kim, K. Watanabe, T. Taniguchi, J. Hone, P. Kim, C. Nuckolls, Organic field effect transistors based on graphene and hexagonal boron nitride heterostructures, Adv. Funct. Mater. 24 (32) (2014) 5157–5163, https://doi.org/10.1002/adfm.201400348.
[27] T.H. Lee, K. Kim, G. Kim, H.J. Park, D. Scullion, L. Shaw, M.G. Kim, X.D. Gu, W.G. Bae, E.J.G. Santos, Z. Lee, H.S. Shin, Y. Nishi, Z. Bao, Chemical vapor-deposited hexagonal boron nitride as a scalable template for high-performance organic field-effect transistors, Chem. Mat. 29 (5) (2017) 2341–2347, https://doi.org/10.1021/acs.chemmater.6b05517.
[28] M. Sajjad, G. Morell, P. Feng, Advance in novel boron nitride nanosheets to nanoelectronic device applications, ACS Appl. Mater. Interfaces 5 (11) (2013) 5051–5056, https://doi.org/10.1021/am400871s.
[29] C. Anichini, W. Czepa, D. Pakulski, A. Aliprandi, A. Ciesielski, P. Samori, Chemical sensing with 2D materials, Chem. Soc. Rev. 47 (13) (2018) 4860–4908, https://doi.org/10.1039/c8cs00417j.
[30] G. Liu, S.L. Rumyantsev, C. Jiang, M.S. Shur, A.A. Balandin, Selective gas sensing with h-BN capped MoS_2 heterostructure thin-film transistors, IEEE Electron Device Lett 36 (11) (2015) 1202–1204, https://doi.org/10.1109/LED.2015.2481388.
[31] A. Mishchenko, Y. Cao, G.L. Yu, C.R. Woods, R.V. Gorbachev, K.S. Novoselov, A.K. Geim, L.S. Levitov, Nonlocal response and anamorphosis: the case of few-layer black phosphorus, Nano Lett. 15 (10) (2015) 6991–6995, https://doi.org/10.1021/acs.nanolett.5b03004.
[32] S. Liu, B. Lu, Q. Zhao, J. Li, T. Gao, Y.B. Chen, Y.F. Zhang, Z.F. Liu, Z.C. Fan, F.H. Yang, L.P. You, D.P. Yu, Boron nitride nanopores: highly sensitive DNA single-molecule detectors, Adv. Mater. 25 (33) (2013) 4549–4554, https://doi.org/10.1002/adma.201301336.
[33] Q. Han, B.M. Yan, T. Gao, J. Meng, Y.F. Zhang, Z.F. Liu, X.S. Wu, D.P. Yu, Boron nitride film as a buffer layer in deposition of dielectrics on graphene, Small 10 (11) (2014) 2293–2299, https://doi.org/10.1002/smll.201303697.
[34] K. Watanabe, T. Taniguchi, T. Niiyama, K. Miya, M. Taniguchi, Far-ultraviolet plane-emission handheld device based on hexagonal boron nitride, Nat. Photonics 3 (10) (2009) 591–594, https://doi.org/10.1038/NPHOTON.2009.167.
[35] H.X. Jiang, J.Y. Lin, Hexagonal boron nitride for deep ultraviolet photonic devices, Semicond. Sci. Technol. 29 (8) (2014) 084003, https://doi.org/10.1088/0268-1242/29/8/084003.
[36] T.C. Doan, S. Majety, S. Grenadier, J. Li, J.Y. Lin, H.X. Jiang, Hexagonal boron nitride thin film thermal neutron detectors with high energy resolution of the reaction products, Nucl. Instrum. Methods Phys. Res. Sect. A-Accel. Spectrom. Dect. Assoc. Equip. 783 (2015) 121–127, https://doi.org/10.1016/j.nima.2015.02.045.
[37] N. Izyumskaya, D.O. Demchenko, S. Das, U. Ozgur, V. Avrutin, H. Morkoc, Recent development of boron nitride towards electronic applications, Adv. Electron. Mater. 3 (5) (2017) 1600485, https://doi.org/10.1002/aelm.201600485.
[38] J.T. Grant, C.A. Carrero, F. Goeltl, J. Venegas, P. Mueller, S.P. Burt, S.E. Specht, W.P. McDermott, A. Chieregato, I. Hermans, Selective oxidative dehydrogenation of propane to propene using boron nitride catalysts, Science 354 (6319) (2016) 1570–1573, https://doi.org/10.1126/science.aaf7885.
[39] W.L. Sun, Y. Meng, Q.R. Fu, F. Wang, G.J. Wang, W.H. Gao, X.C. Huang, F.S. Lu, High-yield production of boron nitride nanosheets and its uses as a catalyst support for hydrogenation of nitroaromatics, ACS Appl. Mater. Interfaces 8 (15) (2016) 9881–9888, https://doi.org/10.1021/acsami.6b01008.
[40] L. Shi, D.Q. Wang, W. Song, D. Shao, W.P. Zhang, A.H. Lu, Edge-hydroxylated boron nitride for oxidative dehydrogenation of propane to propylene, ChemCatChem 9 (10) (2017) 1788–1793, https://doi.org/10.1002/cctc.201700004.
[41] C. Lee, Q.Y. Li, W. Kalb, X.Z. Liu, H. Berger, R.W. Carpick, J. Hone, Frictional characteristics of atomically thin sheets, Science 328 (5974) (2010) 76–80, https://doi.org/10.1126/science.1184167.
[42] G. Tocci, L. Joly, A. Michaelides, Friction of water on graphene and hexagonal boron nitride from ab initio methods: very different slippage despite very similar interface structures, Nano Lett. 14 (12) (2014) 6872–6877, https://doi.org/10.1021/nl502837d.
[43] S. Bernard, C. Salameh, P. Miele, Boron nitride ceramics from molecular precursors: synthesis, properties and applications, Dalton Trans 45 (3) (2016) 861–873, https://doi.org/10.1039/c5dt03633j.
[44] F. Zhang, K. Nemeth, J. Bareno, F. Dogan, I.D. Bloom, L.L. Shaw, Experimental and theoretical investigations of functionalized boron nitride as electrode materials

for Li-ion batteries, RSC Adv. 6 (33) (2016) 27901–27914, https://doi.org/10.1039/c6ra03141b.
[45] Q.H. Weng, B.J. Wang, X.B. Wang, N. Hanagata, X. Li, D.Q. Liu, X. Wang, X.F. Jiang, Y. Bando, D. Golberg, Highly water-soluble, porous, and biocompatible boron nitrides for anticancer drug delivery, ACS Nano 8 (6) (2014) 6123–6130, https://doi.org/10.1021/nn5014808.
[46] S.P.S. Arya, A. Damico, Preparation, properties and applications of boron-nitride thin-films, Thin Solid Films 157 (2) (1988) 267–282, https://doi.org/10.1016/0040-6090(88)90008-9.
[47] Y. Lin, J.W. Connell, Advances in 2D boron nitride nanostructures: nanosheets, nanoribbons, nanomeshes, and hybrids with graphene, Nanoscale 4 (22) (2012) 6908–6939, https://doi.org/10.1039/c2nr32201c.
[48] A. Pakdel, Y. Bando, D. Golberg, Nano boron nitride flatland, Chem. Soc. Rev. 43 (3) (2014) 934–959, https://doi.org/10.1039/c3cs60260e.
[49] X.B. Wang, C.Y. Zhi, Q.H. Weng, Y. Bando, D. Golberg, Boron nitride nanosheets: novel syntheses and applications in polymeric composites, J. Phys. Conf. Ser. 471 (2013) 012003, https://doi.org/10.1088/1742-6596/471/1/012003.
[50] M. Jana, R.N. Singh, A review: progress in CVD synthesis of layered hexagonal boron nitride with tunable properties and their applications, Int. Mater. Rev. 63 (3) (2018) 162–203. https://doi.org/10.1080/09506608.2017.1322833.
[51] F. Hui, C.B. Pan, Y.Y. Shi, Y.F. Ji, E. Grustan-Gutierrez, M. Lanza, On the use of two dimensional hexagonal boron nitride as dielectric, Microelectron. Eng. 163 (2016) 119–133, https://doi.org/10.1016/j.mee.2016.06.015.
[52] J.G. Wang, F.C. Ma, M.T. Sun, Graphene, hexagonal boron nitride, and their heterostructures: properties and applications, RSC Adv. 7 (27) (2017) 16801–16822, https://doi.org/10.1039/c7ra00260b.
[53] J. Yin, J.D. Li, Y. Hang, J. Yu, G.A. Tai, X.M. Li, Z.H. Zhang, W.L. Guo, Boron nitride nanostructures: fabrication, functionalization and applications, Small 12 (22) (2016) 2942–2968, https://doi.org/10.1002/smll.201600053.
[54] K.L. Zhang, Y.L. Feng, F. Wang, Z.C. Yang, J. Wang, Two dimensional hexagonal boron nitride (2D-hBN): synthesis, properties and applications, J. Mater. Chem. C 5 (46) (2017) 11992–12022, https://doi.org/10.1039/c7tc04300g.
[55] T.W. Han, Y. Luo, C.Y. Wang, Effects of temperature and strain rate on the mechanical properties of hexagonal boron nitride nanosheets, J. Phys. D-Appl. Phys. 47 (2) (2014) 025303, https://doi.org/10.1088/0022-3727/47/2/025303.
[56] F. Mahvash, E. Paradis, D. Drouin, T. Szkopek, M. Siaj, Space-charge limited transport in large-area monolayer hexagonal boron nitride, Nano Lett. 15 (4) (2015) 2263–2268, https://doi.org/10.1021/nl504197c.
[57] A. Falin, Q.R. Cai, E.J.G. Santos, D. Scullion, D. Qian, R. Zhang, Z. Yang, S.M. Huang, K. Watanabe, T. Taniguchi, M.R. Barnett, Y. Chen, R.S. Ruoff, L.H. Li, Mechanical properties of atomically thin boron nitride and the role of interlayer interactions, Nat. Commun. 8 (2017) 15815, https://doi.org/10.1038/ncomms15815.
[58] S. Thomas, K.M. Ajith, M.C. Valsakumar, Directional anisotropy, finite size effect and elastic properties of hexagonal boron nitride, J. Phys.-Condes. Matter 28 (29) (2016) 295302, https://doi.org/10.1088/0953-8984/28/29/295302.
[59] Q. Peng, W. Ji, S. De, Mechanical properties of the hexagonal boron nitride monolayer: ab initio study, Comput. Mater. Sci. 56 (2012) 11–17, https://doi.org/10.1016/j.commatsci.2011.12.029.
[60] G.J. Slotman, A. Fasolino, Structure, stability and defects of single layer hexagonal BN in comparison to graphene, J. Phys.-Condes. Matter 25 (4) (2013) 045009, https://doi.org/10.1088/0953-8984/25/4/045009.
[61] M. Seel, R. Pandey, Proton and hydrogen transport through two-dimensional monolayers, 2D Mater. 3 (2) (2016) 025004, https://doi.org/10.1088/2053-1583/3/2/025004.
[62] C.M. Orofeo, S. Suzuki, H. Kageshima, H. Hibino, Growth and low-energy electron microscopy characterization of monolayer hexagonal boron nitride on epitaxial cobalt, Nano Res. 6 (5) (2013) 335–347, https://doi.org/10.1007/s12274-013-0310-1.
[63] G. Kim, A.R. Jang, H.Y. Jeong, Z. Lee, D.J. Kang, H.S. Shin, Growth of high-crystalline, single-layer hexagonal boron nitride on recyclable platinum foil, Nano Lett. 13 (4) (2013) 1834–1839, https://doi.org/10.1021/nl400559s.
[64] A. Bhattacharya, S. Bhattacharya, G.P. Das, Band gap engineering by functionalization of BN sheet, Phys. Rev. B 85 (3) (2012) 035415, https://doi.org/10.1103/PhysRevB.85.035415.
[65] Y.P. Wang, H.P. Cheng, First-principles simulations of a graphene-based field-effect transistor, Phys. Rev. B 91 (24) (2015) 245307, https://doi.org/10.1103/PhysRevB.91.245307.
[66] R.V. Gorbachev, I. Riaz, R.R. Nair, R. Jalil, L. Britnell, B.D. Belle, E.W. Hill, K.S. Novoselov, K. Watanabe, T. Taniguchi, A.K. Geim, P. Blake, Hunting for monolayer boron nitride: optical and Raman signatures, Small 7 (4) (2011) 465–468, https://doi.org/10.1002/smll.201001628.
[67] L. Britnell, R.V. Gorbachev, R. Jalil, B.D. Belle, F. Schedin, M.I. Katsnelson, L. Eaves, S.V. Morozov, A.S. Mayorov, N.M.R. Peres, A.H.C. Neto, J. Leist, A.K. Geim, L.A. Ponomarenko, K.S. Novoselov, Electron tunneling through ultrathin boron nitride crystalline barriers, Nano Lett. 12 (3) (2012) 1707–1710, https://doi.org/10.1021/nl3002205.
[68] L. Lindsay, D.A. Broido, Enhanced thermal conductivity and isotope effect in single-layer hexagonal boron nitride, Phys. Rev. B 84 (15) (2011) 155421, https://doi.org/10.1103/PhysRevB.84.155421.
[69] O.Y. Tao, Y.P. Chen, Y.E. Xie, K.K. Yang, Z.G. Bao, J.X. Zhong, Thermal transport in hexagonal boron nitride nanoribbons, Nanotechnology 21 (24) (2010) 245701, https://doi.org/10.1088/0957-4484/21/24/245701.
[70] K.K. Kim, A. Hsu, X.T. Jia, S.M. Kim, Y.M. Shi, M. Dresselhaus, T. Palacios, J. Kong, Synthesis and characterization of hexagonal boron nitride film as a dielectric layer for graphene devices, ACS Nano 6 (10) (2012) 8583–8590, https://doi.org/10.1021/nn301675f.
[71] A.F. Young, C.R. Dean, I. Meric, S. Sorgenfrei, H. Ren, K. Watanabe, T. Taniguchi, J. Hone, K.L. Shepard, P. Kim, Electronic compressibility of layer-polarized bilayer graphene, Phys. Rev. B 85 (23) (2012) 235458, https://doi.org/10.1103/PhysRevB.85.235458.
[72] Y. Hattori, T. Taniguchi, K. Watanabe, K. Nagashio, Layer-by-layer dielectric breakdown of hexagonal boron nitride, ACS Nano 9 (1) (2015) 916–921, https://doi.org/10.1021/nn506645q.
[73] I. Jo, M.T. Pettes, J. Kim, K. Watanabe, T. Taniguchi, Z. Yao, L. Shi, Thermal conductivity and phonon transport in suspended few-layer hexagonal boron nitride, Nano Lett. 13 (2) (2013) 550–554, https://doi.org/10.1021/nl304060g.
[74] H.Q. Zhou, J.X. Zhu, Z. Liu, Z. Yan, X.J. Fan, J. Lin, G. Wang, Q.Y. Yan, T. Yu, P.M. Ajayan, J.M. Tour, High thermal conductivity of suspended few-layer hexagonal boron nitride sheets, Nano Res. 7 (8) (2014) 1232–1240, https://doi.org/10.1007/s12274-014-0486-z.
[75] M.T. Alam, M.S. Bresnehan, J.A. Robinson, M.A. Haque, Thermal conductivity of ultra-thin chemical vapor deposited hexagonal boron nitride films, Appl. Phys. Lett. 104 (1) (2014) 013113, https://doi.org/10.1063/1.4861468.
[76] T. Wittkowski, J. Jorzick, K. Jung, B. Hillebrands, Elastic properties of thin h-BN films investigated by Brillouin light scattering, Thin Solid Films 353 (1–2) (1999) 137–143, https://doi.org/10.1016/S0040-6090(99)00388-0.
[77] C. Li, Y. Bando, C.Y. Zhi, Y. Huang, D. Golberg, Thickness-dependent bending modulus of hexagonal boron nitride nanosheets, Nanotechnology 20 (38) (2009) 385707, https://doi.org/10.1088/0957-4484/20/38/385707.
[78] R.S. Pease, An x-ray study of boron nitride, Acta Cryst 5 (3) (1952) 356, https://doi.org/10.1107/S0365110X52001064.
[79] W. Paszkowicz, J.B. Pelka, M. Knapp, T. Szyszko, S. Podsiadlo, Lattice parameters and anisotropic thermal expansion of hexagonal boron nitride in the 10-297.5 K temperature range, Appl. Phys. A-Mater. Sci. Process. 75 (3) (2002) 431–435, https://doi.org/10.1007/s003390100999.
[80] A. Bosak, J. Serrano, M. Krisch, K. Watanabe, T. Taniguchi, H. Kanda, Elasticity of hexagonal boron nitride: inelastic x-ray scattering measurements, Phys. Rev. B 73 (4) (2006) 041402, https://doi.org/10.1103/PhysRevB.73.041402.
[81] E.K. Sichel, R.E. Miller, M.S. Abrahams, C.J. Buiocchi, Heat-capacity and thermal-conductivity of hexagonal pyrolytic boron-nitride, Phys. Rev. B 13 (10) (1976) 4607–4611, https://doi.org/10.1103/PhysRevB.13.4607.
[82] R. Geick, C.H. Perry, G. Rupprech, Normal modes in hexagonal boron nitride, Phys. Rev. 146 (2) (1966) 543, https://doi.org/10.1103/PhysRev.146.543.
[83] Y.N. Xu, W.Y. Ching, Calculation of ground-state and optical properties of boron nitrides in the hexagonal, cubic, and wurtzite structures, Phys. Rev. B 44 (15) (1991) 7787–7798, https://doi.org/10.1103/PhysRevB.44.7787.
[84] J.W. He, D.W. Goodman, Interaction of borazine with a Re(0001) surface, studied by LEED, TDS, AES and ELS, Surf. Sci. 232 (1–2) (1990) 138–148, https://doi.org/10.1016/0039-6028(90)90594-X.
[85] M.T. Paffett, R.J. Simonson, P. Papin, R.T. Paine, Borazine adsorption and decomposition at Pt(111) and Ru(001) surfaces, Surf. Sci. 232 (3) (1990) 286–296, https://doi.org/10.1016/0039-6028(90)90121-N.
[86] R.J. Simonson, M.T. Paffett, M.E. Jones, B.E. Koel, A vibrational study of borazine adsorbed on Pt(111) and Au(111) surfaces, Surf. Sci. 254 (1–3) (1991) 29–44, https://doi.org/10.1016/0039-6028(91)90635-6.
[87] M. Corso, W. Auwärter, M. Muntwiler, A. Tamai, T. Greber, J. Osterwalder, Boron nitride nanomesh, Science 303 (5655) (2004) 217–220, https://doi.org/10.1126/science.1091979.
[88] A.B. Preobrajenski, M.A. Nesterov, M.L. Ng, A.S. Vinogradov, N. Mårtensson, Monolayer h-BN on lattice-mismatched metal surfaces: on the formation of the nanomesh, Chem. Phys. Lett. 446 (1–3) (2007) 119–123, https://doi.org/10.1016/j.cplett.2007.08.028.
[89] T. Brugger, S. Günther, B. Wang, J.H. Dil, M.L. Bocquet, J. Osterwalder, J. Wintterlin, T. Greber, Comparison of electronic structure and template function of single-layer graphene and a hexagonal boron nitride nanomesh on Ru(0001), Phys. Rev. B 79 (4) (2009) 045407, https://doi.org/10.1103/PhysRevB.79.045407.
[90] J.M. MacLeod, F. Rosei, Molecular self-assembly on graphene, Small 10 (6) (2014) 1038–1049, https://doi.org/10.1002/smll.201301982.
[91] A. Kumar, K. Banerjee, P. Liljeroth, Molecular assembly on two-dimensional materials, Nanotechnology 28 (8) (2017), https://doi.org/10.1088/1361-6528/aa564f 082001–082001.
[92] J. Yang, K. Kim, Y. Lee, K. Kim, W. Lee, J. Park, Self-organized growth and self-assembly of nanostructures on 2D materials, FlatChem 5 (2017) 50–68.
[93] W. Chen, A.T.S. Wee, Self-assembly on silicon carbide nanomesh templates, J. Phys. D-Appl. Phys. 40 (20) (2007) 6287–6299, https://doi.org/10.1088/0022-3727/40/20/S13.
[94] H. Huang, S.L. Wong, J.T. Sun, W. Chen, A.T.S. Wee, Trapping single polar molecules in SiC nanomesh via out-of-plane dipoles, ACS Nano 6 (3) (2012) 2774–2778, https://doi.org/10.1021/nn300258b.
[95] L. Vitali, M.G. Ramsey, F.P. Netzer, Nanodot formation on the Si(111)-(7x7) surface by adatom trapping, Phys. Rev. Lett. 83 (2) (1999) 316–319, https://doi.org/10.1103/PhysRevLett.83.316.
[96] I. Ošťádal, P. Kocán, P. Sobotík, J. Pudl, Direct observation of long-range assisted formation of Ag clusters on Si(111)7x7, Phys. Rev. Lett. 95 (14) (2005) 146101, https://doi.org/10.1103/PhysRevLett.95.146101.
[97] M.A.K. Zilani, Y.Y. Sun, H. Xu, L. Liu, Y.P. Feng, X.S. Wang, A.T.S. Wee, Reactive Co magic cluster formation on Si(111)-(7x7), Phys. Rev. B 72 (19) (2005) 193402, https://doi.org/10.1103/PhysRevB.72.193402.

[98] D.D. Chambliss, R.J. Wilson, S. Chiang, Nucleation of ordered Ni island arrays on Au(111) by surface-lattice dislocations, Phys. Rev. Lett. 66 (13) (1991) 1721–1724, https://doi.org/10.1103/PhysRevLett.66.1721.

[99] M. Böhringer, K. Morgenstern, W.D. Schneider, R. Berndt, F. Mauri, A. De Vita, R. Car, Two-dimensional self-assembly of supramolecular clusters and chains, Phys. Rev. Lett. 83 (2) (1999) 324–327, https://doi.org/10.1103/PhysRevLett.83.324.

[100] I. Fernandez-Torrente, S. Monturet, K.J. Franke, J. Fraxedas, N. Lorente, J.I. Pascual, Long-range repulsive interaction between molecules on a metal surface induced by charge transfer, Phys. Rev. Lett. 99 (17) (2007) 176103, https://doi.org/10.1103/PhysRevLett.99.176103.

[101] L. Gao, Q. Liu, Y.Y. Zhang, N. Jiang, H.G. Zhang, Z.H. Cheng, W.F. Qiu, S.X. Du, Y.Q. Liu, W.A. Hofer, H.J. Gao, Constructing an array of anchored single-molecule rotors on gold surfaces, Phys. Rev. Lett. 101 (19) (2008) 197209, https://doi.org/10.1103/PhysRevLett.101.197209.

[102] M. Corso, L. Fernandez, F. Schiller, J.E. Ortega, Au(111)-based nanotemplates by Gd alloying, ACS Nano 4 (3) (2010) 1603–1611, https://doi.org/10.1021/nn901345s.

[103] L. Fernandez, M. Blanco-Rey, M. Ilyn, L. Vitali, A. Magana, A. Correa, P. Ohresser, J.E. Ortega, A. Ayuela, F. Schiller, Co nanodot arrays grown on a $GdAu_2$ template: substrate/nanodot antiferromagnetic coupling, Nano Lett. 14 (6) (2014) 2977–2981, https://doi.org/10.1021/nl403471z.

[104] A. Wäckerlin, S. Fatayer, T. Nijs, S. Nowakowska, S.F. Mousavi, O. Popova, A. Ahsan, T.A. Jung, C. Wäckerlin, Molecular chessboard assemblies sorted by site-specific interactions of out-of-plane d-orbitals with a semimetal template, Nano Lett. 17 (3) (2017) 1956–1962, https://doi.org/10.1021/acs.nanolett.6b05344.

[105] V. Repain, G. Baudot, H. Ellmer, S. Rousset, Two-dimensional long-range-ordered growth of uniform cobalt nanostructures on a Au(111) vicinal template, Europhys. Lett. 58 (5) (2002) 730–736, https://doi.org/10.1209/epl/i2002-00410-4.

[106] J. Kröger, N. Néel, H. Jensen, R. Berndt, R. Rurali, N. Lorente, Molecules on vicinal Au surfaces studied by scanning tunnelling microscopy, J. Phys.-Condes. Matter 18 (13) (2006) S51–S66, https://doi.org/10.1088/0953-8984/18/13/S04.

[107] B. Cirera, Y.Q. Zhang, J. Björk, S. Klyatskaya, Z. Chen, M. Ruben, J.V. Barth, F. Klappenberger, Synthesis of extended graphdiyne wires by vicinal surface templating, Nano Lett. 14 (4) (2014) 1891–1897, https://doi.org/10.1021/nl4046747.

[108] H. Brune, M. Giovannini, K. Bromann, K. Kern, Self-organized growth of nanostructure arrays on strain-relief patterns, Nature 394 (6692) (1998) 451–453.

[109] P. Ruffieux, K. Ait-Mansour, A. Bendounan, R. Fasel, L. Patthey, P. Gröning, O. Gröning, Mapping the electronic surface potential of nanostructured surfaces, Phys. Rev. Lett. 102 (8) (2009) 086807, https://doi.org/10.1103/PhysRevLett.102.086807.

[110] K. Ait-Mansour, P. Ruffieux, P. Gröning, R. Fasel, O. Gröning, Positional and orientational templating of C_{60} molecules on the Ag/Pt(111) strain-relief pattern, J. Phys. Chem. C 113 (13) (2009) 5292–5299, https://doi.org/10.1021/jp8101749.

[111] T.G. Gopakumar, N. Néel, J. Kröger, R. Berndt, Spatial modulation of d states in a nanoscale Co island, Chem. Phys. Lett. 484 (1–3) (2009) 59–63, https://doi.org/10.1016/j.cplett.2009.11.012.

[112] C. Becker, K. Wandelt, Surfaces: two-dimensional templates, in: P. Broekmann, K.H. Dötz, C.A. Schalley (Eds.), Templates in Chemistry III, Top. Curr. Chem., vol. 287, 2009https://doi.org/10.1007/128-2008-151.

[113] Z.C. Dong, X.L. Guo, A.S. Trifonov, P.S. Dorozhkin, K. Miki, K. Kimura, S. Yokoyama, S. Mashiko, Vibrationally resolved fluorescence from organic molecules near metal surfaces in a scanning tunneling microscope, Phys. Rev. Lett. 92 (8) (2004) 086801, https://doi.org/10.1103/PhysRevLett.92.086801.

[114] K.J. Franke, G. Schulze, N. Henningsen, I. Fernandez-Torrente, J.I. Pascual, S. Zarwell, K. Ruck-Braun, M. Cobian, N. Lorente, Reducing the molecule-substrate coupling in C_{60}-based nanostructures by molecular interactions, Phys. Rev. Lett. 100 (3) (2008) 036807, https://doi.org/10.1103/PhysRevLett.100.036807.

[115] R. Decker, U. Schlickum, F. Klappenberger, G. Zoppellaro, S. Klyatskaya, M. Ruben, J.V. Barth, H. Brune, Using metal-organic templates to steer the growth of Fe and Co nanoclusters, Appl. Phys. Lett. 93 (24) (2008) 243102, https://doi.org/10.1063/1.3040328.

[116] Z.C. Dong, X.L. Zhang, H.Y. Gao, Y. Luo, C. Zhang, L.G. Chen, R. Zhang, X. Tao, Y. Zhang, J.L. Yang, J.G. Hou, Generation of molecular hot electroluminescence by resonant nanocavity plasmons, Nat. Photonics 4 (1) (2010) 50–54, https://doi.org/10.1038/NPHOTON.2009.257.

[117] S. Vijayaraghavan, W. Auwärter, D. Ecija, K. Seufert, S. Rusponi, T. Houwaart, P. Sautet, M.L. Bocquet, P. Thakur, S. Stepanow, U. Schlickum, M. Etzkorn, H. Brune, J.V. Barth, Restoring the Co magnetic moments at interfacial Co-porphyrin arrays by site-selective uptake of iron, ACS Nano 9 (4) (2015) 3605–3616, https://doi.org/10.1021/nn507346x.

[118] L.A. Rochford, T.S. Jones, C.B. Nielsen, Epitaxial templating of C_{60} with a molecular monolayer, J. Phys. Chem. Lett. 7 (17) (2016) 3487–3490, https://doi.org/10.1021/acs.jpclett.6b01656.

[119] J.A. Theobald, N.S. Oxtoby, M.A. Phillips, N.R. Champness, P.H. Beton, Controlling molecular deposition and layer structure with supramolecular surface assemblies, Nature 424 (6952) (2003) 1029–1031, https://doi.org/10.1038/nature01915.

[120] Z.H. Cheng, M.M. Luo, J. Wyrick, D.Z. Sun, D.H. Kim, Y.M. Zhu, W.H. Lu, K. Kim, T.L. Einstein, L. Bartels, Power of confinement: adsorbate dynamics on nanometer-scale exposed facets, Nano Lett. 10 (9) (2010) 3700–3703, https://doi.org/10.1021/nl1022018.

[121] Y. Pennec, W. Auwärter, A. Schiffrin, A. Weber-Bargioni, A. Riemann, J.V. Barth, Supramolecular gratings for tuneable confinement of electrons on metal surfaces, Nat. Nanotechnol. 2 (2) (2007) 99–103, https://doi.org/10.1038/nnano.2006.212.

[122] D. Kühne, F. Klappenberger, W. Krenner, S. Klyatskaya, M. Ruben, J.V. Barth, Rotational and constitutional dynamics of caged supramolecules, Proc. Natl. Acad. Sci. 107 (50) (2010) 21332–21336, https://doi.org/10.1073/pnas.1008991107.

[123] M. Pivetta, G.E. Pacchioni, U. Schlickum, J.V. Barth, H. Brune, Formation of Fe cluster superlattice in a metal-organic quantum-box network, Phys. Rev. Lett. 110 (8) (2013) 086102, https://doi.org/10.1103/PhysRevLett.110.086102.

[124] A. Schiffrin, J. Reichert, W. Auwärter, G. Jahnz, Y. Pennec, A. Weber-Bargioni, V.S. Stepanyuk, L. Niebergall, P. Bruno, J.V. Barth, Self-aligning atomic strings in surface-supported biomolecular gratings, Phys. Rev. B 78 (3) (2008) 035424, https://doi.org/10.1103/PhysRevB.78.035424.

[125] J.A. Lloyd, A.C. Papageorgiou, S. Fischer, S.C. Oh, Ö. Salam, K. Diller, D.A. Duncan, F. Allegretti, F. Klappenberger, M. Stöhr, R.J. Maurer, K. Reuter, J. Reichert, J.V. Barth, Dynamics of spatially confined bisphenol a trimers in a unimolecular network on Ag(111), Nano Lett. 16 (3) (2016) 1884–1889, https://doi.org/10.1021/acs.nanolett.5b05026.

[126] L. Bartels, Tailoring molecular layers at metal surfaces, Nat. Chem. 2 (2) (2010) 87–95, https://doi.org/10.1038/NCHEM.517.

[127] K. Müller, M. Enache, M. Stöhr, Confinement properties of 2D porous molecular networks on metal surfaces, J. Phys.-Condes. Matter 28 (15) (2016) 153003, https://doi.org/10.1088/0953-8984/28/15/153003.

[128] J.I. Urgel, S. Vijayaraghavan, D. Ecija, W. Auwärter, J.V. Barth, Tetracene confinement in L-methionine gratings on the Ag(111) surface, Surf. Sci. 643 (2016) 87–90, https://doi.org/10.1016/j.susc.2015.08.015.

[129] S. Nowakowska, A. Wäckerlin, S. Kawai, T. Ivas, J. Nowakowski, S. Fatayer, C. Wäckerlin, T. Nijs, E. Meyer, J. Björk, M. Stöhr, L.H. Gade, T.A. Jung, Interplay of weak interactions in the atom-by-atom condensation of xenon within quantum boxes, Nat. Commun. 6 (2015) 6071, https://doi.org/10.1038/ncomms7071.

[130] E.N. Yitamben, L. Niebergall, R.B. Rankin, E.V. Iski, R.A. Rosenberg, J.P. Greeley, V.S. Stepanyuk, N.P. Guisinger, Tracking amino acids in chiral quantum corrals, J. Phys. Chem. C 117 (22) (2013) 11757–11763, https://doi.org/10.1021/jp400074r.

[131] S. Nowakowska, F. Mazzola, M.N. Alberti, F. Song, T. Voigt, J. Nowakowski, A. Wäckerlin, C. Wäckerlin, J. Wiss, W.B. Schweizer, M. Broszio, C. Polley, M. Leandersson, S. Fatayer, T. Ivas, M. Baljozovic, S.F. Mousavi, A. Ahsan, T. Nijs, O. Popova, J. Zhang, M. Muntwiler, C. Thilgen, M. Stöhr, I.A. Pasti, N.V. Skorodumova, F. Diederich, J. Wells, T.A. Jung, Adsorbate-induced modification of the confining barriers in a quantum box array, ACS Nano 12 (1) (2018) 768–778, https://doi.org/10.1021/acsnano.7b07989.

[132] X.H. Qiu, G.V. Nazin, W. Ho, Vibrationally resolved fluorescence excited with submolecular precision, Science 299 (5606) (2003) 542–546, https://doi.org/10.1126/science.1078675.

[133] N. Nilius, E.D.L. Rienks, H.P. Rust, H.J. Freund, Self-organization of gold atoms on a polar FeO(111) surface, Phys. Rev. Lett. 95 (6) (2005) 066101, https://doi.org/10.1103/PhysRevLett.95.066101.

[134] C. Becker, K. von Bergmann, A. Rosenhahn, J. Schneider, K. Wandelt, Preferential cluster nucleation on long-range superstructures on $Al_2O_3/Ni_3Al(111)$, Surf. Sci. 486 (1–2) (2001) L443–L448, https://doi.org/10.1016/S0039-6028(01)01052-4.

[135] M. Marsault, G. Sitja, C.R. Henry, Regular arrays of Pd and PdAu clusters on ultrathin alumina films for reactivity studies, Phys. Chem. Chem. Phys. 16 (48) (2014) 26458–26466, https://doi.org/10.1039/c4cp02200a.

[136] L. Gavioli, E. Cavaliere, S. Agnoli, G. Barcaro, A. Fortunelli, G. Granozzi, Template-assisted assembly of transition metal nanoparticles on oxide ultrathin films, Prog. Surf. Sci. 86 (3–4) (2011) 59–81, https://doi.org/10.1016/j.progsurf.2011.02.001.

[137] Y. Pan, N. Nilius, W.D. Schneider, H.J. Freund, Adsorption of thioether molecules on an alumina thin film, Surf. Sci. 628 (2014) 111–115, https://doi.org/10.1016/j.susc.2014.05.021.

[138] M. Glaser, H. Peisert, H. Adler, U. Aygul, M. Ivanovic, P. Nagel, M. Merz, S. Schuppler, T. Chassé, Electronic structure at transition metal phthalocyanine-transition metal oxide interfaces: cobalt phthalocyanine on epitaxial MnO films, J. Chem. Phys. 142 (10) (2015) 101918, https://doi.org/10.1063/1.4907899.

[139] S. Degen, C. Becker, K. Wandelt, Thin alumina films on $Ni_3Al(111)$: a template for nanostructured Pd cluster growth, Faraday Discuss 125 (2004) 343–356, https://doi.org/10.1039/b303244b.

[140] N. Ogawa, G. Mikaelian, W. Ho, Spatial variations in submolecular vibronic spectroscopy on a thin insulating film, Phys. Rev. Lett. 98 (16) (2007) 166103, https://doi.org/10.1103/PhysRevLett.98.166103.

[141] C. Becker, A. Rosenhahn, A. Wiltner, K. von Bergmann, J. Schneider, P. Pervan, M. Milun, M. Kralj, K. Wandelt, Al_2O_3-films on $Ni_3Al(111)$: a template for nanostructured cluster growth, New J. Phys. 4 (2002) 75, https://doi.org/10.1088/1367-2630/4/1/375.

[142] Y. Cui, C. Stiehler, N. Nilius, H.J. Freund, Probing the electronic properties and charge state of gold nanoparticles on ultrathin MgO versus thick doped CaO films, Phys. Rev. B 92 (7) (2015) 075444, https://doi.org/10.1103/PhysRevB.92.075444.

[143] X. Lin, N. Nilius, Self-assembly of MgPc molecules on polar FeO thin films, J. Phys. Chem. C 112 (39) (2008) 15325–15328, https://doi.org/10.1021/jp8053026.

[144] M. Hollerer, D. Lüftner, P. Hurdax, T. Ules, S. Soubatch, F.S. Tautz, G. Koller, P. Puschnig, M. Sterrer, M.G. Ramsey, Charge transfer and orbital level alignment at inorganic/organic interfaces: the role of dielectric interlayers, ACS Nano 11 (6) (2017) 6252–6260, https://doi.org/10.1021/acsnano.7b02449.

[145] F. Donati, S. Rusponi, S. Stepanow, C. Wäckerlin, A. Singha, L. Persichetti, R. Baltic, K. Diller, F. Patthey, E. Fernandes, J. Dreiser, Z. Sljivancanin, K. Kummer, C. Nistor, P. Gambardella, H. Brune, Magnetic remanence in single atoms, Science 352 (6283) (2016) 318–321, https://doi.org/10.1126/science.aad9898.

[146] C.F. Hirjibehedin, C.Y. Lin, A.F. Otte, M. Ternes, C.P. Lutz, B.A. Jones, A.J. Heinrich, Large magnetic anisotropy of a single atomic spin embedded in a surface molecular network, Science 317 (5842) (2007) 1199–1203, https://doi.org/10.1126/science.1146110.

[147] T. Choi, C.D. Ruggiero, J.A. Gupta, Tunneling spectroscopy of ultrathin insulating Cu_2N films, and single Co adatoms, J. Vac. Sci. Technol. B 27 (2) (2009) 887–890, https://doi.org/10.1116/1.3010720.

[148] V.C. Zoldan, R. Faccio, C.L. Gao, A.A. Pasa, Coupling of cobalt-tetraphenylporphyrin molecules to a copper nitride layer, J. Phys. Chem. C 117 (31) (2013) 15984–15990, https://doi.org/10.1021/jp4013625.

[149] A.F. Otte, M. Ternes, K. von Bergmann, S. Loth, H. Brune, C.P. Lutz, C.F. Hirjibehedin, A.J. Heinrich, The role of magnetic anisotropy in the Kondo effect, Nat. Phys. 4 (11) (2008) 847–850, https://doi.org/10.1038/nphys1072.

[150] J. Repp, G. Meyer, S.M. Stojkovic, A. Gourdon, C. Joachim, Molecules on insulating films: scanning-tunneling microscopy imaging of individual molecular orbitals, Phys. Rev. Lett. 94 (2) (2005) 026803, https://doi.org/10.1103/PhysRevLett.94.026803.

[151] C.J. Villagomez, T. Zambelli, S. Gauthier, A. Gourdon, S. Stojkovic, C. Joachim, STM images of a large organic molecule adsorbed on a bare metal substrate or on a thin insulating layer: visualization of HOMO and LUMO, Surf. Sci. 603 (10–12) (2009) 1526–1532, https://doi.org/10.1016/j.susc.2008.10.057.

[152] C.J. Villagomez, T. Zambelli, S. Gauthier, A. Gourdon, C. Barthes, S. Stojkovic, C. Joachim, A local view on hyperconjugation, Chem. Phys. Lett. 450 (1–3) (2007) 107–111, https://doi.org/10.1016/j.cplett.2007.11.005.

[153] J. Repp, G. Meyer, Scanning tunneling spectroscopy of molecules on insulating films, Chimia 64 (6) (2010) 370–375, https://doi.org/10.2533/chimia.2010.370.

[154] M. Abel, S. Clair, O. Ourdjini, M. Mossoyan, L. Porte, Single layer of polymeric Fe-phthalocyanine: an organometallic sheet on metal and thin insulating film, J. Am. Chem. Soc. 133 (5) (2011) 1203–1205, https://doi.org/10.1021/ja108628r.

[155] P. Liljeroth, J. Repp, G. Meyer, Current-induced hydrogen tautomerization and conductance switching of naphthalocyanine molecules, Science 317 (5842) (2007) 1203–1206, https://doi.org/10.1126/science.1144366.

[156] X.Z. Meng, J. Guo, J.B. Peng, J. Chen, Z.C. Wang, J.R. Shi, X.Z. Li, E.G. Wang, Y. Jiang, Direct visualization of concerted proton tunnelling in a water nanocluster, Nat. Phys. 11 (3) (2015) 235–239, https://doi.org/10.1038/NPHYS3225.

[157] J. Guo, J.T. Lu, Y.X. Feng, J. Chen, J.B. Peng, Z.R. Lin, X.Z. Meng, Z.C. Wang, X.Z. Li, E.G. Wang, Y. Jiang, Nuclear quantum effects of hydrogen bonds probed by tip-enhanced inelastic electron tunneling, Science 352 (6283) (2016) 321–325, https://doi.org/10.1126/science.aaf2042.

[158] F. Mohn, L. Gross, N. Moll, G. Meyer, Imaging the charge distribution within a single molecule, Nat. Nanotechnol. 7 (4) (2012) 227–231, https://doi.org/10.1038/NNANO.2012.20.

[159] X.W. Tu, G. Mikaelian, W. Ho, Controlling single-molecule negative differential resistance in a double-barrier tunnel junction, Phys. Rev. Lett. 100 (12) (2008) 126807, https://doi.org/10.1103/PhysRevLett.100.126807.

[160] G. Meyer, L. Gross, F. Mahn, J. Repp, Scanning probe microscopy of atoms and molecules on insulating films: from imaging to molecular manipulation, Chimia 66 (1–2) (2012) 10–15, https://doi.org/10.2533/chimia.2012.10.

[161] B. Doppagne, M.C. Chong, E. Lorchat, S. Berciaud, M. Romeo, H. Bulou, A. Boeglin, F. Scheurer, G. Schull, Vibronic spectroscopy with submolecular resolution from STM-induced electroluminescence, Phys. Rev. Lett. 118 (12) (2017) 127401, https://doi.org/10.1103/PhysRevLett.118.127401.

[162] S. Schintke, S. Messerli, M. Pivetta, F. Patthey, L. Libioulle, M. Stengel, A. De Vita, W.D. Schneider, Insulator at the ultrathin limit: MgO on Ag(001), Phys. Rev. Lett. 87 (27) (2001) 276801, https://doi.org/10.1103/PhysRevLett.87.276801.

[163] S. Schintke, W.D. Schneider, Insulators at the ultrathin limit: electronic structure studied by scanning tunnelling microscopy and scanning tunnelling spectroscopy, J. Phys.-Condes. Matter 16 (4) (2004) R49–R81, https://doi.org/10.1088/0953-8984/16/4/R02.

[164] S. Baumann, I.G. Rau, S. Loth, C.P. Lutz, A.J. Heinrich, Measuring the three-dimensional structure of ultrathin insulating films at the atomic scale, ACS Nano 8 (2) (2014) 1739–1744, https://doi.org/10.1021/nn4061034.

[165] N. Nilius, Exploring routes to tailor the physical and chemical properties of oxides via doping: an STM study, J. Phys.-Condes. Matter 27 (30) (2015) 303001, https://doi.org/10.1088/0953-8984/27/30/303001.

[166] J. Repp, G. Meyer, F.E. Olsson, M. Persson, Controlling the charge state of individual gold adatoms, Science 305 (5683) (2004) 493–495, https://doi.org/10.1126/science.1099557.

[167] L. Ramoino, M. von Arx, S. Schintke, A. Baratoff, H.J. Güntherodt, T.A. Jung, Layer-selective epitaxial self-assembly of porphyrins on ultrathin insulators, Chem. Phys. Lett. 417 (1–3) (2006) 22–27, https://doi.org/10.1016/j.cplett.2005.10.006.

[168] J. Repp, W. Steurer, I. Scivetti, M. Persson, L. Gross, G. Meyer, Charge-state-dependent diffusion of individual gold adatoms on ionic thin NaCl films, Phys. Rev. Lett. 117 (14) (2016) 146102, https://doi.org/10.1103/PhysRevLett.117.146102.

[169] R. Hoffmann-Vogel, Imaging prototypical aromatic molecules on insulating surfaces: a review, Rep. Prog. Phys. 81 (1) (2018) 016501, https://doi.org/10.1088/1361-6633/aa8fda.

[170] M. Kittelmann, P. Rahe, M. Nimmrich, C.M. Hauke, A. Gourdon, A. Kühnle, On-surface covalent linking of organic building blocks on a bulk insulator, ACS Nano 5 (10) (2011) 8420–8425, https://doi.org/10.1021/nn2033192.

[171] J.L. Neff, P. Milde, C.P. Leon, M.D. Kundrat, L.M. Eng, C.R. Jacob, R. Hoffmann-Vogel, Epitaxial growth of pentacene on alkali halide surfaces studied by Kelvin probe force microscopy, ACS Nano 8 (4) (2014) 3294–3301, https://doi.org/10.1021/nn404257v.

[172] A. Hoshino, Y. Takenaka, H. Miyaji, Redetermination of the crystal structure of alpha-copper phthalocyanine grown on KCl, Acta Crystallogr. Sect. B-Struct. Sci. 59 (2003) 393–403, https://doi.org/10.1107/S010876810300942X.

[173] M. Kittelmann, M. Nimmrich, R. Lindner, A. Gourdon, A. Kühnle, Sequential and site-specific on-surface synthesis on a bulk insulator, ACS Nano 7 (6) (2013) 5614–5620, https://doi.org/10.1021/nn402018w.

[174] C.Y. Guo, Y. Wang, M. Kittelmann, L. Kantorovitch, A. Kühnle, A. Floris, Mechanisms of covalent dimerization on a bulk insulating surface, J. Phys. Chem. C 121 (18) (2017) 10053–10062, https://doi.org/10.1021/acs.jpcc.7b02687.

[175] V. Langlais, O. Guillermet, D. Martrou, A. Gourdon, S. Gauthier, nc-AFM imaging and manipulation of a triphenylene derivative on KBr(001), J. Phys. Chem. C 120 (32) (2016) 18151–18157, https://doi.org/10.1021/acs.jpcc.6b06113.

[176] L. Schuller, V. Haapasilta, S. Kuhn, H. Pinto, R. Bechstein, A.S. Foster, A. Kühnle, Deposition order controls the first stages of a metal-organic coordination network on an insulator surface, J. Phys. Chem. C 120 (27) (2016) 14730–14735, https://doi.org/10.1021/acs.jpcc.6b04672.

[177] V.V. Korolkov, S.A. Svatek, A. Summerfield, J. Kerfoott, L.X. Yang, T. Taniguchi, K. Watanabe, N.R. Champness, N.A. Besley, P.H. Beton, van der Waals-induced chromatic shifts in hydrogen-bonded two-dimensional porphyrin arrays on boron nitride, ACS Nano 9 (10) (2015) 10347–10355, https://doi.org/10.1021/acsnano.5b04443.

[178] V.V. Korolkov, M. Baldoni, K. Watanabe, T. Taniguchi, E. Besley, P.H. Beton, Supramolecular heterostructures formed by sequential epitaxial deposition of two-dimensional hydrogen-bonded arrays, Nat. Chem. 9 (12) (2017) 1191–1197, https://doi.org/10.1038/NCHEM.2824.

[179] W. Steurer, S. Fatayer, L. Gross, G. Meyer, Probe-based measurement of lateral single-electron transfer between individual molecules, Nat. Commun. 6 (2015) 8353, https://doi.org/10.1038/ncomms9353.

[180] S. Fatayer, B. Schuler, W. Steurer, I. Scivetti, J. Repp, L. Gross, M. Persson, M. G, Reorganization energy upon charging a single molecule on an insulator measured by atomic force microscopy, Nat. Nanotechnol. 13 (2018) 376–380, https://doi.org/10.1038/s41565-018-0087-1.

[181] F. Para, F. Bocquet, L. Nony, C. Loppacher, M. Féron, F. Cherioux, D.Z. Gao, F.F. Canova, M.B. Watkins, Micrometre-long covalent organic fibres by photoinitiated chain-growth radical polymerization on an alkali-halide surface, Nat. Chem. 10 (11) (2018) 1112–1117. https://doi.org/10.1038/s41557-018-0120-x.

[182] H. Sachdev, F. Müller, S. Hüfner, BN analogues of graphene: on the formation mechanism of boronitrene layers - solids with extreme structural anisotropy, Diam. Relat. Mat. 19 (7–9) (2010) 1027–1033, https://doi.org/10.1016/j.diamond.2010.03.021.

[183] K. Hermann, Periodic overlayers and moire patterns: theoretical studies of geometric properties, J. Phys.-Condes. Matter 24 (31) (2012) 314210, https://doi.org/10.1088/0953-8984/24/31/314210.

[184] P. Zeller, S. Günther, What are the possible moire patterns of graphene on hexagonally packed surfaces? Universal solution for hexagonal coincidence lattices, derived by a geometric construction, New J. Phys. 16 (2014) 083028, https://doi.org/10.1088/1367-2630/16/8/083028.

[185] A. Artaud, L. Magaud, T. Le Quang, V. Guisset, P. David, C. Chapelier, J. Coraux, Universal classification of twisted, strained and sheared graphene moire superlattices, Sci. Rep. 6 (2016) 25670, https://doi.org/10.1038/srep25670.

[186] S. Günther, P. Zeller, Moiré patterns of graphene on metals, Encyclopedia of Interfacial Chemistry (2018) 295–307, https://doi.org/10.1016/B978-0-12-409547-2.13116-6.

[187] R. Laskowski, P. Blaha, K. Schwarz, Bonding of hexagonal BN to transition metal surfaces: an ab initio density-functional theory study, Phys. Rev. B 78 (4) (2008) 045409, https://doi.org/10.1103/PhysRevB.78.045409.

[188] M. Bokdam, G. Brocks, M.I. Katsnelson, P.J. Kelly, Schottky barriers at hexagonal boron nitride/metal interfaces: a first-principles study, Phys. Rev. B 90 (8) (2014) 085415, https://doi.org/10.1103/PhysRevB.90.085415.

[189] F. Späth, J. Gebhardt, F. Dull, U. Bauer, P. Bachmann, C. Gleichweit, A. Görling, H.P. Steinrück, C. Papp, Hydrogenation and hydrogen intercalation of hexagonal boron nitride on Ni(111): reactivity and electronic structure, 2D Mater. 4 (3) (2017) 035026, https://doi.org/10.1088/2053-1583/aa7d6b.

[190] M. Will, N. Atodiresei, V. Caciuc, P. Valerius, C. Herbig, T. Michely, A monolayer of hexagonal boron nitride on Ir(111) as a template for cluster superlattices, ACS Nano 12 (7) (2018) 6871–6880.

[191] F. Müller, S. Hüfner, H. Sachdev, One-dimensional structure of boron nitride on chromium (110) - a study of the growth of boron nitride by chemical vapour deposition of borazine, Surf. Sci. 602 (22) (2008) 3467–3476, https://doi.org/10.1016/j.susc.2008.06.037.

[192] A.B. Preobrajenski, A.S. Vinogradov, M.L. Ng, E. Cavar, R. Westerström, A. Mikkelsen, E. Lundgren, N. Mårtensson, Influence of chemical interaction at the lattice-mismatched h-BN/Rh(111) and h-BN/Pt(111) interfaces on the overlayer

morphology, Phys. Rev. B 75 (24) (2007) 245412, https://doi.org/10.1103/PhysRevB.75.245412.
[193] H. Hibino, S. Wang, C.M. Orofeo, H. Kageshima, Growth and low-energy electron microscopy characterizations of graphene and hexagonal boron nitride, Prog. Cryst. Growth Charact. Mater. 62 (2) (2016) 155–176, https://doi.org/10.1016/j.perysgrow.2016.04.008.
[194] H. Wang, Y. Zhao, Y. Xie, X. Ma, X. Zhang, Recent progress in synthesis of two-dimensional hexagonal boron nitride, J. Semicond. 38 (2017) 031003.
[195] M.H. Khan, H.K. Liu, X.D. Sun, Y. Yamauchi, Y. Bando, D. Golberg, Z. Huang, Few-atomic-layered hexagonal boron nitride: CVD growth, characterization, and applications, Mater. Today 20 (10) (2017) 611–628, https://doi.org/10.1016/j.mattod.2017.04.027.
[196] J.H. Warner, M.H. Rummeli, A. Bachmatiuk, B. Buchner, Atomic resolution imaging and topography of boron nitride sheets produced by chemical exfoliation, ACS Nano 4 (3) (2010) 1299–1304, https://doi.org/10.1021/nn901648q.
[197] L.H. Li, Y. Chen, G. Behan, H.Z. Zhang, M. Petravic, A.M. Glushenkov, Large-scale mechanical peeling of boron nitride nanosheets by low-energy ball milling, J. Mater. Chem. 21 (32) (2011) 11862–11866, https://doi.org/10.1039/c1jm11192b.
[198] Z.F. Wang, Z.J. Tang, Q. Xue, Y. Huang, Y. Huang, M.S. Zhu, Z.X. Pei, H.F. Li, H.B. Jiang, C.X. Fu, C.Y. Zhi, Fabrication of boron nitride nanosheets by exfoliation, Chem. Rec. 16 (3) (2016) 1204–1215, https://doi.org/10.1002/tcr.201500302.
[199] S. Nakhaie, J.M. Wofford, T. Schumann, U. Jahn, M. Ramsteiner, M. Hanke, J.M.J. Lopes, H. Riechert, Synthesis of atomically thin hexagonal boron nitride films on nickel foils by molecular beam epitaxy, Appl. Phys. Lett. 106 (21) (2015) 213108, https://doi.org/10.1063/1.4921921.
[200] A.A. Tonkikh, E.N. Voloshina, P. Werner, H. Blumtritt, B. Senkovskiy, G. Güntherodt, S.S.P. Parkin, Y.S. Dedkov, Structural and electronic properties of epitaxial multilayer h-BN on Ni(111) for spintronics applications, Sci. Rep. 6 (2016) 23547, https://doi.org/10.1038/srep23547.
[201] Y.J. Cho, A. Summerfield, A. Davies, T.S. Cheng, E.F. Smith, C.J. Mellor, A.N. Khlobystov, C.T. Foxon, L. Eaves, P.H. Beton, S.V. Novikov, Hexagonal boron nitride tunnel barriers grown on graphite by high temperature molecular beam epitaxy, Sci. Rep. 6 (2016) 34474, https://doi.org/10.1038/srep34474.
[202] Y.J. Cho, A. Summerfield, A. Davies, T.S. Cheng, E.F. Smith, C.J. Mellor, A.N. Khlobystov, C.T. Foxon, L. Eaves, P.H. Beton, S.V. Novikov, Hexagonal boron nitride tunnel barriers grown on graphite by high temperature molecular beam epitaxy, Sci. Rep. 7 (2017) 46799, https://doi.org/10.1038/srep46799.
[203] T.Q.P. Vuong, G. Cassabois, P. Valvin, E. Rousseau, A. Summerfield, C.J. Mellor, Y. Cho, T.S. Cheng, J.D. Albar, L. Eaves, C.T. Foxon, P.H. Beton, S.V. Novikov, B. Gil, Deep ultraviolet emission in hexagonal boron nitride grown by high-temperature molecular beam epitaxy, 2D Mater. 4 (2) (2017) 021023, https://doi.org/10.1088/2053-1583/aa604a.
[204] J.M. Wofford, S. Nakhaie, T. Krause, X.J. Liu, M. Ramsteiner, M. Hanke, H. Riechert, J.M.J. Lopes, A hybrid MBE-based growth method for large-area synthesis of stacked hexagonal boron nitride/graphene heterostructures, Sci. Rep. 7 (2017) 43644, https://doi.org/10.1038/srep43644.
[205] D. Pierucci, J. Zribi, H. Henck, J. Chaste, M.G. Silly, F. Bertran, P. Le Fevre, B. Gil, A. Summerfield, P.H. Beton, S.V. Novikov, G. Cassabois, J.E. Rault, A. Ouerghi, Van der Waals epitaxy of two-dimensional single-layer h-BN on graphite by molecular beam epitaxy: electronic properties and band structure, Appl. Phys. Lett. 112 (25) (2018) 253102, https://doi.org/10.1063/1.5029220.
[206] T.S. Cheng, A. Summerfield, C.J. Mellor, A. Davies, A.N. Khlobystov, L. Eaves, C.T. Foxon, P.H. Beton, S.V. Novikov, High-temperature molecular beam epitaxy of hexagonal boron nitride layers, J. Vac. Sci. Technol. B 36 (2) (2018), https://doi.org/10.1116/1.5011280 02D103.
[207] A. Khanaki, H. Tian, Z.G. Xu, R.J. Zheng, Y.W. He, Z.J. Cui, J.C. Yang, J.L. Liu, Effect of high carbon incorporation in Co substrates on the epitaxy of hexagonal boron nitride/graphene heterostructures, Nanotechnology 29 (3) (2018) 035602, https://doi.org/10.1088/1361-6528/aa9c58.
[208] Z.G. Xu, H. Tian, A. Khanaki, R.J. Zheng, M. Suja, J.L. Liu, Large-area growth of multi-layer hexagonal boron nitride on polished cobalt foils by plasma-assisted molecular beam epitaxy, Sci. Rep. 7 (2017) 43100, https://doi.org/10.1038/srep43100.
[209] N.R. Glavin, M.L. Jespersen, M.H. Check, J. Hu, A.M. Hilton, T.S. Fisher, A.A. Voevodin, Synthesis of few-layer, large area hexagonal-boron nitride by pulsed laser deposition, Thin Solid Films 572 (2014) 245–250, https://doi.org/10.1016/j.tsf.2014.07.059.
[210] W. Auwärter, H.U. Suter, H. Sachdev, T. Greber, Synthesis of one monolayer of hexagonal boron nitride on Ni(111) from B-trichloroborazine $(ClBNH)_3$, Chem. Mat. 16 (2) (2004) 343–345, https://doi.org/10.1021/cm034805s.
[211] F. Müller, K. Stowe, H. Sachdev, Symmetry versus commensurability: epitaxial growth of hexagonal boron nitride on Pt(111) from B-trichloroborazine $(ClBNH)_3$, Chem. Mat. 17 (13) (2005) 3464–3467, https://doi.org/10.1021/cm048629e.
[212] G.E. Wood, Z.P.L. Laker, A.J. Marsden, G.R. Bell, N.R. Wilson, In situ gas analysis during the growth of hexagonal boron nitride from ammonia borane, Mater. Res. Express 4 (11) (2017) 115905, https://doi.org/10.1088/2053-1591/aa9a7f.
[213] V. Babenko, G. Lane, A.A. Koos, A.T. Murdock, K. So, J. Britton, S.S. Meysami, J. Moffat, N. Grobert, Time dependent decomposition of ammonia borane for the controlled production of 2D hexagonal boron nitride, Sci. Rep. 7 (2017) 14297, https://doi.org/10.1038/s41598-017-14663-8.
[214] R.M. Desrosiers, D.W. Greve, A.J. Gellman, Nucleation of boron nitride thin films on Ni(100), Surf. Sci. 382 (1–3) (1997) 35–48, https://doi.org/10.1016/S0039-6028(97)00092-7.
[215] F. Müller, S. Hüfner, H. Sachdev, S. Gsell, M. Schreck, Epitaxial growth of hexagonal boron nitride monolayers by a three-step boration-oxidation-nitration process, Phys. Rev. B 82 (7) (2010) 075405, https://doi.org/10.1103/PhysRevB.82.075405.
[216] H. Sachdev, F. Müller, S. Hüfner, Formation of boron-based films and boron nitride layers by CVD of a boron ester, Angew. Chem.-Int. Edit. 50 (16) (2011) 3701–3705, https://doi.org/10.1002/anie.201003012.
[217] M.P. Allan, S. Berner, M. Corso, T. Greber, J. Osterwalder, Tunable self-assembly of one-dimensional nanostructures with orthogonal directions, Nanoscale Res. Lett. 2 (2) (2007) 94–99, https://doi.org/10.1007/s11671-006-9036-2.
[218] Y. Qi, N.N. Han, Y.C. Li, Z.P. Zhang, X.B. Zhou, B. Deng, Q.C. Li, M.X. Liu, J.J. Zhao, Z.F. Liu, Y.F. Zhang, Strong adlayer-substrate interactions "break" the patching growth of h-BN onto graphene on Re(0001), ACS Nano 11 (2) (2017) 1807–1815, https://doi.org/10.1021/acsnano.6b07773.
[219] Y. Qi, Z.P. Zhang, B. Deng, X.B. Zhou, Q.C. Li, M. Hong, Y.C. Li, Z.F. Liu, Y.F. Zhang, Irreparable defects produced by the patching of h-BN frontiers on strongly interacting Re(0001) and their electronic properties, J. Am. Chem. Soc. 139 (16) (2017) 5849–5856, https://doi.org/10.1021/jacs.7b00647.
[220] N.A. Vinogradov, A.A. Zakharov, M.L. Ng, A. Mikkelsen, E. Lundgren, N. Mårtensson, A.B. Preobrajenski, One-dimensional corrugation of the h-BN monolayer on Fe(110), Langmuir 28 (3) (2012) 1775–1781, https://doi.org/10.1021/la2035642.
[221] P. Sutter, J. Lahiri, P. Albrecht, E. Sutter, Chemical vapor deposition and etching of high-quality monolayer hexagonal boron nitride films, ACS Nano 5 (9) (2011) 7303–7309, https://doi.org/10.1021/nn202141k.
[222] J. Lu, P.S.E. Yeo, Y. Zheng, H. Xu, C.K. Gan, M.B. Sullivan, A.H. Castro Neto, K.P. Loh, Step flow versus mosaic film growth in hexagonal boron nitride, J. Am. Chem. Soc. 135 (6) (2013) 2368–2373, https://doi.org/10.1021/ja3117735.
[223] P. Sutter, J. Lahiri, P. Zahl, B. Wang, E. Sutter, Scalable synthesis of uniform few-layer hexagonal boron nitride dielectric films, Nano Lett. 13 (1) (2013) 276–281, https://doi.org/10.1021/nl304080y.
[224] A. Kutana, A. Goriachko, Z.L. Hu, H. Sachdev, H. Over, B.I. Yakobson, Buckling patterns of graphene-boron nitride alloy on Ru(0001), Adv. Mater. Interfaces 2 (18) (2015) 1500322, https://doi.org/10.1002/admi.201500322.
[225] Q. Zhang, Y.X. Chen, C.D. Zhang, C.R. Pan, M.Y. Chou, C.G. Zeng, C.K. Shih, Bandgap renormalization and work function tuning in $MoSe_2$/hBN/Ru(0001) heterostructures, Nat. Commun. 7 (2016) 13843, https://doi.org/10.1038/ncomms13843.
[226] A. Goriachko, Y.B. He, M. Knapp, H. Over, M. Corso, T. Brugger, S. Berner, J. Osterwalder, T. Greber, Self-assembly of a hexagonal boron nitride nanomesh on Ru(0001), Langmuir 23 (6) (2007) 2928–2931, https://doi.org/10.1021/la062990t.
[227] D. Martoccia, T. Brugger, M. Bjorck, C.M. Schleputz, S.A. Pauli, T. Greber, B.D. Patterson, P.R. Willmott, h-BN/Ru(0001) nanomesh: a 14-on-13 superstructure with 3.5 nm periodicity, Surf. Sci. 604 (5–6) (2010) L16–L19, https://doi.org/10.1016/j.susc.2010.01.003.
[228] Y. Yang, Q. Fu, M.M. Wei, H. Bluhm, X.H. Bao, Stability of BN/metal interfaces in gaseous atmosphere, Nano Res. 8 (1) (2015) 227–237, https://doi.org/10.1007/s12274-014-0639-0.
[229] J. Beatty, Y. Cao, I. Tanabe, M.S. Driver, P.A. Dowben, J.A. Kelber, Atomic layer-by-layer deposition of h-BN(0001) on cobalt: a building block for spintronics and graphene electronics, Mater. Res. Express 1 (4) (2014) 046410, https://doi.org/10.1088/2053-1591/1/4/046410.
[230] M.S. Driver, J.D. Beatty, O. Olanipekun, K. Reid, A. Rath, P.M. Voyles, J.A. Kelber, Atomic layer epitaxy of h-BN(0001) multilayers on Co(0001) and molecular beam epitaxy growth of graphene on h-BN(0001)/Co(0001), Langmuir 32 (11) (2016) 2601–2607, https://doi.org/10.1021/acs.langmuir.5b03653.
[231] A.B. Preobrajenski, S.A. Krasnikov, A.S. Vinogradov, M.L. Ng, T. Kaambre, A.A. Cafolla, N. Mårtensson, Adsorption-induced gap states of h-BN on metal surfaces, Phys. Rev. B 77 (8) (2008) 085421, https://doi.org/10.1103/PhysRevB.77.085421.
[232] O. Bunk, M. Corso, D. Martoccia, R. Herger, P.R. Willmott, B.D. Patterson, J. Osterwalder, I. van der Veen, T. Greber, Surface x-ray diffraction study of boron-nitride nanomesh in air, Surf. Sci. 601 (2) (2007) L7–L10, https://doi.org/10.1016/j.susc.2006.11.018.
[233] T. Greber, M. Corso, J. Osterwalder, Fermi surfaces of single layer dielectrics on transition metals, Surf. Sci. 603 (10–12) (2009) 1373–1377, https://doi.org/10.1016/j.susc.2008.08.043.
[234] G.C. Dong, E.B. Fourre, F.C. Tabak, J.W.M. Frenken, How boron nitride forms a regular nanomesh on Rh(111), Phys. Rev. Lett. 104 (9) (2010) 096102, https://doi.org/10.1103/PhysRevLett.104.096102.
[235] S. Koch, M. Langer, S. Kawai, E. Meyer, T. Glatzel, Contrast inversion of the h-BN nanomesh investigated by nc-AFM and Kelvin probe force microscopy, J. Phys.-Condes. Matter 24 (31) (2012) 314212, https://doi.org/10.1088/0953-8984/24/31/314212.
[236] A. Hemmi, C. Bernard, H. Cun, S. Roth, M. Klöckner, T. Kälin, M. Weinl, S. Gsell, M. Schreck, J. Osterwalder, T. Greber, High quality single atomic layer deposition of hexagonal boron nitride on single crystalline Rh(111) four-inch wafers, Rev. Sci. Instrum. 85 (3) (2014) 035101, https://doi.org/10.1063/1.4866648.
[237] Q. Dubout, F. Calleja, G. Sclauzero, M. Etzkorn, A. Lehnert, L. Claude, M. Papagno, F.D. Natterer, F. Patthey, S. Rusponi, A. Pasquarello, H. Brune, Giant apparent lattice distortions in STM images of corrugated sp^2-hybridised monolayers, New J. Phys. 18 (2016) 103027, https://doi.org/10.1088/1367-2630/18/10/103027.

[238] T. Herden, M. Ternes, K. Kern, Lateral and vertical stiffness of the epitaxial h-BN monolayer on Rh(111), Nano Lett. 14 (6) (2014) 3623–3627, https://doi.org/10.1021/nl501349r.

[239] H.Y. Cun, A. Hemmi, E. Miniussi, C. Bernard, B. Probst, K. Liu, D.T.L. Alexander, A. Kleibert, G. Mette, M. Weinl, M. Schreck, J. Osterwalder, A. Radenovic, T. Greber, Centimeter-sized single-orientation monolayer hexagonal boron nitride with or without nanovoids, Nano Lett. 18 (2) (2018) 1205–1212, https://doi.org/10.1021/acs.nanolett.7b04752.

[240] S. Berner, M. Corso, R. Widmer, O. Gröning, R. Laskowski, P. Blaha, K. Schwarz, A. Goriachko, H. Over, S. Gsell, M. Schreck, H. Sachdev, T. Greber, J. Osterwalder, Boron nitride nanomesh: functionality from a corrugated monolayer, Angew. Chem.-Int. Edit. 46 (27) (2007) 5115–5119, https://doi.org/10.1002/anie.200700234.

[241] R. Widmer, S. Berner, O. Gröning, T. Brugger, E. Osterwalder, T. Greber, Electrolytic in situ STM investigation of h-BN-nanomesh, Electrochem. Commun. 9 (10) (2007) 2484–2488, https://doi.org/10.1016/j.elecom.2007.07.019.

[242] A.P. Farkas, P. Torok, F. Solymosi, J. Kiss, Z. Konya, Investigation of the adsorption properties of borazine and characterisation of boron nitride on Rh(111) by electron spectroscopic methods, Appl. Surf. Sci. 354 (2015) 367–372, https://doi.org/10.1016/j.apsusc.2015.05.060.

[243] R. Gubo, G. Vari, J. Kiss, A.P. Farkas, K. Palotas, L. Ovari, A. Berko, Z. Konya, Tailoring the hexagonal boron nitride nanomesh on Rh(111) with gold, Phys. Chem. Chem. Phys. 20 (22) (2018) 15473–15485, https://doi.org/10.1039/c8cp00790j.

[244] A. Martínez-Galera, J. Gómez-Rodríguez, Influence of metal support in-plane symmetry on the corrugation of hexagonal boron nitride and graphene monolayers, Nano Res. 11 (9) (2018) 4643–4653, https://doi.org/10.1007/s12274-018-2045-5.

[245] F. Orlando, R. Larciprete, P. Lacovig, I. Boscarato, A. Baraldi, S. Lizzit, Epitaxial growth of hexagonal boron nitride on Ir(111), J. Phys. Chem. C 116 (1) (2012) 157–164, https://doi.org/10.1021/jp207571n.

[246] D. Usachov, A. Fedorov, O. Vilkov, V.K. Adamchuk, L.V. Yashina, L. Bondarenko, A.A. Saranin, A. Grüneis, D.V. Vyalikh, Experimental and computational insight into the properties of the lattice-mismatched structures: monolayers of h-BN and graphene on Ir(111), Phys. Rev. B 86 (15) (2012) 155151, https://doi.org/10.1103/PhysRevB.86.155151.

[247] F. Schulz, R. Drost, S.K. Hämäläinen, T. Demonchaux, A.P. Seitsonen, P. Liljeroth, Epitaxial hexagonal boron nitride on Ir(111): a work function template, Phys. Rev. B 89 (23) (2014) 235429, https://doi.org/10.1103/PhysRevB.89.235429.

[248] F. Orlando, P. Lacovig, L. Omiciuolo, N.G. Apostol, R. Larciprete, A. Baraldi, S. Lizzit, Epitaxial growth of a single-domain hexagonal boron nitride mono layer, ACS Nano 8 (12) (2014) 12063–12070, https://doi.org/10.1021/nn5058968.

[249] M.X. Liu, Y.C. Li, P.C. Chen, J.Y. Sun, D.L. Ma, Q.C. Li, T. Gao, Y.B. Gao, Z.H. Cheng, X.H. Qiu, Y. Fang, Y.F. Zhang, Z.F. Liu, Quasi-freestanding monolayer heterostructure of graphene and hexagonal boron nitride on Ir(111) with a zigzag boundary, Nano Lett. 14 (11) (2014) 6342–6347, https://doi.org/10.1021/nl502780u.

[250] F.H.F. zum Hagen, D.M. Zimmermann, C.C. Silva, C. Schlueter, N. Atodiresei, W. Jolie, A.J. Martinez-Galera, D. Dombrowski, U.A. Schröder, M. Will, P. Lazic, V. Caciuc, S. Blügel, T.L. Lee, T. Michely, C. Busse, Structure and growth of hexagonal boron nitride on Ir(111), ACS Nano 10 (12) (2016) 11012–11026, https://doi.org/10.1021/acsnano.6b05819.

[251] F. Schulz, R. Drost, S.K. Hämäläinen, P. Liljeroth, Templated self-assembly and local doping of molecules on epitaxial hexagonal boron nitride, ACS Nano 7 (12) (2013) 11121–11128, https://doi.org/10.1021/nn404840h.

[252] M. Petrovic, U. Hagemann, M. Horn-von Hoegen, F.J.M. zu Heringdorf, Micro-analysis of single-layer hexagonal boron nitride islands on Ir(111), Appl. Surf. Sci. 420 (2017) 504–510, https://doi.org/10.1016/j.apsusc.2017.05.155.

[253] F. Schulz, J. Ritala, O. Krejci, A.P. Seitsonen, A.S. Foster, P. Liljeroth, Elemental identification by combining atomic force microscopy and Kelvin probe force microscopy, ACS Nano 12 (6) (2018) 5274–5283, https://doi.org/10.1021/acsnano.7b08997.

[254] A. Nagashima, N. Tejima, Y. Gamou, T. Kawai, C. Oshima, Electronic dispersion-relations of monolayer hexagonal boron-nitride formed on the Ni(111) surface, Phys. Rev. B 51 (7) (1995) 4606–4613, https://doi.org/10.1103/PhysRevB.51.4606.

[255] Y. Gamou, M. Terai, A. Nagashima, C. Oshima, Atomic structural analysis of a monolayer epitaxial film of hexagonal boron nitride Ni(111) studied by LEED intensity analysis, Sci. Rep. Res. Inst. Tohoku Univ. Ser. A-Phys. Chem. Metall. 44 (2) (1997) 211–214.

[256] E. Rokuta, Y. Hasegawa, K. Suzuki, Y. Gamou, C. Oshima, A. Nagashima, Phonon dispersion of an epitaxial monolayer film of hexagonal boron nitride on Ni(111), Phys. Rev. Lett. 79 (23) (1997) 4609–4612, https://doi.org/10.1103/PhysRevLett.79.4609.

[257] A. Nagashima, N. Tejima, Y. Gamou, T. Kawai, C. Oshima, Electronic-structure of monolayer hexagonal boron-nitride physisorbed on metal-surfaces, Phys. Rev. Lett. 75 (21) (1995) 3918–3921, https://doi.org/10.1103/PhysRevLett.75.3918.

[258] I. Shimoyama, Y. Baba, T. Sekiguchi, K.G. Nath, NEXAFS spectra of an epitaxial boron nitride film on Ni(111), J. Electron Spectrosc. Relat. Phenom. 137 (2004) 573–578, https://doi.org/10.1016/j.elspec.2004.02.040.

[259] W. Auwärter, T.J. Kreutz, T. Greber, J. Osterwalder, XPD and STM investigation of hexagonal boron nitride on Ni(111), Surf. Sci. 429 (1–3) (1999) 229–236, https://doi.org/10.1016/S0039-6028(99)00381-7.

[260] C. Oshima, A. Nagashima, Ultra-thin epitaxial films of graphite and hexagonal boron nitride on solid surfaces, J. Phys.-Condes. Matter 9 (1) (1997) 1–20, https://doi.org/10.1088/0953-8984/9/1/004.

[261] W. Auwärter, M. Muntwiler, J. Osterwalder, T. Greber, Defect lines and two-domain structure of hexagonal boron nitride films on Ni(111), Surf. Sci. 545 (1–2) (2003) L735–L740, https://doi.org/10.1016/j.susc.2003.08.046.

[262] H. Nakamura, N. Fujihara, M. Nojima, K. Tamura, H. Ishii, M. Owari, C. Oshima, Y. Nihei, Surface structural analysis of monolayer films composed of light elements by x-ray photoelectron diffraction, Surf. Interface Anal. 36 (12) (2004) 1513–1515, https://doi.org/10.1002/sia.1935.

[263] A.B. Preobrajenski, A.S. Vinogradov, N. Mårtensson, Ni 3d-BN π hybridization at the h-BN/Ni(111) interface observed with core-level spectroscopies, Phys. Rev. B 70 (16) (2004) 165404, https://doi.org/10.1103/PhysRevB.70.165404.

[264] T. Greber, W. Auwärter, M. Hoesch, G. Grad, P. Blaha, J. Osterwalder, The Fermi surface in a magnetic metal-insulator interface, Surf. Rev. Lett. 9 (2) (2002) 1243–1250, https://doi.org/10.1142/S0218625X02001884.

[265] A.B. Preobrajenski, A.S. Vinogradov, N. Mårtensson, Monolayer of h-BN chemisorbed on Cu(111) and Ni(111): the role of the transition metal 3d states, Surf. Sci. 582 (1–3) (2005) 21–30, https://doi.org/10.1016/j.susc.2005.02.047.

[266] J. Osterwalder, A. Tamai, W. Auwärter, M.P. Allan, T. Greber, Photoelectron diffraction for a look inside nanostructures, Chimia 60 (11) (2006) A795–A799, https://doi.org/10.2533/chimia.2006.795.

[267] J. Rusz, A.B. Preobrajenski, M.L. Ng, N.A. Vinogradov, N. Mårtensson, O. Wessely, B. Sanyal, O. Eriksson, Dynamical effects in x-ray absorption spectra of graphene and monolayered h-BN on Ni(111), Phys. Rev. B 81 (7) (2010) 073402, https://doi.org/10.1103/PhysRevB.81.073402.

[268] D. Leuenberger, H. Yanagisawa, S. Roth, J. Osterwalder, M. Hengsberger, Disentanglement of electron dynamics and space-charge effects in time-resolved photoemission from h-BN/Ni(111), Phys. Rev. B 84 (12) (2011) 125107, https://doi.org/10.1103/PhysRevB.84.125107.

[269] M. Muntwiler, J. Zhang, R. Stania, F. Matsui, P. Oberta, U. Flechsig, L. Patthey, C. Quitmann, T. Glatzel, R. Widmer, E. Meyer, T.A. Jung, P. Aebi, R. Fasel, T. Greber, Surface science at the PEARL beamline of the swiss light source, J. Synchrot. Radiat. 24 (2017) 354–366, https://doi.org/10.1107/S1600577516018646.

[270] K. Zumbrägel, K. Wulff, C. Eibl, M. Donath, M. Hengsberger, Exchange-split interface state at h-BN/Ni(111), Phys. Rev. B 78 (8) (2008) 085422, https://doi.org/10.1103/PhysRevB.78.085422.

[271] K.R. Koswattage, I. Shimoyama, Y. Baba, T. Sekiguchi, K. Nakagawa, Selective adsorption of atomic hydrogen on a h-BN thin film, J. Chem. Phys. 135 (1) (2011) 014706, https://doi.org/10.1063/1.3605497.

[272] K.R. Koswattage, I. Shimoyama, Y. Baba, T. Sekiguchi, K. Nakagawa, Study on selective adsorption of deuterium on boron nitride using photon-stimulated ion-desorption, Appl. Surf. Sci. 258 (4) (2011) 1561–1564, https://doi.org/10.1016/j.apsusc.2011.09.133.

[273] R. Drost, S. Kezilebieke, M.M. Ervasti, S.K. Hämäläinen, F. Schulz, A. Harju, P. Liljeroth, Synthesis of extended atomically perfect zigzag graphene - boron nitride interfaces, Sci. Rep. 5 (2015) 16741, https://doi.org/10.1038/srep16741.

[274] M. Ohtomo, Y. Yamauchi, A.A. Kuzubov, N.S. Eliseeva, P.V. Avramov, S. Entani, Y. Matsumoto, H. Naramoto, S. Sakai, Contact-induced spin polarization of monolayer hexagonal boron nitride on Ni(111), Appl. Phys. Lett. 104 (5) (2014) 051604, https://doi.org/10.1063/1.4863324.

[275] M. Ohtomo, Y. Yamauchi, X. Sun, A.A. Kuzubov, N.S. Mikhaleva, P.V. Avramov, S. Entani, Y. Matsumoto, H. Naramoto, S. Sakai, Direct observation of site-selective hydrogenation and spin-polarization in hydrogenated hexagonal boron nitride on Ni(111), Nanoscale 9 (6) (2017) 2369–2375, https://doi.org/10.1039/c6nr06308j.

[276] M. Cattelan, B. Markman, G. Lucchini, P.K. Das, I. Vobornik, J.A. Robinson, S. Agnoli, G. Granozzi, New strategy for the growth of complex heterostructures based on different 2D materials, Chem. Mat. 27 (11) (2015) 4105–4113, https://doi.org/10.1021/acs.chemmater.5b01170.

[277] Y. Yang, Q. Fu, H.B. Li, M.M. Wei, J.P. Xiao, W. Wei, X.H. Bao, Creating a nanospace under an h-BN cover for adlayer growth on nickel(111), ACS Nano 9 (12) (2015) 11589–11598, https://doi.org/10.1021/acsnano.5b05509.

[278] T. Greber, L. Brandenberger, M. Corso, A. Tamai, J. Osterwalder, Single layer hexagonal boron nitride films on Ni(110), e-J. Surf. Sci. Nanotech. 4 (2006) 410–413.

[279] M. Morscher, M. Corso, T. Greber, J. Osterwalder, Formation of single layer h-BN on Pd(111), Surf. Sci. 600 (16) (2006) 3280–3284, https://doi.org/10.1016/j.susc.2006.06.016.

[280] M. Corso, T. Greber, J. Osterwalder, h-BN on Pd(110): a tunable system for self-assembled nanostructures? Surf. Sci. 577 (2–3) (2005) L78–L84, https://doi.org/10.1016/j.susc.2005.01.015.

[281] R.J. Simonson, M. Trenary, An infrared study of the adsorption of borazine, $(BHNH)_3$, on the Pt(111) surface, J. Electron Spectrosc. Relat. Phenom. 54 (1990) 717–728, https://doi.org/10.1016/0368-2048(90)80264-B.

[282] E. Cavar, R. Westerström, A. Mikkelsen, E. Lundgren, A.S. Vinogradov, M.L. Ng, A.B. Preobrajenski, A.A. Zakharov, N. Mårtensson, A single h-BN layer on Pt(111), Surf. Sci. 602 (9) (2008) 1722–1726, https://doi.org/10.1016/j.susc.2008.03.008.

[283] Y.H. Zhang, X.F. Weng, H. Li, H.B. Li, M.M. Wei, J.P. Xiao, Z. Liu, M.S. Chen, Q. Fu, X.H. Bao, Hexagonal boron nitride cover on Pt(111): a new route to tune molecule-metal interaction and metal-catalyzed reactions, Nano Lett. 15 (5) (2015) 3616–3623, https://doi.org/10.1021/acs.nanolett.5b01205.

[284] S. Joshi, D. Ecija, R. Koitz, M. Iannuzzi, A.P. Seitsonen, J. Hutter, H. Sachdev, S. Vijayaraghavan, F. Bischoff, K. Seufert, J.V. Barth, W. Auwärter, Boron nitride on Cu(111): an electronically corrugated monolayer, Nano Lett. 12 (11) (2012) 5821–5828, https://doi.org/10.1021/nl303170m.

[285] B. Hwang, J. Kwon, M. Lee, S.J. Lim, S. Jeon, S. Kim, U. Ham, Y.J. Song, Y. Kuk, Electron-beam assisted growth of hexagonal boron-nitride layer, Curr. Appl. Phys. 13 (7) (2013) 1365–1369, https://doi.org/10.1016/j.cap.2013.04.018.
[286] B. Hwang, J. Hwang, J.K. Yoon, S. Lim, S. Kim, M. Lee, J.H. Kwon, H. Baek, D. Sung, G. Kim, S. Hong, J. Ihm, J.A. Stroscio, Y. Kuk, Energy bandgap and edge states in an epitaxially grown graphene/h-BN heterostructure, Sci. Rep. 6 (2016) 31160, https://doi.org/10.1038/srep31160.
[287] M. Schwarz, A. Riss, M. Garnica, J. Ducke, P.S. Deimel, D.A. Duncan, P.K. Thakur, T.L. Lee, A.P. Seitsonen, J.V. Barth, F. Allegretti, W. Auwärter, Corrugation in the weakly interacting hexagonal-BN/Cu(111) system: structure determination by combining noncontact atomic force microscopy and x-ray standing waves, ACS Nano 11 (9) (2017) 9151–9161, https://doi.org/10.1021/acsnano.7b04022.
[288] C. Brülke, T. Heepenstrick, N. Humberg, I. Krieger, M. Sokolowski, S. Weiß, T.S. Tautz, S. Soubatch, Long vertical distance bonding of the hexagonal boron nitride monolayer on the Cu(111) surface, J. Phys. Chem. C 121 (43) (2017) 23964–23973, https://doi.org/10.1021/acs.jpcc.7b06107.
[289] Q. Zhang, J. Yu, P. Ebert, C. Zhang, C.R. Pan, M.Y. Chou, C.K. Shih, C. Zeng, S. Yuan, Tuning band gap and work function modulations in monolayer hBN/Cu(111) heterostructures with moiré patterns, ACS Nano 12 (9) (2018) 9355–9362, https://doi.org/10.1021/acsnano.8b04444.
[290] Q.C. Li, X.L. Zou, M.X. Liu, J.Y. Sun, Y.B. Gao, Y. Qi, X.B. Zhou, B.I. Yakobson, Y.F. Zhang, Z.F. Liu, Grain boundary structures and electronic properties of hexagonal boron nitride on Cu(111), Nano Lett. 15 (9) (2015) 5804–5810, https://doi.org/10.1021/acs.nanolett.5b01852.
[291] C. Herrmann, P. Omelchenko, K.L. Kavanagh, Growth of h-BN on copper (110) in a LEEM, Surf. Sci. 669 (2018) 133–139, https://doi.org/10.1016/j.susc.2017.11.021.
[292] F. Müller, S. Hüfner, H. Sachdev, R. Laskowski, P. Blaha, K. Schwarz, Epitaxial growth of hexagonal boron nitride on Ag(111), Phys. Rev. B 82 (11) (2010) 113406, https://doi.org/10.1103/PhysRevB.82.113406.
[293] M. Garnica, M. Schwarz, J. Ducke, Y.Q. He, F. Bischoff, J.V. Barth, W. Auwärter, D. Stradi, Comparative study of the interfaces of graphene and hexagonal boron nitride with silver, Phys. Rev. B 94 (15) (2016) 155431, https://doi.org/10.1103/PhysRevB.94.155431.
[294] F. Müller, S. Grandthyll, Monolayer formation of hexagonal boron nitride on Ag(001), Surf. Sci. 617 (2013) 207–210, https://doi.org/10.1016/j.susc.2013.07.024.
[295] L. Camilli, E. Sutter, P. Sutter, Growth of two-dimensional materials on non-catalytic substrates: h-BN/Au(111), 2D Mater. 1 (2) (2014) 025003, https://doi.org/10.1088/2053-1583/1/2/025003.
[296] G. Siegel, C.V. Ciobanu, B. Narayanan, M. Snure, S.C. Badescu, Heterogeneous pyrolysis: a route for epitaxial growth of hBN atomic layers on copper using separate boron and nitrogen precursors, Nano Lett. 17 (4) (2017) 2404–2413, https://doi.org/10.1021/acs.nanolett.6b05409.
[297] S. Suzuki, R.M. Pallares, H. Hibino, Growth of atomically thin hexagonal boron nitride films by diffusion through a metal film and precipitation, J. Phys. D-Appl. Phys. 45 (38) (2012) 385304, https://doi.org/10.1088/0022-3727/45/38/385304.
[298] C.H. Zhang, L. Fu, S.L. Zhao, Y. Zhou, H.L. Peng, Z.F. Liu, Controllable co-segregation synthesis of wafer-scale hexagonal boron nitride thin films, Adv. Mater. 26 (11) (2014) 1776–1781, https://doi.org/10.1002/adma.201304301.
[299] S. Caneva, R.S. Weatherup, B.C. Bayer, B. Brennan, S.J. Spencer, K. Mingard, A. Cabrero-Vilatela, C. Baehtz, A.J. Pollard, S. Hofmann, Nucleation control for large, single crystalline domains of mono layer hexagonal boron nitride via Si-doped Fe catalysts, Nano Lett. 15 (3) (2015) 1867–1875, https://doi.org/10.1021/nl5046632.
[300] S. Caneva, R.S. Weatherup, B.C. Bayer, R. Blume, A. Cabrero-Vilatela, P. Braeuninger-Weirner, M.B. Martin, R.Z. Wang, C. Baehtz, R. Schloegl, J.C. Meyer, S. Hofmann, Controlling catalyst bulk reservoir effects for monolayer hexagonal boron nitride CVD, Nano Lett. 16 (2) (2016) 1250–1261, https://doi.org/10.1021/acs.nanolett.5b04586.
[301] P.R. Kidambi, R. Blume, J. Kling, J.B. Wagner, C. Baehtz, R.S. Weatherup, R. Schloegl, B.C. Bayer, S. Hofmann, In situ observations during chemical vapor deposition of hexagonal boron nitride on polycrystalline copper, Chem. Mat. 26 (22) (2014) 6380–6392, https://doi.org/10.1021/cm502603n.
[302] X.H. Hu, T. Bjorkman, H. Lipsanen, L.T. Sun, A.V. Krasheninnikov, Solubility of boron, carbon, and nitrogen in transition metals: getting insight into trends from first-principles calculations, J. Phys. Chem. Lett. 6 (16) (2015) 3263–3268, https://doi.org/10.1021/acs.jpclett.5b01377.
[303] H. Tian, A. Khanaki, P. Das, R.J. Zheng, Z.J. Cui, Y.W. He, W.H. Shi, Z.G. Xu, R. Lake, J.L. Liu, Role of carbon interstitials in transition metal substrates on controllable synthesis of high-quality large-area two-dimensional hexagonal boron nitride layers, Nano Lett. 18 (6) (2018) 3352–3361, https://doi.org/10.1021/acs.nanolett.7b05179.
[304] R.Q. Zhao, F.F. Li, Z.R. Liu, Z.F. Liuc, F. Ding, The transition metal surface passivated edges of hexagonal boron nitride (h-BN) and the mechanism of h-BN's chemical vapor deposition (CVD) growth, Phys. Chem. Chem. Phys. 17 (43) (2015) 29327–29334, https://doi.org/10.1039/c5cp04833h.
[305] W. Auwärter, M. Muntwiler, T. Greber, J. Osterwalder, Co on h-BN/Ni(111): from island to island-chain formation and Co intercalation, Surf. Sci. 511 (1–3) (2002) 379–386, https://doi.org/10.1016/S0039-6028(02)01545-5.
[306] N.I. Verbitskiy, A.V. Fedorov, G. Profeta, A. Stroppa, L. Petaccia, B. Senkovskiy, A. Nefedov, C. Wöll, D.Y. Usachov, D.V. Vyalikh, L.V. Yashina, A.A. Eliseev, T. Pichler, A. Grüneis, Atomically precise semiconductor-graphene and hBN interfaces by Ge intercalation, Sci. Rep. 5 (2015) 17700, https://doi.org/10.1038/srep17700.
[307] M. Bazarnik, J. Brede, R. Decker, R. Wiesendanger, Tailoring molecular self-assembly of magnetic phthalocyanine molecules on Fe- and Co-intercalated graphene, ACS Nano 7 (12) (2013) 11341–11349, https://doi.org/10.1021/nn405172q.
[308] T. Brugger, H.F. Ma, M. Iannuzzi, S. Berner, A. Winkler, J. Hutter, J. Osterwalder, T. Greber, Nanotexture switching of single-layer hexagonal boron nitride on rhodium by intercalation of hydrogen atoms, Angew. Chem.-Int. Edit. 49 (35) (2010) 6120–6124, https://doi.org/10.1002/anie.201001064.
[309] A.Y. Dong, Q. Fu, H. Wu, M.M. Wei, X.H. Bao, Factors controlling the CO intercalation of h-BN overlayers on Ru(0001), Phys. Chem. Chem. Phys. 18 (35) (2016) 24278–24284, https://doi.org/10.1039/c6cp03660k.
[310] A.B. Preobrajenski, M.L. Ng, N.A. Vinogradov, A.S. Vinogradov, E. Lundgren, A. Mikkelsen, N. Mårtensson, Impact of oxygen coadsorption on intercalation of cobalt under the h-BN nanomesh, Nano Lett. 9 (7) (2009) 2780–2787, https://doi.org/10.1021/nl901316p.
[311] Y.H. Zhang, M.M. Wei, Q. Fu, X.H. Bao, Oxygen intercalation under hexagonal boron nitride (h-BN) on Pt(111), Sci. Bull. 60 (18) (2015) 1572–1579, https://doi.org/10.1007/s11434-015-0875-z.
[312] C.X. Ma, J. Park, L. Liu, Y.S. Kim, M. Yoon, A.P. Baddorf, G. Gu, A.P. Li, Interplay between intercalated oxygen superstructures and monolayer h-BN on Cu(100), Phys. Rev. B 94 (6) (2016) 064106, https://doi.org/10.1103/PhysRevB.94.064106.
[313] M.L. Ng, A. Shavorskiy, C. Rameshan, A. Mikkelsen, E. Lundgren, A. Preobrajenski, H. Bluhm, Reversible modification of the structural and electronic properties of a boron nitride monolayer by CO intercalation, ChemPhysChem 16 (5) (2015) 923–927, https://doi.org/10.1002/cphc.201500031.
[314] J. Ducke, A. Riss, A.P. Paz, K. Seufert, M. Schwarz, M. Garnica, A. Rubio, W. Auwärter, Layered insulator/molecule/metal heterostructures with molecular functionality through porphyrin intercalation, ACS Nano 12 (3) (2018) 2677–2684, https://doi.org/10.1021/acsnano.7b08887.
[315] G.L. Doll, J.S. Speck, G. Dresselhaus, M.S. Dresselhaus, K. Nakamura, S.I. Tanuma, Intercalation of hexagonal boron-nitride with potassium, J. Appl. Phys. 66 (6) (1989) 2554–2558, https://doi.org/10.1063/1.344219.
[316] M.S. Dresselhaus, G. Dresselhaus, Intercalation compounds of graphite, Adv. Phys. 51 (1) (2002) 1–186, https://doi.org/10.1080/00018730110113644.
[317] N.I. Kovtyukhova, Y.X. Wang, R.T. Lv, M. Terrones, V.H. Crespi, T.E. Mallouk, Reversible intercalation of hexagonal boron nitride with bronsted acids, J. Am. Chem. Soc. 135 (22) (2013) 8372–8381, https://doi.org/10.1021/ja403197h.
[318] D. Usachov, V.K. Adamchuk, D. Haberer, A. Grüneis, H. Sachdev, A.B. Preobrajenski, C. Laubschat, D.V. Vyalikh, Quasifreestanding single-layer hexagonal boron nitride as a substrate for graphene synthesis, Phys. Rev. B 82 (7) (2010) 075415, https://doi.org/10.1103/PhysRevB.82.075415.
[319] J.H. Meng, X.W. Zhang, Y. Wang, Z.G. Yin, H. Liu, J. Xia, H.L. Wang, J.B. You, P. Jin, D.G. Wang, X.M. Meng, Aligned growth of millimeter-size hexagonal boron nitride single-crystal domains on epitaxial nickel thin film, Small 13 (18) (2017) 1604179, https://doi.org/10.1002/smll.201604179.
[320] S. Gsell, M. Fischer, M. Schreck, B. Stritzker, Epitaxial films of metals from the platinum group (Ir, Rh, Pt and Ru) on YSZ-buffered Si(111), J. Cryst. Growth 311 (14) (2009) 3731–3736, https://doi.org/10.1016/j.jcrysgro.2009.04.034.
[321] A. Goriachko, Y.B. He, H. Over, Complex growth of nano-Au on BN nanomeshes supported by Ru(0001), J. Phys. Chem. C 112 (22) (2008) 8147–8152, https://doi.org/10.1021/jp7119608.
[322] R. Drost, A. Uppstu, F. Schulz, S.K. Hämäläinen, M. Ervasti, A. Harju, P. Liljeroth, Electronic states at the graphene-hexagonal boron nitride zigzag interface, Nano Lett. 14 (9) (2014) 5128–5132, https://doi.org/10.1021/nl501895h.
[323] B.C. Bayer, S. Caneva, T.J. Pennycook, J. Kotakoski, C. Mangler, S. Hofmann, J.C. Meyer, Introducing overlapping grain boundaries in chemical vapor deposited hexagonal boron nitride monolayer films, ACS Nano 11 (5) (2017) 4521–4527, https://doi.org/10.1021/acsnano.6b08315.
[324] S.M. Kim, A. Hsu, M.H. Park, S.H. Chae, S.J. Yun, J.S. Lee, D.H. Cho, W.J. Fang, C. Lee, T. Palacios, M. Dresselhaus, K.K. Kim, Y.H. Lee, J. Kong, Synthesis of large-area multilayer hexagonal boron nitride for high material performance, Nat. Commun. 6 (2015) 8662, https://doi.org/10.1038/ncomms9662.
[325] T. Takahashi, H. Itoh, A. Takeuchi, Chemical vapor-deposition of hexagonal boron-nitride thick-film on iron, J. Cryst. Growth 47 (2) (1979) 245–250, https://doi.org/10.1016/0022-0248(79)90248-3.
[326] M. Corso, Boron Nitride Nanostructures on Transition Metals: Flat Layers and Nanomesh. (Ph.D. thesis), Universität Zürich, 2006.
[327] C. Bjelkevig, Z. Mi, J. Xiao, P.A. Dowben, L. Wang, W.N. Mei, J.A. Kelber, Electronic structure of a graphene/hexagonal-BN heterostructure grown on Ru(0001) by chemical vapor deposition and atomic layer deposition: extrinsically doped graphene, J. Phys.-Condes. Matter 22 (30) (2010) 302002, https://doi.org/10.1088/0953-8984/22/30/302002.
[328] N. Joshi, P. Ghosh, Substrate-induced changes in the magnetic and electronic properties of hexagonal boron nitride, Phys. Rev. B 87 (23) (2013) 235440, https://doi.org/10.1103/PhysRevB.87.235440.
[329] Y.G. Zhou, X.T. Zu, F. Gao, Substrate-induced magnetism in BN layer: a first-principles study, Solid State Commun. 151 (12) (2011) 883–886, https://doi.org/10.1016/j.ssc.2011.04.001.
[330] R. Koitz, J.K. Norskov, F. Studt, A systematic study of metal-supported boron nitride materials for the oxygen reduction reaction, Phys. Chem. Chem. Phys. 17 (19) (2015) 12722–12727, https://doi.org/10.1039/c5cp01384d.
[331] Z.G. Xu, R.J. Zheng, A. Khanaki, Z. Zuo, J.L. Liu, Direct growth of graphene on in situ epitaxial hexagonal boron nitride flakes by plasma-assisted molecular beam epitaxy, Appl. Phys. Lett. 107 (21) (2015) 213103, https://doi.org/10.1063/1.4936378.

[332] R. Laskowski, P. Blaha, T. Gallauner, K. Schwarz, Single-layer model of the hexagonal boron nitride nanomesh on the Rh(111) surface, Phys. Rev. Lett. 98 (10) (2007) 106802, https://doi.org/10.1103/PhysRevLett.98.106802.

[333] R. Laskowski, P. Blaha, Unraveling the structure of the h-BN/Rh(111) nanomesh with ab initio calculations, J. Phys.-Condes. Matter 20 (6) (2008) 064207, https://doi.org/10.1088/0953-8984/20/6/064207.

[334] D. Martoccia, S.A. Pauli, T. Brugger, T. Greber, B.D. Patterson, P.R. Willmott, h-BN on Rh(111): persistence of a commensurate 13-on-12 superstructure up to high temperatures, Surf. Sci. 604 (5–6) (2010) L9–L11, https://doi.org/10.1016/j.susc.2009.12.016.

[335] S.F.L. Mertens, A. Hemmi, S. Muff, O. Gröning, S. De Feyter, J. Osterwalder, T. Greber, Switching stiction and adhesion of a liquid on a solid, Nature 534 (7609) (2016) 676–679, https://doi.org/10.1038/nature18275.

[336] F. Müller, S. Hüfner, H. Sachdev, Epitaxial growth of boron nitride on a Rh(111) multilayer system: formation and fine tuning of a BN-nanomesh, Surf. Sci. 603 (3) (2009) 425–432, https://doi.org/10.1016/j.susc.2008.10.033.

[337] M. Iannuzzi, F. Tran, R. Widmer, T. Dienel, K. Radican, Y. Ding, J.R. Hutter, O. Gröning, Site-selective adsorption of phthalocyanine on h-BN/Rh(111) nanomesh, Phys. Chem. Chem. Phys. 16 (24) (2014) 12374–12384, https://doi.org/10.1039/c4cp01466a.

[338] Y. Ding, M. Iannuzzi, J. Hutter, Investigation of boron nitride nanomesh interacting with water, J. Phys. Chem. C 115 (28) (2011) 13685–13692, https://doi.org/10.1021/jp110235y.

[339] H. Dil, J. Lobo-Checa, R. Laskowski, P. Blaha, S. Berner, J. Osterwalder, T. Greber, Surface trapping of atoms and molecules with dipole rings, Science 319 (5871) (2008) 1824–1826, https://doi.org/10.1126/science.1154179.

[340] K. Wandelt, The local work function: concept and implications, Appl. Surf. Sci. 111 (1997) 1–10, https://doi.org/10.1016/S0169-4332(96)00692-7.

[341] K. Wandelt, Surface characterization by photoemission of adsorbed xenon (PAX), J. Vac. Sci. Technol. A-Vac. Surf. Films 2 (2) (1984) 802–807, https://doi.org/10.1116/1.572509.

[342] K. Wandelt, K. Markert, P. Dolle, A. Jablonski, J.W. Niemantsverdriet, Surface characterization by means of photoemission of adsorbed xenon (PAX), Surf. Interface Anal. 12 (1–12) (1988) 15–20, https://doi.org/10.1002/sia.740120106.

[343] T. Greber, Graphene and hexagonal boron nitride layers: nanostructures with 3 bond hierarchy levels, e-J. Surf. Sci. Nanotech. 8 (2010) 62–64.

[344] T. Greber, Graphene and Boron Nitride Single Layers, 2009, arXiv:0904.1520v1.

[345] H.F. Ma, M. Thomann, J. Schmidlin, S. Roth, M. Morscher, T. Greber, Corrugated single layer templates for molecules: from h-BN nanomesh to graphene based quantum dot arrays, Front. Phys. China 5 (4) (2010) 387–392, https://doi.org/10.1007/s11467-010-0137-0.

[346] M.C. Patterson, B.F. Habenicht, R.L. Kurtz, L. Liu, Y. Xu, P.T. Sprunger, Formation and stability of dense arrays of Au nanoclusters on hexagonal boron nitride/Rh(111), Phys. Rev. B 89 (20) (2014) 205423, https://doi.org/10.1103/PhysRevB.89.205423.

[347] R. Laskowski, T. Gallauner, P. Blaha, K. Schwarz, Density functional theory simulations of B K and N K NEXAFS spectra of h-BN/transition metal(111) interfaces, J. Phys.-Condes. Matter 21 (10) (2009) 104210, https://doi.org/10.1088/0953-8984/21/10/104210.

[348] T. Musso, S. Caravati, J. Hutter, M. Iannuzzi, Second generation Car-Parrinello MD: application to the h-BN/Rh(111) nanomesh, Eur. Phys. J. B 91 (7) (2018) 148, https://doi.org/10.1140/epjb/e2018-90104-y.

[349] A.P. Seitsonen, F. Schulz, P. Liljeroth, Benchmarking van der Waals-treated DFT: The case of hexagonal boron nitride and graphene on Ir(111), 2018, arXiv:1805.08880v1.

[350] G.B. Grad, P. Blaha, K. Schwarz, W. Auwärter, T. Greber, Density functional theory investigation of the geometric and spintronic structure of h-BN/Ni(111) in view of photoemission and STM experiments, Phys. Rev. B 68 (8) (2003) 085404, https://doi.org/10.1103/PhysRevB.68.085404.

[351] M. Muntwiler, W. Auwärter, F. Baumberger, M. Hoesch, T. Greber, J. Osterwalder, Determining adsorbate structures from substrate emission x-ray photoelectron diffraction, Surf. Sci. 472 (1–2) (2001) 125–132, https://doi.org/10.1016/S0039-6028(00)00928-6.

[352] A. Ebnonnasir, S. Kodambaka, C.V. Ciobanu, Strongly and weakly interacting configurations of hexagonal boron nitride on nickel, Surf. Rev. Lett. 22 (6) (2015) 1550078, https://doi.org/10.1142/S0218625X1550078X.

[353] S.M. Kozlov, F. Vines, A. Gorling, Bonding mechanisms of graphene on metal surfaces, J. Phys. Chem. C 116 (13) (2012) 7360–7366, https://doi.org/10.1021/jp210667f.

[354] M. Muntwiler, M. Hengsberger, A. Dolocan, H. Neff, T. Greber, J. Osterwalder, Energetics and dynamics of unoccupied electronic states at the h-BN/Ni(111) interface, Phys. Rev. B 75 (7) (2007) 075407, https://doi.org/10.1103/PhysRevB.75.075407.

[355] M.N. Huda, L. Kleinman, h-BN monolayer adsorption on the Ni(111) surface: a density functional study, Phys. Rev. B 74 (7) (2006) 075418, https://doi.org/10.1103/PhysRevB.74.075418.

[356] J.G. Che, H.P. Cheng, First-principles investigation of a monolayer of C_{60} on h-BN/Ni(111), Phys. Rev. B 72 (11) (2005) 115436, https://doi.org/10.1103/PhysRevB.72.115436.

[357] X. Sun, A. Pratt, Z.Y. Li, M. Ohtomo, S. Sakai, Y. Yamauchi, The adsorption of h-BN monolayer on the Ni(111) surface studied by density functional theory calculations with a semiempirical long-range dispersion correction, J. Appl. Phys. 115 (17) (2014) 17C117, https://doi.org/10.1063/1.4866237.

[358] A. Lyalin, A. Nakayama, K. Uosaki, T. Taketsugu, Functionalization of monolayer h-BN by a metal support for the oxygen reduction reaction, J. Phys. Chem. C 117 (41) (2013) 21359–21370, https://doi.org/10.1021/jp406751n.

[359] P.V. Avramov, A.A. Kuzubov, S. Sakai, M. Ohtomo, S. Entani, Y. Matsumoto, H. Naramoto, N.S. Eleseeva, Contact-induced spin polarization in graphene/h-BN/Ni nanocomposites, J. Appl. Phys. 112 (11) (2012) 114303, https://doi.org/10.1063/1.4767134.

[360] A.H.M.A. Wasey, S. Chakrabarty, G.P. Das, C. Majumder, h-BN monolayer on the Ni(111) surface: a potential catalyst for oxidation, ACS Appl. Mater. Interfaces 5 (21) (2013) 10404–10408, https://doi.org/10.1021/am404321x.

[361] X.M. Gao, S.J. Wang, S. Lin, Defective hexagonal boron nitride nanosheet on Ni(111) and Cu(111): stability, electronic structures, and potential applications, ACS Appl. Mater. Interfaces 8 (36) (2016) 24238–24247, https://doi.org/10.1021/acsami.6b08097.

[362] S. Liu, A.C.T. van Duin, D.M. van Duin, B. Liu, J.H. Edgart, Atomistic insights into nucleation and formation of hexagonal boron nitride on nickel from first-principles-based reactive molecular dynamics simulations, ACS Nano 11 (4) (2017) 3585–3596, https://doi.org/10.1021/acsnano.6b06736.

[363] M. Muntwiler, Nanostructured Magnetic Interfaces: Case Studies and New Experiment Control Software. (Ph.D. thesis), Universität Zürich, 2004.

[364] Y.M. Shi, C. Hamsen, X.T. Jia, K.K. Kim, A. Reina, M. Hofmann, A.L. Hsu, K. Zhang, H.N. Li, Z.Y. Juang, M.S. Dresselhaus, L.J. Li, J. Kong, Synthesis of few-layer hexagonal boron nitride thin film by chemical vapor deposition, Nano Lett. 10 (10) (2010) 4134–4139, https://doi.org/10.1021/nl1023707.

[365] S.K. Kim, H. Cho, M.J. Kim, H.J. Lee, J.H. Park, Y.B. Lee, H.C. Kim, C.W. Yoon, S.W. Nam, S.O. Kang, Efficient catalytic conversion of ammonia borane to borazine and its use for hexagonal boron nitride (white graphene), J. Mater. Chem. A 1 (6) (2013) 1976–1981, https://doi.org/10.1039/c2ta00758d.

[366] S. Chatterjee, Z.T. Luo, M. Acerce, D.M. Yates, A.T.C. Johnson, L.G. Sneddon, Chemical vapor deposition of boron nitride nanosheets on metallic substrates via decaborane/ammonia reactions, Chem. Mat. 23 (20) (2011) 4414–4416, https://doi.org/10.1021/cm201955v.

[367] Y.H. Lee, K.K. Liu, A.Y. Lu, C.Y. Wu, C.T. Lin, W.J. Zhang, C.Y. Su, C.L. Hsu, T.W. Lin, K.H. Wei, Y.M. Shi, L.J. Li, Growth selectivity of hexagonal-boron nitride layers on Ni with various crystal orientations, RSC Adv. 2 (1) (2012) 111–115, https://doi.org/10.1039/c1ra00703c.

[368] H. Cho, S. Park, D.I. Won, S.O. Kang, S.S. Pyo, D.I. Kim, S.M. Kim, H.C. Kim, M.J. Kim, Growth kinetics of white graphene (h-BN) on a planarised Ni foil surface, Sci. Rep. 5 (2015) 11985, https://doi.org/10.1038/srep11985.

[369] P.C. Mende, Q. Gao, A. Ismach, H. Chou, M. Widom, R. Ruoff, L. Colombo, R.M. Feenstra, Characterization of hexagonal boron nitride layers on nickel surfaces by low-energy electron microscopy, Surf. Sci. 659 (2017) 31–42, https://doi.org/10.1016/j.susc.2017.02.004.

[370] A. Ismach, H. Chou, D.A. Ferrer, Y.P. Wu, S. McDonnell, H.C. Floresca, A. Covacevich, C. Pope, R. Piner, M.J. Kim, R.M. Wallace, L. Colombo, R.S. Ruoff, Toward the controlled synthesis of hexagonal boron nitride films, ACS Nano 6 (7) (2012) 6378–6385, https://doi.org/10.1021/nn301940k.

[371] H. Oh, J. Jo, Y. Tchoe, H. Yoon, H.H. Lee, S.S. Kim, M. Kim, B.H. Sohn, G.C. Yi, Centimeter-sized epitaxial h-BN films, NPG Asia Mater 8 (2016), https://doi.org/10.1038/am.2016.178 e330.

[372] A. Ismach, H. Chou, P. Mende, A. Dolocan, R. Addou, S. Aloni, R. Wallace, R. Feenstra, R.S. Ruoff, L. Colombo, Carbon-assisted chemical vapor deposition of hexagonal boron nitride, 2D Mater. 4 (2) (2017) 025117, https://doi.org/10.1088/2053-1583/aa74a5.

[373] Y. Gao, W.C. Ren, T. Ma, Z.B. Liu, Y. Zhang, W.B. Liu, L.P. Ma, X.L. Ma, H.M. Cheng, Repeated and controlled growth of monolayer, bilayer and few-layer hexagonal boron nitride on Pt foils, ACS Nano 7 (6) (2013) 5199–5206, https://doi.org/10.1021/nn4009356.

[374] K.K. Kim, A. Hsu, X.T. Jia, S.M. Kim, Y.S. Shi, M. Hofmann, D. Nezich, J.F. Rodriguez-Nieva, M. Dresselhaus, T. Palacios, J. Kong, Synthesis of monolayer hexagonal boron nitride on Cu foil using chemical vapor deposition, Nano Lett. 12 (1) (2012) 161–166, https://doi.org/10.1021/nl203249a.

[375] K.S. Lee, Y.S. Kim, M. Tosa, A. Kasahara, K. Yosihara, Hexagonal boron nitride film substrate for fabrication of nanostructures, Appl. Surf. Sci. 169 (2001) 415–419, https://doi.org/10.1016/S0169-4332(00)00695-4.

[376] N. Guo, J.Q. Wei, L.L. Fan, Y. Jia, D.Y. Liang, H.W. Zhu, K.L. Wang, D.H. Wu, Controllable growth of triangular hexagonal boron nitride domains on copper foils by an improved low-pressure chemical vapor deposition method, Nanotechnology 23 (41) (2012) 415605, https://doi.org/10.1088/0957-4484/23/41/415605.

[377] J.C. Koepke, J.D. Wood, Y.F. Chen, S.W. Schmucker, X.M. Liu, N.N. Chang, L. Nienhaus, J.W. Do, E.A. Carrion, J. Hewaparakrama, A. Ranaarajan, I. Datye, R. Mehta, R.T. Haasch, M. Gruebele, G.S. Girolami, E. Pop, J.W. Lyding, Role of pressure in the growth of hexagonal boron nitride thin films from ammonia-borane, Chem. Mat. 28 (12) (2016) 4169–4179, https://doi.org/10.1021/acs.chemmater.6b00396.

[378] X.M. Li, Y. Li, Q. Wang, J. Yin, J.D. Li, J. Yu, W.L. Guo, Oxygen-suppressed selective growth of monolayer hexagonal boron nitride on copper twin crystals, Nano Res. 10 (3) (2017) 826–833, https://doi.org/10.1007/s12274-016-1338-9.

[379] R.Y. Tay, M.H. Griep, G. Mallick, S.H. Tsang, R.S. Singh, T. Tumlin, E.H.T. Teo, S.P. Karna, Growth of large single-crystalline two-dimensional boron nitride hexagons on electropolished copper, Nano Lett. 14 (2) (2014) 839–846, https://doi.org/10.1021/nl404207f.

[380] K.S. Lee, Y.S. Kim, M. Tosa, A. Kasahara, K. Yosihara, Mechanical properties of hexagonal boron nitride synthesized from film of Cu/BN mixture by surface segregation, Appl. Surf. Sci. 169 (2001) 420–424, https://doi.org/10.1016/S0169-4332(00)00696-6.

[381] L. Song, L.J. Ci, H. Lu, P.B. Sorokin, C.H. Jin, J. Ni, A.G. Kvashnin, D.G. Kvashnin, J. Lou, B.I. Yakobson, P.M. Ajayan, Large scale growth and characterization of atomic hexagonal boron nitride layers, Nano Lett. 10 (8) (2010) 3209–3215, https://doi.org/10.1021/nl1022139.
[382] R.Y. Tay, H.J. Park, G.H. Ryu, D.L. Tan, S.H. Tsang, H.L. Li, W.W. Liu, E.H.T. Teo, Z. Lee, Y. Lifshitz, R.S. Ruoff, Synthesis of aligned symmetrical multifaceted monolayer hexagonal boron nitride single crystals on resolidified copper, Nanoscale 8 (4) (2016) 2434–2444, https://doi.org/10.1039/c5nr08036c.
[383] X.J. Song, T. Gan, Y.F. Nie, J.N. Zhuang, J.Y. Sun, D.L. Ma, J.P. Shi, Y.W. Lin, F. Ding, Y.F. Zhang, Z.F. Liu, Seed-assisted growth of single-crystalline patterned graphene domains on hexagonal boron nitride by chemical vapor deposition, Nano Lett. 16 (10) (2016) 6109–6116, https://doi.org/10.1021/acs.nanolett.6b02279.
[384] S. Sharma, K. Sharma, M.S. Rosmi, Y. Yaakob, M.I. Araby, H. Ohtani, G. Kalita, M. Tanemura, Morphology-controlled synthesis of hexagonal boron nitride crystals by chemical vapor deposition, Cryst. Growth Des. 16 (11) (2016) 6440–6445, https://doi.org/10.1021/acs.cgd.6b01110.
[385] S. Sharma, G. Kalita, R. Vishwakarma, Z. Zulkifli, M. Tanemura, Opening of triangular hole in triangular-shaped chemical vapor deposited hexagonal boron nitride crystal, Sci. Rep. 5 (2015) 10426, https://doi.org/10.1038/srep10426.
[386] L.F. Wang, B. Wu, L.L. Jiang, J.S. Chen, Y.T. Li, W. Guo, P.G. Hu, Y.Q. Liu, Growth and etching of monolayer hexagonal boron nitride, Adv. Mater. 27 (33) (2015) 4858–4864, https://doi.org/10.1002/adma.201501166.
[387] X.F. Song, Q.G. Li, J.P. Ji, Z. Yan, Y. Gu, C.X. Huo, Y.S. Zou, C.Y. Zhi, H.B. Zeng, A comprehensive investigation on CVD growth thermokinetics of h-BN white graphene, 2D Mater. 3 (3) (2016) 035007, https://doi.org/10.1088/2053-1583/3/3/035007.
[388] J. Park, J. Lee, L. Liu, K.W. Clark, C. Durand, C. Park, B.G. Sumpter, A.P. Baddorf, A. Mohsin, M. Yoon, G. Gu, A.P. Li, Spatially resolved one-dimensional boundary states in graphene-hexagonal boron nitride planar heterostructures, Nat. Commun. 5 (2014) 5403, https://doi.org/10.1038/ncomms6403.
[389] G.E. Wood, A.J. Marsden, J.J. Mudd, M. Walker, M. Asensio, J. Avila, K. Chen, G.R. Bell, N.R. Wilson, Van der Waals epitaxy of monolayer hexagonal boron nitride on copper foil: growth, crystallography and electronic band structure, 2D Mater. 2 (2) (2015) 025003, https://doi.org/10.1088/2053-1583/2/2/025003.
[390] Y. Stehle, H.M. Meyer, R.R. Unocic, M. Kidder, G. Polizos, P.G. Datskos, R. Jackson, S.N. Smirnov, I.V. Vlassiouk, Synthesis of hexagonal boron nitride mono layer: control of nucleation and crystal morphology, Chem. Mat. 27 (23) (2015) 8041–8047, https://doi.org/10.1021/acs.chemmater.5b03607.
[391] M.H. Khan, Z.G. Huang, F. Xiao, G. Casillas, Z.X. Chen, P.J. Molino, H.K. Liu, Synthesis of large and few atomic layers of hexagonal boron nitride on melted copper, Sci. Rep. 5 (2015) 7743, https://doi.org/10.1038/srep07743.
[392] M.H. Khan, Z.G. Huang, F. Xiao, G. Casillas, Z.X. Chen, P.J. Molino, H.K. Liu, Synthesis of large and few atomic layers of hexagonal boron nitride on melted copper (vol 5, 7743, 2015), Sci. Rep. 5 (2015) 9547, https://doi.org/10.1038/srep09547.
[393] Y.Y. Stehle, X.H. Sang, R.R. Unocic, D. Voylov, R.K. Jackson, S. Smirnov, I. Vlassiouk, Anisotropic etching of hexagonal boron nitride and graphene: question of edge terminations, Nano Lett. 17 (12) (2017) 7306–7314, https://doi.org/10.1021/acs.nanolett.7b02841.
[394] J. Yin, J. Yu, X.M. Li, J.D. Li, J.X. Zhou, Z.H. Zhang, W.L. Guo, Large single-crystal hexagonal boron nitride monolayer domains with controlled morphology and straight merging boundaries, Small 11 (35) (2015) 4497–4502, https://doi.org/10.1002/smll.201500210.
[395] C.P. Wu, A.M. Soomro, F.P. Sun, H.C. Wang, Y.Y. Huang, J.J. Wu, C. Liu, X.D. Yang, N. Gao, X.H. Chen, J.Y. Kang, D.J. Cai, Large-roll growth of 25-inch hexagonal BN monolayer film for self-release buffer layer of free-standing GaN wafer, Sci. Rep. 6 (2016) 34766, https://doi.org/10.1038/srep34766.
[396] Y.X. Ji, B. Calderon, Y.M. Han, P. Cueva, N.R. Jungwirth, H.A. Alsalman, J. Hwang, G.D. Fuchs, D.A. Muller, M.G. Spencer, Chemical vapor deposition growth of large single-crystal mono-, bi-, tri-layer hexagonal boron nitride and their interlayer stacking, ACS Nano 11 (12) (2017) 12057–12066, https://doi.org/10.1021/acsnano.7b04841.
[397] R.J. Chang, X.C. Wang, S.S. Wang, Y.W. Sheng, B. Porter, H. Bhaskaran, J.H. Warner, Growth of large single-crystalline monolayer hexagonal boron nitride by oxide-assisted chemical vapor deposition, Chem. Mat. 29 (15) (2017) 6252–6260, https://doi.org/10.1021/acs.chemmater.7b01285.
[398] S. Joshi, F. Bischoff, R. Koitz, D. Ecija, K. Seufert, A.P. Seitsonen, J. Hutter, K. Diller, J.I. Urgel, H. Sachdev, J.V. Barth, W. Auwärter, Control of molecular organization and energy level alignment by an electronically nanopatterned boron nitride template, ACS Nano 8 (1) (2014) 430–442, https://doi.org/10.1021/nn406024m.
[399] R. Koitz, A.P. Seitsonen, M. Iannuzzi, J. Hutter, Structural and electronic properties of a large-scale moire pattern of hexagonal boron nitride on Cu(111) studied with density functional theory, Nanoscale 5 (12) (2013) 5589–5595, https://doi.org/10.1039/c3nr00709j.
[400] B.N. Feigelson, V.M. Bermudez, J.K. Hite, Z.R. Robinson, V.D. Wheeler, K. Sridhara, S.C. Hernandez, Growth and spectroscopic characterization of monolayer and few-layer hexagonal boron nitride on metal substrates, Nanoscale 7 (8) (2015) 3694–3702, https://doi.org/10.1039/c4nr05557h.
[401] A. Lyalin, A. Nakayama, K. Uosaki, T. Taketsugu, Adsorption and catalytic activation of the molecular oxygen on the metal supported h-BN, Top. Catal. 57 (10–13) (2014) 1032–1041, https://doi.org/10.1007/s11244-014-0267-7.
[402] S. Lin, J. Huang, X.M. Gao, A Cu(111) supported h-BN nanosheet: a potential low-cost and high-performance catalyst for CO oxidation, Phys. Chem. Chem. Phys. 17 (34) (2015) 22097–22105, https://doi.org/10.1039/c5cp03027g.
[403] J.G. Diaz, Y. Ding, R. Koitz, A.P. Seitsonen, M. Iannuzzi, J. Hutter, Hexagonal boron nitride on transition metal surfaces, Theor. Chem. Acc. 132 (4) (2013) 1350, https://doi.org/10.1007/s00214-013-1350-z.
[404] M. Bokdam, G. Brocks, P.J. Kelly, Large potential steps at weakly interacting metal-insulator interfaces, Phys. Rev. B 90 (20) (2014) 201411, https://doi.org/10.1103/PhysRevB.90.201411.
[405] R. Stania, W. Heckel, I. Kalichava, C. Bernard, T.C. Kerscher, H.Y. Cun, P.R. Willmott, B. Schönfeld, J. Osterwalder, S. Müller, T. Greber, Self-assembly of nanoscale lateral segregation profiles, Phys. Rev. B 93 (16) (2016) 161402, https://doi.org/10.1103/PhysRevB.93.161402.
[406] G.Y. Lu, T.R. Wu, Q.H. Yuan, H.S. Wang, H.M. Wang, F. Ding, X.M. Xie, M.H. Jiang, Synthesis of large single-crystal hexagonal boron nitride grains on Cu-Ni alloy, Nat. Commun. 6 (2015) 6160, https://doi.org/10.1038/ncomms7160.
[407] G.Y. Lu, T.R. Wu, H.M. Wang, P. Yang, Z.Y. Shi, C. Yang, X.M. Xie, Synthesis of continuous hexagonal boron nitride films on alloy substrate, Mater. Lett. 196 (2017) 252–255, https://doi.org/10.1016/j.matlet.2017.03.075.
[408] G.S. Hutchings, J.H. Jhang, C. Zhou, D. Hynek, U.D. Schwarz, E.I. Altman, Epitaxial Ni_xPd_{1-x}(111) alloy substrates with continuously tunable lattice constants for 2D materials growth, ACS Appl. Mater. Interfaces 9 (12) (2017) 11266–11271, https://doi.org/10.1021/acsami.7b01369.
[409] H.C. Shin, Y. Jang, T.H. Kim, J.H. Lee, D.H. Oh, S.J. Ahn, J.H. Lee, Y. Moon, J.H. Park, S.J. Yoo, C.Y. Park, D. Whang, C.W. Yang, J.R. Ahn, Epitaxial growth of a single-crystal hybridized boron nitride and graphene layer on a wide-band gap semiconductor, J. Am. Chem. Soc. 137 (21) (2015) 6897–6905, https://doi.org/10.1021/jacs.5b03151.
[410] J. Yin, X.F. Liu, W.L. Lu, J.D. Li, Y.Z. Cao, Y. Li, Y. Xu, X.M. Li, J. Zhou, C.H. Jin, W.L. Guo, Aligned growth of hexagonal boron nitride monolayer on germanium, Small 11 (40) (2015) 5375–5380, https://doi.org/10.1002/smll.201501439.
[411] Y.P. Ye, U. Graupner, R. Kruger, Hexagonal boron nitride from a borazine precursor for coating of SiBNC fibers using a continuous atmospheric pressure CVD process, Chem. Vapor Depos. 17 (7–9) (2011) 221–227, https://doi.org/10.1002/cvde.201106911.
[412] A.R. Jang, S. Hong, C. Hyun, S.I. Yoon, G. Kim, H.Y. Jeong, T.J. Shin, S.O. Park, K. Wong, S.K. Kwak, N. Park, K. Yu, E. Choi, A. Mishchenko, F. Withers, K.S. Novoselov, H. Lim, H.S. Shin, Wafer-scale and wrinkle-free epitaxial growth of single-orientated multilayer hexagonal boron nitride on sapphire, Nano Lett. 16 (5) (2016) 3360–3366, https://doi.org/10.1021/acs.nanolett.6b01051.
[413] X. Li, S. Sundaram, Y. El Gmili, T. Ayari, R. Puybaret, G. Patriarche, P.L. Voss, J.P. Salvestrini, A. Ougazzaden, Large-area two-dimensional layered hexagonal boron nitride grown on sapphire by metalorganic vapor phase epitaxy, Cryst. Growth Des. 16 (6) (2016) 3409–3415, https://doi.org/10.1021/acs.cgd.6b00398.
[414] A. Summerfield, A. Kozikoy, T.S. Cheng, A. Dayies, Y.J. Cho, A.N. Khlobystov, C.J. Mellor, C.T. Foxon, K. Watanabe, T. Taniguchi, L. Eaves, K.S. Novoseloy, S.V. Novikov, P.H. Beton, Moire-modulated conductance of hexagonal boron nitride tunnel barriers, Nano Lett. 18 (7) (2018) 4241–4246, https://doi.org/10.1021/acs.nanolett.8b01223.
[415] Z.G. Xu, A. Khanaki, H. Tian, R.J. Zheng, M. Suja, J.G. Zheng, J.L. Liu, Direct growth of hexagonal boron nitride/graphene heterostructures on cobalt foil substrates by plasma-assisted molecular beam epitaxy, Appl. Phys. Lett. 109 (4) (2016) 043110, https://doi.org/10.1063/1.4960165.
[416] J. Lu, L.C. Gomes, R.W. Nunes, A.H.C. Neto, K.P. Loh, Lattice relaxation at the interface of two-dimensional crystals: graphene and hexagonal boron-nitride, Nano Lett. 14 (9) (2014) 5133–5139, https://doi.org/10.1021/nl501900x.
[417] S.A. Shevlin, Z.X. Guo, Hydrogen sorption in defective hexagonal BN sheets and BN nanotubes, Phys. Rev. B 76 (2) (2007) 024104, https://doi.org/10.1103/PhysRevB.76.024104.
[418] S. Azevedo, J.R. Kaschny, C.M.C. de Castilho, F.D. Mota, A theoretical investigation of defects in a boron nitride monolayer, Nanotechnology 18 (49) (2007) 495707, https://doi.org/10.1088/0957-4484/18/49/495707.
[419] S. Azevedo, J.R. Kaschny, C.M.C. de Castilho, F.D. Mota, Theoretical investigation of native defects in a boron nitride monolayer, Nanotechnology 23 (48) (2012) 489501, https://doi.org/10.1088/0957-4484/23/48/489501.
[420] S. Azevedo, J.R. Kaschny, C.M.C. de Castilho, F.D. Mota, Electronic structure of defects in a boron nitride monolayer, Eur. Phys. J. B 67 (4) (2009) 507–512, https://doi.org/10.1140/epjb/e2009-00043-5.
[421] M.X. Liu, Y.F. Zhang, Z.F. Liu, Scanning tunneling microscopy study of in-plane graphene-hexagonal boron nitride heterostructures, Acta Phys. Sin. 64 (7) (2015) 078101, https://doi.org/10.7498/aps.64.078101.
[422] X.L. Li, X.J. Wu, X.C. Zeng, J.L. Yang, Band-gap engineering via tailored line defects in boron-nitride nanoribbons, sheets, and nanotubes, ACS Nano 6 (5) (2012) 4104–4112, https://doi.org/10.1021/nn300495t.
[423] Y. Sakai, S. Saito, M.L. Cohen, Electronic properties of B-C-N ternary kagome lattices, Phys. Rev. B 91 (16) (2015) 165434, https://doi.org/10.1103/PhysRevB.91.165434.
[424] Y. Fujimoto, Formation and physical properties of h-BN atomic layers: a first-principles density-functional study, Adv. Mater. Sci. Eng. (2017) 2676432, https://doi.org/10.1155/2017/2676432.
[425] M.S. Si, D.S. Xue, Magnetic properties of vacancies in a graphitic boron nitride sheet by first-principles pseudopotential calculations, Phys. Rev. B 75 (19) (2007) 193409, https://doi.org/10.1103/PhysRevB.75.193409.
[426] W. Chen, Y.F. Li, G.T. Yu, Z. Zhou, Z.F. Chen, Electronic structure and reactivity of boron nitride nanoribbons with Stone-Wales defects, J. Chem. Theory Comput. 5 (11) (2009) 3088–3095, https://doi.org/10.1021/ct900388x.

[427] Y.Y. Liu, X.L. Zou, B.I. Yakobson, Dislocations and grain boundaries in two-dimensional boron nitride, ACS Nano 6 (8) (2012) 7053–7058, https://doi.org/10.1021/nn302099q.

[428] E.C. Anota, M.S. Villanueva, H.H. Cocoletzi, Density functional theory study of lithium and fluoride doped boron nitride sheet, Phys. Status Solidi C 7 (10) (2010) 2559–2561, https://doi.org/10.1002/pssc.200983909.

[429] L.C. Gomes, S.S. Alexandre, H. Chacham, R.W. Nunes, Stability of edges and extended defects on boron nitride and graphene monolayers: the role of chemical environment, J. Phys. Chem. C 117 (22) (2013) 11770–11779, https://doi.org/10.1021/jp400420m.

[430] J.T. Obodo, K.O. Obodo, U. Schwingenschlogl, Negative differential conductance in two-dimensional C-functionalized boronitrene, New J. Phys. 17 (2015) 093012, https://doi.org/10.1088/1367-2630/17/9/093012.

[431] R. Wang, J.L. Yang, X.Z. Wu, S.F. Wang, Local charge states in hexagonal boron nitride with Stone-Wales defects, Nanoscale 8 (15) (2016) 8210–8219, https://doi.org/10.1039/c5nr09099g.

[432] E.C. Anota, R.E.R. Gutierrez, A.E. Morales, G.H. Cocoletzi, Influence of point defects on the electronic properties of boron nitride nanosheets, J. Mol. Model. 18 (5) (2012) 2175–2184, https://doi.org/10.1007/s00894-011-1233-y.

[433] M.S. Si, J.Y. Li, H.G. Shi, X.N. Niu, D.S. Xue, Divacancies in graphitic boron nitride sheets, EPL 86 (4) (2009) 46002, https://doi.org/10.1209/0295-5075/86/46002.

[434] J. Ding, D. Ahmed, H. Sun, S. Chen, Q. Yao, C. Huang, K. Deng, E. Kan, Hexagonal boron nitride–metal junction: removing the Schottky barriers by grain boundary, Adv. Theor. Simulat. 1 (9) (2018) 1800045, https://doi.org/10.1002/adts.201800045.

[435] J.C. Meyer, A. Chuvilin, G. Algara-Siller, J. Biskupek, U. Kaiser, Selective sputtering and atomic resolution imaging of atomically thin boron nitride membranes, Nano Lett. 9 (7) (2009) 2683–2689, https://doi.org/10.1021/nl9011497.

[436] A.L. Gibb, N. Alem, J.H. Chen, K.J. Erickson, J. Ciston, A. Gautam, M. Linck, A. Zettl, Atomic resolution imaging of grain boundary defects in monolayer chemical vapor deposition-grown hexagonal boron nitride, J. Am. Chem. Soc. 135 (18) (2013) 6758–6761, https://doi.org/10.1021/ja400637n.

[437] C.H. Jin, F. Lin, K. Suenaga, S. Iijima, Fabrication of a freestanding boron nitride single layer and its defect assignments, Phys. Rev. Lett. 102 (19) (2009) 195505, https://doi.org/10.1103/PhysRevLett.102.195505.

[438] O.L. Krivanek, M.F. Chisholm, V. Nicolosi, T.J. Pennycook, G.J. Corbin, N. Dellby, M.F. Murfitt, C.S. Own, Z.S. Szilagyi, M.P. Oxley, S.T. Pantelides, S.J. Pennycook, Atom-by-atom structural and chemical analysis by annular dark-field electron microscopy, Nature 464 (7288) (2010) 571–574, https://doi.org/10.1038/nature08879.

[439] O. Cretu, Y.C. Lin, K. Suenaga, Evidence for active atomic defects in monolayer hexagonal boron nitride: a new mechanism of plasticity in two-dimensional materials, Nano Lett. 14 (2) (2014) 1064–1068, https://doi.org/10.1021/nl404735w.

[440] P. Sutter, R. Cortes, J. Lahiri, E. Sutter, Interface formation in monolayer graphene-boron nitride heterostructures, Nano Lett. 12 (9) (2012) 4869–4874, https://doi.org/10.1021/nl302398m.

[441] P. Sutter, Y. Huang, E. Sutter, Nanoscale integration of two-dimensional materials by lateral heteroepitaxy, Nano Lett. 14 (8) (2014) 4846–4851, https://doi.org/10.1021/nl502110q.

[442] Y.B. Gao, Y.F. Zhang, P.C. Chen, Y.C. Li, M.X. Liu, T. Gao, D.L. Ma, Y.B. Chen, Z.H. Cheng, X.H. Qju, W.H. Duan, Z.F. Liu, Toward single-layer uniform hexagonal boron nitride-graphene patchworks with zigzag linking edges, Nano Lett. 13 (7) (2013) 3439–3443, https://doi.org/10.1021/nl4021123.

[443] J. Lu, K. Zhang, X.F. Liu, H. Zhang, T.C. Sum, A.H.C. Neto, K.P. Loh, Order-disorder transition in a two-dimensional boron-carbon-nitride alloy, Nat. Commun. 4 (2013) 2681, https://doi.org/10.1038/ncomms3681.

[444] R. Martinez-Gordillo, M. Pruneda, Polar discontinuities and 1D interfaces in monolayered materials, Prog. Surf. Sci. 90 (4) (2015) 444–463, https://doi.org/10.1016/j.progsurf.2015.08.001.

[445] H. Wang, F.C. Liu, W. Fu, Z.Y. Fang, W. Zhou, Z. Liu, Two-dimensional heterostructures: fabrication, characterization, and application, Nanoscale 6 (21) (2014) 12250–12272, https://doi.org/10.1039/c4nr03435j.

[446] Q.C. Li, M.X. Liu, Y.F. Zhang, Z.F. Liu, Hexagonal boron nitride-graphene heterostructures: synthesis and interfacial properties, Small 12 (1) (2016) 32–50, https://doi.org/10.1002/smll.201501766.

[447] Q.K. Wu, W. Wongwiriyapan, J.H. Park, S. Park, S.J. Jung, T. Jeong, S. Lee, Y.H. Lee, Y.J. Song, In situ chemical vapor deposition of graphene and hexagonal boron nitride heterostructures, Curr. Appl. Phys. 16 (9) (2016) 1175–1191, https://doi.org/10.1016/j.cap.2016.04.024.

[448] C. Sanchez-Sanchez, S. Brüller, H. Sachdev, K. Müllen, M. Krieg, H.F. Bettinger, A. Nicolai, V. Meunier, L. Talirz, R. Fasel, P. Ruffieux, On-surface synthesis of BN-substituted heteroaromatic networks, ACS Nano 9 (9) (2015) 9228–9235, https://doi.org/10.1021/acsnano.5b03895.

[449] S. Kawai, S. Nakatsuka, T. Hatakeyama, R. Pawlak, T. Meier, J. Tracey, E. Meyer, A.S. Foster, Multiple heteroatom substitution to graphene nanoribbon, Sci. Adv. 4 (2018) eaar7181.

[450] S. Beniwal, J. Hooper, D.P. Miller, P.S. Costa, G. Chen, S.Y. Liu, P.A. Dowben, E.C.H. Sykes, E. Zurek, A. Enders, Graphene-like boron-carbon-nitrogen monolayers, ACS Nano 11 (3) (2017) 2486–2493, https://doi.org/10.1021/acsnano.6b08136.

[451] K.E. Eshkalak, S. Sadeghzadeh, M. Jalaly, Mechanical properties of defective hybrid graphene-boron nitride nanosheets: a molecular dynamics study, Comput. Mater. Sci. 149 (2018) 170–181, https://doi.org/10.1016/j.commatsci.2018.03.023.

[452] S.F.L. Mertens, Copper underpotential deposition on boron nitride nanomesh, Electrochim. Acta 246 (2017) 730–736, https://doi.org/10.1016/j.electacta.2017.06.082.

[453] Y.Y. Liu, S. Bhowmick, B.I. Yakobson, BN white graphene with "colorful" edges: the energies and morphology, Nano Lett. 11 (8) (2011) 3113–3116, https://doi.org/10.1021/nl2011142.

[454] X.X. Fu, R.Q. Zhang, Energetics of hexagonal boron nitride nanostructures: edge dependence and truncation effects, Nanoscale 9 (20) (2017) 6734–6740, https://doi.org/10.1039/c7nr00933j.

[455] M. Batzill, The surface science of graphene: metal interfaces, CVD synthesis, nanoribbons, chemical modifications, and defects, Surf. Sci. Rep. 67 (3–4) (2012) 83–115, https://doi.org/10.1016/j.surfrep.2011.12.001.

[456] F. Tran, R. Laskowski, P. Blaha, K. Schwarz, Performance on molecules, surfaces, and solids of the Wu-Cohen GGA exchange-correlation energy functional, Phys. Rev. B 75 (11) (2007) 115131, https://doi.org/10.1103/PhysRevB.75.115131.

[457] J. Wintterlin, M.L. Bocquet, Graphene on metal surfaces, Surf. Sci. 603 (10–12) (2009) 1841–1852, https://doi.org/10.1016/j.susc.2008.08.037.

[458] Y. Dedkov, E. Voloshina, M. Fonin, Scanning probe microscopy and spectroscopy of graphene on metals, Phys. Status Solidi B-Basic Solid State Phys. 252 (3) (2015) 451–468, https://doi.org/10.1002/pssb.201451466.

[459] S. Grandthyll, S. Gsell, M. Weinl, M. Schreck, S. Hüfner, F. Müller, Epitaxial growth of graphene on transition metal surfaces: chemical vapor deposition versus liquid phase deposition, J. Phys.-Condes. Matter 24 (31) (2012) 314204, https://doi.org/10.1088/0953-8984/24/31/314204.

[460] J. Ducke, A. Riss, M. Garnica, W. Auwärter, Quantification of Minute Height Variations in Graphene on Cu(111) by nc-AFM, 2019 (unpublished).

[461] M. Sicot, S. Bouvron, O. Zander, U. Rüdiger, Y.S. Dedkov, M. Fonin, Nucleation and growth of nickel nanoclusters on graphene moire on Rh(111), Appl. Phys. Lett. 96 (7) (2010) 093115, https://doi.org/10.1063/1.3341176.

[462] M. Sicot, S. Bouvron, O. Zander, U. Rüdiger, Y.S. Dedkov, M. Fonin, Nucleation and growth of nickel nanoclusters on graphene moire on Rh(111), Appl. Phys. Lett. 97 (7) (2010) 079901, https://doi.org/10.1063/1.3481374.

[463] A.B. Preobrajenski, M.L. Ng, A.S. Vinogradov, N. Mårtensson, Controlling graphene corrugation on lattice-mismatched substrates, Phys. Rev. B 78 (7) (2008) 073401, https://doi.org/10.1103/PhysRevB.78.073401.

[464] Y. Dedkov, E. Voloshina, Multichannel scanning probe microscopy and spectroscopy of graphene moire structures, Phys. Chem. Chem. Phys. 16 (9) (2014) 3894–3908, https://doi.org/10.1039/c3cp54541e.

[465] L. Gao, J.R. Guest, N.P. Guisinger, Epitaxial graphene on Cu(111), Nano Lett. 10 (9) (2010) 3512–3516, https://doi.org/10.1021/nl1016706.

[466] L. Zhao, K.T. Rim, H. Zhou, R. He, T.F. Heinz, A. Pinczuk, G.W. Flynn, A.N. Pasupathy, Influence of copper crystal surface on the CVD growth of large area monolayer graphene, Solid State Commun. 151 (7) (2011) 509–513, https://doi.org/10.1016/j.ssc.2011.01.014.

[467] S.K. Hämäläinen, M. Stepanova, R. Drost, P. Liljeroth, J. Lahtinen, J. Sainio, Self-assembly of cobalt-phthalocyanine molecules on epitaxial graphene on Ir(111), J. Phys. Chem. C 116 (38) (2012) 20433–20437, https://doi.org/10.1021/jp306439h.

[468] B. Wang, M. Caffio, C. Bromley, H. Fruchtl, R. Schaub, Coupling epitaxy, chemical bonding, and work function at the local scale in transition metal-supported graphene, ACS Nano 4 (10) (2010) 5773–5782, https://doi.org/10.1021/nn101520k.

[469] M. Schwarz, D. Duncan, M. Garnica, J. Ducke, P. Deimel, P. Thakur, T.-L. Lee, F. Allegretti, W. Auwärter, Quantitative determination of a model organic/insulator/metal interface structure, Nanoscale 10 (2018) 21971–21977, https://doi.org/10.1039/C8NR06387G.

[470] B. Gumhalter, K. Hermann, K. Wandelt, Lateral surface Stark-effect in chemisorbed molecules, Vacuum 41 (1–3) (1990) 192–194, https://doi.org/10.1016/0042-207X(90)90306-J.

[471] M. Neek-Amal, J. Beheshtian, A. Sadeghi, K.H. Michel, F.M. Peeters, Boron nitride mono layer: a strain-tunable nanosensor, J. Phys. Chem. C 117 (25) (2013) 13261–13267, https://doi.org/10.1021/jp402122c.

[472] Y. Fujimoto, T. Koretsune, S. Saito, Electronic structures of hexagonal boron-nitride monolayer: strain-induced effects, J. Ceram. Soc. Jpn. 122 (1425) (2014) 346–348.

[473] G.N. Derry, M.E. Kern, E.H. Worth, Recommended values of clean metal surface work functions, J. Vac. Sci. Technol. A 33 (6) (2015) 060801, https://doi.org/10.1116/1.4934685.

[474] J. Felter, M. Franke, C. Kumpf, In-situ LEEM Investigation of the Growth of Hexagonal Boron Nitride on Metal Surfaces, DPG Verhandlungen, 2017. DPG Frühjahrstagung.

[475] A. Fedorov, C.S. Praveen, N.I. Verbitskiy, D. Haberer, D. Usachov, D.V. Vyalikh, A. Nefedov, C. Wöll, L. Petaccia, S. Piccinin, H. Sachdev, M. Knupfer, B. Büchner, S. Fabris, A. Grüneis, Efficient gating of epitaxial boron nitride monolayers by substrate functionalization, Phys. Rev. B 92 (12) (2015) 125440, https://doi.org/10.1103/PhysRevB.92.125440.

[476] H. Henck, D. Pierucci, G. Fugallo, J. Avila, G. Cassabois, Y.J. Dappe, M.G. Silly, C.Y. Chen, B. Gil, M. Gatti, F. Sottile, F. Sirotti, M.C. Asensio, A. Ouerghi, Direct observation of the band structure in bulk hexagonal boron nitride, Phys. Rev. B 95 (8) (2017) 085410, https://doi.org/10.1103/PhysRevB.95.085410.

[477] I. Swart, T. Sonnleitner, J. Repp, Charge state control of molecules reveals modification of the tunneling barrier with intramolecular contrast, Nano Lett. 11 (4) (2011) 1580–1584, https://doi.org/10.1021/nl104452x.

[478] Z.Y. Zheng, M. Cox, B. Li, Surface modification of hexagonal boron nitride nanomaterials: a review, J. Mater. Sci. 53 (1) (2018) 66–99, https://doi.org/10.1007/s10853-017-1472-0.

[479] N.B. Hannay, T.H. Geballe, B.T. Matthias, K. Andres, P. Schmidt, D. Macnair, Superconductivity in graphitic compounds, Phys. Rev. Lett. 14 (7) (1965) 225, https://doi.org/10.1103/PhysRevLett.14.225.

[480] T.E. Weller, M. Ellerby, S.S. Saxena, R.P. Smith, N.T. Skipper, Superconductivity in the intercalated graphite compounds C_6Yb and C_6Ca, Nat. Phys. 1 (1) (2005) 39–41, https://doi.org/10.1038/nphys0010.

[481] C.P. Shen, S.G. Mayorga, R. Biagioni, C. Piskoti, M. Ishigami, A. Zettl, N. Bartlett, Intercalation of hexagonal boron nitride by strong oxidizers and evidence for the metallic nature of the products, J. Solid State Chem. 147 (1) (1999) 74–81, https://doi.org/10.1006/jssc.1999.8176.

[482] E. Budak, C. Bozkurt, The effect of transition metals on the structure of h-BN intercalation compounds, J. Solid State Chem. 177 (4–5) (2004) 1768–1770, https://doi.org/10.1016/j.jssc.2003.12.038.

[483] A. Sumiyoshi, H. Hyodo, K. Kimura, Li-intercalation into hexagonal boron nitride, J. Phys. Chem. Solids 71 (4) (2010) 569–571, https://doi.org/10.1016/j.jpcs.2009.12.038.

[484] S. Ross, W.W. Pultz, On physical adsorption: X. Adsorbed monolayers of argon and nitrogen on boron nitride and on a graded series of partially graphitized carbon blacks, J. Colloid Sci. 13 (4) (1958) 397–406.

[485] R.A. Pierotti, J.C. Petriccianni, The interaction of argon with hexagonal boron nitride, J. Phys. Chem. 64 (10) (1960) 1596–1597, https://doi.org/10.1021/j100839a518.

[486] H.E. Thomas, R.N. Ramsey, R.A. Pierotti, Physical adsorption of argon on boron-nitride. A two-surface analysis of high-temperature adsorption data, J. Chem. Phys. 59 (11) (1973) 6163–6170, https://doi.org/10.1063/1.1679986.

[487] A.C. Levy, T.R. Rybolt, R.A. Pierotti, High-temperature physical adsorption of argon, krypton, and xenon on hexagonal boron-nitride, J. Colloid Interface Sci. 70 (1) (1979) 74–82, https://doi.org/10.1016/0021-9797(79)90009-2.

[488] A. Diama, A.D. Migone, Multilayer Kr films adsorbed on BN, Phys. Rev. B 60 (23) (1999) 16103–16108, https://doi.org/10.1103/PhysRevB.60.16103.

[489] W. Li, P. Shrestha, A.D. Migone, A. Marmier, C. Girardet, Monolayer Kr films adsorbed on BN, Phys. Rev. B 54 (12) (1996) 8833–8843, https://doi.org/10.1103/PhysRevB.54.8833.

[490] A.D. Migone, M.T. Alkhafaji, G. Vidali, M. Karimi, Thermodynamic study of argon films adsorbed on boron-nitride, Phys. Rev. B 47 (11) (1993) 6685–6696, https://doi.org/10.1103/PhysRevB.47.6685.

[491] P. Shrestha, M.T. Alkhafaji, M.M. Lukowitz, G.L. Yang, A.D. Migone, Adsorption studies on boron-nitride substrates, Langmuir 10 (9) (1994) 3244–3249, https://doi.org/10.1021/la00021a056.

[492] K. Morishige, K. Inoue, K. Imai, X-ray study of Kr, Xe, and N_2 monolayers on boron nitride, Langmuir 12 (20) (1996) 4889–4891, https://doi.org/10.1021/la960354x.

[493] B. Kiraly, E.V. Iski, A.J. Mannix, B.L. Fisher, M.C. Hersam, N.P. Guisinger, Solid-source growth and atomic-scale characterization of graphene on Ag(111), Nat. Commun. 4 (2013) 2804, https://doi.org/10.1038/ncomms3804.

[494] Y.Q. He, M. Garnica, F. Bischoff, J. Ducke, M.L. Bocquet, M. Batzill, W. Auwärter, J.V. Barth, Fusing tetrapyrroles to graphene edges by surface-assisted covalent coupling, Nat. Chem. 9 (1) (2017) 33–38, https://doi.org/10.1038/NCHEM.2600.

[495] C. Brun, K.H. Müller, I.P. Hong, F. Patthey, C. Flindt, W.D. Schneider, Dynamical coulomb blockade observed in nanosized electrical contacts, Phys. Rev. Lett. 108 (12) (2012) 126802, https://doi.org/10.1103/PhysRevLett.108.126802.

[496] L.H. de Lima, H.Y. Cun, A. Hemmi, T. Kälin, T. Greber, Note: an ion source for alkali metal implantation beneath graphene and hexagonal boron nitride monolayers on transition metals, Rev. Sci. Instrum. 84 (12) (2013) 126104, https://doi.org/10.1063/1.4848936.

[497] H. Cun, A. Spescha, A. Schuler, M. Hengsberger, J. Osterwalder, T. Greber, Characterization of a cold cathode penning ion source for the implantation of noble gases beneath 2D monolayers on metals: ions and neutrals, J. Vac. Sci. Technol. A 34 (2) (2016) 020602, https://doi.org/10.1116/1.4939507.

[498] K.A. Simonov, N.A. Vinogradov, M.L. Ng, A.S. Vinogradov, N. Mårtensson, A.B. Preobrajenski, Controllable oxidation of h-BN monolayer on Ir(111) studied by core-level spectroscopies, Surf. Sci. 606 (3–4) (2012) 564–570, https://doi.org/10.1016/j.susc.2011.11.031.

[499] I. Brihuega, C.H. Michaelis, J. Zhang, S. Bose, V. Sessi, J. Honolka, M.A. Schneider, A. Enders, K. Kern, Electronic decoupling and templating of Co nanocluster arrays on the boron nitride nanomesh, Surf. Sci. 602 (14) (2008) L95–L99, https://doi.org/10.1016/j.susc.2008.04.040.

[500] I. Brihuega, A.M. Garcia-Garcia, P. Ribeiro, M.M. Ugeda, C.H. Michaelis, S. Bose, K. Kern, Experimental observation of thermal fluctuations in single superconducting Pb nanoparticles through tunneling measurements, Phys. Rev. B 84 (10) (2011) 104525, https://doi.org/10.1103/PhysRevB.84.104525.

[501] S. Bose, A.M. Garcia-Garcia, M.M. Ugeda, J.D. Urbina, C.H. Michaelis, I. Brihuega, K. Kern, Observation of shell effects in superconducting nanoparticles of Sn, Nat. Mater. 9 (7) (2010) 550–554, https://doi.org/10.1038/NMAT2768.

[502] Y. Fukamori, M. König, B. Yoon, B. Wang, F. Esch, U. Heiz, U. Landman, Fundamental insight into the substrate-dependent ripening of monodisperse clusters, ChemCatChem 5 (11) (2013) 3330–3341, https://doi.org/10.1002/cctc.201300250.

[503] G.C. Loh, S. Nigam, G. Mallick, R. Pandey, Carbon-doped boron nitride nanomesh: stability and electronic properties of adsorbed hydrogen and oxygen, J. Phys. Chem. C 118 (41) (2014) 23888–23896, https://doi.org/10.1021/jp508229w.

[504] Y.B. Hwang, Y.C. Chung, Comparative study of metal atom adsorption on free-standing h-BN and h-BN/Ni (111) surfaces, Appl. Surf. Sci. 299 (2014) 29–34, https://doi.org/10.1016/j.apsusc.2014.01.172.

[505] Y.F. Guo, W.L. Guo, Hydroxylation of a metal-supported hexagonal boron nitride monolayer by oxygen induced water dissociation, Phys. Chem. Chem. Phys. 17 (25) (2015) 16428–16433, https://doi.org/10.1039/c5cp02494c.

[506] Y.F. Guo, W.L. Guo, Insulating to metallic transition of an oxidized boron nitride nanosheet coating by tuning surface oxygen adsorption, Nanoscale 6 (7) (2014) 3731–3736, https://doi.org/10.1039/c3nr06227a.

[507] S. Rose, P. Nemes-Incze, M. Pratzer, V. Caciuc, N. Atodiresei, M. Morgenstern, One-dimensional Si Chains Embedded in Pt(111) and Protected by a Hexagonal Boron-Nitride Monolayer, 2018, arXiv:1806.02174v1.

[508] H.Y. Cun, M. Iannuzzi, A. Hemmi, S. Roth, J. Osterwalder, T. Greber, Immobilizing individual atoms beneath a corrugated single layer of boron nitride, Nano Lett. 13 (5) (2013) 2098–2103, https://doi.org/10.1021/nl400449y.

[509] H.Y. Cun, M. Iannuzzi, A. Hemmi, J. Osterwalder, T. Greber, Implantation length and thermal stability of interstitial Ar atoms in boron nitride nanotents, ACS Nano 8 (1) (2014) 1014–1021, https://doi.org/10.1021/nn405907a.

[510] M. Iannuzzi, Ar implantation at the hBN/Rh(111) nanomesh by ab Initio molecular dynamics, J. Phys. Chem. C 119 (38) (2015) 22198–22207, https://doi.org/10.1021/acs.jpcc.5b06774.

[511] F.D. Natterer, F. Patthey, H. Brune, Quantifying residual hydrogen adsorption in low-temperature STMs, Surf. Sci. 615 (2013) 80–87, https://doi.org/10.1016/j.susc.2013.04.008.

[512] F.D. Natterer, F. Patthey, H. Brune, Ring state for single transition metal atoms on boron nitride on Rh(111), Phys. Rev. Lett. 109 (6) (2012) 066101, https://doi.org/10.1103/PhysRevLett.109.066101.

[513] Y. Zhang, Y.F. Zhang, D.L. Ma, Q.Q. Ji, W. Fang, J.P. Shi, T. Gao, M.X. Liu, Y.B. Gao, Y.B. Chen, L.M. Xu, Z.F. Liu, Mn atomic layers under inert covers of graphene and hexagonal boron nitride prepared on Rh(111), Nano Res. 6 (12) (2013) 887–896, https://doi.org/10.1007/s12274-013-0365-z.

[514] O.V. Yazyev, A. Pasquarello, Metal adatoms on graphene and hexagonal boron nitride: towards rational design of self-assembly templates, Phys. Rev. B 82 (4) (2010) 045407, https://doi.org/10.1103/PhysRevB.82.045407.

[515] P. Jacobson, T. Herden, M. Muenks, G. Laskin, O. Brovko, V. Stepanyuk, M. Ternes, K. Kern, Quantum engineering of spin and anisotropy in magnetic molecular junctions, Nat. Commun. 6 (2015) 8536, https://doi.org/10.1038/ncomms9536.

[516] F.L. Wu, D.L. Huang, Y. Yue, L. Liu, Template growth of Au, Ni and Ni-Au nanoclusters on hexagonal boron nitride/Rh(111): a combined STM, TPD and AES study, RSC Adv. 7 (70) (2017) 44169–44177, https://doi.org/10.1039/c7ra08880a.

[517] W.C. McKee, M.C. Patterson, J.R. Frick, P.T. Sprunger, Y. Xu, Adsorption of transition metal adatoms on h-BN/Rh(111): implications for nanocluster self-assembly, Catal. Today 280 (2017) 220–231, https://doi.org/10.1016/j.cattod.2016.09.030.

[518] C. Morchutt, J. Björk, S. Krotzky, R. Gutzler, K. Kern, Covalent coupling via dehalogenation on Ni(111) supported boron nitride and graphene, Chem. Commun. 51 (12) (2015) 2440–2443, https://doi.org/10.1039/c4cc07107g.

[519] A. Goriachko, H. Over, Modern nanotemplates based on graphene and single layer h-BN, Z. Phys. Chemie 223 (1–2) (2009) 157–168, https://doi.org/10.1524/zpch.2009.6030.

[520] R. Widmer, D. Passerone, T. Mattle, H. Sachdev, O. Gröning, Probing the selectivity of a nanostructured surface by xenon adsorption, Nanoscale 2 (4) (2010) 502–508, https://doi.org/10.1039/b9nr00431a.

[521] P. Valerius, C. Herbig, M. Will, M.A. Arman, J. Knudsen, V. Caciuc, N. Atodiresei, T. Michely, Annealing of ion-irradiated hexagonal boron nitride on Ir(111), Phys. Rev. B 96 (23) (2017) 235410, https://doi.org/10.1103/PhysRevB.96.235410.

[522] A. Goriachko, A.A. Zakharov, H. Over, Oxygen-etching of h-BN/Ru(0001) nanomesh on the nano- and mesoscopic scale, J. Phys. Chem. C 112 (28) (2008) 10423–10427, https://doi.org/10.1021/jp802359u.

[523] B. Wang, M.L. Bocquet, Monolayer graphene and h-BN on metal substrates as versatile templates for metallic nanoclusters, J. Phys. Chem. Lett. 2 (18) (2011) 2341–2345, https://doi.org/10.1021/jz201047c.

[524] M.L. Ng, A.B. Preobrajenski, A.S. Vinogradov, N. Mårtensson, Formation and temperature evolution of Au nanoparticles supported on the h-BN nanomesh, Surf. Sci. 602 (6) (2008) 1250–1255, https://doi.org/10.1016/j.susc.2008.01.028.

[525] H.P. Koch, R. Laskowski, P. Blaha, K. Schwarz, Adsorption of gold atoms on the h-BN/Rh(111) nanomesh, Phys. Rev. B 84 (24) (2011) 245410, https://doi.org/10.1103/PhysRevB.84.245410.

[526] W.C. McKee, M.C. Patterson, D. Huang, J.R. Frick, R.L. Kurtz, P.T. Sprunger, L. Liu, Y. Xu, CO adsorption on Au nanoparticles grown on hexagonal boron nitride/Rh(111), J. Phys. Chem. C 120 (20) (2016) 10909–10918, https://doi.org/10.1021/acs.jpcc.6b01645.

[527] H.P. Koch, R. Laskowski, P. Blaha, K. Schwarz, Adsorption of small gold clusters on the h-BN/Rh(111) nanomesh, Phys. Rev. B 86 (15) (2012) 155404, https://doi.org/10.1103/PhysRevB.86.155404.

[528] G. Elumalai, H. Noguchi, A. Lyalin, T. Taketsugu, K. Uosaki, Gold nanoparticle decoration of insulating boron nitride nanosheet on inert gold electrode toward an efficient electrocatalyst for the reduction of oxygen to water, Electrochem. Commun. 66 (2016) 53–57, https://doi.org/10.1016/j.elecom.2016.02.021.

[529] J. Osterwalder, W. Auwärter, M. Muntwiler, T. Greber, Growth morphologies and defect structure in hexagonal boron nitride films on Ni(111): a combined STM and XPD study, e-J. Surf. Sci. Nanotech. 1 (2003) 124.

[530] V.M. Karpan, P.A. Khomyakov, G. Giovannetti, A.A. Starikov, P.J. Kelly, Ni(111) | graphene | h-BN junctions as ideal spin injectors, Phys. Rev. B 84 (15) (2011) 153406, https://doi.org/10.1103/PhysRevB.84.153406.

[531] Y.P. Wang, X.G. Zhang, J.N. Fry, H.P. Cheng, Comparative investigation of electronic transport across three-dimensional nanojunctions, Phys. Rev. B 95 (8) (2017) 085303, https://doi.org/10.1103/PhysRevB.95.085303.

[532] F. Oba, A. Togo, I. Tanaka, K. Watanabe, T. Taniguchi, Doping of hexagonal boron nitride via intercalation: a theoretical prediction, Phys. Rev. B 81 (7) (2010) 075125, https://doi.org/10.1103/PhysRevB.81.075125.

[533] F.D. Natterer, Graphene and Boron Nitride Monolayers on Close-Packed Metal Surfaces: Growth and Interaction with Transition Metal Atoms. (Ph.D. thesis), EPFL, 2013.

[534] P. Jacobson, M. Muenks, G. Laskin, O. Brovko, V. Stepanyuk, M. Ternes, K. Kern, Potential energy-driven spin manipulation via a controllable hydrogen ligand, Sci. Adv. 3 (4) (2017), https://doi.org/10.1126/sciadv.1602060 e1602060–e1602060.

[535] A. Farkas, A. Ádám, G. Vári, R. Gubó, L. Óvári, A. Berkó, J. Kiss, Z. Kónya, Effect of gold on the adsorption properties of acetaldehyde on clean and h-BN covered Rh(111) surface, Top. Catal. (2018), https://doi.org/10.1007/s11244-018-0979-1.

[536] M. Gao, A. Lyalin, T. Taketsugu, Catalytic activity of Au and Au_2 on the h-BN surface: adsorption and activation of O_2, J. Phys. Chem. C 116 (16) (2012) 9054–9062, https://doi.org/10.1021/jp300684v.

[537] K.K. Mao, L. Li, W.H. Zhang, Y. Pei, X.C. Zeng, X.J. Wu, J.L. Yang, A theoretical study of single-atom catalysis of CO oxidation using Au embedded 2D h-BN monolayer: a CO-promoted O_2 activation, Sci. Rep. 4 (2014) 5441, https://doi.org/10.1038/srep05441.

[538] J. Zhang, V. Sessi, C.H. Michaelis, I. Brihuega, J. Honolka, K. Kern, R. Skomski, X. Chen, G. Rojas, A. Enders, Ordered layers of Co clusters on BN template layers, Phys. Rev. B 78 (16) (2008) 165430, https://doi.org/10.1103/PhysRevB.78.165430.

[539] P. Bacle, A.P. Seitsonen, M. Iannuzzi, J. Hutter, Chemical reactions on metal-supported hexagonal boron nitride investigated with density functional theory, Chimia 68 (9) (2014) 596–601, https://doi.org/10.2533/chimia.2014.596.

[540] H.Y. Cun, M. Iannuzzi, A. Hemmi, J. Osterwalder, T. Greber, Ar implantation beneath graphene on Ru(0001): nanotents and "can-opener" effect, Surf. Sci. 634 (2015) 95–102, https://doi.org/10.1016/j.susc.2014.11.004.

[541] H. Cun, M. Iannuzzi, A. Hemmi, J. Osterwalder, T. Greber, Two-nanometer voids in single-layer hexagonal boron nitride: formation via the "can-opener" effect and annihilation by self-healing, ACS Nano 8 (7) (2014) 7423–7431, https://doi.org/10.1021/nn502645w.

[542] M.V. Serzhantova, A.A. Kuzubov, A.S. Fedorov, P.O. Krasnov, F.N. Tomilin, Theoretical study of the influence of vacancies on the electronic structure of a hexagonal boron nitride monolayer, J. Exp. Theor. Phys. 112 (4) (2011) 664–667, https://doi.org/10.1134/S1063776111030150.

[543] A. Lyalin, M. Gao, T. Taketsugu, When inert becomes active: a fascinating route for catalyst design, Chem. Rec. 16 (5) (2016) 2324–2337, https://doi.org/10.1002/tcr.201600035.

[544] C.R. Henry, 2D-arrays of nanoparticles as model catalysts, Catal. Lett. 145 (3) (2015) 731–749, https://doi.org/10.1007/s10562-014-1402-6.

[545] O.V. Yazyev, A. Pasquarello, Magnetoresistive junctions based on epitaxial graphene and hexagonal boron nitride, Phys. Rev. B 80 (3) (2009) 035408, https://doi.org/10.1103/PhysRevB.80.035408.

[546] M. Turner, V.B. Golovko, O.P.H. Vaughan, P. Abdulkin, A. Berenguer-Murcia, M.S. Tikhov, B.F.G. Johnson, R.M. Lambert, Selective oxidation with dioxygen by gold nanoparticle catalysts derived from 55-atom clusters, Nature 454 (7207) (2008), https://doi.org/10.1038/nature07194 981–U31.

[547] Z.H. Zhou, F. Gao, D.W. Goodman, Deposition of metal clusters on single-layer graphene/Ru(0001): factors that govern cluster growth, Surf. Sci. 604 (13–14) (2010), https://doi.org/10.1016/j.susc.2010.03.008 1071–L38.

[548] A.T. N'Diaye, T. Gerber, C. Busse, J. Myslivecek, J. Coraux, T. Michely, A versatile fabrication method for cluster superlattices, New J. Phys. 11 (2009) 103045, https://doi.org/10.1088/1367-2630/11/10/103045.

[549] A.T. N'Diaye, S. Bleikamp, P.J. Feibelman, T. Michely, Two-dimensional Ir cluster lattice on a graphene moire on Ir(111), Phys. Rev. Lett. 97 (21) (2006) 215501, https://doi.org/10.1103/PhysRevLett.97.215501.

[550] Q.R. Fu, Y. Meng, Z.L. Fang, Q.Q. Hu, L. Xu, W.H. Gao, X.C. Huang, Q. Xue, Y.P. Sun, F.S. Lu, Boron nitride nanosheet-anchored Pd-Fe core-shell nanoparticles as highly efficient catalysts for Suzuki-Miyaura coupling reactions, ACS Appl. Mater. Interfaces 9 (3) (2017) 2469–2476, https://doi.org/10.1021/acsami.6b13570.

[551] D. Golze, J. Hutter, M. Iannuzzi, Wetting of water on hexagonal boron nitride@Rh(111): a QM/MM model based on atomic charges derived for nanostructured substrates, Phys. Chem. Chem. Phys. 17 (22) (2015) 14307–14316, https://doi.org/10.1039/c4cp04638b.

[552] J.Q. Zhong, M.G. Wang, N. Akter, J.D. Kestell, A.M. Boscoboinik, T.J. Kim, D.J. Stacchiola, D.Y. Lu, J.A. Boscoboinik, Immobilization of single argon atoms in nano-cages of two-dimensional zeolite model systems, Nat. Commun. 8 (2017) 16118, https://doi.org/10.1038/ncomms16118.

[553] J. Yang, D. Kim, J. Hong, Potential room temperature ferromagnetic O/BN and F/BN bilayers, J. Phys.-Condes. Matter 23 (6) (2011) 066001, https://doi.org/10.1088/0953-8984/23/6/066001.

[554] J. Zhou, Q. Wang, Q. Sun, P. Jena, Electronic and magnetic properties of a BN sheet decorated with hydrogen and fluorine, Phys. Rev. B 81 (8) (2010) 085442, https://doi.org/10.1103/PhysRevB.81.085442.

[555] Y.G. Zhou, X.T. Zu, P. Yang, H.Y. Xiao, F. Gao, Oxygen-induced magnetic properties and metallic behavior of a BN sheet, J. Phys.-Condes. Matter 22 (46) (2010) 465303, https://doi.org/10.1088/0953-8984/22/46/465303.

[556] Y. Zhao, X.J. Wu, J.L. Yang, X.C. Zeng, Oxidation of a two-dimensional hexagonal boron nitride monolayer: a first-principles study, Phys. Chem. Chem. Phys. 14 (16) (2012) 5545–5550, https://doi.org/10.1039/c2cp40081b.

[557] C. Ataca, S. Ciraci, Functionalization of BN honeycomb structure by adsorption and substitution of foreign atoms, Phys. Rev. B 82 (16) (2010) 165402, https://doi.org/10.1103/PhysRevB.82.165402.

[558] R. Ponce-Perez, G.H. Cocoletzi, Hydrogenated boron nitride monolayer functionalization: a density functional theory study, Comput. Theor. Chem. 1111 (2017) 33–39, https://doi.org/10.1016/j.comptc.2017.04.008.

[559] S.H. Li, J.M. Yuan, Y.W. Hu, J.X. Zhong, Y.L. Mao, Engineering by Mn embedment and adsorption in defective boron nitrogen sheet, Physica E 56 (2014) 24–31, https://doi.org/10.1016/j.physe.2013.08.006.

[560] Y.M. Ding, J.J. Shi, M. Zhang, X.H. Jiang, H.X. Zhong, P. Huang, M. Wu, X. Cao, Improvement of n-type conductivity in hexagonal boron nitride monolayers by doping, strain and adsorption, RSC Adv. 6 (35) (2016) 29190–29196, https://doi.org/10.1039/c5ra25141a.

[561] L. Weston, D. Wickramaratne, C.G. Van de Walle, Hole polarons and p-type doping in boron nitride polymorphs, Phys. Rev. B 96 (10) (2017) 100102, https://doi.org/10.1103/PhysRevB.96.100102.

[562] L. Weston, D. Wickramaratne, C.G. Van de Walle, Hole polarons and p-type doping in boron nitride polymorphs, Phys. Rev. B 97 (1) (2018) 019908, https://doi.org/10.1103/PhysRevB.97.019908.

[563] M. Sagynbaeva, T. Hussain, P. Panigrahi, B. Johansson, R. Ahuja, Complementing the adsorption energies of CO_2, H_2S and NO_2 to h-BN sheets by doping with carbon, EPL 109 (5) (2015) 57008, https://doi.org/10.1209/0295-5075/109/57008.

[564] M. Gao, M. Adachi, A. Lyalin, T. Taketsugu, Long range functionalization of h-BN monolayer by carbon doping, J. Phys. Chem. C 120 (29) (2016) 15993–16001, https://doi.org/10.1021/acs.jpcc.5b12706.

[565] R. Muhammad, Y. Shuai, H.P. Tan, A first-principles study on alkaline earth metal atom substituted monolayer boron nitride (BN), J. Mater. Chem. C 5 (32) (2017) 8112–8127, https://doi.org/10.1039/c7tc02894f.

[566] Q.H. Weng, D.G. Kvashnin, X. Wang, O. Cretu, Y. Yang, M. Zhou, C. Zhang, D.M. Tang, P.B. Sorokin, Y. Bando, D. Golberg, Tuning of the optical, electronic, and magnetic properties of boron nitride nanosheets with oxygen doping and functionalization, Adv. Mater. 29 (28) (2017) 1700695, https://doi.org/10.1002/adma.201700695.

[567] S. Elahi, S. Valedbaigi, Aluminum and vacancy defects on electronic and magnetic properties of BN sheet: a density functional theory study, Fuller. Nanotub. Carbon Nanostruct. 23 (2) (2015) 113–119, https://doi.org/10.1080/1536383X.2013.787597.

[568] A.A. Darwish, M.M. Fadlallah, A. Badawi, A.A. Maarouf, Adsorption of sugars on Al- and Ga-doped boron nitride surfaces: a computational study, Appl. Surf. Sci. 377 (2016) 9–16, https://doi.org/10.1016/j.apsusc.2016.03.082.

[569] J. Castro-Medina, D. Garcia-Toral, M. Lopez-Fuentes, A. Sanchez-Castillo, S. Torres-Morales, L.M. de la Garza, G.H. Cocoletzi, Thymine adsorption on two-dimensional boron nitride structures: first-principles studies, J. Mol. Model. 23 (4) (2017) 109, https://doi.org/10.1007/s00894-017-3280-5.

[570] J.J. Meng, D. Li, Y. Niu, H.M. Zhao, C.J. Liang, Z.Q. He, Structural, electronic, and magnetic properties of 3D metal trioxide and tetraoxide superhalogen cluster-doped monolayer BN, Phys. Lett. A 380 (29–30) (2016) 2300–2306, https://doi.org/10.1016/j.physleta.2016.04.042.

[571] J.J. He, N. Jiao, C.X. Zhang, H.P. Xiao, X.S. Chen, L.Z. Sun, Spin switch of the transition-metal-doped boron nitride sheet through H/F chemical decoration, J. Phys. Chem. C 118 (17) (2014) 8899–8906, https://doi.org/10.1021/jp410716q.

[572] T.L. Mitran, A. Nicolaev, G.A. Nemnes, L. Ion, S. Antohe, Magnetic behavior and clustering effects in Mn-doped boron nitride sheets, J. Phys.-Condes. Matter 24 (32) (2012) 326003, https://doi.org/10.1088/0953-8984/24/32/326003.

[573] S. Lin, X.X. Ye, R.S. Johnson, H. Guo, First-principles investigations of metal (Cu, Ag, Au, Pt, Rh, Pd, Fe, Co, and Ir) doped hexagonal boron nitride nanosheets: stability and catalysis of CO oxidation, J. Phys. Chem. C 117 (33) (2013) 17319–17326, https://doi.org/10.1021/jp4055445.

[574] D. Farmanzadeh, N.A. Ardehjani, Theoretical study of ozone adsorption on the surface of Fe, Co and Ni doped boron nitride nanosheets, Appl. Surf. Sci. 444 (2018) 642–649, https://doi.org/10.1016/j.apsusc.2018.02.253.

[575] Z.S. Lu, P. Lv, Y.L. Liang, D.W. Ma, Y. Zhang, W.J. Zhang, X.W. Yang, Z.X. Yang, CO oxidation catalyzed by the single Co atom embedded hexagonal boron nitride nanosheet: a DFT-D study, Phys. Chem. Chem. Phys. 18 (31) (2016) 21865–21870, https://doi.org/10.1039/c6cp02221a.

[576] A. Taherpour, Z. Shahri, O. Rezaei, M. Jamshidi, T. Fellowes, Adsorption, intercalation and sensing of helium on yttrium functionalized open edge boron nitride: a first principle DFT and TDDFT study, Chem. Phys. Lett. 691 (2018) 231–237, https://doi.org/10.1016/j.cplett.2017.11.033.

[577] J.X. Zhao, Z.F. Chen, Single Mo atom supported on defective boron nitride monolayer as an efficient electrocatalyst for nitrogen fixation: a computational study, J. Am. Chem. Soc. 139 (36) (2017) 12480–12487, https://doi.org/10.1021/jacs.7b05213.

[578] C.J. Huang, X.X. Ye, C. Chen, S. Lin, D.Q. Xie, A computational investigation of CO oxidation on ruthenium-embedded hexagonal boron nitride nanosheet, Comput. Theor. Chem. 1011 (2013) 5–10, https://doi.org/10.1016/j.comptc.2013.02.004.

[579] M.D. Esrafili, S. Asadollahi, A single Pd atom stabilized on boron-vacancy of h-BN nanosheet: a promising catalyst for CO oxidation, ChemistrySelect 3 (32) (2018) 9181–9188, https://doi.org/10.1002/slct.201801848.

[580] Z.S. Lu, P. Lv, Z.X. Yang, S. Li, D.W. Ma, R.Q. Wu, A promising single atom catalyst for CO oxidation: Ag on boron vacancies of h-BN sheets, Phys. Chem. Chem. Phys. 19 (25) (2017) 16795–16805, https://doi.org/10.1039/c7cp02430d.

[581] M. Gao, A. Lyalin, T. Taketsugu, Oxygen activation and dissociation on h-BN supported Au atoms, Int. J. Quantum Chem. 113 (4) (2013) 443–452, https://doi.org/10.1002/qua.24066.
[582] B. Huang, H.J. Xiang, J.J. Yu, S.H. Wei, Effective control of the charge and magnetic states of transition-metal atoms on single-layer boron nitride, Phys. Rev. Lett. 108 (20) (2012) 206802, https://doi.org/10.1103/PhysRevLett.108.206802.
[583] Y.L. Wang, Electronic properties of two-dimensional hydrogenated and semihydrogenated hexagonal boron nitride sheets, Phys. Status Solidi-Rapid Res. Lett. 4 (1–2) (2010) 34–36, https://doi.org/10.1002/pssr.200903374.
[584] S.B. Tang, Z.X. Cao, Structural and electronic properties of the fully hydrogenated boron nitride sheets and nanoribbons: insight from first-principles calculations, Chem. Phys. Lett. 488 (1–3) (2010) 67–72, https://doi.org/10.1016/j.cplett.2010.01.073.
[585] J.M.H. Kroes, A. Fasolino, M.I. Katsnelson, Energetics, barriers and vibrational spectra of partially and fully hydrogenated hexagonal boron nitride, Phys. Chem. Chem. Phys. 18 (28) (2016) 19359–19367, https://doi.org/10.1039/c6cp01018k.
[586] J.M.H. Kroes, A. Fasolino, M.I. Katsnelson, Energetics, barriers and vibrational spectra of partially and fully hydrogenated hexagonal boron nitride, Phys. Chem. Chem. Phys. 19 (16) (2017) 10698, https://doi.org/10.1039/c7cp90075a.
[587] X.X. Li, J. Zhao, J.L. Yang, Semihydrogenated BN sheet: a promising visible-light driven photocatalyst for water splitting, Sci. Rep. 3 (2013) 1858, https://doi.org/10.1038/srep01858.
[588] B. Marlid, K. Larsson, J.O. Carlsson, Hydrogen and fluorine adsorption on the h-BN (001) plane, J. Phys. Chem. B 103 (36) (1999) 7637–7642, https://doi.org/10.1021/jp984797g.
[589] J. Zou, L.M. Tang, K.Q. Chen, Y.X. Feng, Contrasting properties of hydrogenated and protonated single-layer h-BN from first-principles, J. Phys.-Condes. Matter 30 (6) (2018) 065001, https://doi.org/10.1088/1361-648X/aaa2d7.
[590] J.H. Hao, Z.J. Wang, Y.F. Wang, Y.H. Yin, R. Jiang, Q.H. Jin, Adsorption of alkali and alkaline-earth metal atoms on the reconstructed graphene-like BN single sheet, Solid State Sci 50 (2015) 69–73, https://doi.org/10.1016/j.solidstatesciences.2015.10.015.
[591] M. Rafique, M. Unar, I. Ahmed, A. Chachar, S. Y, Ab-initio investigations on physisorption of alkaline earth metal atoms on monolayer hexagonal boron nitride (h-BN), J. Phys. Chem. Solids 118 (2018) 114–125.
[592] J. Li, G. Zhou, Y. Chen, B.L. Gu, W.H. Duan, Magnetism of C adatoms on BN nanostructures: implications for functional nanodevices, J. Am. Chem. Soc. 131 (5) (2009) 1796–1801, https://doi.org/10.1021/ja805632p.
[593] V.O. Ozcelik, S. Ciraci, Self-assembly mechanisms of short atomic chains on single-layer graphene and boron nitride, Phys. Rev. B 86 (15) (2012) 155421, https://doi.org/10.1103/PhysRevB.86.155421.
[594] S.L. Tang, Y.J. Liu, H.X. Wang, J.X. Zhao, Q.H. Cai, X.Z. Wang, Modifying the electronic and magnetic properties of the boron nitride (BN) nanosheet by NH_x (x=0, 1, and 2) groups, Diam. Relat. Mat. 44 (2014) 54–61, https://doi.org/10.1016/j.diamond.2013.12.005.
[595] S.J. Li, M. Zhou, M.L. Li, G. Lu, X.H. Wang, F.W. Zheng, P. Zhang, Adsorption of 3d, 4d, and 5d transition-metal atoms on single-layer boron nitride, J. Appl. Phys. 123 (9) (2018) 095110, https://doi.org/10.1063/1.5012549.
[596] J. Li, M.L. Hu, Z.Z. Yu, J.X. Zhong, L.Z. Sun, Structural, electronic and magnetic properties of single transition-metal adsorbed BN sheet: a density functional study, Chem. Phys. Lett. 532 (2012) 40–46, https://doi.org/10.1016/j.cplett.2012.02.045.
[597] Y.Z. Abdullahi, M.M. Rahman, A. Shuaibu, S. Abubakar, H. Zainuddin, R. Muhida, H. Setiyanto, Density functional study of manganese atom adsorption on hydrogen-terminated armchair boron nitride nanoribbons, Physica B 447 (2014) 65–69, https://doi.org/10.1016/j.physb.2014.04.043.
[598] D.W. Ma, Z.S. Lu, W.W. Ju, Y.N. Tang, First-principles studies of BN sheets with absorbed transition metal single atoms or dimers: stabilities, electronic structures, and magnetic properties, J. Phys.-Condes. Matter 24 (14) (2012) 145501, https://doi.org/10.1088/0953-8984/24/14/145501.
[599] D.W. Ma, W.W. Ju, X.L. Chu, Z.S. Lu, Z.M. Fu, First-principles studies of Fe atoms adsorption on hydrogen-terminated boron nitride nanoribbons, Phys. Lett. A 377 (13) (2013) 1016–1020, https://doi.org/10.1016/j.physleta.2013.02.027.
[600] T.T. Zhang, G.B. Chen, L.Y. Zhu, Enhanced adsorption of Co atoms on grain boundary of boron nitride, J. Nanopart. Res. 19 (11) (2017) 371, https://doi.org/10.1007/s11051-017-4060-y.
[601] N.S. Venkataramanan, M. Khazaei, R. Sahara, H. Mizuseki, Y. Kawazoe, First-principles study of hydrogen storage over Ni and Rh doped BN sheets, Chem. Phys. 359 (1–3) (2009) 173–178, https://doi.org/10.1016/j.chemphys.2009.04.001.
[602] X. Liu, T. Duan, Y.H. Sui, C.G. Meng, Y. Han, Copper atoms embedded in hexagonal boron nitride as potential catalysts for CO oxidation: a first-principles investigation, RSC Adv. 4 (73) (2014) 38750–38760, https://doi.org/10.1039/c4ra06436d.
[603] D. Sen, R. Thapa, K. Bhattacharjee, K.K. Chattopadhyay, Site dependent metal adsorption on (3 x 3) h-BN monolayer: stability, magnetic and optical properties, Comput. Mater. Sci. 51 (1) (2012) 165–171, https://doi.org/10.1016/j.commatsci.2011.07.042.
[604] R. Schimmenti, R. Cortese, D. Duca, M. Mavrikakis, Boron nitride-supported sub-nanometer Pd_6 clusters for formic acid decomposition: a DFT study, ChemCatChem 9 (9) (2017) 1610–1620, https://doi.org/10.1002/cctc.201700248.
[605] F. Ersan, G. Gokoglu, E. Akturk, Bimetallic two-dimensional PtAg coverage on h-BN substrate: first-principles calculations, Appl. Surf. Sci. 303 (2014) 306–311, https://doi.org/10.1016/j.apsusc.2014.02.171.
[606] M. Gao, A. Lyalin, T. Taketsugu, CO oxidation on h-BN supported Au atom, J. Chem. Phys. 138 (3) (2013) 034701, https://doi.org/10.1063/1.4774216.
[607] G.H. Li, X.D. Liu, H.Y. Zhang, X.P. Wang, H.X. Bu, M. Chen, F. Li, M.W. Zhao, Adsorption and diffusion of gold adatoms on boron nitride nanoribbons: a first-principles study, J. Appl. Phys. 112 (10) (2012) 104305, https://doi.org/10.1063/1.4766411.
[608] P. Shrestha, A.D. Migone, Adsorption isotherm study of multilayer N_2 films on BN, Phys. Rev. B 54 (23) (1996) 17102–17107, https://doi.org/10.1103/PhysRevB.54.17102.
[609] K. Morishige, T. Komura, X-ray study of CHF_3 and CH_3Cl monolayers on boron nitride, Langmuir 14 (17) (1998) 4887–4890, https://doi.org/10.1021/la980183r.
[610] M.T. Alkhafaji, A.D. Migone, Multilayer adsorption-isotherm study of Ar films on boron-nitride, Phys. Rev. B 45 (15) (1992) 8767–8770, https://doi.org/10.1103/PhysRevB.45.8767.
[611] F.D. Natterer, F. Patthey, H. Brune, Distinction of nuclear spin states with the scanning tunneling microscope, Phys. Rev. Lett. 111 (17) (2013) 175303, https://doi.org/10.1103/PhysRevLett.111.175303.
[612] F.D. Natterer, F. Patthey, H. Brune, Resonant-enhanced spectroscopy of molecular rotations with a scanning tunneling microscope, ACS Nano 8 (7) (2014) 7099–7105, https://doi.org/10.1021/nn501999k.
[613] M. Wei, Q. Fu, H. Wu, A.Y. Dong, X.H. Bao, Hydrogen intercalation of graphene and boron nitride monolayers grown on Pt(111), Top. Catal. 59 (5–7) (2016) 543–549, https://doi.org/10.1007/s11244-015-0516-4.
[614] G. Kim, S.C. Jung, Y.K. Han, Selectively strong molecular adsorption on boron nitride monolayer induced by transition metal substrate, Curr. Appl. Phys. 13 (9) (2013) 2059–2063, https://doi.org/10.1016/j.cap.2013.09.010.
[615] K. Uosaki, G. Elumalai, H. Noguchi, T. Masuda, A. Lyalin, A. Nakayama, T. Taketsugu, Boron nitride nanosheet on gold as an electrocatalyst for oxygen reduction reaction: theoretical suggestion and experimental proof, J. Am. Chem. Soc. 136 (18) (2014) 6542–6545, https://doi.org/10.1021/ja500393g.
[616] H.F. Ma, T. Brugger, S. Berner, Y. Ding, M. Iannuzzi, J. Hutter, J. Osterwalder, T. Greber, Nano-ice on boron nitride nanomesh: accessing proton disorder, ChemPhysChem 11 (2) (2010) 399–403, https://doi.org/10.1002/cphc.200900857.
[617] H.F. Ma, Y. Ding, M. Iannuzzi, T. Brugger, S. Berner, J. Hutter, J. Osterwalder, T. Greber, Chiral distortion of confined ice oligomers (n=5,6), Langmuir 28 (43) (2012) 15246–15250, https://doi.org/10.1021/la302561r.
[618] Y. Ding, M. Iannuzzi, J. Hutter, Investigation of h-BN/Rh(111) nanomesh interacting with water and atomic hydrogen, Chimia 65 (4) (2011) 256–259, https://doi.org/10.2533/chimia.2011.256.
[619] Y. Ding, M. Iannuzzi, J. Hutter, Nano-ice models for the water aggregates observed on the h-BN/Rh(111) nanomesh, J. Phys.-Condes. Matter 24 (44) (2012) 445002, https://doi.org/10.1088/0953-8984/24/44/445002.
[620] M. Wang, M. Kim, D. Odkhuu, N. Park, J. Lee, W.J. Jang, S.J. Kahng, R.S. Ruoff, Y.J. Song, S. Lee, Catalytic transparency of hexagonal boron nitride on copper for chemical vapor deposition growth of large-area and high-quality graphene, ACS Nano 8 (6) (2014) 5478–5483, https://doi.org/10.1021/nn501837c.
[621] Z. Zuo, Z.G. Xu, R.J. Zheng, A. Khanaki, J.G. Zheng, J.L. Liu, In-situ epitaxial growth of graphene/h-BN van der Waals heterostructures by molecular beam epitaxy, Sci. Rep. 5 (2015) 14760, https://doi.org/10.1038/srep14760.
[622] Z. Liu, L. Song, S.Z. Zhao, J.Q. Huang, L.L. Ma, J.N. Zhang, J. Lou, P.M. Ajayan, Direct growth of graphene/hexagonal boron nitride stacked layers, Nano Lett. 11 (5) (2011) 2032–2037, https://doi.org/10.1021/nl200464j.
[623] M. Wang, M. Kim, D. Odkhuu, J. Lee, W.J. Jang, S.J. Kahng, N. Park, R.S. Ruoff, Y.J. Song, S. Lee, Catalytic transparency of hexagonal boron nitride on copper for chemical vapor deposition growth of large-area and high-quality graphene, ACS Nano 8 (8) (2014) 8711, https://doi.org/10.1021/nn503982j.
[624] S. Lopez-Moreno, A.H. Romero, Atomic and molecular oxygen adsorbed on (111) transition metal surfaces: Cu and Ni, J. Chem. Phys. 142 (15) (2015) 154702, https://doi.org/10.1063/1.4917259.
[625] K. Uosaki, G. Elumalai, H.C. Dinh, A. Lyalin, T. Taketsugu, H. Noguchi, Highly efficient electrochemical hydrogen evolution reaction at insulating boron nitride nanosheet on inert gold substrate, Sci. Rep. 6 (2016) 32217, https://doi.org/10.1038/srep32217.
[626] T. Shibata, Y. Murakami, T. Watanuki, H. Suematsu, Crystal structures and magnetism of oxygen monolayers on hexagonal boron nitride, Surf. Sci. 405 (2–3) (1998) 153–171, https://doi.org/10.1016/S0039-6028(97)00827-3.
[627] Q. Sun, Z. Li, D.J. Searles, Y. Chen, G.Q. Lu, A.J. Du, Charge-controlled switchable CO_2 capture on boron nitride nanomaterials, J. Am. Chem. Soc. 135 (22) (2013) 8246–8253, https://doi.org/10.1021/ja400243r.
[628] M. Pashangpour, Electronic structure calculation of adsorbate gas molecules on a BN nanolayer, a first principle study, in: Proceedings of International Conference on Nanotechnology and Biosensors (ICNB 2010), 2010.
[629] S.H. Jhi, Y.K. Kwon, Hydrogen adsorption on boron nitride nanotubes: a path to room-temperature hydrogen storage, Phys. Rev. B 69 (24) (2004) 245407, https://doi.org/10.1103/PhysRevB.69.245407.
[630] H.Y. Guo, W.H. Zhang, N. Lu, Z.W. Zhuo, X.C. Zeng, X.J. Wu, J.L. Yang, CO_2 capture on h-BN sheet with high selectivity controlled by external electric field, J. Phys. Chem. C 119 (12) (2015) 6912–6917, https://doi.org/10.1021/acs.jpcc.5b00681.
[631] C. Bhat, R. Brajpuriya, P. Mishra, S.K. Jain, A. Srivastava, Electronic and transport properties of BN sheet on adsorption of amine (NH_2) group, in: 9th International Conference on Industrial and Informations Systems (ICIIS), 2014https://doi.org/10.1109/ICIINFS.2014.7036653.

[632] H.M. Wang, Y.J. Liu, H.X. Wang, J.X. Zhao, Q.H. Cai, X.Z. Wang, Stability and properties of the two-dimensional hexagonal boron nitride monolayer functionalized by hydroxyl (OH) radicals: a theoretical study, J. Mol. Model. 19 (12) (2013) 5143–5152, https://doi.org/10.1007/s00894-013-2013-7.

[633] B. Grosjean, C. Pean, A. Siria, L. Bocquet, R. Vuilleumier, M.L. Bocquet, Chemisorption of hydroxide on 2D materials from DFT calculations: graphene versus hexagonal boron nitride, J. Phys. Chem. Lett. 7 (22) (2016) 4695–4700, https://doi.org/10.1021/acs.jpclett.6b02248.

[634] Y.J. Liu, B. Gao, D. Xu, H.M. Wang, J.X. Zhao, Theoretical study on Si-doped hexagonal boron nitride (h-BN) sheet: electronic, magnetic properties, and reactivity, Phys. Lett. A 378 (40) (2014) 2989–2994, https://doi.org/10.1016/j.physleta.2014.07.053.

[635] Y. Tian, X.F. Pan, Y.J. Liu, J.X. Zhao, Theoretical study of the adsorption of CHO radicals on hexagonal boron nitride sheet: structural and electronic changes, Appl. Surf. Sci. 295 (2014) 137–143, https://doi.org/10.1016/j.apsusc.2014.01.017.

[636] Y. Jiao, A.J. Du, Z.H. Zhu, V. Rudolph, G.Q. Lu, S.C. Smith, A density functional theory study on CO_2 capture and activation by graphene-like boron nitride with boron vacancy, Catal. Today 175 (1) (2011) 271–275, https://doi.org/10.1016/j.cattod.2011.02.043.

[637] R. Ponce-Perez, G.H. Cocoletzi, N. Takeuchi, Two-dimensional boron nitride structures functionalization: first principles studies, J. Mol. Model. 22 (9) (2016) 226, https://doi.org/10.1007/s00894-016-3100-3.

[638] I. Baraille, M. Rerat, P. Mora, Ab initio calculations of the dispersion contribution to the physisorption potential: application to the N_2-BN system, Phys. Rev. B 73 (7) (2006) 075410, https://doi.org/10.1103/PhysRevB.73.075410.

[639] M. Halo, S. Casassa, L. Maschio, C. Pisani, R. Dovesi, D. Ehinon, I. Baraille, M. Rerat, D. Usvyat, Periodic ab initio estimates of the dispersive interaction between molecular nitrogen and a monolayer of hexagonal BN, Phys. Chem. Chem. Phys. 13 (10) (2011) 4434–4443, https://doi.org/10.1039/c0cp01687j.

[640] J.X. Zhao, Y.Y. Yu, Y. Bai, B. Lu, B.X. Wang, Chemical functionalization of BN graphene with the metal-arene group: a theoretical study, J. Mater. Chem. 22 (18) (2012) 9343–9350, https://doi.org/10.1039/c2jm30580a.

[641] E.C. Anota, H.H. Cocoletzi, E.R. Rosas, LDA approximation based analysis of the adsorption of O_3 by boron nitride sheet, Eur. Phys. J. D 63 (2) (2011) 271–273, https://doi.org/10.1140/epjd/e2011-10608-4.

[642] M. Arabieh, Y.T. Azar, Adsorption modes of molecular iodine on defected boron nitrides: a DFT study, Appl. Surf. Sci. 434 (2018) 604–612, https://doi.org/10.1016/j.apsusc.2017.10.232.

[643] H.W. Guo, Y.L. Liu, Y. Xu, N. Meng, H.T. Wang, T. Hasan, X.R. Wang, J.K. Luo, B. Yu, Fluorinated graphene and hexagonal boron nitride as ALD seed layers for graphene-based van der Waals heterostructures, Nanotechnology 25 (35) (2014) 355202, https://doi.org/10.1088/0957-4484/25/35/355202.

[644] Y.S. Al-Hamdani, M. Ma, D. Alfe, O.A. von Lilienfeld, A. Michaelides, Communication: water on hexagonal boron nitride from diffusion Monte Carlo, J. Chem. Phys. 142 (18) (2015) 181101, https://doi.org/10.1063/1.4921106.

[645] E.C. Anota, A.R. Juarez, M. Castro, H.H. Cocoletzi, A density functional theory analysis for the adsorption of the amine group on graphene and boron nitride nanosheets, J. Mol. Model. 19 (1) (2013) 321–328, https://doi.org/10.1007/s00894-012-1539-4.

[646] A. Srivastava, C. Bhat, S.K. Jain, P.K. Mishra, R. Brajpuriya, Electronic transport properties of BN sheet on adsorption of ammonia (NH_3) gas, J. Mol. Model. 21 (3) (2015) 39, https://doi.org/10.1007/s00894-015-2595-3.

[647] M. Yokoyama, K. Nakada, A. Ishii, Density functional theory calculations for Pd adsorption on SO_4 adsorbed on h-BN, Comput. Mater. Sci. 82 (2014) 231–236, https://doi.org/10.1016/j.commatsci.2013.08.058.

[648] H. Heidari, S. Afshari, E. Habibi, Sensing properties of pristine, Al-doped, and defected boron nitride nanosheet toward mercaptans: a first-principles study, RSC Adv. 5 (114) (2015) 94201–94209, https://doi.org/10.1039/c5ra09923d.

[649] M. Rezaei-Sameti, N. Jukar, A computational study of nitramide adsorption on the electrical properties of pristine and C-replaced boron nitride nanosheet, J. Nanostruct. Chem. 7 (2017) 293–307, https://doi.org/10.1007/s40097-017-0237-2.

[650] A.L. Kuang, T.W. Zhou, G.Z. Wang, Y. Li, G. Wu, H.K. Yuan, H. Chen, X.L. Yang, Dehydrogenation of ammonia borane catalyzed by pristine and defective h-BN sheets, Appl. Surf. Sci. 362 (2016) 562–571, https://doi.org/10.1016/j.apsusc.2015.11.011.

[651] M. Terrones, J.M. Romo-Herrera, E. Cruz-Silva, F. Lopez-Urias, E. Munoz-Sandoval, J.J. Velazquez-Salazar, H. Terrones, Y. Bando, D. Golberg, Pure and doped boron nitride nanotubes, Mater. Today 10 (5) (2007) 30–38, https://doi.org/10.1016/S1369-7021(07)70077-9.

[652] R.S. Singh, Influence of oxygen impurity on electronic properties of carbon and boron nitride nanotubes: a comparative study, AIP Adv. 5 (11) (2015) 117150, https://doi.org/10.1063/1.4936765.

[653] J.B. Wu, W.Y. Zhang, Tuning the magnetic and transport properties of boron-nitride nanotubes via oxygen-doping, Solid State Commun. 149 (11–12) (2009) 486–490, https://doi.org/10.1016/j.ssc.2008.12.030.

[654] S. Sinthika, E.M. Kumar, V.J. Surya, Y. Kawazoe, N. Park, K. Iyakutti, R. Thapa, Activation of CO and CO_2 on homonuclear boron bonds of fullerene-like BN cages: first principles study, Sci. Rep. 5 (2015) 17460, https://doi.org/10.1038/srep17460.

[655] A. Lyalin, A. Nakayama, K. Uosaki, T. Taketsugu, Theoretical predictions for hexagonal BN based nanomaterials as electrocatalysts for the oxygen reduction reaction, Phys. Chem. Chem. Phys. 15 (8) (2013) 2809–2820, https://doi.org/10.1039/c2cp42907a.

[656] S. Sinthika, E.M. Kumar, R. Thapa, Doped h-BN monolayer as efficient noble metal-free catalysts for CO oxidation: the role of dopant and water in activity and catalytic de-poisoning, J. Mater. Chem. A 2 (32) (2014) 12812–12820, https://doi.org/10.1039/c4ta02434f.

[657] X.H. Deng, D.Y. Zhang, M.S. Si, M.S. Deng, The improvement of the adsorption abilities of some gas molecules on g-BN sheet by carbon doping, Physica E 44 (2) (2011) 495–500, https://doi.org/10.1016/j.physe.2011.09.027.

[658] S. Lin, X.X. Ye, J. Huang, Can metal-free silicon-doped hexagonal boron nitride nanosheets and nanotubes exhibit activity toward CO oxidation? Phys. Chem. Chem. Phys. 17 (2) (2015) 888–895, https://doi.org/10.1039/c4cp05007j.

[659] P. Zhao, Y. Su, Y. Zhang, S.J. Li, G. Chen, CO catalytic oxidation on iron-embedded hexagonal boron nitride sheet, Chem. Phys. Lett. 515 (1–3) (2011) 159–162, https://doi.org/10.1016/j.cplett.2011.09.034.

[660] J.M. Gottfried, Surface chemistry of porphyrins and phthalocyanines, Surf. Sci. Rep. 70 (3) (2015) 259–379, https://doi.org/10.1016/j.surfrep.2015.04.001.

[661] W. Auwärter, D. Ecija, F. Klappenberger, J.V. Barth, Porphyrins at interfaces, Nat. Chem. 7 (2) (2015) 105–120, https://doi.org/10.1038/nchem.2159.

[662] C.A. Mirkin, W.B. Caldwell, Thin film, fullerene-based materials, Tetrahedron 52 (14) (1996) 5113–5130, https://doi.org/10.1016/0040-4020(96)00118-4.

[663] D. Bonifazi, O. Enger, F. Diederich, Supramolecular [60]fullerene chemistry on surfaces, Chem. Soc. Rev. 36 (2) (2007) 390–414, https://doi.org/10.1039/b604308a.

[664] C.B. France, F.A. Frame, B.A. Parkinson, Multiple two-dimensional structures formed at monolayer and submonolayer coverages of p-sexiphenyl on the Au(111) surface, Langmuir 22 (18) (2006) 7507–7511, https://doi.org/10.1021/la052924b.

[665] J. Cornil, D. Beljonne, Z. Shuai, T.W. Hagler, I. Campbell, D.D.C. Bradley, J.L. Bredas, C.W. Spangler, K. Müllen, Vibronic structure in the optical absorption spectra of phenylene vinylene oligomers: a joint experimental and theoretical study, Chem. Phys. Lett. 247 (4–6) (1995) 425–432, https://doi.org/10.1016/S0009-2614(95)01224-9.

[666] E. Zojer, J. Cornil, G. Leising, J.L. Bredas, Theoretical investigation of the geometric and optical properties of neutral and charged oligophenylenes, Phys. Rev. B 59 (12) (1999) 7957–7968, https://doi.org/10.1103/PhysRevB.59.7957.

[667] J.Q. Zhong, H. Huang, H.Y. Mao, R. Wang, S. Zhong, W. Chen, Molecular-scale investigation of C_{60}/p-sexiphenyl organic heterojunction interface, J. Chem. Phys. 134 (15) (2011) 154706, https://doi.org/10.1063/1.3582789.

[668] F. Klappenberger, D. Kühne, M. Marschall, S. Neppl, W. Krenner, A. Nefedov, T. Strunskus, K. Fink, C. Wöll, S. Klyatskaya, O. Fuhr, M. Ruben, J.V. Barth, Uniform π-system alignment in thin films of template-grown dicarbonitrile-oligophenyls, Adv. Funct. Mater. 21 (9) (2011) 1631–1642, https://doi.org/10.1002/adfm.201001940.

[669] F. Sellam, T. Schmitz-Hubsch, M. Toerker, S. Mannsfeld, H. Proehl, T. Fritz, K. Leo, C. Simpson, K. Müllen, LEED and STM investigations of organic-organic heterostructures grown by molecular beam epitaxy, Surf. Sci. 478 (1–2) (2001) 113–121, https://doi.org/10.1016/S0039-6028(01)00901-3.

[670] S. Lukas, G. Witte, C. Wöll, Novel mechanism for molecular self-assembly on metal substrates: unidirectional rows of pentacene on Cu(110) produced by a substrate-mediated repulsion, Phys. Rev. Lett. 88 (2) (2002) 028301, https://doi.org/10.1103/PhysRevLett.88.028301.

[671] L. Gross, F. Mohn, N. Moll, P. Liljeroth, G. Meyer, The chemical structure of a molecule resolved by atomic force microscopy, Science 325 (5944) (2009) 1110–1114, https://doi.org/10.1126/science.1176210.

[672] M. Treier, P. Ruffieux, R. Schillinger, T. Greber, K. Müllen, R. Fasel, Living on the edge: a nanographene molecule adsorbed across gold step edges, Surf. Sci. 602 (13) (2008) L84–L88, https://doi.org/10.1016/j.susc.2008.04.031.

[673] I. Diez-Perez, Z.H. Li, J. Hihath, J.H. Li, C.Y. Zhang, X.M. Yang, L. Zang, Y.J. Dai, X.L. Feng, K. Müllen, N.J. Tao, Gate-controlled electron transport in coronenes as a bottom-up approach towards graphene transistors, Nat. Commun. 1 (2010) 31, https://doi.org/10.1038/ncomms1029.

[674] N. Pavlicek, A. Mistry, Z. Majzik, N. Moll, G. Meyer, D.J. Fox, L. Gross, Synthesis and characterization of triangulene, Nat. Nanotechnol. 12 (4) (2017) 308–311, https://doi.org/10.1038/NNANO.2016.305.

[675] X.Y. Wang, M. Richter, Y.Q. He, J. Björk, A. Riss, R. Rajesh, M. Garnica, F. Hennersdorf, J.J. Weigand, A. Narita, R. Berger, X.L. Feng, W. Auwärter, J.V. Barth, C.A. Palma, K. Müllen, Exploration of pyrazine-embedded antiaromatic polycyclic hydrocarbons generated by solution and on-surface azomethine ylide homocoupling, Nat. Commun. 8 (2017) 1948, https://doi.org/10.1038/s41467-017-01934-1.

[676] L. Sosa-Vargas, E. Kim, A.J. Attias, Beyond "decorative" 2D supramolecular self-assembly: strategies towards functional surfaces for nanotechnology, Mater. Horizons 4 (4) (2017) 570–583, https://doi.org/10.1039/c7mh00127d.

[677] T. Tian, C.J. Shih, Molecular epitaxy on two-dimensional materials: the interplay between interactions, Ind. Eng. Chem. Res. 56 (38) (2017) 10552–10581, https://doi.org/10.1021/acs.iecr.7b02669.

[678] L.W. Liu, T. Dienel, R. Widmer, O. Gröning, Interplay between energy-level position and charging effect of manganese phthalocyanines on an atomically thin insulator, ACS Nano 9 (10) (2015) 10125–10132, https://doi.org/10.1021/acsnano.5b03741.

[679] F. Schulz, M. Ijäs, R. Drost, S.K. Hämäläinen, A. Harju, A.P. Seitsonen, P. Liljeroth, Many-body transitions in a single molecule visualized by scanning tunnelling microscopy, Nat. Phys 11 (3) (2015) 229–234, https://doi.org/10.1038/NPHYS3212.

[680] C. Wäckerlin, F. Donati, A. Singha, R. Baltic, S. Rusponi, K. Diller, F. Patthey, M. Pivetta, Y.H. Lan, S. Klyatskaya, M. Ruben, H. Brune, J. Dreiser, Giant hysteresis of single-molecule magnets adsorbed on a nonmagnetic insulator, Adv. Mater. 28 (26) (2016) 5195–5199, https://doi.org/10.1002/adma.201506305.

[681] T. Dienel, J. Gomez-Diaz, A.P. Seitsonen, R. Widmer, M. Iannuzzi, K. Radican, H. Sachdev, K. Müllen, J. Hutter, O. Gröning, Dehalogenation and coupling of a polycyclic hydrocarbon on an atomically thin insulator, ACS Nano 8 (7) (2014) 6571–6579, https://doi.org/10.1021/nn501906w.

[682] M. Muntwiler, W. Auwärter, A.P. Seitsonen, J. Osterwalder, T. Greber, Rocking-motion-induced charging of C_{60} on h-BN/Ni(111), Phys. Rev. B 71 (12) (2005) 121402, https://doi.org/10.1103/PhysRevB.71.121402.

[683] L. Li, Y.N. Wu, H.P. Cheng, First-principles calculations of Fe-doped monolayer C_{60} on h-BN/Ni(111) surface, J. Chem. Phys. 132 (7) (2010) 074702, https://doi.org/10.1063/1.3291080.

[684] J.I. Urgel, M. Schwarz, M. Garnica, D. Stassen, D. Bonifazi, D. Ecija, J.V. Barth, W. Auwärter, Controlling coordination reactions and assembly on a Cu(111) supported boron nitride monolayer, J. Am. Chem. Soc. 137 (7) (2015) 2420–2423, https://doi.org/10.1021/ja511611r.

[685] W. Zhao, L. Dong, C. Huang, Z.M. Win, N.A. Lin, Cu- and Pd-catalyzed Ullmann reaction on a hexagonal boron nitride layer, Chem. Commun. 52 (90) (2016) 13225–13228, https://doi.org/10.1039/c6cc05029h.

[686] T. Kaposi, S. Joshi, T. Hoh, A. Wiengarten, K. Seufert, M. Paszkiewicz, F. Klappenberger, D. Ecija, L. Dordevic, T. Marangoni, D. Bonifazi, J.V. Barth, W. Auwärter, Supramolecular spangling, crocheting, and knitting of functionalized pyrene molecules on a silver surface, ACS Nano 10 (8) (2016) 7665–7674, https://doi.org/10.1021/acsnano.6b02989.

[687] R. Forker, T. Dienel, A. Krause, M. Gruenewald, M. Meissner, T. Kirchhuebel, O. Gröning, T. Fritz, Optical transition energies of isolated molecular monomers and weakly interacting two-dimensional aggregates, Phys. Rev. B 93 (16) (2016) 165426, https://doi.org/10.1103/PhysRevB.93.165426.

[688] R. Forker, T. Dienel, A. Krause, M. Gruenewald, M. Meissner, T. Kirchhuebel, O. Gröning, T. Fritz, Optical transition energies of isolated molecular monomers and weakly interacting two-dimensional aggregates, Phys. Rev. B 94 (15) (2016) 159901, https://doi.org/10.1103/PhysRevB.94.159901.

[689] H. Cun, A.P. Seitsonen, S. Roth, S. Decurtins, S. Liu, J. Osterwalder, T. Greber, An electron acceptor molecule in a nanomesh: F_4TCNQ on h-BN/Rh(111), Surf. Sci. 678 (2018) 183–188, https://doi.org/10.1016/j.susc.2018.04.026.

[690] M.L. Ng, A.B. Preobrajenski, A.A. Zakharov, A.S. Vinogradov, S.A. Krasnikov, A.A. Cafolla, N. Mårtensson, Effect of substrate nanopatterning on the growth and structure of pentacene films, Phys. Rev. B 81 (11) (2010) 115449, https://doi.org/10.1103/PhysRevB.81.115449.

[691] C.A. Palma, S. Joshi, T. Hoh, D. Ecija, J.V. Barth, W. Auwärter, Two-level spatial modulation of vibronic conductance in conjugated oligophenylenes on boron nitride, Nano Lett. 15 (4) (2015) 2242–2248, https://doi.org/10.1021/nl503956p.

[692] S. Kahle, Z.T. Deng, N. Malinowski, C. Tonnoir, A. Forment-Aliaga, N. Thontasen, G. Rinke, D. Le, V. Turkowski, T.S. Rahman, S. Rauschenbach, M. Ternes, K. Kern, The quantum magnetism of individual manganese-12-acetate molecular magnets anchored at surfaces, Nano Lett. 12 (1) (2012) 518–521, https://doi.org/10.1021/nl204141z.

[693] P. Erler, P. Schmitt, N. Barth, A. Irmler, S. Bouvron, T. Huhn, U. Groth, F. Pauly, L. Gragnaniello, M. Fonin, Highly ordered surface self-assembly of Fe_4 single molecule magnets, Nano Lett. 15 (7) (2015) 4546–4552, https://doi.org/10.1021/acs.nanolett.5b01120.

[694] W. Auwärter, One Monolayer of Hexagonal Boron Nitride on Ni(111): an Atomically Sharp Interface. (Ph.D. thesis), Universität Zürich, 2003.

[695] Y. Wei, A. Riss, M. Schwarz, J.V. Barth, W. Auwärter, L. Diekhöner, Self-assembled C_{60} nanostructures on h-BN/Cu(111), 2019 (unpublished).

[696] K. Diller, F. Klappenberger, F. Allegretti, A.C. Papageorgiou, S. Fischer, A. Wiengarten, S. Joshi, K. Seufert, D. Ecija, W. Auwärter, J.V. Barth, Investigating the molecule-substrate interaction of prototypic tetrapyrrole compounds: adsorption and self-metalation of porphine on Cu(111), J. Chem. Phys. 138 (15) (2013) 154710, https://doi.org/10.1063/1.4800771.

[697] F. Bischoff, K. Seufert, W. Auwärter, S. Joshi, S. Vijayaraghavan, D. Ecija, K. Diller, A.C. Papageorgiou, S. Fischer, F. Allegretti, D.A. Duncan, F. Klappenberger, F. Blobner, R.Y. Han, J.V. Barth, How surface bonding and repulsive interactions cause phase transformations: ordering of a prototype macrocyclic compound on Ag(111), ACS Nano 7 (4) (2013) 3139–3149, https://doi.org/10.1021/nn305487c.

[698] M. Pörtner, Y. Wei, A. Riss, K. Seufert, M. Garnica, J. Barth, L. Diekhöner, W. Auwärter, Charge State control of F_{16}CoPc on h-BN on Cu(111), 2019 (in preparation).

[699] Q. Tang, Z. Zhou, Z.F. Chen, Molecular charge transfer: a simple and effective route to engineer the band structures of BN nanosheets and nanoribbons, J. Phys. Chem. C 115 (38) (2011) 18531–18537, https://doi.org/10.1021/jp2067205.

[700] D. Zimmermann, K. Seufert, T. Hoh, J. Sushobhan, L. Dordevic, T. Marangoni, D. Bonifazi, W. Auwärter, Bis- and tetra-pyridin-4-ylethynyl functionalized pyrene molecule on h-BN/Cu(111), 2019 (in preparation).

[701] J.I. Urgel, D. Ecija, W. Auwärter, D. Stassen, D. Bonifazi, J.V. Barth, Orthogonal insertion of lanthanide and transition-metal atoms in metal-organic networks on surfaces, Angew. Chem.-Int. Edit. 54 (21) (2015) 6163–6167, https://doi.org/10.1002/anie.201410802.

[702] F. Bischoff, Y.Q. He, K. Seufert, D. Stassen, D. Bonifazi, J.V. Barth, W. Auwärter, Tailoring large pores of porphyrin networks on Ag(111) by metal-organic coordination, Chem.-Eur. J. 22 (43) (2016) 15298–15306, https://doi.org/10.1002/chem.201602154.

[703] W. Chen, H. Huang, A. Thye, S. Wee, Molecular orientation transition of organic thin films on graphite: the effect of intermolecular electrostatic and interfacial dispersion forces, Chem. Commun. 36 (2008) 4276–4278, https://doi.org/10.1039/b805788c.

[704] Y.H. Zhang, J.S. Qiao, S. Gao, F.R. Hu, D.W. He, B. Wu, Z.Y. Yang, B.C. Xu, Y. Li, Y. Shi, W. Ji, P. Wang, X.Y. Wang, M. Xiao, H.X. Xu, J.B. Xu, X.R. Wang, Probing carrier transport and structure-property relationship of highly ordered organic semiconductors at the two-dimensional limit, Phys. Rev. Lett. 116 (1) (2016) 016602, https://doi.org/10.1103/PhysRevLett.116.016602.

[705] S. Koslowski, D. Rosenblatt, A. Kabakchiev, K. Kuhnke, K. Kern, U. Schlickum, Adsorption and electronic properties of pentacene on thin dielectric decoupling layers, Beilstein J. Nanotechnol. 8 (2017) 1388–1395, https://doi.org/10.3762/bjnano.8.140.

[706] U. Schlickum, R. Decker, F. Klappenberger, G. Zoppellaro, S. Klyatskaya, W. Auwärter, S. Neppl, K. Kern, H. Brune, M. Ruben, J.V. Barth, Chiral kagome lattice from simple ditopic molecular bricks, J. Am. Chem. Soc. 130 (35) (2008) 11778–11782, https://doi.org/10.1021/ja8028119.

[707] S. Klyatskaya, F. Klappenberger, U. Schlickum, D. Kühne, M. Marschall, J. Reichert, R. Decker, W. Krenner, G. Zoppellaro, H. Brune, J.V. Barth, M. Ruben, Surface-confined self-assembly of di-carbonitrile polyphenyls, Adv. Funct. Mater. 21 (7) (2011) 1230–1240, https://doi.org/10.1002/adfm.201001437.

[708] C. Si, Z.Z. Lin, J. Zhou, Z.M. Sun, Controllable Schottky barrier in GaSe/graphene heterostructure: the role of interface dipole, 2D Mater. 4 (1) (2017) 015027, https://doi.org/10.1088/2053-1583/4/1/015027.

[709] T. Le Quang, V. Cherkez, K. Nogajewski, M. Potemski, M.T. Dau, M. Jamet, P. Mallet, J.Y. Veuillen, Scanning tunneling spectroscopy of van der Waals graphene/semiconductor interfaces: absence of Fermi level pinning, 2D Mater. 4 (3) (2017) 035019, https://doi.org/10.1088/2053-1583/aa7b03.

[710] D. Pierucci, H. Henck, J. Avila, A. Balan, C.H. Naylor, G. Patriarche, Y.J. Dappe, M.G. Silly, F. Sirotti, A.T.C. Johnson, M.C. Asensio, A. Ouerghi, Band alignment and minigaps in monolayer MoS_2-graphene van der Waals heterostructures, Nano Lett. 16 (7) (2016) 4054–4061, https://doi.org/10.1021/acs.nanolett.6b00609.

[711] M. Willenbockel, D. Lüftner, B. Stadtmüller, G. Koller, C. Kumpf, S. Soubatch, P. Puschnig, M.G. Ramsey, F.S. Tautz, The interplay between interface structure, energy level alignment and chemical bonding strength at organic-metal interfaces, Phys. Chem. Chem. Phys. 17 (3) (2015) 1530–1548, https://doi.org/10.1039/c4cp04595e.

[712] A. Kumar, K. Banerjee, M. Dvorak, F. Schulz, A. Harju, P. Rinke, P. Liljeroth, Charge-transfer-driven nonplanar adsorption of F_4TCNQ molecules on epitaxial graphene, ACS Nano 11 (5) (2017) 4960–4968, https://doi.org/10.1021/acsnano.7b01599.

[713] S. Barja, M. Garnica, J.J. Hinarejos, A.L.V. de Parga, N. Martin, R. Miranda, Self-organization of electron acceptor molecules on graphene, Chem. Commun. 46 (43) (2010) 8198–8200, https://doi.org/10.1039/c0cc02675a.

[714] D. Maccariello, M. Garnica, M.A. Nino, C. Navio, P. Perna, S. Barja, A.L.V. de Parga, R. Miranda, Spatially resolved, site-dependent charge transfer and induced magnetic moment in TCNQ adsorbed on graphene, Chem. Mat. 26 (9) (2014) 2883–2890, https://doi.org/10.1021/cm5005467.

[715] M. Garnica, F. Calleja, A.L.V. de Parga, R. Miranda, Mapping spin distributions in electron acceptor molecules adsorbed on nanostructured graphene by the Kondo effect, Surf. Sci. 630 (2014) 356–360, https://doi.org/10.1016/j.susc.2014.07.028.

[716] J.H. Mao, H.G. Zhang, Y.H. Jiang, Y. Pan, M. Gao, W.D. Xiao, H.J. Gao, Tunability of supramolecular kagome lattices of magnetic phthalocyanines using graphene-based moire patterns as templates, J. Am. Chem. Soc. 131 (40) (2009) 14136–14137, https://doi.org/10.1021/ja904907z.

[717] H.G. Zhang, J.T. Sun, T. Low, L.Z. Zhang, Y. Pan, Q. Liu, J.H. Mao, H.T. Zhou, H.M. Guo, S.X. Du, F. Guinea, H.J. Gao, Assembly of iron phthalocyanine and pentacene molecules on a graphene monolayer grown on Ru(0001), Phys. Rev. B 84 (24) (2011) 245436, https://doi.org/10.1103/PhysRevB.84.245436.

[718] K. Yang, W.D. Xiao, Y.H. Jiang, H.G. Zhang, L.W. Liu, J.H. Mao, H.T. Zhou, S.X. Du, H.J. Gao, Molecule-substrate coupling between metal phthalocyanines and epitaxial graphene grown on Ru(0001) and Pt(111), J. Phys. Chem. C 116 (26) (2012) 14052–14056, https://doi.org/10.1021/jp304068a.

[719] H.T. Zhou, L.Z. Zhang, J.H. Mao, G. Li, Y. Zhang, Y.L. Wang, S.X. Du, W.A. Hofer, H.J. Gao, Template-directed assembly of pentacene molecules on epitaxial graphene on Ru(0001), Nano Res. 6 (2) (2013) 131–137, https://doi.org/10.1007/s12274-013-0288-8.

[720] F. Geng, Y.M. Kuang, Y.J. Yu, Y. Liao, Y. Zhang, Y. Zhang, Z.C. Dong, Tunneling electron induced luminescence from porphyrin molecules on monolayer graphene, J. Lumines. 157 (2015) 39–45, https://doi.org/10.1016/j.jlumin.2014.08.033.

[721] M. Garnica, D. Stradi, S. Barja, F. Calleja, C. Diaz, M. Alcami, N. Martin, A.L.V. de Parga, F. Martin, R. Miranda, Long-range magnetic order in a purely organic 2D layer adsorbed on epitaxial graphene, Nat. Phys. 9 (6) (2013) 368–374, https://doi.org/10.1038/NPHYS2610.

[722] H.T. Zhou, J.H. Mao, G. Li, Y.L. Wang, X.L. Feng, S.X. Du, K. Müllen, H.J. Gao, Direct imaging of intrinsic molecular orbitals using two-dimensional, epitaxially-grown, nanostructured graphene for study of single molecule and interactions, Appl. Phys. Lett. 99 (15) (2011) 153101, https://doi.org/10.1063/1.3646406.

[723] J. Uihlein, M. Polek, M. Glaser, H. Adler, R. Ovsyannikov, M. Bauer, M. Ivanovic, A.B. Preobrajenski, A.V. Generalov, T. Chassé, H. Peisert, Influence of graphene on charge transfer between CoPc and metals: the role of graphene-substrate coupling, J. Phys. Chem. C 119 (27) (2015) 15240–15247, https://doi.org/10.1021/acs.jpcc.5b02912.

[724] N. Néel, J. Kröger, Template effect of the graphene moire lattice on phthalocyanine assembly, Molecules 22 (5) (2017) 731, https://doi.org/10.3390/molecules22050731.

[725] M. Scardamaglia, C. Struzzi, S. Lizzit, M. Dalmiglio, P. Lacovig, A. Baraldi, C. Mariani, M.G. Betti, Energetics and hierarchical interactions of metal phthalocyanines adsorbed on graphene/Ir(111), Langmuir 29 (33) (2013) 10440–10447, https://doi.org/10.1021/1a401850v.

[726] M. Scardamaglia, S. Lisi, S. Lizzit, A. Baraldi, R. Larciprete, C. Mariani, M.G. Betti, Graphene-induced substrate decoupling and ideal doping of a self-assembled iron-phthalocyanine single layer, J. Phys. Chem. C 117 (6) (2013) 3019–3027, https://doi.org/10.1021/jp308861b.

[727] P. Järvinen, S.K. Hämäläinen, M. Ijäs, A. Harju, P. Liljeroth, Self-assembly and orbital imaging of metal phthalocyanines on a graphene model surface, J. Phys. Chem. C 118 (24) (2014) 13320–13325, https://doi.org/10.1021/jp504813v.

[728] S.J. Altenburg, M. Lattelais, B. Wang, M.L. Bocquet, R. Berndt, Reaction of phthalocyanines with graphene on Ir(111), J. Am. Chem. Soc. 137 (29) (2015) 9452–9458, https://doi.org/10.1021/jacs.5b05558.

[729] S.J. Altenburg, R. Berndt, Local work function and STM tip-induced distortion of graphene on Ir(111), New J. Phys. 16 (2014) 053036, https://doi.org/10.1088/1367-2630/16/5/053036.

[730] Q.R. Cai, A.J. Du, G.P. Gao, S. Mateti, B.C.C. Cowie, D. Qian, S. Zhang, Y.R. Lu, L. Fu, T. Taniguchi, S.M. Huang, Y. Chen, R.S. Ruoff, L.H. Li, Molecule-induced conformational change in boron nitride nanosheets with enhanced surface adsorption, Adv. Funct. Mater. 26 (45) (2016) 8202–8210, https://doi.org/10.1002/adfm.201603160.

[731] X. Ling, W.J. Fang, Y.H. Lee, P.T. Araujo, X. Zhang, J.F. Rodriguez-Nieva, Y.X. Lin, J. Zhang, J. Kong, M.S. Dresselhaus, Raman enhancement effect on two-dimensional layered materials: graphene, h-BN and MoS_2, Nano Lett. 14 (6) (2014) 3033–3040, https://doi.org/10.1021/nl404610c.

[732] X.F. Chen, S.L. Jia, N. Ding, J.B. Shi, Z.H. Wang, Capture of aromatic organic pollutants by hexagonal boron nitride nanosheets: density functional theoretical and molecular dynamic investigation, Environ.-Sci. Nano 3 (6) (2016) 1493–1503, https://doi.org/10.1039/c6en00378h.

[733] J.M.G. Hernandez, G.H. Cocoletzi, E.C. Anota, DFT studies of the phenol adsorption on boron nitride sheets, J. Mol. Model. 18 (1) (2012) 137–144, https://doi.org/10.1007/s00894-011-1046-z.

[734] Y.H. Zhao, Q.S. Wu, Q. Chen, J.L. Wang, Molecular self-assembly on two-dimensional atomic crystals: insights from molecular dynamics simulations, J. Phys. Chem. Lett. 6 (22) (2015) 4518–4524, https://doi.org/10.1021/acs.jpclett.5b02147.

[735] A. Rimola, Intrinsic ladders of affinity for amino-acid-analogues on boron nitride nanomaterials: a B3LYP-D2∗ periodic study, J. Phys. Chem. C 119 (31) (2015) 17707–17717, https://doi.org/10.1021/acs.jpcc.5b04601.

[736] N. Ding, X.F. Chen, C.M.L. Wu, H. Li, Adsorption of nucleobase pairs on hexagonal boron nitride sheet: hydrogen bonding versus stacking, Phys. Chem. Chem. Phys. 15 (26) (2013) 10767–10776, https://doi.org/10.1039/c3cp50912e.

[737] E.C. Anota, Y. Tlapale, M.S. Villanueva, J.A.R. Marquez, Non-covalent functionalization of hexagonal boron nitride nanosheets with guanine, J. Mol. Model. 21 (8) (2015) 215, https://doi.org/10.1007/s00894-015-2768-0.

[738] Y.X. Yu, A dispersion-corrected DFT study on adsorption of battery active materials anthraquinone and its derivatives on monolayer graphene and h-BN, J. Mater. Chem. A 2 (23) (2014) 8910–8917, https://doi.org/10.1039/c4ta00103f.

[739] M. Bernardi, M. Palummo, J.C. Grossman, Semiconducting monolayer materials as a tunable platform for excitonic solar cells, ACS Nano 6 (11) (2012) 10082–10089, https://doi.org/10.1021/nn303815z.

[740] V. Caciuc, N. Atodiresei, M. Callsen, P. Lazic, S. Blügel, Ab initio and semi-empirical van der Waals study of graphene-boron nitride interaction from a molecular point of view, J. Phys.-Condes. Matter 24 (42) (2012) 424214, https://doi.org/10.1088/0953-8984/24/42/424214.

[741] J.H. Lee, Y.K. Choi, H.J. Kim, R.H. Scheicher, J.H. Cho, Physisorption of DNA nucleobases on h-BN and graphene: vdW-corrected DFT calculations, J. Phys. Chem. C 117 (26) (2013) 13435–13441, https://doi.org/10.1021/jp402403f.

[742] Q. Lin, X.L. Zou, G. Zhou, R. Liu, J. Wu, J. Li, W.H. Duan, Adsorption of DNA/RNA nucleobases on hexagonal boron nitride sheet: an ab initio study, Phys. Chem. Chem. Phys. 13 (26) (2011) 12225–12230, https://doi.org/10.1039/c1cp20783k.

[743] K. Waters, R. Pandey, S. Karna, Amino acid analogue-conjugated BN nanomaterials in a solvated phase: first principles study of topology-dependent interactions with a monolayer and a (5,0) nanotube, ACS Omega 2 (2017) 76–83.

[744] H. Kobayashi, A. Fukuoka, Hexagonal boron nitride for adsorption of saccharides, J. Phys. Chem. C 121 (32) (2017) 17332–17338, https://doi.org/10.1021/acs.jpcc.7b05077.

[745] S.L. Jia, Z.H. Wang, N. Ding, Y.L.E. Wong, X.F. Chen, G.Y. Qiu, T.W.D. Chan, Hexagonal boron nitride nanosheets as adsorbents for solid-phase extraction of polychlorinated biphenyls from water samples, Anal. Chim. Acta 936 (2016) 123–129, https://doi.org/10.1016/j.aca.2016.07.019.

[746] J. Beheshtian, H. Soleymanabadi, A.A. Peyghan, Z. Bagheri, A DFT study on the functionalization of a BN nanosheet with PC-X, (PC = phenyl carbamate, X = OCH_3, CH_3, NH_2, NO_2 and CN), Appl. Surf. Sci. 268 (2013) 436–441, https://doi.org/10.1016/j.apsusc.2012.12.119.

[747] A. Matkovic, J. Genser, D. Lüftner, M. Kratzer, R. Gajic, P. Puschnig, C. Teichert, Epitaxy of highly ordered organic semiconductor crystallite networks supported by hexagonal boron nitride, Sci. Rep. 6 (2016) 38519, https://doi.org/10.1038/srep38519.

[748] A. Matkovic, J. Genser, D. Lüftner, M. Kratzer, R. Gajic, P. Puschnig, C. Teichert, Epitaxy of highly ordered organic semiconductor crystallite networks supported by hexagonal boron nitride, Sci. Rep. 7 (2017) 46794, https://doi.org/10.1038/srep46794.

[749] V.V. Korolkov, S.A. Svatek, S. Allen, C.J. Roberts, S.J.B. Tendler, T. Taniguchi, K. Watanabe, N.R. Champness, P.H. Beton, Bimolecular porous supramolecular networks deposited from solution on layered materials: graphite, boron nitride and molybdenum disulphide, Chem. Commun. 50 (64) (2014) 8882–8885, https://doi.org/10.1039/c4cc03720k.

[750] H.J. Karmel, T.Y. Chien, V. Demers-Carpentier, J.J. Garramone, M.C. Hersam, Self-assembled two-dimensional heteromolecular nanoporous molecular arrays on epitaxial graphene, J. Phys. Chem. Lett. 5 (2) (2014) 270–274, https://doi.org/10.1021/jz4025518.

[751] E. Verveniotis, Y. Okawa, M.V. Makarova, Y. Koide, J.W. Liu, B. Smid, K. Watanabe, T. Taniguchi, K. Komatsu, T. Minari, X.Y. Liu, C. Joachim, M. Aono, Self-assembling diacetylene molecules on atomically flat insulators, Phys. Chem. Chem. Phys. 18 (46) (2016) 31600–31605, https://doi.org/10.1039/c6cp06749b.

[752] M.V. Makarova, Y. Okawa, E. Verveniotis, T. Watanuki, T. Taniguchi, C. Joachim, M. Aono, Self-assembled diacetylene molecular wire polymerization on an insulating hexagonal boron nitride (0001) surface, Nanotechnology 27 (39) (2016) 395303, https://doi.org/10.1088/0957-4484/27/39/395303.

[753] D.W. He, Y.A. Zhang, Q.S. Wu, R. Xu, H.Y. Nan, J.F. Liu, J.J. Yao, Z.L. Wang, S.J. Yuan, Y. Li, Y. Shi, J.L. Wang, Z.H. Ni, L. He, F. Miao, F.Q. Song, H.X. Xu, K. Watanabe, T. Taniguchi, J.B. Xu, X.R. Wang, Two-dimensional quasi-freestanding molecular crystals for high-performance organic field-effect transistors, Nat. Commun. 5 (2014) 5162, https://doi.org/10.1038/ncomms6162.

[754] C.H. Lee, T. Schiros, E.J.G. Santos, B. Kim, K.G. Yager, S.J. Kang, S. Lee, J. Yu, K. Watanabe, T. Taniguchi, J. Hone, E. Kaxiras, C. Nuckolls, P. Kim, Epitaxial growth of molecular crystals on van der Waals substrates for high-performance organic electronics, Adv. Mater. 26 (18) (2014) 2812–2817, https://doi.org/10.1002/adma.201304973.

[755] T. Arnold, M. Forster, A.A. Fragkoulis, J.E. Parker, Structure of normal-alkanes adsorbed on hexagonal-boron nitride, J. Phys. Chem. C 118 (5) (2014) 2418–2428, https://doi.org/10.1021/jp4063059.

[756] M. Forster, J.E. Parker, A. Inaba, C.A. Murray, N.A. Strange, J.Z. Larese, T. Arnold, The mixing behavior of alkanes adsorbed on hexagonal boron nitride, J. Phys. Chem. C 120 (45) (2016) 25796–25805, https://doi.org/10.1021/acs.jpcc.6b07701.

[757] B. Boddenberg, V. Grundke, A deuteron NMR-study on the dynamics of fluorobenzene molecules adsorbed on graphite and boron-nitride, Z. Naturfors. Sect. A-J. Phys. Sci. 46 (3) (1991) 211–220.

[758] C.R. Dean, A.F. Young, I. Meric, C. Lee, L. Wang, S. Sorgenfrei, K. Watanabe, T. Taniguchi, P. Kim, K.L. Shepard, J. Hone, Boron nitride substrates for high-quality graphene electronics, Nat. Nanotechnol. 5 (10) (2010) 722–726, https://doi.org/10.1038/nnano.2010.172.

[759] J.M. Xue, J. Sanchez-Yamagishi, D. Bulmash, P. Jacquod, A. Deshpande, K. Watanabe, T. Taniguchi, P. Jarillo-Herrero, B.J. LeRoy, Scanning tunnelling microscopy and spectroscopy of ultra-flat graphene on hexagonal boron nitride, Nat. Mater. 10 (4) (2011) 282–285, https://doi.org/10.1038/NMAT2968.

[760] R. Decker, Y. Wang, V.W. Brar, W. Regan, H.Z. Tsai, Q. Wu, W. Gannett, A. Zettl, M.F. Crommie, Local electronic properties of graphene on a BN substrate via scanning tunneling microscopy, Nano Lett. 11 (6) (2011) 2291–2295, https://doi.org/10.1021/nl2005115.

[761] W. Yang, G.R. Chen, Z.W. Shi, C.C. Liu, L.C. Zhang, G.B. Xie, M. Cheng, D.M. Wang, R. Yang, D.X. Shi, K. Watanabe, T. Taniguchi, Y.G. Yao, Y.B. Zhang, G.Y. Zhang, Epitaxial growth of single-domain graphene on hexagonal boron nitride, Nat. Mater. 12 (9) (2013) 792–797, https://doi.org/10.1038/NMAT3695.

[762] Z.W. Zhang, S.Q. Hu, J. Chen, B.W. Li, Hexagonal boron nitride: a promising substrate for graphene with high heat dissipation, Nanotechnology 28 (22) (2017) 225704, https://doi.org/10.1088/1361-6528/aa6e49.

[763] G. Ahn, H.R. Kim, T.Y. Ko, K. Choi, K. Watanabe, T. Taniguchi, B.H. Hong, S. Ryu, Optical probing of the electronic interaction between graphene and hexagonal boron nitride, ACS Nano 7 (2) (2013) 1533–1541, https://doi.org/10.1021/nn305306n.

[764] M. Yankowitz, J.M. Xue, B.J. LeRoy, Graphene on hexagonal boron nitride, J. Phys.-Condes. Matter 26 (30) (2014) 303201, https://doi.org/10.1088/0953-8984/26/30/303201.

[765] G. Giovannetti, P.A. Khomyakov, G. Brocks, P.J. Kelly, J. van den Brink, Substrate-induced band gap in graphene on hexagonal boron nitride: ab initio density functional calculations, Phys. Rev. B 76 (7) (2007) 073103, https://doi.org/10.1103/PhysRevB.76.073103.

[766] G. Giovannetti, P.A. Khomyakov, G. Brocks, P.J. Kelly, J. van den Brink, Publisher's note: substrate-induced band gap in graphene on hexagonal boron nitride: ab initio density functional calculations, Phys. Rev. B 76 (7) (2007) 079902, https://doi.org/10.1103/PhysRevB.76.079902.

[767] M. Bokdam, P.A. Khomyakov, G. Brocks, Z.C. Zhong, P.J. Kelly, Electrostatic doping of graphene through ultrathin hexagonal boron nitride films, Nano Lett. 11 (11) (2011) 4631–4635, https://doi.org/10.1021/nl202131q.

[768] J. Velasco, L. Ju, D. Wong, S. Kahn, J. Lee, H.Z. Tsai, C. Germany, S. Wickenburg, J. Lu, T. Taniguchi, K. Watanabe, A. Zettl, F. Wang, M.F. Crommie, Nanoscale control of rewriteable doping patterns in pristine graphene/boron nitride heterostructures, Nano Lett. 16 (3) (2016) 1620–1625, https://doi.org/10.1021/acs.nanolett.5b04441.

[769] B. Hunt, J.D. Sanchez-Yamagishi, A.F. Young, M. Yankowitz, B.J. LeRoy, K. Watanabe, T. Taniguchi, P. Moon, M. Koshino, P. Jarillo-Herrero, R.C. Ashoori, Massive Dirac fermions and Hofstadter butterfly in a van der Waals heterostructure, Science 340 (6139) (2013) 1427–1430, https://doi.org/10.1126/science.1237240.

[770] M. Yankowitz, J.M. Xue, D. Cormode, J.D. Sanchez-Yamagishi, K. Watanabe, T. Taniguchi, P. Jarillo-Herrero, P. Jacquod, B.J. LeRoy, Emergence of superlattice Dirac points in graphene on hexagonal boron nitride, Nat. Phys. 8 (5) (2012) 382–386, https://doi.org/10.1038/NPHYS2272.

[771] N.M. Freitag, T. Reisch, L.A. Chizhova, P. Nemes-Incze, C. Holl, C.R. Woods, R.V. Gorbachev, Y. Cao, A.K. Geim, K.S. Novoselov, J. Burgdorfer, F. Libisch, M. Morgenstern, Large tunable valley splitting in edge-free graphene quantum dots on boron nitride, Nat. Nanotechnol. 13 (5) (2018) 392–397, https://doi.org/10.1038/s41565-018-0080-8.

[772] G.L. Wang, S. Wu, T.T. Zhang, P. Chen, X.B. Lu, S.P. Wang, D.M. Wang, K. Watanabe, T. Taniguchi, D.X. Shi, R. Yang, G.Y. Zhang, Patterning monolayer graphene with zigzag edges on hexagonal boron nitride by anisotropic etching, Appl. Phys. Lett. 109 (5) (2016) 053101, https://doi.org/10.1063/1.4959963.

[773] F. Withers, O. Del Pozo-Zamudio, A. Mishchenko, A.P. Rooney, A. Gholinia, K. Watanabe, T. Taniguchi, S.J. Haigh, A.K. Geim, A.I. Tartakovskii, K.S. Novoselov, Light-emitting diodes by band-structure engineering in van der Waals heterostructures, Nat. Mater. 14 (3) (2015) 301–306.

[774] C. Handschin, P. Makk, P. Rickhaus, M.H. Liu, K. Watanabe, T. Taniguchi, K. Richter, C. Schönenberger, Fabry-Pérot resonances in a graphene/hBN moire superlattice, Nano Lett. 17 (1) (2017) 328–333, https://doi.org/10.1021/acs.nanolett.6b04137.

[775] Y. Wang, V.W. Brar, A.V. Shytov, Q. Wu, W. Regan, H.Z. Tsai, A. Zettl, L.S. Levitov, M.F. Crommie, Mapping Dirac quasiparticles near a single coulomb impurity on graphene, Nat. Phys. 8 (9) (2012) 653–657, https://doi.org/10.1038/NPHYS2379.

[776] Y. Cao, V. Fatemi, A. Demir, S. Fang, S.L. Tomarken, J.Y. Luo, J.D. Sanchez-Yamagishi, K. Watanabe, T. Taniguchi, E. Kaxiras, R.C. Ashoori, P. Jarillo-Herrero, Correlated insulator behaviour at half-filling in magic-angle graphene superlattices, Nature 556 (7699) (2018) 80–84, https://doi.org/10.1038/nature26154.

[777] Y. Cao, V. Fatemi, S. Fang, K. Watanabe, T. Taniguchi, E. Kaxiras, P. Jarillo-Herrero, Unconventional superconductivity in magic-angle graphene superlattices, Nature 556 (7699) (2018) 43–50, https://doi.org/10.1038/nature26160.

[778] P. Ribeiro-Palau, C. Zhang, K. Watanabe, T. Taniguchi, J. Hone, C.R. Dean, Twistable electronics with dynamically rotatable heterostructures, Science 361 (2018) 690–693.

[779] G. Argentero, A. Mittelberger, M.R.A. Monazam, Y. Cao, T.J. Pennycook, C. Mangler, C. Kramberger, J. Kotakoski, A.K. Geim, J.C. Meyer, Unraveling the 3D atomic structure of a suspended graphene/hBN van der Waals heterostructure, Nano Lett. 17 (3) (2017) 1409–1416, https://doi.org/10.1021/acs.nanolett.6b04360.

[780] N.Y. Kim, H.Y. Jeong, J.H. Kim, G. Kim, H.S. Shin, Z. Lee, Evidence of local commensurate state with lattice match of graphene on hexagonal boron nitride, ACS Nano 11 (7) (2017) 7084–7090, https://doi.org/10.1021/acsnano.7b02716.

[781] B. Sachs, T.O. Wehling, M.I. Katsnelson, A.I. Lichtenstein, Adhesion and electronic structure of graphene on hexagonal boron nitride substrates, Phys. Rev. B 84 (19) (2011) 195414, https://doi.org/10.1103/PhysRevB.84.195414.

[782] X. Lin, Y. Xu, A.A. Hakro, T. Hasan, R. Hao, B.L. Zhang, H.S. Chen, Ab initio optical study of graphene on hexagonal boron nitride and fluorographene substrates, J. Mater. Chem. C 1 (8) (2013) 1618–1627, https://doi.org/10.1039/c2tc00570k.

[783] N. Marom, J. Bernstein, J. Garel, A. Tkatchenko, E. Joselevich, L. Kronik, O. Hod, Stacking and registry effects in layered materials: the case of hexagonal boron nitride, Phys. Rev. Lett. 105 (4) (2010) 046801, https://doi.org/10.1103/PhysRevLett.105.046801.

[784] P. Fu, J. Wang, E. R.I, H. Zhang, 3D-graphene/boron nitride-stacking material: a fundamental van der Waals heterostructure, Chem. Res. Chin. Univ. 34 (3) (2018) 434–439, https://doi.org/10.1007/s40242-018-8075-4.

[785] S.J. Haigh, A. Gholinia, R. Jalil, S. Romani, L. Britnell, D.C. Elias, K.S. Novoselov, L.A. Ponomarenko, A.K. Geim, R. Gorbachev, Cross-sectional imaging of individual layers and buried interfaces of graphene-based heterostructures and superlattices, Nat. Mater. 11 (9) (2012) 764–767, https://doi.org/10.1038/NMAT3386.

[786] A.P. Rooney, A. Kozikov, A.N. Rudenko, E. Prestat, M.J. Hamer, F. Withers, Y. Cao, K.S. Noyoselov, M.I. Katsnelson, R. Gorbachev, S.J. Haigh, Observing imperfection in atomic interfaces for van der Waals heterostructures, Nano Lett. 17 (9) (2017) 5222–5228, https://doi.org/10.1021/acs.nanolett.7b01248.

[787] J. Dabrowski, G. Lippert, T. Schroeder, G. Lupina, Role of defects in the process of graphene growth on hexagonal boron nitride from atomic carbon, Appl. Phys. Lett. 105 (19) (2014) 191610, https://doi.org/10.1063/1.4901161.

[788] Y.F. Yu, G.Q. Li, L.J. Huang, A. Barrette, Y.Q. Ca, Y.L. Yu, K. Gundogdu, Y.W. Zhang, L.Y. Cao, Enhancing multifunctionalities of transition-metal dichalcogenide monolayers via cation intercalation, ACS Nano 11 (9) (2017) 9390–9396, https://doi.org/10.1021/acsnano.7b04880.

[789] Y. Cao, A. Mishchenko, G.L. Yu, E. Khestanova, A.P. Rooney, E. Prestat, A.V. Kretinin, P. Blake, M.B. Shalom, C. Woods, J. Chapman, G. Balakrishnan, I.V. Grigorieva, K.S. Novoselov, B.A. Piot, M. Potemski, K. Watanabe, T. Taniguchi, S.J. Haigh, A.K. Geim, R.V. Gorbachev, Quality heterostructures from two-dimensional crystals unstable in air by their assembly in inert atmosphere, Nano Lett. 15 (8) (2015) 4914–4921, https://doi.org/10.1021/acs.nanolett.5b00648.

[790] X.J. Song, J.Y. Sun, Y. Qi, T. Gao, Y.F. Zhang, Z.F. Liu, Graphene/h-BN heterostructures: recent advances in controllable preparation and functional applications, Adv. Energy Mater. 6 (17) (2016) 1600541, https://doi.org/10.1002/aenm.201600541.

[791] T.C. Niu, A. Li, From two-dimensional materials to heterostructures, Prog. Surf. Sci. 90 (1) (2015) 21–45, https://doi.org/10.1016/j.progsurf.2014.11.001.

[792] L. Song, Z. Liu, A.L.M. Reddy, N.T. Narayanan, J. Taha-Tijerina, J. Peng, G.H. Gao, J. Lou, R. Vajtai, P.M. Ajayan, Binary and ternary atomic layers built from carbon, boron, and nitrogen, Adv. Mater. 24 (36) (2012) 4878–4895, https://doi.org/10.1002/adma.201201792.

[793] W. Gannett, W. Regan, K. Watanabe, T. Taniguchi, M.F. Crommie, A. Zettl, Boron nitride substrates for high mobility chemical vapor deposited graphene, Appl. Phys. Lett. 98 (24) (2011) 242105, https://doi.org/10.1063/1.3599708.

[794] X.L. Ding, G.Q. Ding, X.M. Xie, F.Q. Huang, M.H. Jiang, Direct growth of few layer graphene on hexagonal boron nitride by chemical vapor deposition, Carbon 49 (7) (2011) 2522–2525, https://doi.org/10.1016/j.carbon.2011.02.022.

[795] M. Okada, T. Sawazaki, K. Watanabe, T. Taniguch, H. Hibino, H. Shinohara, R. Kitaura, Direct chemical vapor deposition growth of WS_2 atomic layers on hexagonal boron nitride, ACS Nano 8 (8) (2014) 8273–8277, https://doi.org/10.1021/nn503093k.

[796] A.M. Yan, J. Velasco, S. Kahn, K. Watanabe, T. Taniguchi, F. Wang, M.F. Crommie, A. Zettl, Direct growth of single- and few-layer MoS_2 on h-BN with preferred relative rotation angles, Nano Lett. 15 (10) (2015) 6324–6331, https://doi.org/10.1021/acs.nanolett.5b01311.

[797] M. Zhang, Y.M. Zhu, X.S. Wang, Q.L. Feng, S.L. Qiao, W. Wen, Y.F. Chen, M.H. Cui, J. Zhang, C.Z. Cai, L.M. Xie, Controlled synthesis of ZrS_2 mono layer and few layers on hexagonal boron nitride, J. Am. Chem. Soc. 137 (22) (2015) 7051–7054, https://doi.org/10.1021/jacs.5b03807.

[798] Y.M. Zhu, X.S. Wang, M. Zhang, C.Z. Cai, L.M. Xie, Thickness and temperature dependent electrical properties of ZrS_2 thin films directly grown on hexagonal boron nitride, Nano Res. 9 (10) (2016) 2931–2937, https://doi.org/10.1007/s12274-016-1178-7.

[799] L. Fu, Y.Y. Sun, N. Wu, R.G. Mendes, L.F. Chen, Z. Xu, T. Zhang, M.H. Rummeli, B. Rellinghaus, D. Pohl, L. Zhuang, L. Fu, Direct growth of MoS_2/h-BN heterostructures via a sulfide-resistant alloy, ACS Nano 10 (2) (2016) 2063–2070, https://doi.org/10.1021/acsnano.5b06254.

[800] S.S. Wang, X.C. Wang, J.H. Warner, All chemical vapor deposition growth of MoS_2:h-BN vertical van der Waals heterostructures, ACS Nano 9 (5) (2015) 5246–5254, https://doi.org/10.1021/acsnano.5b00655.

[801] S. Behura, P. Nguyen, S.W. Che, R. Debbarma, V. Berry, Large-area, transfer-free, oxide-assisted synthesis of hexagonal boron nitride films and their heterostructures with MoS_2 and WS_2, J. Am. Chem. Soc. 137 (40) (2015) 13060–13065, https://doi.org/10.1021/jacs.5b07739.

[802] D.Y. Fu, X.X. Zhao, Y.Y. Zhang, L.J. Li, H. Xu, A.R. Jang, S.I. Yoon, P. Song, S.M. Poh, T.H. Ren, Z. Ding, W. Fu, T.J. Shin, H.S. Shin, S.T. Pantelides, W. Zhou, K.P. Loh, Molecular beam epitaxy of highly crystalline monolayer molybdenum disulfide on hexagonal boron nitride, J. Am. Chem. Soc. 139 (27) (2017) 9392–9400, https://doi.org/10.1021/jacs.7b05131.

[803] A. Nagashima, Y. Gamou, M. Terai, M. Wakabayashi, C. Oshima, Electronic states of the heteroepitaxial double-layer system: graphite/monolayer hexagonal boron nitride/Ni(111), Phys. Rev. B 54 (19) (1996) 13491–13494, https://doi.org/10.1103/PhysRevB.54.13491.

[804] C. Oshima, A. Itoh, E. Rokuta, N. Tanaka, K. Yamashita, Hetero-epitaxial double-atomic-layer system of monolayer graphene monolayer h-BN on Ni(111) studied by HREELS, in: Proceedings of the International Conference on Microbeam Analysis, 2000.

[805] C. Oshima, N. Tanaka, A. Itoh, E. Rokuta, K. Yamashita, T. Sakurai, A heteroepitaxial multi-atomic-layer system of graphene and h-BN, Surf. Rev. Lett. 7 (5–6) (2000) 521–525, https://doi.org/10.1142/S0218625X00000683.

[806] C. Oshima, A. Itoh, E. Rokuta, T. Tanaka, K. Yamashita, T. Sakurai, A hetero-epitaxial-double-atomic-layer system of monolayer graphene/monolayer h-BN on Ni(111), Solid State Commun. 116 (1) (2000) 37–40, https://doi.org/10.1016/S0038-1098(00)00268-4.

[807] T. Kawasaki, T. Ichimura, H. Kishimoto, A.A. Akbar, T. Ogawa, C. Oshima, Double atomic layers of graphene/monolayer h-BN on Ni(111) studied by scanning tunneling microscopy and scanning tunneling spectroscopy, Surf. Rev. Lett. 9 (3–4) (2002) 1459–1464, https://doi.org/10.1142/S0218625X02003883.

[808] T. Gao, X.J. Song, H.W. Du, Y.F. Nie, Y.B. Chen, Q.Q. Ji, J.Y. Sun, Y.L. Yang, Y.F. Zhang, Z.F. Liu, Temperature-triggered chemical switching growth of in-plane and vertically stacked graphene-boron nitride heterostructures, Nat. Commun. 6 (2015) 6835, https://doi.org/10.1038/ncomms7835.

[809] S. Roth, F. Matsui, T. Greber, J. Osterwalder, Chemical vapor deposition and characterization of aligned and incommensurate graphene/hexagonal boron nitride heterostack on Cu(111), Nano Lett. 13 (6) (2013) 2668–2675, https://doi.org/10.1021/nl400815w.

[810] S. Roth, T. Greber, J. Osterwalder, Some like it flat: decoupled h-BN monolayer substrates for aligned graphene growth, ACS Nano 10 (12) (2016) 11187–11195, https://doi.org/10.1021/acsnano.6b06240.

[811] D.M. Wang, G.R. Chen, C.K. Li, M. Cheng, W. Yang, S. Wu, G.B. Xie, J. Zhang, J. Zhao, X.B. Lu, P. Chen, G.L. Wang, J.L. Meng, J. Tang, R. Yang, C.L. He, D.H. Liu, D.X. Shi, K. Watanabe, T. Taniguchi, J. Feng, Y.B. Zhang, G.Y. Zhang, Thermally induced graphene rotation on hexagonal boron nitride, Phys. Rev. Lett. 116 (12) (2016) 126101, https://doi.org/10.1103/PhysRevLett.116.126101.

[812] J.M. Garcia, U. Wurstbauer, A. Levy, L.N. Pfeiffer, A. Pinczuk, A.S. Plaut, L. Wang, C.R. Dean, R. Buizza, A.M. Van Der Zande, J. Hone, K. Watanabe, T. Taniguchi, Graphene growth on h-BN by molecular beam epitaxy, Solid State Commun. 152 (12) (2012) 975–978, https://doi.org/10.1016/j.ssc.2012.04.005.

[813] A. Summerfield, A. Davies, T.S. Cheng, V.V. Korolkov, Y.J. Cho, C.J. Mellor, C.T. Foxon, A.N. Khlobystov, K. Watanabe, T. Taniguchi, L. Eaves, S.V. Novikov, P.H. Beton, Strain-engineered graphene grown on hexagonal boron nitride by molecular beam epitaxy, Sci. Rep. 6 (2016) 22440, https://doi.org/10.1038/srep22440.

[814] M. Wang, S.K. Jang, W.J. Jang, M. Kim, S.Y. Park, S.W. Kim, S.J. Kahng, J.Y. Choi, R.S. Ruoff, Y.J. Song, S. Lee, A platform for large-scale graphene electronics - CVD growth of single-layer graphene on CVD-grown hexagonal boron nitride, Adv. Mater. 25 (19) (2013) 2746–2752, https://doi.org/10.1002/adma.201204904.

[815] S.M. Kim, A. Hsu, P.T. Araujo, Y.H. Lee, T. Palacios, M. Dresselhaus, J.C. Idrobo, K.K. Kim, J. Kong, Synthesis of patched or stacked graphene and hBN flakes: a route to hybrid structure discovery, Nano Lett. 13 (3) (2013) 933–941, https://doi.org/10.1021/nl303760m.

[816] J.H. Meng, X.W. Zhang, H.L. Wang, X.B. Ren, C.H. Jin, Z.G. Yin, X. Liu, H. Liu, Synthesis of in-plane and stacked graphene/hexagonal boron nitride heterostructures by combining with ion beam sputtering deposition and chemical vapor deposition, Nanoscale 7 (38) (2015) 16046–16053, https://doi.org/10.1039/c5nr04490a.

[817] Z.Y. Chen, P. Darancet, L. Wang, A.C. Crowther, Y.D. Gao, C.R. Dean, T. Taniguchi, K. Watanabe, J. Hone, C.A. Marianetti, L.E. Brus, Physical adsorption and charge transfer of molecular Br_2 on graphene, ACS Nano 8 (3) (2014) 2943–2950, https://doi.org/10.1021/nn500265f.

[818] M. Son, H. Lim, M. Hong, H.C. Choi, Direct growth of graphene pad on exfoliated hexagonal boron nitride surface, Nanoscale 3 (8) (2011) 3089–3093, https://doi.org/10.1039/c1nr10504c.

[819] S.J. Tang, G.Q. Ding, X.M. Xie, J. Chen, C. Wang, X.L. Ding, F.Q. Huang, W. Lu, M.H. Jiang, Nucleation and growth of single crystal graphene on hexagonal boron nitride, Carbon 50 (1) (2012) 329–331, https://doi.org/10.1016/j.carbon.2011.07.062.

[820] S.J. Tang, H.M. Wang, Y. Zhang, A. Li, H. Xie, X.Y. Liu, L.Q. Liu, T.X. Li, F.Q. Huang, X.M. Xie, M.H. Jiang, Precisely aligned graphene grown on hexagonal boron nitride by catalyst free chemical vapor deposition, Sci. Rep. 3 (2013) 2666, https://doi.org/10.1038/srep02666.

[821] S.J. Tang, H.M. Wang, H.S. Wang, Q.J. Sun, X.Y. Zhang, C.X. Cong, H. Xie, X.Y. Liu, X.H. Zhou, F.Q. Huang, X.S. Chen, T. Yu, F. Ding, X.M. Xie, M.H. Jiang, Silane-catalysed fast growth of large single-crystalline graphene on hexagonal boron nitride, Nat. Commun. 6 (2015) 6499, https://doi.org/10.1038/ncomms7499.

[822] P. Järvinen, A. Kumar, R. Drost, S. Kezilebieke, A. Uppstu, A. Harju, P. Liljeroth, Field-emission resonances on graphene on insulators, J. Phys. Chem. C 119 (42) (2015) 23951–23954, https://doi.org/10.1021/acs.jpcc.5b06374.

[823] X.B. Lu, W. Yang, S.P. Wang, S. Wu, P. Chen, J. Zhang, J. Zhao, J.L. Meng, G.B. Xie, D.M. Wang, G.L. Wang, T.T. Zhang, K. Watanabe, T. Taniguchi, R. Yang, D.X. Shi, G.Y. Zhang, Graphene nanoribbons epitaxy on boron nitride, Appl. Phys. Lett. 108 (11) (2016) 113103, https://doi.org/10.1063/1.4943940.

[824] V.V. Ilyasov, B.C. Meshi, V.C. Nguyen, I.V. Ershov, D.C. Nguyen, Edge and substrate-induced bandgap in zigzag graphene nanoribbons on the hexagonal nitride boron 8-ZGNR/h-BN(0001), AIP Adv. 3 (9) (2013) 092105, https://doi.org/10.1063/1.4821110.

[825] S.B. Tang, J.P. Yu, L.X. Liu, Tunable doping and band gap of graphene on functionalized hexagonal boron nitride with hydrogen and fluorine, Phys. Chem. Chem. Phys. 15 (14) (2013) 5067–5077, https://doi.org/10.1039/c3cp44460k.

[826] H.Z. Tsai, A.A. Omrani, S. Coh, H. Oh, S. Wickenburg, Y.W. Son, D. Wong, A. Riss, H.S. Jung, G.D. Nguyen, G.F. Rodgers, A.S. Aikawa, T. Taniguchi, K. Watanabe, A. Zettl, S.G. Louie, J. Lu, M.L. Cohen, M.F. Crommie, Molecular self-assembly in a poorly screened environment: F_4TCNQ on graphene/BN, ACS Nano 9 (12) (2015) 12168–12173, https://doi.org/10.1021/acsnano.5b05322.

[827] A. Riss, S. Wickenburg, L.Z. Tan, H.Z. Tsai, Y. Kim, J. Lu, A.J. Bradley, M.M. Ugeda, K.L. Meaker, K. Watanabe, T. Taniguchi, A. Zettl, F.R. Fischer, S.G. Louie, M.F. Crommie, Imaging and tuning molecular levels at the surface of a gated graphene device, ACS Nano 8 (6) (2014) 5395–5401, https://doi.org/10.1021/nn501459v.

[828] S. Wickenburg, J. Lu, J. Lischner, H.Z. Tsai, A.A. Omrani, A. Riss, C. Karrasch, A. Bradley, H.S. Jung, R. Khajeh, D. Wong, K. Watanabe, T. Taniguchi, A. Zettl, A.H.C. Neto, S.G. Louie, M.F. Crommie, Tuning charge and correlation effects for a single molecule on a graphene device, Nat. Commun. 7 (2016) 13553, https://doi.org/10.1038/ncomms13553.

[829] K.H. Ernst, Charged-molecule physics, ACS Nano 8 (6) (2014) 5375–5379, https://doi.org/10.1021/nn5030219.

[830] P. Järvinen, S.K. Hämäläinen, K. Banerjee, P. Häkkinen, M. Ijäs, A. Harju, P. Liljeroth, Molecular self-assembly on graphene on SiO_2 and h-BN substrates, Nano Lett. 13 (7) (2013) 3199–3204, https://doi.org/10.1021/nl401265f.

[831] J. Repp, P. Liljeroth, G. Meyer, Coherent electron-nuclear coupling in oligothiophene molecular wires, Nat. Phys. 6 (12) (2010) 975–979, https://doi.org/10.1038/NPHYS1802.

[832] T. Meier, R. Pawlak, S. Kawai, Y. Geng, X.S. Liu, S. Decurtins, P. Hapala, A. Baratoff, S.X. Liu, P. Jelinek, E. Meyer, T. Glatzel, Donor-acceptor properties of a single-molecule altered by on-surface complex formation, ACS Nano 11 (8) (2017) 8413–8420, https://doi.org/10.1021/acsnano.7b03954.

[833] F. Huttmann, N. Schleheck, N. Atodiresei, T. Michely, On-surface synthesis of sandwich molecular nanowires on graphene, J. Am. Chem. Soc. 139 (29) (2017) 9895–9900, https://doi.org/10.1021/jacs.7b03381.

[834] A. Kumar, K. Banerjee, A. Foster, P. Liljeroth, Two-dimensional band structure in honeycomb metal-organic frameworks, Nano Lett. 18 (2018) 5596–5602. https://doi.org/10.1021/acs.nanolett.8b02062.

[835] J.W. Colson, A.R. Woll, A. Mukherjee, M.P. Levendorf, E.L. Spitler, V.B. Shields, M.G. Spencer, J. Park, W.R. Dichtel, Oriented 2D covalent organic framework thin films on single-layer graphene, Science 332 (6026) (2011) 228–231, https://doi.org/10.1126/science.1202747.

[836] D. Ecija, J.I. Urgel, A.P. Seitsonen, W. Auwärter, J.V. Barth, Lanthanide-directed assembly of interfacial coordination architectures-from complex networks to functional nanosystems, Accounts Chem. Res. 51 (2) (2018) 365–375, https://doi.org/10.1021/acs.accounts.7b00379.

[837] F. Huttmann, D. Klar, N. Atodiresei, C. Schmitz-Antoniak, A. Smekhova, A.J. Martinez-Galera, V. Caciuc, G. Bihlmayer, S. Blügel, T. Michely, H. Wende, Magnetism in a graphene-4f-3d hybrid system, Phys. Rev. B 95 (7) (2017) 075427, https://doi.org/10.1103/PhysRevB.95.075427.

[838] J. Brede, J. Slawinska, M. Abadia, C. Rogero, J.E. Ortega, I. Piquero-Zulaica, J. Lobo-Checa, A. Arnau, J.I. Cerda, Tuning the graphene on Ir(111) adsorption regime by Fe/Ir surface-alloying, 2D Mater. 4 (1) (2017) 015016, https://doi.org/10.1088/2053-1583/4/1/015016.

[839] V. Corradini, A. Candini, D. Klar, R. Biagi, V. De Renzi, A.L. Rizzini, N. Cavani, U. del Pennino, S. Klyatskaya, M. Ruben, E. Velez-Fort, K. Kummer, N.B. Brookes, P. Gargiani, H. Wende, M. Affronte, Probing magnetic coupling between $LnPc_2$ (Ln=Tb, Er) molecules and the graphene/Ni(111) substrate with and without Au-intercalation: role of the dipolar field, Nanoscale 10 (1) (2018) 277–283, https://doi.org/10.1039/c7nr06610d.

[840] A. Barla, V. Bellini, S. Rusponi, P. Ferriani, M. Pivetta, F. Donati, F. Patthey, L. Persichetti, S.K. Mahatha, M. Papagno, C. Piarnonteze, S. Fichtner, S. Heinze, P. Gambardella, H. Brune, C. Carbone, Complex magnetic exchange coupling between Co nanostructures and Ni(111) across epitaxial graphene, ACS Nano 10 (1) (2016) 1101–1107, https://doi.org/10.1021/acsnano.5b06410.

[841] I. Grimaldi, M. Papagno, L. Ferrari, P.M. Sheverdyaeva, S.K. Mahatha, D. Pacile, C. Carbone, Magnetic decoupling of ferromagnetic metals through a graphene spacer, J. Magn. Magn. Mater. 426 (2017) 440–443, https://doi.org/10.1016/j.jmmm.2016.11.100.

[842] R. Petuya, A. Arnau, Magnetic coupling between 3d transition metal adatoms on graphene supported by metallic substrates, Carbon 116 (2017) 599–605, https://doi.org/10.1016/j.carbon.2017.02.027.

[843] C.F. Hermanns, K. Tarafder, M. Bernien, A. Kruger, Y.M. Chang, P.M. Oppeneer, W. Kuch, Magnetic coupling of porphyrin molecules through graphene, Adv. Mater. 25 (25) (2013) 3473–3477, https://doi.org/10.1002/adma.201205275.

[844] S. Bhandary, O. Eriksson, B. Sanyal, Defect controlled magnetism in FeP/graphene/Ni(111), Sci. Rep. 3 (2013) 3405, https://doi.org/10.1038/srep03405.

[845] A. Candini, V. Bellini, D. Klar, V. Corradini, R. Biagi, V. De Renzi, K. Kummer, N.B. Brookes, U. del Pennino, H. Wende, M. Affronte, Ferromagnetic exchange coupling between Fe phthalocyanine and Ni(111) surface mediated by the extended states of graphene, J. Phys. Chem. C 118 (31) (2014) 17670–17676, https://doi.org/10.1021/jp5041663.

[846] D. Klar, S. Bhandary, A. Candini, L. Joly, P. Ohresser, S. Klyatskaya, M. Schleberger, M. Ruben, M. Affronte, O. Eriksson, B. Sanyal, H. Wende, Field-regulated switching of the magnetization of Co-porphyrin on graphene, Phys. Rev. B 89 (14) (2014) 144411, https://doi.org/10.1103/PhysRevB.89.144411.

[847] V.D. Pham, J. Lagoute, O. Mouhoub, F. Joucken, V. Repain, C. Chacon, A. Bellec, Y. Girard, S. Rousset, Electronic interaction between nitrogen-doped graphene and porphyrin molecules, ACS Nano 8 (9) (2014) 9403–9409, https://doi.org/10.1021/nn503753e.

[848] B. de la Torre, M. Švec, P. Hapala, J. Redondo, O. Krejci, R. Lo, D. Manna, A. Sarmah, D. Nachtigallova, J. Tucek, P. Blonski, M. Otyepka, R. Zboril, P. Hobza, P. Jelinek, Non-covalent control of spin-state in metal-organic complex by positioning on N-doped graphene, Nat. Commun. 9 (2018) 2831, https://doi.org/10.1038/s41467-018-05163-y.

[849] J. Li, N. Lei, H.J. Hao, J. Zhou, A series of BCN nanosheets with enhanced photoelectrochemical performances, Chem. Phys. Lett. 672 (2017) 99–104, https://doi.org/10.1016/j.cplett.2017.01.054.

[850] Y.S. Al-Hamdani, D. Alfe, O.A. von Lilienfeld, A. Michaelides, Tuning dissociation using isoelectronically doped graphene and hexagonal boron nitride: Water and other small molecules, J. Chem. Phys. 144 (15) (2016) 154706, https://doi.org/10.1063/1.4945783.

[851] I. Guilhon, M. Marques, L.K. Teles, F. Bechstedt, Optical absorbance and band-gap engineering of $(BN)_{1-x}(C_2)_x$ two-dimensional alloys: Phase separation and composition fluctuation effects, Phys. Rev. B 95 (3) (2017) 035407, https://doi.org/10.1103/PhysRevB.95.035407.

[852] M. Müller, S. Behnle, C. Maichle-Mössmer, H.F. Bettinger, Boron-nitrogen substituted perylene obtained through photocyclisation, Chem. Commun. 50 (58) (2014) 7821–7823, https://doi.org/10.1039/c4cc01424c.

[853] D. Bonifazi, F. Fasano, M.M. Lorenzo-Garcia, D. Marinelli, H. Oubaha, J. Tasseroul, Boron-nitrogen doped carbon scaffolding: organic chemistry, self-assembly and materials applications of borazine and its derivatives, Chem. Commun. 51 (83) (2015) 15222–15236, https://doi.org/10.1039/c5cc06611e.

[854] M. Krieg, F. Reicherter, P. Haiss, M. Ströbele, K. Eichele, M.J. Treanor, R. Schaub, H.F. Bettinger, Construction of an internally B_3N_3-doped nanographene molecule, Angew. Chem.-Int. Edit. 54 (28) (2015) 8284–8286, https://doi.org/10.1002/anie.201412165.
[855] X.Y. Wang, F.D. Zhuang, X.C. Wang, X.Y. Cao, J.Y. Wang, J. Pei, Synthesis, structure and properties of C_3-symmetric heterosuperbenzene with three BN units, Chem. Commun. 51 (21) (2015) 4368–4371, https://doi.org/10.1039/c4cc10105g.
[856] X.Y. Wang, F.D. Zhuang, R.B. Wang, X.C. Wang, X.Y. Cao, J.Y. Wang, J. Pei, A straightforward strategy toward large BN-embedded π-systems: Synthesis, structure, and optoelectronic properties of extended BN heterosuperbenzenes, J. Am. Chem. Soc. 136 (10) (2014) 3764–3767, https://doi.org/10.1021/ja500117z.
[857] J. Dosso, J. Tasseroul, F. Fasano, D. Marinelli, N. Biot, A. Fermi, D. Bonifazi, Synthesis and optoelectronic properties of hexa-peri-hexabenzoborazinocoronene, Angew. Chem.-Int. Edit. 56 (16) (2017) 4483–4487, https://doi.org/10.1002/anie.201700907.
[858] M.M. Lorenzo-Garcia, D. Bonifazi, Renaissance of an old topic: From borazines to BN-doped nanographenes, Chimia 71 (9) (2017) 550–557, https://doi.org/10.2533/chimia.2017.550.
[859] F. Ciccullo, A. Calzolari, I. Pis, S.A. Savu, M. Krieg, H.F. Bettinger, E. Magnano, T. Chassé, M.B. Casu, A quasi-free-standing single layer of a B_3N_3-doped nanographene molecule deposited on Au(111) single crystals, J. Phys. Chem. C 120 (31) (2016) 17645–17651, https://doi.org/10.1021/acs.jpcc.6b06237.
[860] X.Y. Wang, J.Y. Wang, J. Pei, BN heterosuperbenzenes: Synthesis and properties, Chem.-Eur. J. 21 (9) (2015) 3528–3539, https://doi.org/10.1002/chem.201405627.
[861] M. Schwarz, M. Garnica, F. Fasano, N. Demitri, D. Bonifazi, W. Auwärter, BN-patterning of metallic substrates through metal coordination of decoupled borazines, Chem.-Eur. J. 24 (38) (2018) 9565–9671, https://doi.org/10.1002/chem.201800849.
[862] D.P. Gopalan, P.C. Mende, S.C. de la Barrera, S. Dhingra, J. Li, K.H. Zhang, N.A. Simonson, J.A. Robinson, N. Lu, Q.X. Wang, M.J. Kim, B. D'Urso, R.M. Feenstra, Formation of hexagonal boron nitride on graphene-covered copper surfaces, J. Mater. Res. 31 (7) (2016) 945–958, https://doi.org/10.1557/jmr.2016.82.
[863] K. Sakaushi, A. Lyalin, S. Tominaka, T. Taketsugu, K. Uosaki, Two-dimensional corrugated porous carbon-, nitrogen-framework/metal heterojunction for efficient multielectron transfer processes with controlled kinetics, ACS Nano 11 (2) (2017) 1770–1779, https://doi.org/10.1021/acsnano.6b07711.
[864] Q.H. Weng, X.B. Wang, X. Wang, Y. Bando, D. Golberg, Functionalized hexagonal boron nitride nanomaterials: emerging properties and applications, Chem. Soc. Rev. 45 (14) (2016) 3989–4012, https://doi.org/10.1039/c5cs00869g.
[865] B. Cai, S.L. Zhang, Z. Yan, H.B. Zeng, Noncovalent molecular doping of two-dimensional materials, ChemNanoMat 1 (8) (2015) 542–557, https://doi.org/10.1002/cnma.201500102.
[866] A.P.M. Barboza, M.J.S. Matos, H. Chacham, R.J.C. Batista, A.B. de Oliveira, M.S.C. Mazzoni, B.R.A. Neves, Compression-induced modification of boron nitride layers: A conductive two-dimensional BN compound, ACS Nano 12 (6) (2018) 5866–5872, https://doi.org/10.1021/acsnano.8b01911.
[867] H. Lim, S.I. Yoon, G. Kim, A.R. Jang, H.S. Shin, Stacking of two-dimensional materials in lateral and vertical directions, Chem. Mat. 26 (17) (2014) 4891–4903, https://doi.org/10.1021/cm502170q.
[868] J. Pan, S. Lany, Y. Qi, Computationally driven two-dimensional materials design: What is next? ACS Nano 11 (8) (2017) 7560–7564, https://doi.org/10.1021/acsnano.7b04327.
[869] A. Hirsch, The era of carbon allotropes, Nat. Mater. 9 (11) (2010) 868–871, https://doi.org/10.1038/nmat2885.
[870] F. Zhang, Y. Wang, C. Erd, K. Wang, P. Moradifar, V. Crespi, N. Alem, Full Orientation Control of Epitaxial MoS_2 on hBN Assisted by Substrate Defects, 2018, arXiv:1801.00487.
[871] A.I. Khan, T. Chakraborty, N. Acharjee, S. Subrina, Stanene-hexagonal boron nitride heterobilayer: Structure and characterization of electronic property, Sci. Rep. 7 (2017) 16347, https://doi.org/10.1038/s41598-017-16650-5.
[872] M.Y. Wang, L.P. Liu, C.C. Liu, Y.G. Yao, Van der Waals heterostructures of germanene, stanene, and silicene with hexagonal boron nitride and their topological domain walls, Phys. Rev. B 93 (15) (2016) 155412, https://doi.org/10.1103/PhysRevB.93.155412.
[873] C. Wang, J. Sun, B.T. Zhang, J. Zhang, X.T. Tao, An ab initio investigation of phosphorene/hexagonal boron nitride heterostructures with defects for high performance photovoltaic applications, Appl. Surf. Sci. 423 (2017) 1003–1011, https://doi.org/10.1016/j.apsusc.2017.06.274.
[874] L. Liu, J. Park, D.A. Siegel, K.F. McCarty, K.W. Clark, W. Deng, L. Basile, J.C. Idrobo, A.P. Li, G. Gu, Heteroepitaxial growth of two-dimensional hexagonal boron nitride templated by graphene edges, Science 343 (6167) (2014) 163–167, https://doi.org/10.1126/science.1246137.
[875] G.H. Han, J.A. Rodriguez-Manzo, C.W. Lee, N.J. Kybert, M.B. Lerner, Z.J. Qi, E.N. Dattoli, A.M. Rappe, M. Drndic, A.T.C. Johnson, Continuous growth of hexagonal graphene and boron nitride in-plane heterostructures by atmospheric pressure chemical vapor deposition, ACS Nano 7 (11) (2013) 10129–10138, https://doi.org/10.1021/nn404331f.
[876] C.X. Wang, J.L. Zuo, L.F. Tan, M.Q. Zeng, Q.Q. Zhang, H.N. Xia, W.H. Zhang, Y.S. Fu, L. Fu, Hexagonal boron nitride-graphene core-shell arrays formed by self-symmetrical etching growth, J. Am. Chem. Soc. 139 (40) (2017) 13997–14000, https://doi.org/10.1021/jacs.7b07718.
[877] E. Maeda, Y. Miyata, H. Hibino, Y. Kobayashi, R. Kitaura, H. Shinohara, Orientation-controlled growth of hexagonal boron nitride monolayers templated from graphene edges, Appl. Phys. Express 10 (5) (2017) 055102, https://doi.org/10.7567/APEX.10.055102.
[878] L. Ci, L. Song, C.H. Jin, D. Jariwala, D.X. Wu, Y.J. Li, A. Srivastava, Z.F. Wang, K. Storr, L. Balicas, F. Liu, P.M. Ajayan, Atomic layers of hybridized boron nitride and graphene domains, Nat. Mater. 9 (5) (2010) 430–435, https://doi.org/10.1038/nmat2711.
[879] A. Goriachko, P.V. Melnik, M.G. Nakhodkin, A.A. Zakharov, H. Over, Hexagonal C and BN superstructures on Ru(0001) and Ge(111), Materialwiss. Werkstofftech. 44 (2–3) (2013) 129–135, https://doi.org/10.1002/mawe.201300108.
[880] S. Nappini, I. Pis, T.O. Mentes, A. Sala, M. Cattelan, S. Agnoli, F. Bondino, E. Magnano, Formation of a quasi-free-standing single layer of graphene and hexagonal boron nitride on Pt(111) by a single molecular precursor, Adv. Funct. Mater. 26 (7) (2016) 1120–1126, https://doi.org/10.1002/adfm.201503591.
[881] S. Nappini, I. Pis, G. Carraro, E. Celasco, M. Smerieri, L. Savio, E. Magnano, F. Bondino, On-surface synthesis of different boron-nitrogen-carbon heterostructures from dimethylamine borane, Carbon 120 (2017) 185–193, https://doi.org/10.1016/j.carbon.2017.05.026.
[882] M. Petrovic, M. Horn-von Hoegen, F.J.M. zu Heringdorf, Lateral heterostructures of hexagonal boron nitride and graphene: BCN alloy formation and microstructuring mechanism, Appl. Surf. Sci. 455 (2018) 1086–1094, https://doi.org/10.1016/j.apsusc.2018.06.057.
[883] M.P. Levendorf, C.J. Kim, L. Brown, P.Y. Huang, R.W. Havener, D.A. Muller, J. Park, Graphene and boron nitride lateral heterostructures for atomically thin circuitry, Nature 488 (7413) (2012) 627–632, https://doi.org/10.1038/nature11408.
[884] Z. Liu, L.L. Ma, G. Shi, W. Zhou, Y.J. Gong, S.D. Lei, X.B. Yang, J.N. Zhang, J.J. Yu, K.P. Hackenberg, A. Babakhani, J.C. Idrobo, R. Vajtai, J. Lou, P.M. Ajayan, In-plane heterostructures of graphene and hexagonal boron nitride with controlled domain sizes, Nat. Nanotechnol. 8 (2) (2013) 119–124, https://doi.org/10.1038/NNANO.2012.256.
[885] L.X. Chen, L. He, H.S. Wang, H.M. Wang, S.J. Tang, C.X. Cong, H. Xie, L. Li, H. Xia, T.X. Li, T.R. Wu, D.L. Zhang, L.W. Deng, T. Yu, X.M. Xie, M.H. Jiang, Oriented graphene nanoribbons embedded in hexagonal boron nitride trenches, Nat. Commun. 8 (2017) 14703, https://doi.org/10.1038/ncomms14703.
[886] M.C. Lemme, D.C. Bell, J.R. Williams, L.A. Stern, B.W.H. Baugher, P. Jarillo-Herrero, C.M. Marcus, Etching of graphene devices with a helium ion beam, ACS Nano 3 (9) (2009) 2674–2676, https://doi.org/10.1021/nn900744z.
[887] X. Tan, H.A. Tahini, S.C. Smith, Hexagonal boron nitride and graphene in-plane heterostructures: An experimentally feasible approach to charge-induced switchable CO_2 capture, Chem. Phys. 478 (2016) 139–144, https://doi.org/10.1016/j.chemphys.2016.04.001.
[888] P. Karamanis, N. Otero, C. Pouchan, Unleashing the quadratic nonlinear optical responses of graphene by confining white-graphene (h-BN) sections in its framework, J. Am. Chem. Soc. 136 (20) (2014) 7464–7473, https://doi.org/10.1021/ja502631w.
[889] M. Kan, J. Zhou, Q. Wang, Q. Sun, P. Jena, Tuning the band gap and magnetic properties of BN sheets impregnated with graphene flakes, Phys. Rev. B 84 (20) (2011) 205412, https://doi.org/10.1103/PhysRevB.84.205412.
[890] M. Maruyama, S. Okada, Magnetic properties of graphene quantum dots embedded in h-BN sheet, J. Phys. Chem. C 120 (2) (2016) 1293–1302, https://doi.org/10.1021/acs.jpcc.5b09882.
[891] M. Zhao, Y.H. Huang, F. Ma, T.W. Hu, K.W. Xu, P.K. Chu, Electronic states in hybrid boron nitride and graphene structures, J. Appl. Phys. 114 (6) (2013) 063707, https://doi.org/10.1063/1.4817883.
[892] S. Cahangirov, S. Ciraci, Two-dimensional C/BN core/shell structures, Phys. Rev. B 83 (16) (2011) 165448, https://doi.org/10.1103/PhysRevB.83.165448.
[893] M. Kan, Y.W. Li, Q. Sun, Recent advances in hybrid graphene-BN planar structures, Wiley Interdiscip. Rev.-Comput. Mol. Sci. 6 (1) (2016) 65–82, https://doi.org/10.1002/wcms.1237.
[894] Q. Peng, S. De, Tunable band gaps of mono-layer hexagonal BNC heterostructures, Physica E 44 (7–8) (2012) 1662–1666, https://doi.org/10.1016/j.physe.2012.04.011.
[895] X.L. Liu, Z.H. Wei, I. Balla, A.J. Mannix, N.P. Guisinger, E. Luijten, M.C. Hersam, Self-assembly of electronically abrupt borophene/organic lateral heterostructures, Sci. Adv. 3 (2) (2017) e1602356, https://doi.org/10.1126/sciadv.1602356.
[896] H.Y. Zhang, J. Ji, A.A. Gonzalez, J.H. Choi, Tailoring photoelectrochemical properties of semiconducting transition metal dichalcogenide nanolayers with porphyrin functionalization, J. Mater. Chem. C 5 (43) (2017) 11233–11238, https://doi.org/10.1039/c7tc02861j.
[897] F. Rückerl, T. Klaproth, R. Schuster, B. Buchner, M. Knupfer, Surface functionalization of WSe_2 by $F_{16}CoPc$, Phys. Status Solidi B-Basic Solid State Phys. 254 (6) (2017) 1600656, https://doi.org/10.1002/pssb.201600656.
[898] X. Ling, Y.X. Lin, Q. Ma, Z.Q. Wang, Y. Song, L.L. Yu, S.X. Huang, W.J. Fang, X. Zhang, A.L. Hsu, Y.Q. Bie, Y.H. Lee, Y.M. Zhu, L.J. Wu, J. Li, P. Jarillo-Herrero, M. Dresselhaus, T. Palacios, J. Kong, Parallel stitching of 2D materials, Adv. Mater. 28 (12) (2016) 2322–2329, https://doi.org/10.1002/adma.201505070.
[899] J.F. Zhang, W.Y. Xie, X.H. Xu, S.B. Zhang, J.J. Zhao, Structural and electronic properties of interfaces in graphene and hexagonal boron nitride lateral heterostructures, Chem. Mat. 28 (14) (2016) 5022–5028, https://doi.org/10.1021/acs.chemmater.6b01764.
[900] S. Bhowrnick, A.K. Singh, B.I. Yakobson, Quantum dots and nanoroads of graphene embedded in hexagonal boron nitride, J. Phys. Chem. C 115 (20) (2011) 9889–9893, https://doi.org/10.1021/jp200671p.

[901] Y.L. Wang, Y. Ding, First-principles study of the electronic and magnetic properties of 4-8 line-defect-embedded BN sheets decorated with transition metals, Ann. Phys. 526 (9–10) (2014) 415–422, https://doi.org/10.1002/andp.201400042.
[902] J. Xie, L. Liao, Y.J. Gong, Y.B. Li, F.F. Shi, A. Pei, J. Sun, R.F. Zhang, B. Kong, R. Subbaraman, J. Christensen, Y. Cui, Stitching h-BN by atomic layer deposition of LiF as a stable interface for lithium metal anode, Sci. Adv. 3 (11) (2017) eaao3170, https://doi.org/10.1126/sciadv.aao3170.
[903] A. Pakdel, Y. Bando, D. Golberg, Plasma-assisted interface engineering of boron nitride nanostructure films, ACS Nano 8 (10) (2014) 10631–10639, https://doi.org/10.1021/nn5041729.
[904] M. Müllner, J. Balajka, M. Schmid, U. Diebold, S.F.L. Mertens, Self-limiting adsorption of WO_3 oligomers on oxide substrates in solution, J. Phys. Chem. C 121 (36) (2017) 19743–19750, https://doi.org/10.1021/acs.jpcc.7b04076.
[905] A.A. Muhabie, C.C. Cheng, J.J. Huang, Z.S. Liao, S.Y. Huang, C.W. Chiu, D.J. Lee, Non-covalently functionalized boron nitride mediated by a highly self-assembled supramolecular polymer, Chem. Mat. 29 (19) (2017) 8513–8520, https://doi.org/10.1021/acs.chemmater.7b03426.
[906] L.R. Xu, X. Zhou, W.Q. Tian, T. Gao, Y.F. Zhang, S.B. Lei, Z.F. Liu, Surface-confined single-layer covalent organic framework on single-layer graphene grown on copper foil, Angew. Chem.-Int. Edit. 53 (36) (2014) 9564–9568, https://doi.org/10.1002/anie.201400273.
[907] J. Sakamoto, J. van Heijst, O. Lukin, A.D. Schlüter, Two-dimensional polymers: Just a dream of synthetic chemists? Angew. Chem.-Int. Edit. 48 (6) (2009) 1030–1069, https://doi.org/10.1002/anie.200801863.
[908] D.H. Deng, K.S. Novoselov, Q. Fu, N.F. Zheng, Z.Q. Tian, X.H. Bao, Catalysis with two-dimensional materials and their heterostructures, Nat. Nanotechnol. 11 (3) (2016) 218–230, https://doi.org/10.1038/NNANO.2015.340.
[909] C.J. Huang, C. Chen, M.W. Zhang, L.H. Lin, X.X. Ye, S. Lin, M. Antonietti, X.C. Wang, Carbon-doped BN nanosheets for metal-free photoredox catalysis, Nat. Commun. 6 (2015) 7698, https://doi.org/10.1038/ncomms8698.